Constitutive Equations for Superelasticity in Crystalline Shape-Memory Materials

by

Prakash Thamburaja

B.Eng. Mechanical Engineering
Imperial College of Science, Technology and Medicine, 1996

S.M. Mechanical Engineering
Massachusetts Institute of Technology, 2000

Submitted to the Department of Mechanical Engineering
in partial fulfillment of the requirements for the degree of

Doctor of Philosophy

at the

MASSACHUSETTS INSTITUTE OF TECHNOLOGY

September 2002

Author .....
Department of Mechanical Engineering
August 9, 2002

Certified by.....
Lallit Anand
Professor of Mechanical Engineering
Thesis Supervisor

Accepted by...
Ain A. Sonin
Chairman, Department Committee on Graduate Students

Constitutive Equations for Superelasticity in Crystalline Shape-Memory Materials

by

Prakash Thamburaja

Submitted to the Department of Mechanical Engineering
on August 9, 2002, in partial fulfillment of the
requirements for the degree of
Doctor of Philosophy

Abstract

A crystal-mechanics-based constitutive model for polycrystalline shape-memory materials has been developed. The model has been implemented in a finite-element program. Finite-element calculations of polycrystal response were performed using two methods: (1) The full-finite element method where each element represents a single crystal chosen from a set of crystal orientations which approximate the initial crystallographic texture; (2) A simplified model using the Taylor assumption (1938) where each element represents a collection of single crystals at a material point. The macroscopic stress-strain responses are calculated as volume averages over the entire aggregate.

A variety of superelastic experiments were performed on initially-textured Ti-Ni rods and sheets. The predicted stress-strain curves from finite-element calculations are shown to be in good accord with the corresponding experiments.

For the Ti-Ni sheet, strain-temperature response at a fixed stress was also experimentally studied. The model was also shown to accurately predict the results from these important experiments. Further, by performing superelastic experiments at moderately high strain rates, the effects of self-heating and cooling due to the phase transformations are shown to be captured well by the constitutive model. The thermo-mechanically-coupled theory is also able to capture the resulting inhomogeneous deformations associated with the nucleation and propagation of transformation fronts.

Finally, an isotropic constitutive model has also been developed and implemented in a finite-element program. This simple model provides a reasonably accurate and computationally-inexpensive tool for purposes of engineering design.

Thesis Supervisor: Lallit Anand
Title: Professor of Mechanical Engineering

Acknowledgments

First and foremost, I would like to thank my advisor Prof. Lallit Anand for his support. His high academic standards and great vision will always be a source of inspiration to me. I would also like to thank Prof. Mary Boyce, Prof. David Parks and Prof. William Carter for serving on my committee.

We are also thankful to Gao Shan and Prof. Yi Sung of the Nanyang Technological University, Singapore for supplying us with the raw material and the experimental results for their Ti-Ni sheet.

To the Mechanics and Materials group - Nicoli Ames, Jeremy Levitan, Matt Busche, Jin Yi, Cheng Su, Theodora Tzianetopoulou, Hang Qi, Rajdeep Sharma, Mats Danielsson, Ethan Parsons, Franco Capaldi and others, thank you very much for all the great conversations and good times we have had. I wish all of you the best of luck in your future endeavors.

To Ray Hardin and Leslie Regan, thank you very much for taking care of all the administrative details and providing me with your unerring advice.

To Brian P. Gearing, my colleague and most of all friend for the last six years, thank you very much for all that you have done for me. May success shine on you constantly.

To my family, Drs. Thamburaja and Surabi, Sree Priya and Jeyalakshmi, your constant love, affection and support have been very instrumental throughout my life journey thus far. Thank you very much for everything.

The financial support for this work was provided by the National Science Foundation under Grant CMS0002930.

Contents

List of Figures

Chapter 1

Introduction

Shape-memory alloys (SMAs) are finding increased use as functional/smart-materials for a variety of applications (see Figure 1-1). The individual grains in these polycrystalline materials can abruptly change their lattice structure in the presence of suitable thermo-mechanical loading. This capability of undergoing a solid-solid, diffusionless, displacive phase transformation leads to the technologically-important properties of *superelasticity*[1] and *shape-memory.*

Currently, the near-equiatomic Ti-Ni alloys are the most popular shape-memory materials for applications. The reversible transformations between the various phases observed upon changing the temperature, under zero stress, in the case of Ti-Ni are as follows. The transformation sequence upon cooling from a high-temperature body-centered-cubic superlattice, B2, austenite phase is first to a rhombohedral R-phase, and then to a monoclinic martensite phase. Upon heating, the reverse transformation takes place; however, the R-phase is not observed. Under certain conditions, the R-phase may be suppressed, and the only transformation in a specimen is the cubic-to-monoclinic transition. Under zero stress, shape-memory materials are distinguished by the following four temperatures: θ_{ms}, martensite start temperature; θ_{mf}, martensite finish temperature; θ_{as}, austenite start temperature; and θ_{af}, austenite finish temperature.

[1]Also called pseudoelasticity by transformation.

As mentioned previously, an important characteristic response of shape-memory materials is *superelasticity*. A schematic diagram for the superelastic response is shown in Figure 1-2a. This is a consequence of a stress-induced transformation from austenite to martensite and back when a sample is tested in cyclic uniaxial extension, between zero and a finite but small ($\approx$5%) strain, under quasi-static conditions at a constant ambient temperature above its austenite finish temperature, θ_{af}. There is little or no permanent deformation experienced by the specimen in such a strain cycle; this gives an impression that the material has only undergone elastic deformation, and hence the term *superelastic*. However, there is hysteresis; the mechanism responsible for the hysteresis is the motion of sharp interfaces between the two material phases. For a given material, the size and other qualitative features of the "flag-type" hysteresis loops usually change with the loading rate and the temperature at which the test takes place. Superelastic response can also be triggered by a change in temperature after a pre-stress is applied on the shape-memory material. This is widely known as the *strain-temperature cycling* response. A schematic diagram for the strain-temperature cycling response is shown in Figure 1-2b.

The *shape-memory effect by transformation* occurs when a material which is initially austenitic is first tested in isothermal uniaxial extension at a temperature $\theta_{ms} < \theta < \theta_{af}$. During forward loading, a transformation from austenite to martensite occurs, but upon reversal and unloading to zero stress, the transformation strain does not recover until the temperature is subsequently raised to $\theta > \theta_{af}$.

If the temperature is lower than the martensite finish temperature, $\theta < \theta_{mf}$, the material is initially in the martensitic state. In this condition SMAs can also exhibit superelastic and shape-memory effects, but the inelastic strain is caused by reorientation of the martensitic variants, and not by transformation (e.g. Saburi and Nenno, 1981; Miyazaki and Otsuka, 1989; Otsuka and Wayman, 1999).

There is substantial activity worldwide to construct suitable constitutive models for shape-memory materials, and several existing one-dimensional constitutive models can capture the major response characteristics of SMAs reasonably well (e.g. Liang and Rogers, 1990; Abeyaratne and Knowles, 1993; Ivshin and Pence, 1994; Bekker

and Brinson, 1997).

Prominent amongst the three-dimensional models are the ones proposed by Sun and Hwang (1993a,b), Boyd and Lagoudas (1994,1996), Patoor et al. (1996), Auricchio and Taylor (1997), Lu and Weng (1998), Gao et al. (2000) and others, but most of these models have been shown to work best for uniaxial loading. It is difficult to test the applicability of these models in real three-dimensional situations because there is a lack of pedigreed multi-axial experimental data, although some nice experiments have been recently reported by Lim and McDowell (1999). Indeed, the predictions from these models which have been calibrated from data for simple tension, have not even been verified for the case of simple shear. Also, these models do not adequately capture the asymmetry observed between tension and compression superelastic experiments, where it is found that at a given test temperature: (*i*) the stress level required to nucleate the martensitic phase from the parent austenitic phase is considerably higher in compression than in tension; (*ii*) the transformation strain measured in compression is smaller than that in tension; and (*iii*) the hysteresis loop generated in compression is wider (measured along the stress axis) than the hysteresis loop generated in tension. These major differences between the tension and compression response of a Ti-Ni rod alloy in superelasticity experiments (to be described more fully later) are shown in Figure 1-3. Anisotropic effects are even manifested in a Ti-Ni sheet alloy, as shown in Figure 1-4 where the superelastic tensile response along the rolling and transverse direction is shown. Further investigation on superelastic behavior at various deformation rates also show that : (i) The stress-strain response "hardens" more as the rate of deformation increases; and (ii) the hysteresis loops get wider (measured along the stress axis) as the deformation rate increases. These experimental results on a Ti-Ni sheet conducted at various deformation rates at the same ambient temperature are shown in Figure 1-5.

It is now well recognized that shape-memory materials derive their unusual and inherently nonlinear and anisotropic properties from the fine-scale rearrangements of phases, or "microstructures," and that the strain produced by the superelasticity effect depends on crystal orientations. Specially-oriented single crystals of some

shape-memory materials can produce sizeable strains ($\approx$ 10%) due to phase transformations. In applications, shape-memory materials are typically polycrystalline in nature, and are usually processed by casting, followed by hot-working (drawing for rods and wires, and rolling for sheet) and suitable heat treatments. Polycrystalline SMAs so produced are usually strongly textured, and various researchers have recently emphasized that crystallographic texture is very important in determining the overall properties of SMAs (e.g. Inoue et al., 1996; Zhao et al., 1998; Shu and Bhattacharya, 1998; Gall and Sehitoglu, 1999).

Shu and Bhattacharya (1998) have developed an analytical geometric model to estimate the effects of initial crystallographic texture on the amount of recoverable strains in SMAs. They show that texture is important in determining the amount of shape-memory effect in polycrystals. In particular, they qualitatively show that even though Ti-Ni and Cu-Zn-Al based SMAs both undergo cubic-monoclinic transformations, and both have similar transformation strains at the single-crystal level, it is the difference in the crystallographic texture between the two polycrystalline SMAs in bulk sheet, rod, and wire forms which gives rise to a larger shape-memory effect in Ti-Ni.

More recently, Gall and Sehitoglu (1999) have studied the stress-strain behavior of polycrystalline Ti-Ni under tension versus compression. They used a micromechanical model which incorporates single-crystal constitutive equations and experimentally measured polycrystalline texture into a "self-consistent" model for polycrystals (Patoor et al., 1996) to argue that the tension/compression asymmetry in Ti-Ni shape-memory alloys was related to the initial crystallographic texture of their specimens[2].

An important feature of the superelastic response of Ti-Ni wires observed by Shaw

[2]We do not completely understand the model and computational procedure used by Gall and Sehitoglu (1999) because sufficient details are not provided by the authors. It appears that these authors consider a model in which the transformation rates are determinable only if the model contains an invertible "interaction energy matrix" (their equation 11). They attribute the magnitude of the tension-compression asymmetry in the superelasticity behavior of their Ti-Ni material to the magnitudes of the terms of the interaction moduli. In contrast, we show in this work that the major features of the tension-compression asymmetry in textured drawn bars of Ti-Ni are captured even if the interaction matrix is set to zero.

and Kyriakides (1997) was that the transformation from austenite-to-martensite did not occur homogeneously in their specimens. Further investigations by Shaw and Kyriakides [2] on Ti-Ni sheets also showed that the phase transformation occurred by the nucleation and propagation of fronts, and that because of the exothermic and endothermic nature of the austenite-to-martensite and martensite-to-austenite transformations, respectively, there were substantial measurable temperature changes in the gage section of their sheet tensile specimens. These temperature changes also result in an "apparent hardening" of the nominal superelastic stress-strain curves, as observed by Entemeyer *et al.* (2000).

With this brief introduction, the purpose of this thesis is to formulate and numerically implement a crystal-mechanics-based constitutive model for shape-memory materials, and to verify whether the model is able to capture the major features of the experimentally-measured effects of crystallographic texture on superelasticity of polycrystalline Ti-Ni alloy, and also to numerically capture the inhomogeneous deformation associated with the nucleation and propagation of transformation fronts, and also the apparent hardening of the nominal stress-strain curves observed in the experiments as the loading rate is increased.

The plan of this thesis is as follows: In Section 2.1, we formulate a rate-independent single-crystal constitutive model, where the inelastic deformations occur by phase transformations. We have implemented our constitutive model in the finite-element program ABAQUS/Explicit (1999,2001); algorithmic details of the time-integration procedure used to implement the model in the finite-element code are given in Appendix A. This computational capability allows us to perform two types of finite-element calculations: (*i*) where a finite-element represents a single grain and the constitutive response is given through a single-crystal constitutive model, and (*ii*) where a finite-element quadrature point represents a material point in a polycrystalline sample and the constitutive response is given through a Taylor-type polycrystal model.

In Section 2.2 the results from experimental measurements of crystallographic texture of a Ti-Ni rod-alloy are described. Material parameters appearing in the

constitutive model for this alloy have been evaluated. The procedure to determine these parameters from differential scanning calorimetric (DSC) measurements, and a room temperature isothermal superelasticity experiment in tension are also outlined in Section 1-3. We show that our model is able to reproduce the stress-strain curve of the initially-textured Ti-Ni alloy in simple tension. Next, with the model so calibrated, we show that the predictions for the stress-strain curves from the model are in good agreement with superelasticity experiments on the same pre-textured material in simple compression, thin-walled tubular torsion, combined tension-torsion, and path change tension-torsion.

To determine the degree to which the initial texture controls the macroscopic asymmetry in the superelastic response in tension and compression, we have also compared the predicted stress-strain responses in simple tension and simple compression if the initial texture is taken to be random. Our calculations show that in this case the response in compression is very similar to that in tension. Accordingly, we conclude that crystallographic texture is the prime cause for the observed tension-compression asymmetry in shape-memory materials.

In Section 2.2.1, we evaluate the applicability of a Taylor-type model for inelastic deformations by phase transformation. Some previous work done by Bhattacharya and Kohn (1996,1997) shows that the Taylor model provides a good approximation in estimating the transformation induced strain. Our calculations also show that such a Taylor-type model is also able to predict reasonably well the macroscopic stress-strain curves.

In Section 2.2.2 we examine the applicability of our model to another Ti-Ni alloy for which Shaw and Kyriakides (1995) have conducted careful experiments at a variety of different temperatures. Unfortunately, these authors do not report on the initial crystallographic texture of their material. However, since they conducted their experiments on drawn Ti-Ni wires, we assume that their material has a texture similar to our drawn rods. We estimate the constitutive parameters for their material from their DSC results, and their stress-strain results from a pseudoleastic tension test at representative temperature. We show that the predictions for the stress-strain

response from our constitutive model are in good agreement with the results from their superelastic experiments at a few temperatures, $\theta > \theta_{af}$.

Shaw and Kyriakides (1995) also report on displacement controlled experiments at temperatures in the range $\theta_{ms} < \theta < \theta_{af}$. In these experiments the martensite that forms during forward deformation does not completely transform back to austenite upon reversing the deformation and decreasing the stress to zero. Although Shaw and Kyriakides (1995) did not subsequently increase the temperature at zero stress to $\theta > \theta_{as}$ to show the shape-memory effect, we have numerically simulated such an experiment, and show that our model is able to also capture the shape-memory effect by transformation.

In Section 2.3 we investigate the superelastic response of initially-textured Ti-Ni sheet. Here we show the constitutive model, when suitably numerically implemented and calibrated, is shown to accurately predict the anisotropic superelastic response of tension specimens which were cut along different directions to the rolling direction of the sheet. Also, the strain-temperature cycling experiments under different constant axial stresses are predicted with reasonable accuracy. The effects of self-heating and cooling due to the exothermic and endothermic nature of the austenite-to-martensite and martensite-to-austenite transformations were investigated by performing superelastic tension experiments at strain rates which are high enough to result in non-isothermal testing conditions. The thermo-mechanically coupled theory is able to capture the resulting *inhomogeneous* deformation associated with the nucleation and propagation of transformation fronts, and also the "apparent hardening" of the nominal stress-strain curves observed in the experiments.

In Section 2 we have successfully applied our crystal-mechanics-based theory to model the superelastic behavior of Ti-Ni rods and sheets under various multi-axial and thermo-mechanical loading conditions. However, as expected, the three-dimensional crystal-mechanics-based theory for polycrystalline materials is computationally intensive, and at present not ideally suited for application in routine engineering design.

Guided by the success of the crystal-mechanics theory, we formulate a simpler "isotropic" theory in Chapter 3, in which the major difference is that the evolution

equation for $\mathbf{F}^p$ is now given by

$$\dot{\mathbf{F}}^p \mathbf{F}^{p-1} = \dot{\xi}\, \mathbf{N}^p, \tag{1.1}$$

where $\dot{\xi}$ denotes a single transformation rate, and $\mathbf{N}^p$ a suitable *symmetric* transformation tensor which determines the direction of transformation and its magnitude. Unlike the crystal-mechanics theory in which the transformation tensors are determined by crystallographically based dyads $\mathbb{S}_0^\alpha$, the transformation tensor in the isotropic theory is based on considerations of the stress state during transformation. Although a crystal-mechanics theory is more accurate, an isotropic theory based on such a flow rule, when suitably numerically implemented and calibrated, and its range of applicability verified, should be more immediately useful for the design of components and systems made from shape-memory materials.

The plan of Chapter 3 paper is as follows. We develop the isotropic model in Section 3.1; we have implemented the model in the finite element programs ABAQUS/Explicit and ABAQUS/Standard (2001). Algorithmic details of the time-integration procedure and Jacobian matrices for the numerical implementation are given in Appendix E and F, respectively. In Section 3.2.1 and 3.2.2 we evaluate the applicability of this isotropic model to reproduce the experimentally-measured superelastic response of the polycrystalline Ti-Ni sheets and rods, which experimental results are reported in Chapter 2. The two manifestations of superelasticity — stress-strain response at a fixed temperature and strain-temperature response at a fixed stress — are explored. In Section 3.3 we use our computational capability to show that it may be used to analyze the response of a technologically important structure — a bio-medical stent.

We conclude and provide suggestions for future work in Chapter 4.

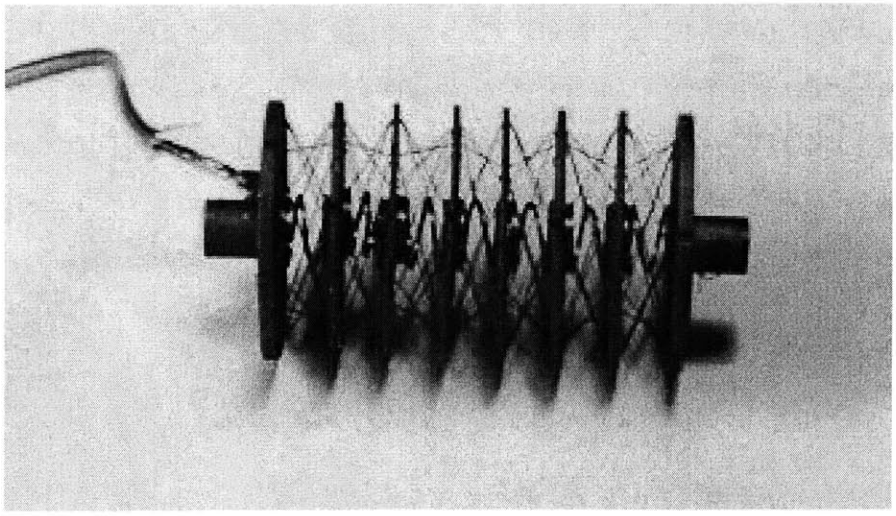

(a)

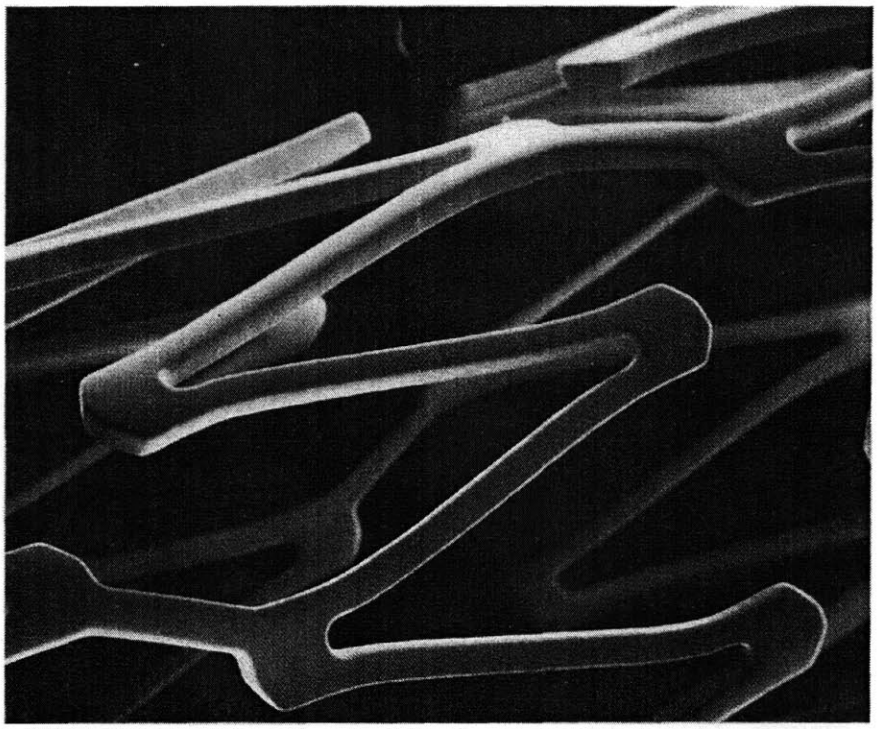

(b)

Figure 1-1: (a) Shape-memory alloy-based actuation device (Baron et al., 1994). (b) Scanning Electron Microscope (SEM) image of a Scimed^{tm} artery stent (Serruys, 1997).

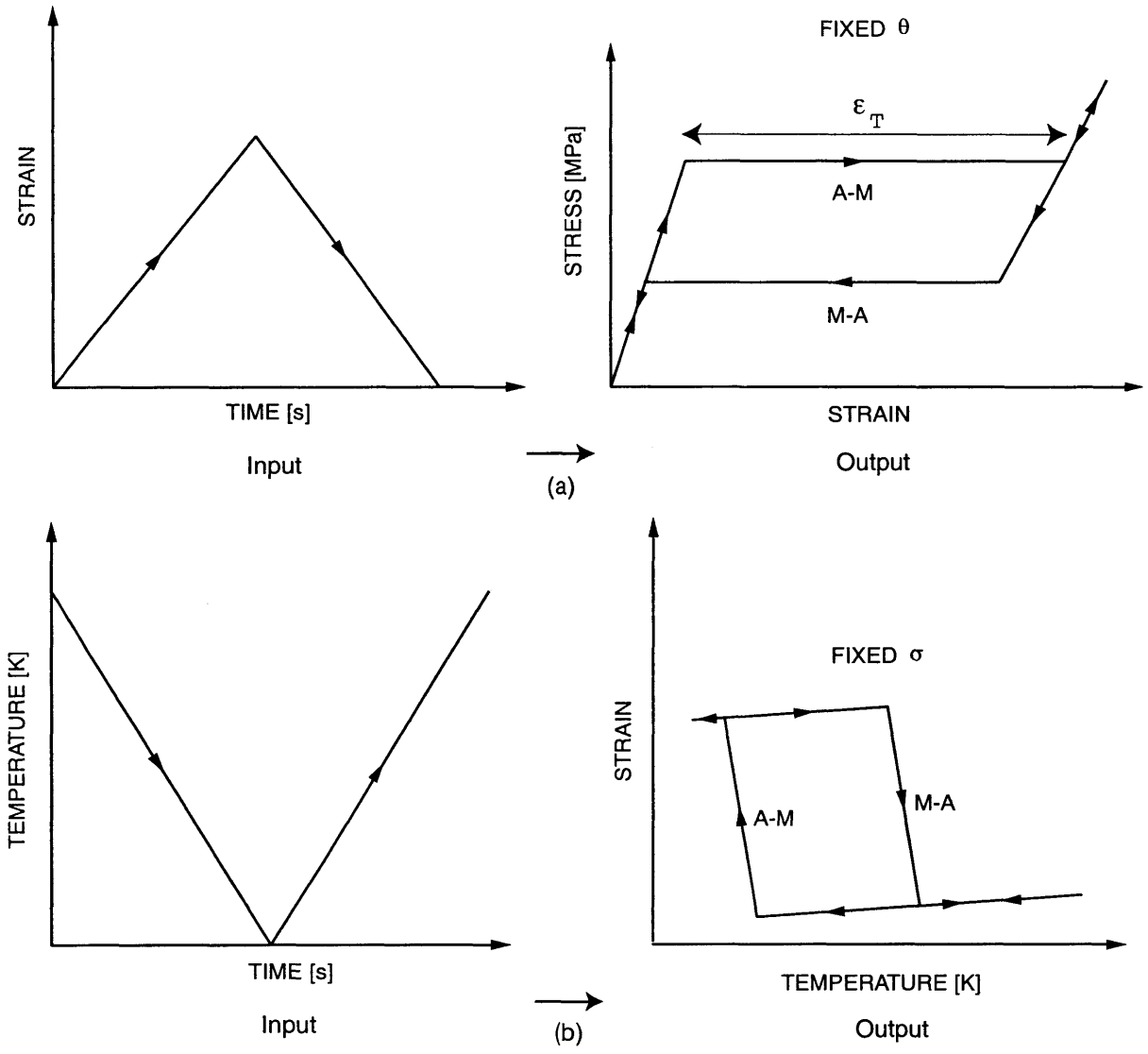

Figure 1-2: Schematic diagram of the (a) superelastic, and (b) strain-temperature cycling response. A-M denotes the austenite-to-martensite transformation whereas M-A denotes the martensite-to-austenite transformation.

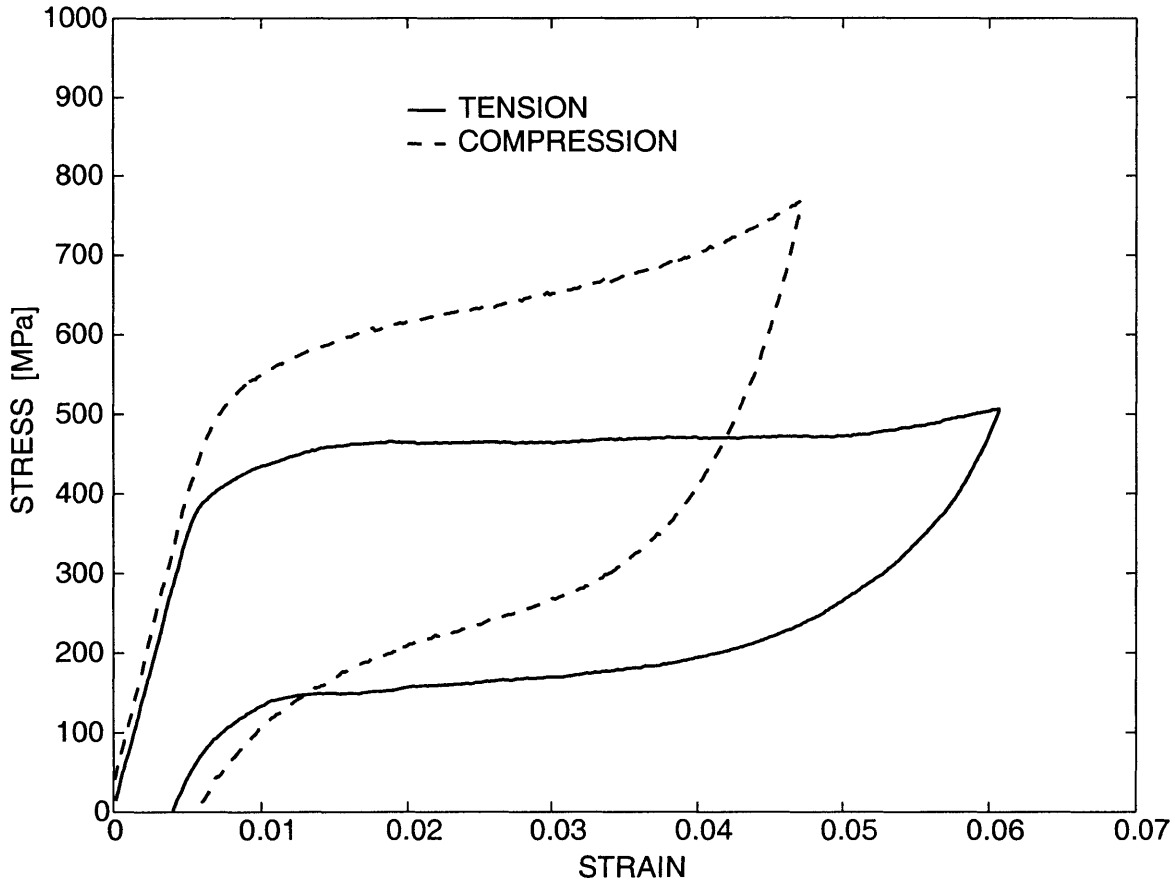

Figure 1-3: Experimental stress-strain curves for Ti-Ni rod at $\theta = 298\,\mathrm{K}$ in simple tension and simple compression. For compression the absolute values of stress and strain are plotted.

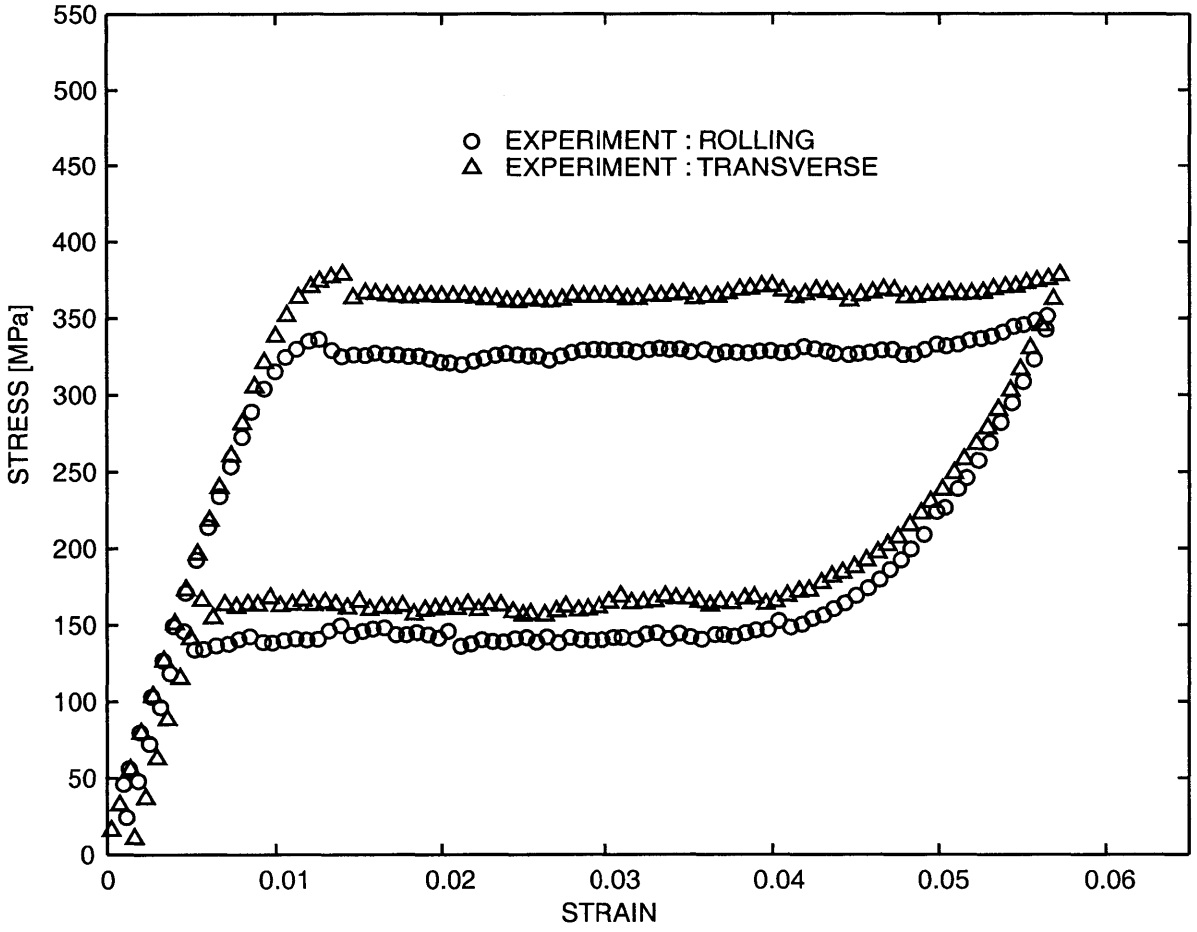

Figure 1-4: Experimental stress-strain curves for Ti-Ni sheet at $\theta = 300\,\mathrm{K}$ in simple tension along the rolling and transverse direction

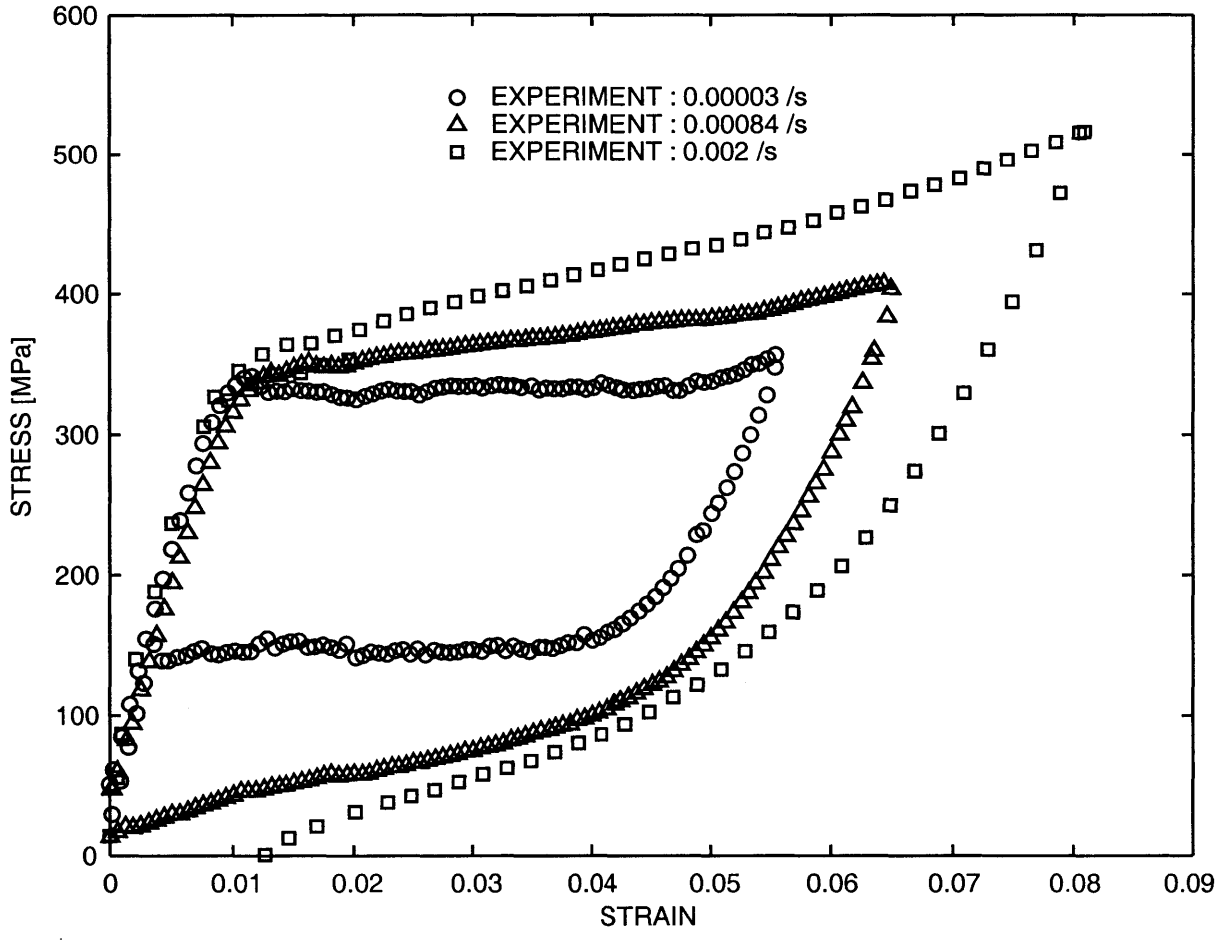

Figure 1-5: Experimental stress-strain curves for a Ti-Ni sheet at $\theta = 300\,\mathrm{K}$ in simple tension at strain rates of 0.00003/sec, 0.00084/sec, and 0.002/sec.

Chapter 2

Crystal-mechanics-based constitutive model

2.1 Single-crystal constitutive equations

In this section we summarize the three-dimensional crystal-mechanics based constitutive model of Thamburaja and Anand (2001,2002), which has recently been reformulated by Anand and Gurtin (2002) to account for thermal influences within a rigorous thermodynamic framework.[1]

The overall inelastic deformation of a crystal is always inhomogeneous at length scales associated with the *fine-scale microstructures* accompanying the austenite-martensite phase transformations. Thus, for the continuum level of interest here, the inelastic deformation should be defined as an average over a volume element that must contain enough transformed regions to result in an acceptably smooth process. The such smallest volume element above which the inelastic response may be considered smooth, is labelled a representative-volume element (RVE). In our constitutive model we choose a single-crystal as a representative volume element. The model does not explicitly account for the fine-scale microstructures, but only for the volume fractions of various types of fine structure. Thus the spatially continuous fields that

[1]This model is not intended to describe a material initially in the martensitic state and inelastic deformation caused by reorientation and de-twinning of the martensitic variants.

define the theory are to be considered as averages meant to apply at length scales which are large compared to those associated with the fine structure.

Using the standard notation of modern continuum mechanics,[2] we recall that the deformation gradient $\mathbf{F}$ maps *referential* segments $\mathbf{dX}$ to segments $\mathbf{dx} = \mathbf{F}\mathbf{dX}$ in the *deformed* configuration. We base the theory on the following multiplicative decomposition of the deformation gradient:[3] $\mathbf{F} = \mathbf{F}^e\mathbf{F}^p$. Here (i) $\mathbf{F}^p(\mathbf{X})$ represents the local deformation of *referential* segments $\mathbf{dX}$ to segments $\mathbf{dl} = \mathbf{F}^p(\mathbf{X})\mathbf{dX}$ in the *relaxed lattice configuration* due to the generation, growth and annihilation of austenitic/martensitic fine structure in a microscopic neighborhood of $\mathbf{X}$. (ii) $\mathbf{F}^e(\mathbf{X})$ represents the mapping of segments $\mathbf{dl}$ in the relaxed lattice configuration into segments $\mathbf{dx} = \mathbf{F}^e(\mathbf{X})\mathbf{dl}$ in the *deformed* configuration due the "elastic mechanisms" of stretching and rotation of the lattice.

In the equilibrium theory of austenite-martensite phase transitions the strain energy minimizers (in the sense of minimizing sequences) generally appear in the form of fine structure, involving abrupt transitions between austenite and twinned martensite in which the *transitions* are jumps in the deformation gradient of the form $\mathbb{S}_0 = \mathbf{b}_0 \otimes \mathbf{m}_0$, with $\mathbf{b}_0$ a vector whose magnitude represents the transition strain, and $\mathbf{m}_0$ a unit vector normal to the habit plane (the plane of the transition). A result of the equilibrium theory is a catalog of such rank-one tensors for various shape-memory alloys (cf. James and Hane (2000) and the references therein). Here we take, as a basic ingredient of the theory, a system of N such *transformation tensors* $\mathbb{S}_0^i = \mathbf{b}_0^i \otimes \mathbf{m}_0^i$, $i = 1, 2, \cdots, N$, where $\mathbf{b}_0^i$ are vectors whose magnitudes represent the *transformation strains*, and $\mathbf{m}_0^i$ are unit vectors representing the corresponding

[2] *Notation*: ∇ and Div denote the gradient and divergence with respect to the material point $\mathbf{X}$ in the *reference configuration*; grad and div denote these operators with respect to the point $\mathbf{x} = \mathbf{y}(\mathbf{X}, t)$ in the deformed configuration, where $\mathbf{y}(\mathbf{X}, t)$ is the motion; a superposed dot denotes the material time-derivative. We write sym $\mathbf{A}$, skw $\mathbf{A}$, respectively, for the symmetric, and skew parts of a tensor $\mathbf{A}$. Also, the inner product of tensors $\mathbf{A}$ and $\mathbf{B}$ is denoted by $\mathbf{A} \cdot \mathbf{B}$, and the magnitude of $\mathbf{A}$ by $|\mathbf{A}| = \sqrt{\mathbf{A} \cdot \mathbf{A}}$. Here repeated indices do not imply a summation over all the possible values the indices can take. For summation the $\sum$ sign is used.

[3] This decomposition is identical in form to the classical decomposition used to formulate dislocation based finite single-crystal plasticity. In this work we use the superscript p for two reasons: (i) to stress similarities between the present theory and single-crystal plasticity; and (ii) as shorthand for "phase transformation".

habit-plane normals; these *constant* vectors are *not necessarily orthogonal*. We denote by $\xi^i(\mathbf{X}, t)$, $0 \leq \xi^i \leq 1$, the local *volume fraction of martensite* at $\mathbf{X}$ associated with the ith system at time t. The presumption that the phase transformations take place through nucleation and growth of plate-like volume elements is based on the hypothesis that the evolution of $\mathbf{F}^p$ is governed by the *transformation rates* $\dot{\xi}^i$ via the relation $\dot{\mathbf{F}}^p = \mathbf{L}^p \mathbf{F}^p$, $\mathbf{L}^p = \sum_i \dot{\xi}^i \mathbb{S}_0^i$. For system i, *transformation from austenite to martensite*, abbreviated $a \to m$, occurs when $\dot{\xi}^i > 0$; a *transformation from martensite to austenite*, abbreviated $m \to a$, occurs when $\dot{\xi}^i < 0$. We write $\xi = \sum_{i=1}^N \xi^i$ for the (local) total volume fraction of transformed regions, and assume, as is natural, that $0 \leq \xi(t) \leq 1$.

The underlying constitutive equations relate the following basic variables :[4]

ψ,		free energy density per unit reference volume,
$\mathbf{F}$,	$\det \mathbf{F} > 0$,	deformation gradient,
θ,	$\theta > 0$,	absolute temperature,
$\mathbf{T}$,	$\mathbf{T} = \mathbf{T}^\mathsf{T}$,	Cauchy stress,
$\mathbf{F}^p$,		transformation deformation gradient,
$(\mathbf{b}_0^i, \mathbf{m}_0^i)$,		transformation systems,
ξ^i,	$0 \leq \xi^i \leq 1$,	martensite volume fraction for the ith system,
ξ,	$0 \leq \xi \leq 1$,	total martensite volume fraction,
$\mathbf{F}^e = \mathbf{F}\mathbf{F}^{p-1}$,	$\det \mathbf{F}^e > 0$,	elastic deformation gradient,
$\mathbf{C}^e = \mathbf{F}^{e\mathsf{T}}\mathbf{F}^e$,		elastic right Cauchy-Green tensor,
$\mathbf{E}^e = (1/2)(\mathbf{C}^e - \mathbf{1})$,		elastic strain,
$\mathbf{T}^e = (\det \mathbf{F})\mathbf{F}^{e-1}\mathbf{T}\mathbf{F}^{e-\mathsf{T}}$,		elastic stress.

The constitutive equations are:

[4]Using the notation of modern continuum mechanics, we write $\mathbf{F}^{e-1} = (\mathbf{F}^e)^{-1}$, $\mathbf{F}^{p-\mathsf{T}} = (\mathbf{F}^p)^{-\mathsf{T}}$, *etc.* throughout.

1. **Free energy**: The free energy is taken in the separable form[5]

$$\psi(\mathbf{E}^e, \theta, \xi) = \psi^e(\mathbf{E}^e, \theta, \xi) + \psi^\theta(\theta) + \psi^{tr}(\theta, \xi), \quad \text{with} \tag{2.1}$$

$$\psi^e(\mathbf{E}^e, \theta, \xi) = (1/2)\mathbf{E}^e \cdot \boldsymbol{\mathcal{C}}(\xi)[\mathbf{E}^e] - (\theta - \theta_0)\mathbf{A}(\xi) \cdot \boldsymbol{\mathcal{C}}(\xi)[\mathbf{E}^e], \tag{2.2}$$

$$\psi^\theta(\theta) = c(\theta - \theta_0) - c\theta \ln(\theta/\theta_0), \tag{2.3}$$

$$\psi^{tr}(\theta, \xi) = (\lambda_T/\theta_T)(\theta - \theta_T)\xi. \tag{2.4}$$

Here $\boldsymbol{\mathcal{C}}(\xi)$ is the elasticity tensor and $\mathbf{A}(\xi)$ is the thermal expansion tensor at the reference temperature θ_0. The constant c is the specific heat per unit volume of the reference configuration. The parameter θ_T is the phase equilibrium temperature, λ_T is the latent heat per unit reference volume of the $a \leftrightarrow m$ transformation at temperature θ_T.[6]

2. **Stress**:

The elastic stress is given by

$$\mathbf{T}^e = \frac{\partial \psi}{\partial \mathbf{E}^e} = \boldsymbol{\mathcal{C}}(\xi)[\mathbf{E}^e - \mathbf{A}(\xi)(\theta - \theta_0)]. \tag{2.5}$$

We define the *resolved force* on the ith system by

$$\tau^i = \mathbf{b}_0^i \cdot (\mathbf{C}^e\mathbf{T}^e)\mathbf{m}_0^i. \tag{2.6}$$

Note that since the magnitude of $\mathbf{b}_0^i$ represents a transformation strain, τ^i has units of energy per unit reference volume, and it is for this reason we call it a resolved force rather than a resolved stress. Further, the derivative

$$b = \frac{\partial \psi^{tr}}{\partial \xi} = (\lambda_T/\theta_T)(\theta - \theta_T), \tag{2.7}$$

represents an energetic *back force*,[7] and the *driving force for phase transformation* on the ith system is given by

$$f^i = (\tau^i - b). \tag{2.8}$$

---

[5] A term of the form $(1/2)\sum_{i,j=1}^{N} g^{ij}\xi^i\xi^j$, where the scalar constants $g^{ij} = g^{ji}$ characterize energetic interactions between the transformation systems, may be included in the free energy ψ^{tr}, but we shall neglect such a contribution in our application of the theory to Ti-Ni.

[6] Here we are guided by the one-dimensional development of Abeyaratne and Knowles (1993). An obvious generalization of ψ^{tr} would be to replace it by $\sum_i (\lambda_T^i/\theta_T^i)(\theta - \theta_T^i)\xi^i$.

[7] We use this terminology by analogy to the "back stress" in the crystal plasticity literature.

From the second law of thermodynamics, the dissipation accompanying the phase transformation is given by

$$\sum_i f^i \dot{\xi}^i \geq 0. \tag{2.9}$$

From the inequality (2.9), we obtain for the *individual* transformation systems that

$$f^i \dot{\xi}^i \geq 0. \tag{2.10}$$

3. **Transformation conditions**:

In the rate-independent theory developed here, transformation is assumed to be possible if the driving force f^i reaches a critical value. From the inequality (2.10) the *transformation conditions* are

$$f^i = f_c^i \quad \text{for} \quad \dot{\xi}^i > 0, \tag{2.11}$$

$$f^i = -f_c^i \quad \text{for} \quad \dot{\xi}^i < 0. \tag{2.12}$$

Here $f_c^i > 0$ is the constant *transformation resistance* for the ith system. In the rate-independent limit the bounds[8] on the driving force for phase transformation are

$$-f_c^i \leq f^i \leq f_c^i. \tag{2.13}$$

4. **Flow rule**:

$$\dot{\mathbf{F}}^p = \left\{ \sum_i \dot{\xi}^i \, \mathbf{b}_0^i \otimes \mathbf{m}_0^i \right\} \mathbf{F}^p,$$

with martensitic volume fractions consistent with $0 \leq \xi^i \leq 1$ and $0 \leq \xi \leq 1$. Moreover,

(i) if $-f_c^i < f^i < f_c^i$, then $\dot{\xi}^i = 0$;

(ii) if $f^i = f_c^i$, $0 \leq \xi^i < 1$ and $0 \leq \xi < 1$, then

$$\dot{\xi}^i \geqslant 0 \quad \text{and} \quad \dot{(\overline{f^i - f_c^i})} \leqslant 0; \tag{2.14}$$

[8]This is analogous to the yield function in crystal-plasticity.

(iii) if $f^i = -f_c^i, \quad 0 < \xi^i \leq 1$ and $0 < \xi \leq 1$, then

$$\dot{\xi}^i \leqslant 0 \quad \text{and} \quad (\overline{\dot{f^i + f_c^i}}) \geqslant 0; \tag{2.15}$$

(iv) if $f^i = f_c^i$ and $\xi^i = 1$, or if $f^i = -f_c^i$ and $\xi^i = 0$, then $\dot{\xi}^i = 0$;

(v) if $f^i = f_c^i$ and $\xi = 1$, then $\dot{\xi}^i = 0$.

The *consistency conditions* (2.14) and (2.15) serve to determine the transformation rates $\dot{\xi}^i$.

5. **Entropy; energy balance; heat flux**:

The *entropy* η is given by

$$\eta = -\frac{\partial \psi}{\partial \theta} = c \ln(\theta/\theta_0) + \mathbf{E}^e \cdot \boldsymbol{\mathcal{C}}(\xi)[\mathbf{A}(\xi)] - (\lambda_T/\theta_T)\xi. \tag{2.16}$$

The balance of energy may be written as

$$\theta \dot{\eta} = -\mathrm{Div}\mathbf{q} + \sum_i f^i \dot{\xi}^i + r, \tag{2.17}$$

where r is the heat supply per unit volume of the reference configuration, and the *referential* heat flux $\mathbf{q}$ is taken to be governed by *Fourier's law*

$$\mathbf{q} = -\mathbf{K}(\xi)\nabla\theta, \tag{2.18}$$

where $\mathbf{K}(\xi)$ is the thermal conductivity tensor at θ_0. Using (2.16) and (2.18), the energy balance (2.17) becomes

$$c\,\dot{\theta} = \mathrm{Div}\left\{\mathbf{K}(\xi)\nabla\theta\right\} + (\lambda_T/\theta_T)\,\theta\,\dot{\xi} + \sum_i f^i \dot{\xi}^i - \theta\,\overline{\dot{\mathbf{E}^e \cdot \boldsymbol{\mathcal{C}}(\xi)[\mathbf{A}(\xi)]}} + r, \tag{2.19}$$

To complete the theory for a particular material the constitutive parameter/functions that need be specified are

$$\left\{\boldsymbol{\mathcal{C}}(\xi), \mathbf{A}(\xi), \mathbf{b}_0^i, \mathbf{m}_0^i, \theta_T, \lambda_T, f_c^i, c, \mathbf{K}(\xi)\right\}.$$

Finally, the standard partial differential equation for the stress referred to the deformed configuration is

$$\mathrm{div}\,\mathbf{T} + J^{-1}\mathbf{f} = \mathbf{0}, \tag{2.20}$$

where div represents the divergence operator in the deformed configuration, $J = \det \mathbf{F}$, and $\mathbf{f}$ is the body force per unit volume in the reference configuration (the body force $\mathbf{f}$ is assumed to include inertial forces). The differential equation for the temperature referred to the deformed configuration is

$$J^{-1} c \dot{\theta} = \operatorname{div} \left\{ J^{-1} \mathbf{F} \mathbf{K}(\xi) \mathbf{F}^{\mathsf{T}} \operatorname{grad} \theta \right\} + J^{-1} (\lambda_T / \theta_T) \theta \dot{\xi} + J^{-1} \sum_i f^i \dot{\xi}^i - J^{-1} \theta \overset{\cdot}{\overline{\mathbf{E}^e \cdot \boldsymbol{\mathcal{C}}(\xi)[\mathbf{A}(\xi)]}} + J^{-1} r. \quad (2.21)$$

The numerical simulations are carried out using the finite-element computer program ABAQUS/Explicit (1999,2001), for which we have written a user material subroutine to implement our constitutive model. Algorithmic details of the numerical implementation are given in Appendix A.

2.2 Evaluation of the constitutive model for a polycrystalline Ti-Ni alloy : Rod-texture

Suitably thermo-mechanically processed and heat-treated Ti-Ni at 55.96 wt.% Ti drawn rods of 12.70 mm diameter, intended for superelastic applications, were obtained from a commercial source. Experimental measurements of crystallographic texture of the as-received Ti-Ni were carried out by X-ray irradiation using a Rigaku RU 200 diffractometer. Pole figures were obtained by using the Schultz reflection method with copper-K radiation. To process the experimental data, the PoPLa software package (Kallend et al., 1989) was employed. Each measured pole figure was corrected for background and defocusing, and also extrapolated for the outer 15^o. The $\{111\}, \{100\}$, and $\{110\}$ pole figures for the as-received Ti-Ni looking into the rod-axis (X3) are shown in Figure 2-1. This figure also shows our numerical approximation of this measured texture using 729 and 343 unweighted grain orientations. The texture representation using 729 grain orientations is slightly better that that using 343 grain orientations. In most of the calculations reported below we shall use the 729 grain orientation representation of the initial texture. However, we note that the computed stress-strain curves using the set of 343 grain orientations are very close to those using the 729 grain orientations, and the smaller number of orientations may be used for reasons of computational efficiency.

By using differential scanning calorimetric (DSC) techniques, we have determined the transformation temperatures for our Ti-Ni bar-stock, Figure 2-2. They are:

$$\theta_{ms} = 251.3\,\mathrm{K}, \quad \theta_{mf} = 213.0\,\mathrm{K}, \quad \theta_{as} = 260.3\,\mathrm{K}, \quad \theta_{af} = 268.5\,\mathrm{K}. \tag{2.22}$$

The volume fraction and temperature dependence of the anisotropic elastic constants of Ti-Ni are not well-documented in the literature. Here, for simplicity, the values of the elastic constants are taken to follow the rule of mixtures

$$\boldsymbol{\mathcal{C}}(\xi, \theta) = (1 - \xi)\boldsymbol{\mathcal{C}}^a(\theta) + \xi\boldsymbol{\mathcal{C}}^m(\theta).$$

The elastic constants for the cubic austenite phase in Ti-Ni at room temperature are taken as (Brill et al., 1991) :

$$C_{11}^a = 130\,\text{GPa}, \quad C_{12}^a = 98\,\text{GPa}, \quad C_{44}^a = 34\,\text{GPa}.$$

We have been unable to find experimentally-measured values of the anisotropic elastic moduli of single-crystal monoclinic martensite of Ti-Ni. Typically, the Young's Modulus of austenite is about two to three times that of martensite, while the Poisson's ratios for the material in the two different phases are approximately equal to each other. Guided by this information, we assume that anisotropic elastic constants of the monoclinic martensite may be approximately treated as those of a cubic material, and that the corresponding values of the stiffnesses, C_{ij}, are one half as large as those for the austenite:

$$C_{11}^m = 65\,\text{GPa}, \quad C_{12}^m = 49\,\text{GPa}, \quad C_{44}^m = 17\,\text{GPa}.$$

We realize that this description for the composite elastic constants is rather simplified and approximate. However, since the main purpose of this paper is to model the inelastic response characteristics of shape-memory materials, we shall not further pursue the matter of a more refined description of the elastic moduli of a two-phase austenite-martensite mixture.

For cubic materials, the thermal expansion tensor is isotropic, $\mathbf{A}^a = \alpha^a \mathbf{1}$, with α^a denoting the coefficient of thermal expansion for the austenite phase. The thermal expansion tensor for the martensite phase is also assumed to be isotropic *i.e.* $\mathbf{A}^m = \alpha^m \mathbf{1}$, with α^m denoting the coefficient of thermal expansion for the martensite phase.

Here, the composite thermal expansion tensor is taken to follow the rule of mixtures

$$\mathbf{A} \equiv \alpha \mathbf{1} = (1 - \xi)\mathbf{A}^a + \xi \mathbf{A}^m,$$

with α^a and α^m for Ti-Ni in the austenitic and martensitic conditions taken as (Boyd and Lagoudas, 1996):

$$\alpha^a = 11 \times 10^{-6}/\text{K}, \quad \alpha^m = 6.6 \times 10^{-6}/\text{K}.$$

The crystallographic theory of martensitic transformation (CTM) shows that phase transformation in Ti-Ni can occur on 192 possible transformation systems

Table 1. Transformation Systems

i	$m^i_{0,1}$	$m^i_{0,2}$	$m^i_{0,3}$	$b^i_{0,1}$	$b^i_{0,2}$	$b^i_{0,3}$
1	-0.8888	-0.4045	0.2153	0.0568	-0.0638	0.0991
2	-0.8888	0.4045	0.2153	0.0568	0.0638	0.0991
3	-0.8888	0.2153	-0.4045	0.0568	0.0991	-0.0638
4	-0.8888	0.2153	0.4045	0.0568	0.0991	0.0638
5	-0.8888	-0.2153	0.4045	0.0568	-0.0991	0.0638
6	-0.8888	-0.2153	-0.4045	0.0568	-0.0991	-0.0638
7	-0.8888	0.4045	-0.2153	0.0568	0.0638	-0.0991
8	-0.8888	-0.4045	-0.2153	0.0568	-0.0638	-0.0991
9	0.4045	-0.8888	0.2153	0.0638	0.0568	0.0991
10	-0.4045	-0.8888	0.2153	-0.0638	0.0568	0.0991
11	0.2153	-0.8888	-0.4045	0.0991	0.0568	-0.0638
12	0.2153	-0.8888	0.4045	0.0991	0.0568	0.0638
13	-0.2153	-0.8888	0.4045	-0.0991	0.0568	0.0638
14	-0.2153	-0.8888	-0.4045	-0.0991	0.0568	-0.0638
15	0.4045	-0.8888	-0.2153	0.0638	0.0568	-0.0991
16	-0.4045	-0.8888	-0.2153	-0.0638	0.0568	-0.0991
17	0.2153	0.4045	-0.8888	0.0991	0.0638	0.0568
18	0.2153	-0.4045	-0.8888	0.0991	-0.0638	0.0568
19	0.4045	0.2153	-0.8888	0.0638	0.0991	0.0568
20	-0.4045	0.2153	-0.8888	-0.0638	0.0991	0.0568
21	0.4045	-0.2153	-0.8888	0.0638	-0.0991	0.0568
22	-0.4045	-0.2153	-0.8888	-0.0638	-0.0991	0.0568
23	-0.2153	0.4045	-0.8888	-0.0991	0.0638	0.0568
24	-0.2153	-0.4045	-0.8888	-0.0991	-0.0638	0.0568

(Hane and Shield, 1999). The CTM theory is discussed and summarized in Appendix B and C.

However, it is not clear whether all the 192 possible systems are actually operative during thermo-mechanical loading. Here, we shall only consider the 24 transformation systems which are unambiguously observed in experiments and used by a variety of recent researchers (e.g. Matsumoto et al., 1987; Lu and Weng, 1998; Gall and Sehitoglu, 1999). The components of the 24 transformation systems $(\mathbf{m}^i_0, \mathbf{b}^i_0)$ with respect to an orthonormal basis associated with the parent cubic austenite crystal lattice are given in Table 1.

Recall that the driving force on each transformation system is taken to be given

by

$$f^i = \tau^i - (\lambda_T/\theta_T)\,(\theta - \theta_T).$$

Using the measured phase transformation temperatures (Figure 2-2), the value for the phase equilibrium temperature, θ_T, is given by

$$\theta_T \equiv (1/2)\,\{\theta_{ms} + \theta_{as}\} = 256\,\mathrm{K}.$$

Further we assume that the the critical values of the driving force f_c^i for the 24 systems are all equal and constant:

$$f_c^i = f_c \equiv \text{constant}.$$

In principle, the values of the latent heat for phase transformation, λ_T, and the critical value of the driving force, f_c, should be determined from experiments performed on single crystals of Ti-Ni. However, such single crystals are difficult to grow, and we did not have access to single crystals of this material. Instead, the values of λ_T and f_c are *estimated* from experiments on polycrystalline Ti-Ni as follows. Consider an idealized schematic stress-strain curve for a superelastic tensile test on a polycrystalline shape-memory material, Figure 2-3. Let σ_{am} denote the value of the stress at which martensite nucleates from austenite during the forward transformation, and let σ_{ma} denote the stress level at which austenite nucleates from martensite during the reverse transformation. Following the analysis performed by Knowles (1999), the value of the mean stress, defined as

$$\sigma_0 \equiv \frac{1}{2}\,(\sigma_{am} + \sigma_{ma})\,,$$

is given by

$$\sigma_0 = (\lambda_T^{poly}/\theta_T\,\epsilon_T)\,(\theta - \theta_T),$$

where λ_T^{poly} is the one-dimensional polycrystalline counterpart of the parameter λ_T and ϵ_T is the *macroscopic transformation strain.* Thus, if one knows θ_T from independent DSC measurements, and one estimates σ_{am}, σ_{ma} and ϵ_T from a superelastic tensile test at a temperature θ, then the macroscopic value of the latent heat for phase transformation, λ_T^{poly}, for a polycrystalline material is easily estimated. As shown in

Knowles (1999), the critical value for the macroscopic driving force, f_c^{poly} , is then given by

$$f_c^{poly} = \epsilon_T \left(\sigma_{am} - \sigma_0\right),$$

where ϵ_T is the value of the transformation strain in tension for a polycrystalline material, see Figure 2-3.

Estimates of the values of the corresponding quantities (λ_T, f_c) at the *single crystal level* are then obtained from

$$\lambda_T \approx \lambda_T^{poly}, \quad \text{and} \quad f_c \approx f_c^{poly}.$$

Figure 1-3 shows the stress-strain curve from a superelastic tension test performed on our initially-textured Ti-Ni at 298 K. The geometry of the tension-compression specimens is shown in Figure 2-4. The experiment was conducted at a very low constant true strain rate in order to ensure isothermal testing conditions. An extensometer was used to obtain the macroscopic strain in the gage section of the specimen. The experimental stress strain curve shows some residual deformation after unloading. This is invariably observed in most experiments on commercial polycrystalline SMAs; seldom is there complete recovery. From this figure,

$$\sigma_{am} \approx 470\,\text{MPa}, \quad \sigma_{ma} \approx 170\,\text{MPa}, \quad \epsilon_T \approx 0.054.$$

Using, the value $\theta_T = 256\,\text{K}$, estimated from our DSC experiments, we obtain

$$\lambda_T^{poly} = 100\,\text{MJ/m}^3, \quad f_c^{poly} = 8.2\,\text{MJ/m}^3,$$

for the polycrystalline material. Hence, the estimates of the values of the corresponding quantities at the *single crystal level* are

$$\lambda_T \approx 100\,\text{MJ/m}^3, \quad \text{and} \quad f_c \approx 8.2\,\text{MJ/m}^3.$$

In our finite-element model of a polycrystalline aggregate, each finite-element represents one crystal, and a set of crystal orientations which approximate the initial crystallographic texture of the shape-memory alloy are assigned to the elements. The macroscopic stress-strain responses are calculated as volume averages over the

entire aggregate. Calculations for simple tension on an aggregate of 729 unweighted different grain orientations representing a polycrystalline material with the initial crystallographic texture, Figure 2-1, were carried out using these estimates for the material parameters. Figure 2-5a shows the initial finite-element mesh. The finite-element mesh after 6% deformation in tension is shown in Figure 2-5b, together with the contours of the martensite volume fraction. The quality of the curve-fit is shown in Figure 2-5c. The numerically-computed stress-strain response is close to the experimentally-observed one. Given the number of approximative assumptions used to arrive at this curve-fit, the result is very encouraging.

Using these values of the material parameters and the numerical representation of the measured initial texture, Figure 2-1, we have also carried out numerical simulations of simple compression and thin-walled tubular torsion, and compared the calculated stress-strain curves against corresponding physical experiments at 298 K.

The initial finite-element mesh for the simple compression simulation is shown in Figure 2-6a. The finite-element mesh after 5 % compression is shown in Figure 2-6b, along with the contours of the martensite volume fraction. The prediction of the stress-strain curve from the constitutive model is shown in Figure 2-6c, where it is compared against corresponding experimental measurements. The experimentally-measured superelastic stress-strain response is well-approximated by the predictions from the constitutive model.

To demonstrate the numerically-predicted tension-compression asymmetry, we plot the numerical stress-strain curves in tension and compression in Figure 2-7a. On comparing the curves in this figure with the corresponding experimental curves, Figure 1-3, we conclude that the constitutive model captures the following major features of the observed tension-compression asymmetry rather well:

- The stress level required to nucleate the martensitic phase from the parent austenitic phase is higher in compression than in tension.
- The transformation strain measured in compression is smaller than that in tension.

- The hysteresis loop generated in compression is wider (measured along the stress axis) than the hysteresis loop generated in tension.

Figure 2-1 shows that the Ti-Ni bar has a strong {111} texture. Using our constitutive model and the estimated single crystal material parameters, we have calculated the stress-strain response for a single crystal subjected to tension and compression along its [111]-direction. The calculated stress-strain response is plotted in Figure 2-7b. Comparison of Figure 2-7a with Figure 2-7b clearly shows that the tension-compression asymmetry in the polycrystalline specimen has its origins in the crystallographic texture of the as-received Ti-Ni bar.

To confirm this conclusion we have repeated the tension and compression simulations for a polycrystalline specimen using a set of 729 crystal orientations representing a "random" texture, instead of the actual crystallographic texture in the Ti-Ni bar shown in Figure 2-1. The {111} pole figure corresponding to this random initial texture is shown in Figure 2-8a. All other material parameters used in these simulations were the same as those used in the previous calculations. The predicted tension and compression superelastic stress-strain curves using the random texture are shown in Figure 2-8b. This result shows that in comparison to the result from the calculation using the actual initial texture, Figure 2-7a, there is not much asymmetry between the compression and tension curves. Also, the small asymmetry in the stress levels between tension and compression observed in the calculation using the random initial texture is in the reverse order. The experiments, Figure 1-3, and the numerical simulations using the actual initial texture for the rod, Figure 2-7a, show that the compression curves are higher than those for tension, whereas the calculation using the random texture shows the reverse trend. Thus, we conclude that *crystallographic texture* is the prime cause for the observed tension-compression asymmetry in shape-memory alloys.

Finally, the specimen geometry for the thin-walled tubular torsion experiment is shown in Figure 2-9. The initial mesh used in the simulation for tubular torsion is shown in Figure 2-10a. The deformed mesh after a shear strain of 9% is shown in Figure 2-10b, together with the contours for the martensite volume fraction. The

predicted nominal shear stress-strain curve is shown in Figure 2-10c, where it is compared against the corresponding experimentally-measured curve from a tubular torsion experiment performed on a thin-walled specimen under a very low shearing strain rate at 298 K. The prediction is in good accord with the experiment.

We have also evaluated the predictive capability of our model for (*i*) a proportional-loading, tension-torsion experiment, and (*ii*) a path-change, tension-torsion experiment. These experiments were also performed under isothermal testing conditions at room temperature ($\theta = 298\,\mathrm{K}$).

Proportional-loading tension-torsion experiment:

The strain-history imposed on a thin-walled tubular specimen during the proportional-loading tension-torsion experiment is shown in Figure 2-11a. The axial strain ϵ is increased at a constant rate from 0% to 3% in 500 seconds, while the shear strain γ is increased at a constant rate from 0% to 4.5% in the same time period. These strains are then linearly reduced to zero, in another 500 seconds.

The initial finite-element mesh using an aggregate of 768 unweighted crystal orientations for the combined tension-torsion simulation is shown in Figure 2-11b, and the finite-element mesh after 3% strain in tension and 4.5% strain in shear is shown in Figure 2-11c, along with the contours of the martensite volume fraction.

Predictions of the axial-stress versus axial-strain, and shear-stress versus shear-strain from the constitutive model are compared against corresponding experimental measurements in Figures 2-11d and 2-11e, respectively. The measured superelastic stress-strain response in the tension-torsion experiment is well-approximated by the predictions from the constitutive model.

Path-change tension-torsion experiment:

The strain-history imposed on a thin-walled tubular specimen during the path-change tension-torsion experiment is shown in Figure 2-12a. First, the axial strain is increased at a constant rate from 0% to 3% in 150 seconds, while the shear strain is maintained at 0%. After this, the shear strain is linearly increased from 0% to 7% in 350 seconds while the tensile strain is maintained at 3%. Next, the shear strain

is linearly reduced from 7% to 0% in 350 seconds, while still maintaining the tensile strain at 3%. Finally, the tensile strain is linearly reduced from 3% to 0% in another 150 seconds, while maintaining the shear strain at 0%.

The initial finite-element mesh using an aggregate of 768 unweighted crystal orientations for the path-change tension-torsion simulation is shown in Figure 2-12b, and the finite-element mesh after 3% strain in tension and 7% strain in shear is shown in Figure 2-12c, along with the contours of the martensite volume fraction.

Predictions of the axial-stress versus axial-strain, and shear-stress versus shear-strain from the constitutive model are compared against corresponding experimental measurements in Figure 2-12d and 2-12e, respectively. Again, the measured superelastic stress-strain response in the tension-torsion experiment is well-approximated by the predictions from the constitutive model.

Of particular note is the result that when the axial strain reaches 3% and is maintained at this level, the axial stress drops when the specimen is subsequently sheared. The axial stress rises again when the direction of shearing is reversed. As shown by the arrows in Figure 2-12d, this response is remarkably well-captured by the simulation.

Further, note from Figure 2-12e, that the shear stress has a negative value after the shear strain has completed its cycle back to zero. This shear stress decreases back to zero only when the axial strain is finally reduced back to zero. This response is also well-predicted by the numerical simulation.

2.2.1 Taylor model

For polycrystalline materials, a widely-used averaging scheme is based on the assumption that the local deformation in each crystal is homogeneous and identical to the macroscopic deformation gradient at the continuum material point (Taylor, 1938). The compatibility between crystals is automatically satisfied in this approximation; however, equilibrium holds only inside a crystal, but is violated across crystal boundaries. For such a model, with $\mathbf{T}^{(k)}$ denoting the constant Cauchy stress in each crystal, the volume-averaged Cauchy stress is given by

$$\overline{\mathbf{T}} = \sum_{k=1}^{N} v^{(k)} \mathbf{T}^{(k)}, \tag{2.23}$$

where $v^{(k)}$ is the volume fraction of each crystal in a representative volume element. When all crystals are assumed to be of equal volume, the stress $\overline{\mathbf{T}}$ is just the number average over all the crystals:

$$\overline{\mathbf{T}} = \frac{1}{N} \sum_{k=1}^{N} \mathbf{T}^{(k)}. \tag{2.24}$$

Taylor model simulations in simple tension, simple compression, simple shear and path-change tension-torsion were performed using a single ABAQUS-C3D8R element, and using 729 unweighted grain orientations to represent the initial rod-texture, Figure 2-1. The material parameters used in the Taylor model simulations were the same as those calibrated for the full finite-element simulations of the polycrystal discussed in the previous section. Figures 2-13a, 2-13b and 2-13c compares the stress-strain predictions from the Taylor model against the actual experiments, as well as the full finite-element calculations. Figure 2-14 compares the stress-strain predictions from the Taylor model against the actual path-change tension-torsion data, as well as predictions from the full finite-element calculations. The Taylor model compares very well to the full finite-element calculations, and therefore it provides a reasonably accurate and computationally-inexpensive method for determining the response of textured Ti-Ni in a multi-axial setting and moderately complex loading modes.

2.2.2 Effect of temperature on the deformation of polycrystalline Ti-Ni

In this section we examine the applicablity of our model to another Ti-Ni alloy for which Shaw and Kyriakides (1995) have conducted careful isothermal, low strain rate experiments at a variety of different temperatures in the range $255.6\,\mathrm{K} \leq \theta \leq 373.2\,\mathrm{K}$. Unfortunately, these authors do not report on the initial crystallographic texture of their material. However, since they conducted their experiments on drawn Ti-Ni wires with a processing history similar to that of our own material, we assume that their material has a texture which may be approximated[9] by the numerical representations of the texture of our drawn rods, Figure 2-1.

We estimate the constitutive parameters for their material from their DSC results, and their stress-strain results from a superelastic tension test at representative temperature. The DSC measurements of Shaw and Kyriakides (1995) (their, Figure 1) yield the following values for the transformation temperatures:

$$\theta_{ms} = 272.2\,\mathrm{K}, \quad \theta_{mf} = 203.2\,\mathrm{K}, \quad \theta_{as} = 302.7\,\mathrm{K}, \quad \theta_{af} = 335.2\,\mathrm{K}. \tag{2.25}$$

The material parameters for their Ti-Ni wire were calibrated by fitting the constitutive model to the superelastic tension experiment conducted at 343.2 K using the methodology outlined in Section 2.2. The quality of the curve-fit is shown in Figure 2-15b. The numerical calculations shown in this figure correspond to using the full finite element model with 729 elements representing 729 grain orientations, as well as a corresponding single element Taylor model calculation. The full finite element model of the polycrystal was used to estimate the material parameters; the numerically-computed stress-strain response from this calculation is close to the experimentally-observed one.

The thermo-elastic constants used in our calculations are

Elastic moduli for austenite: $C^a_{11} = 130\,\mathrm{GPa}, C^a_{12} = 98\,\mathrm{GPa}, C^a_{44} = 21\,\mathrm{GPa}$;

Elastic moduli for martensite: $C^m_{11} = 65\,\mathrm{GPa}, C^m_{12} = 49\,\mathrm{GPa}, \ C^m_{44} = 10.5\,\mathrm{GPa}$;

[9]Wire texture is expected to show a sharper $\{111\}$ component than the rod texture.

Coefficients of thermal expansion: $\alpha^a = 11 \times 10^{-6}/\mathrm{K}$, $\alpha^m = 6.6 \times 10^{-6}/\mathrm{K}$.

The single crystal material parameters used to obtain this fit for the polycrystalline Ti-Ni wire of Shaw and Kyriakides are :

Phase equilibrium temperature: $\theta_T = 287\,\mathrm{K}$;

Latent heat: $\lambda_T = 112\,\mathrm{MJ/m^3}$;

Critical transformation resistance: $f_c = 7.7\,\mathrm{MJ/m^3}$.

Figure 2-15a and 2-15c show the response predicted from the constitutive model compared against the tension experiments at two different temperatures: 333.2 K, and 353.2K. The experimentally measured temperature variation of the superelastic stress-strain response is well-predicted by the constitutive model.

Shaw and Kyriakides (1995) also report on displacement controlled experiments at temperatures in the range $\theta_{ms} < \theta < \theta_{af}$. In these experiments the martensite that forms during forward deformation does not completely transform back to austenite upon reversing the deformation and decreasing the stress to zero. Although Shaw and Kyriakides (1995) did not subsequently increase the temperature at zero stress to show the austenite-martensite-austenite shape-memory effect, we have numerically simulated such an experiment. In our simulation we employ the Taylor model using a single ABAQUS-C3D8R element with 343 grain orientations to represent the initial texture. The calculation was performed by first imposing an isothermal, $\theta = 303.2\,\mathrm{K}$, strain controlled tension to 5% tensile strain, and then reversing the deformation to reach a state of zero stress. As shown in Figure 2-16, the numerical prediction from the model for this part of the simulation is close to the experimental measurements of Shaw and Kyriakides (1995). The temperature in the simulation was then linearly ramped up from 303.2 K to 305.8 K by imposing the temperature ramp on the nodes of the finite element. Figure 1-15 shows that the model is able to capture the shape-memory effect by transformation; it predicts full recovery to the austenite phase after the temperature is increased to 305.8 K.

2.3 Evaluation of the constitutive model for a polycrystalline Ti-Ni alloy : Sheet-texture

Suitably processed Ti-Ni sheet, 0.53 mm thick, intended for superelastic response was obtained from a commercial source. Experimental pole figure measurements of the initially-textured sheet were obtained using standard X-ray diffraction techniques. The {111}, {110} and {100} experimental pole figures are shown in Figure 2-17a. A numerical representation of the experimental pole figures using 48 weighted crystal orientations was obtained by using the computer program PoPLa (Kallend et al., 1989), Figure 2-17b.[10]

The geometry of the tensile specimen used in the superelastic experiments is shown in Figure 2-18a. Tensile specimens were cut for testing along three different directions: 0°, 45° and 90° to the rolling direction. The finite element mesh comprising of 446 three-dimensional ABAQUS-C3D8R elements used in the numerical calculations discussed below is shown in Figure 2-18b. Although not visible, the mesh has a very slight taper such that the gage width at one end of the gage section is slightly narrower than that of the other end. This geometric "imperfection" in the finite-element mesh is introduced to provide an initiation site for phase transformation. We have previously shown that use of the Taylor-model (1938) for simulating the response of polycrystalline Ti-Ni rods produces results which are in reasonably good agreement with experiments, as well as full finite element calculations which do not make this assumption. Accordingly, for computational efficiency, all numerical simulations for polycrystalline Ti-Ni sheet reported in this section have been performed using the Taylor-model (1938).

The thermo-elastic constants used in our calculations are

Elastic moduli for austenite: $C^a_{11} = 130\,\text{GPa}, C^a_{12} = 98\,\text{GPa}, C^a_{44} = 21\,\text{GPa}$;

Elastic moduli for martensite: $C^m_{11} = 65\,\text{GPa}, C^m_{12} = 49\,\text{GPa}, \; C^m_{44} = 10.5\,\text{GPa}$;

[10]This small number of weighted grain orientations, which produces an acceptable representation of the major components of the texture, is used for numerical efficiency. Use of a larger number of orientations does not significantly improve the texture representation, but increases the computational time.

Coefficients of thermal expansion: $\alpha^a = 11 \times 10^{-6}/\mathrm{K}$, $\alpha^m = 6.6 \times 10^{-6}/\mathrm{K}$.

To obtain estimates of the phase transformation parameters a DSC measurement needs to be conducted to obtain the phase equilibrium temperature, θ_T. Since there was difficulty in obtaining pristine DSC experimental results for our polycrystalline sheet Ti-Ni other methods of determining the material must be explored. Therefore an estimate for the phase transformation parameters $\{\theta_T, \lambda_T, f_c\}$ for Ti-Ni single crystals is obtained by fitting the constitutive model to a set of superelastic experiments conducted on our polycrystalline sheet at different temperatures.

The variation of the superelastic forward nucleation resolved force (τ^i_{am}) and reverse nucleation resolved force (τ^i_{ma}) on an active transformation system i with temperature can be plotted in a graph schematically shown in Figure 2-19. The forward nucleation resolved force is the *first* instance where austenite to martensite transformation occurs. The reverse nucleation resolved force is the *first* instance where martensite to austenite transformation occurs. From this, the intercept of the line τ^i_{am} versus θ at zero stress defines the martensite start temperature θ_{ms}, while the intercept of the line τ^i_{ma} versus θ at zero stress defines the austenite start temperature θ_{as}; the mean value

$$\theta_T = \frac{1}{2}(\theta_{as} + \theta_{ms}) \tag{2.26}$$

determines the phase equilibrium temperature.

From (2.8) and (2.11) the forward transformation conditions give us

$$\tau^i_{am}(\theta) - (\lambda_T/\theta_T)\,(\theta - \theta_T) = f_c, \tag{2.27}$$

and the reverse transformation conditions (2.12) yield

$$\tau^i_{ma}(\theta) - (\lambda_T/\theta_T)\,(\theta - \theta_T) = -f_c. \tag{2.28}$$

By adding (2.27) to (2.28), the mean values of these nucleation resolved forces vary linearly with temperature *i.e.*

$$\frac{1}{2}(\tau^i_{am}(\theta) + \tau^i_{ma}(\theta)) = (\lambda_T/\theta_T)\,(\theta - \theta_T).$$

The slope of the line $\frac{1}{2}(\tau^i_{am}(\theta) + \tau^i_{ma}(\theta))$ versus θ will give (λ_T/θ_T), which in turn gives the latent heat of phase transformation, λ_T. The transformation resistance f_c is then given by subtracting (2.28) from (2.27) :

$$f_c = (1/2)\,(\tau^i_{am}(\theta) - \tau^i_{ma}(\theta)).$$

To evaluate these phase transformations parameters superelastic tension experiments were conducted on polycrystalline sheet specimens with the tension axis aligned along the sheet rolling direction – the 0° orientation. The experiments were conducted at three different temperatures, 289 K, 300 K and 306 K, under displacement control at a very low nominal strain rate of 3×10^{-5} /sec, to ensure (near) isothermal conditions. The nominal stress-strain curves from these experiments are shown in Figures 2-20a, 2-20b and 2-20c, respectively[11]. The corresponding numerical simulations at the three different temperatures were carried out on the finite-element mesh shown in Figure 2-18b using 446 ABAQUS-C3D8R elements. For the tension simulation, one end of the finite-element mesh is fixed in all its displacement degrees of freedom, while the other end is subjected to a displacement history corresponding to a nominal axial strain rate of $\pm 3 \times 10^{-5}$ /s.

Following the procedure outlined above the value of the fitted phase transformation parameters are :

Phase equilibrium temperature: $\theta_T = 271\,\mathrm{K}$;

Latent heat: $\lambda_T = 110\,\mathrm{MJ/m^3}$;

Critical transformation resistance: $f_c = 4.7\,\mathrm{MJ/m^3}$.

The resulting nominal superelastic stress-strain curves using the material parameters listed above are also shown in Figures 2-20a, 2-20b and 2-20c. The quality of the fit is very encouraging.

As mentioned previously, phase transformation during superelasticity typically occurs by the nucleation and propagation of phase transformation fronts (Shaw and

[11]The permanent set observed in the experiment at 306 K is probably due to some plastic deformation at the higher stresses in this experiment.

Kyriakides, 1997). Figure 2-21 shows such a phenomenon in our numerical simulations. This figure shows the numerical stress-strain curve from the simulation for 300 K, along with the contours of the martensite volume fraction keyed to instances (a) through (j) at different points along the superelastic stress-strain curve. The contours for (a) through (e) show that martensite nucleates at the right end of the specimen where the gage width is the narrowest, and the transformation front propagates to the left until the gage section is fully transformed to martensite by stage (e). The martensite volume fraction contours for (f) through (j) show that upon reversal of imposed deformation the phase front recedes until the gage section is once again fully austenitic by stage (j).

The results of experiments and corresponding finite-element predictions for superelastic experiments conducted at 300 K on sheet tensile specimens with axes oriented along 45^o and 90^o to the rolling direction[12] are shown in Figure 2-22a and 2-22b, respectively. The small amount of anisotropy in the superelastic stress-strain response in these differently oriented specimens is well-captured by the predictions from the constitutive model.

An important manifestation of the superelastic response of a shape-memory material is the strain-versus-temperature response at a fixed stress level. By cycling the temperature over a narrow range at a fixed stress, one can obtain a recoverable strain cycle. Figures 2-23a and b show experimental strain-temperature curves from 0°-oriented specimens which were first subjected to fixed axial stress levels of 150 MPa and 250 MPa, and then subjected to a temperature history where the temperature is decreased at a constant rate of 0.016 K/s, and then increased back at the same rate. With respect to Figure 2-23a, the initial elastic strain of ≈ 0.005 is due to the axial stress of 150 MPa. The material is initially in the austenitic state. As the temperature is decreased from 315 K, the strain first decreases slightly due to thermal contraction, and then at $\approx$ 276K the austenite-to martensite-transformation occurs and there is a

[12]We have also investigated the behavior of Ti-Ni sheets which were thermo-mechanically processed differently from the sheets studied in this section. In Appendix H we show that our constitutive model is able to predict the anisotropy exhibited in the superelastic tension experiments on sheet Ti-Ni conducted by Shan and Sung (2001) to good accord.

sudden burst of strain of the order 4%. Upon heating, there is at first a slight increase in the strain due to thermal expansion, and then at ≈ 302K the martensite transforms back to austenite with a strain recovery of the order 4%. The temperatures at which the transformations occur can be controlled by the initial stress bias. As shown in Figure 2-23b, an increase in the initial stress increases the austenite-to-martensite as well as the martensite-to-austenite transformation temperatures. Figure 2-23 also shows that the corresponding predictions from the theory are in good agreement with the experiments.

We next consider the *coupled thermo-mechanical* superelastic response of the initially-textured Ti-Ni sheet. In order to examine the effects of heat generation and conduction, we have performed superelastic tension experiments at three different nominal strain rates on 0°-oriented specimens at an initial temperature of 300 K. In addition to the test at the "low" nominal strain rate of 3×10^{-5}/sec reported previously, Figure 2-20b, where the response was expected to be (close to) isothermal, we have conducted two additional experiments at slightly "higher" rates of 8.4×10^{-4}/sec and 2×10^{-3}/sec, where we expect to see some effects of the changes in temperature. The superelastic stress-strain curves for all three strain rates are shown in Figure 2-24. Note that as the strain rate increases, the stress-strain curves at the two higher strain rates show a "hardening response". This apparent hardening due to thermal effects is qualitatively similar to that reported previously by Entemeyer et al. (2000), who have argued that the major contribution to the apparent hardening is due to temperature changes associated with the exothermic $a \rightarrow m$, and endothermic $m \rightarrow a$ transformations.

Recall that the energy balance (2.21) requires computation of the term

$$\operatorname{div}\Big\{J^{-1}\mathbf{F}\mathbf{K}(\xi)\mathbf{F}^{\mathrm{T}}\operatorname{grad}\theta\Big\}.$$

The finite-element program ABAQUS/Explicit (currently) limits user access to modify the computer code, and allows input of only a single scalar value for the thermal conductivity. We have accordingly made several approximations in our calculations. For the cubic austenite the thermal conductivity is isotropic, $\mathbf{K}^a = \kappa^a \mathbf{1}$. For the

monoclinic martensite the anisotropic thermal conductivities are not known, and as with the elastic constants, these are also approximated as that for cubic materials, $\mathbf{K}^m \approx \kappa^m \mathbf{1}$. We shall use a constant value of $\kappa = (\kappa^a + \kappa^m)/2$ in our numerical calculations. Further, since the superelastic strains are small, we neglect the contributions from the J and $\mathbf{F}\mathbf{F}^T$ terms, and make the approximation $\operatorname{div}\left\{J^{-1}\mathbf{F}\mathbf{K}(\xi)\mathbf{F}^T \operatorname{grad}\theta\right\} \approx \kappa \operatorname{div}\operatorname{grad}\theta$. We also neglect the terms $J^{-1}\theta\,\overline{\dot{\mathbf{E}}^e \cdot \boldsymbol{\mathcal{C}}(\xi)[\mathbf{A}(\xi)]} + J^{-1}r$ in (2.21). Under these approximative assumptions the equation governing the change in temperature becomes

$$c\,\dot{\theta} \approx \kappa \operatorname{div}\operatorname{grad}\theta + \frac{\lambda_T}{\theta_T}\,\theta\,\dot{\xi} + \sum_i f^i \dot{\xi}^i. \tag{2.29}$$

Based on values published in the literature, we use the following values of

$$c = 2.1\,\mathrm{MJ/m^3\,K}, \qquad \kappa = 13\mathrm{W/m\,K}$$

for Ti-Ni in our calculations. The calculations were carried out for a Ti-Ni sheet specimen modelled using the mesh shown in Figure 2-18b, this time using 446 C3D8RT ABAQUS elements. Regarding the thermal boundary conditions, the whole mesh is initially at 300K. The nodes at the grip ends are kept at 300K throughout the calculation to simulate massive hard grips which act as constant temperature baths. The heat flux from the remaining faces of the tension strip due to convection in air is taken to be governed by boundary conditions on the heat flux $\mathbf{h}$ in the deformed configuration, of the form $\mathbf{h} = h(\theta - \theta_0)\mathbf{n}$, with a film coefficient h and a sink temperature θ_0. In our calculations we take the film coefficient to have a value $h = 12\,\mathrm{W/m^2\,K}$, and a sink temperature of 300K. Figure 2-24 also shows the resulting superelastic stress-strain curves for all three strain rates. The hysteresis loop corresponding to the lowest strain rate is very similar to that obtained from the isothermal calculation, Figure 2-20b, while the stress-strain curves calculated for the higher strain rates show the experimentally-measured hardening response. Recall that we have set $f_c^i \equiv f_c \cdots \text{constant}$.[13] Thus, the hardening response is *entirely due to thermal effects associated with the phase transformations.* Figure 2-25 shows evolution of the

[13]The interaction terms g^{ij} have also been set to zero in our calculations.

contours of the martensite volume fraction at representative instances during the forward and reverse transformations for the test at the highest strain rate. Note that because of the boundary conditions, both the forward and reverse transformations start from the grip-ends and propagate as "fronts" towards the center of the specimen. Figure 2-26 shows contours of the temperature at representative instances during the forward and reverse transformations. During forward transformation the temperature increases by as much as 22K from the ambient temperature of 300K due to the exothermic austenite-to-martensite transformation, while it decreases by as much as 22K from the ambient temperature during the reverse endothermic transformation from martensite-to-austenite. The nucleation and propagation of phase transformation fronts and the associated temperature changes in our calculations, are qualitatively similar to the results reported by Shaw and Kyriakides (1997) for their polycrystalline sheet tensile specimens.

The effects of heat conduction into and out off the gage section were further studied by performing a superelastic tension-hold experiment. A representative strain-time profile for such an experiment is as follows: the specimen is extended at a strain rate of 1.25×10^{-3}/sec with an intermediate hold of 10 sec, and then after the desired total strain level the straining direction is reversed at a rate of -1.25×10^{-3} /sec, again with an intermediate hold of 10 sec, Figure 2-27a. The experimental nominal stress-strain curve and the corresponding finite-element prediction of this experiment are shown in Figure 2-27b. The finite-element simulation nicely reproduces the stress-dip observed in the experiment during the forward transformation, and the stress-increase during the reverse transformation. The major cause for the stress-dip and stress-increase is the heat conduction out of and into the specimen, respectively, during the forward and reverse transformations.

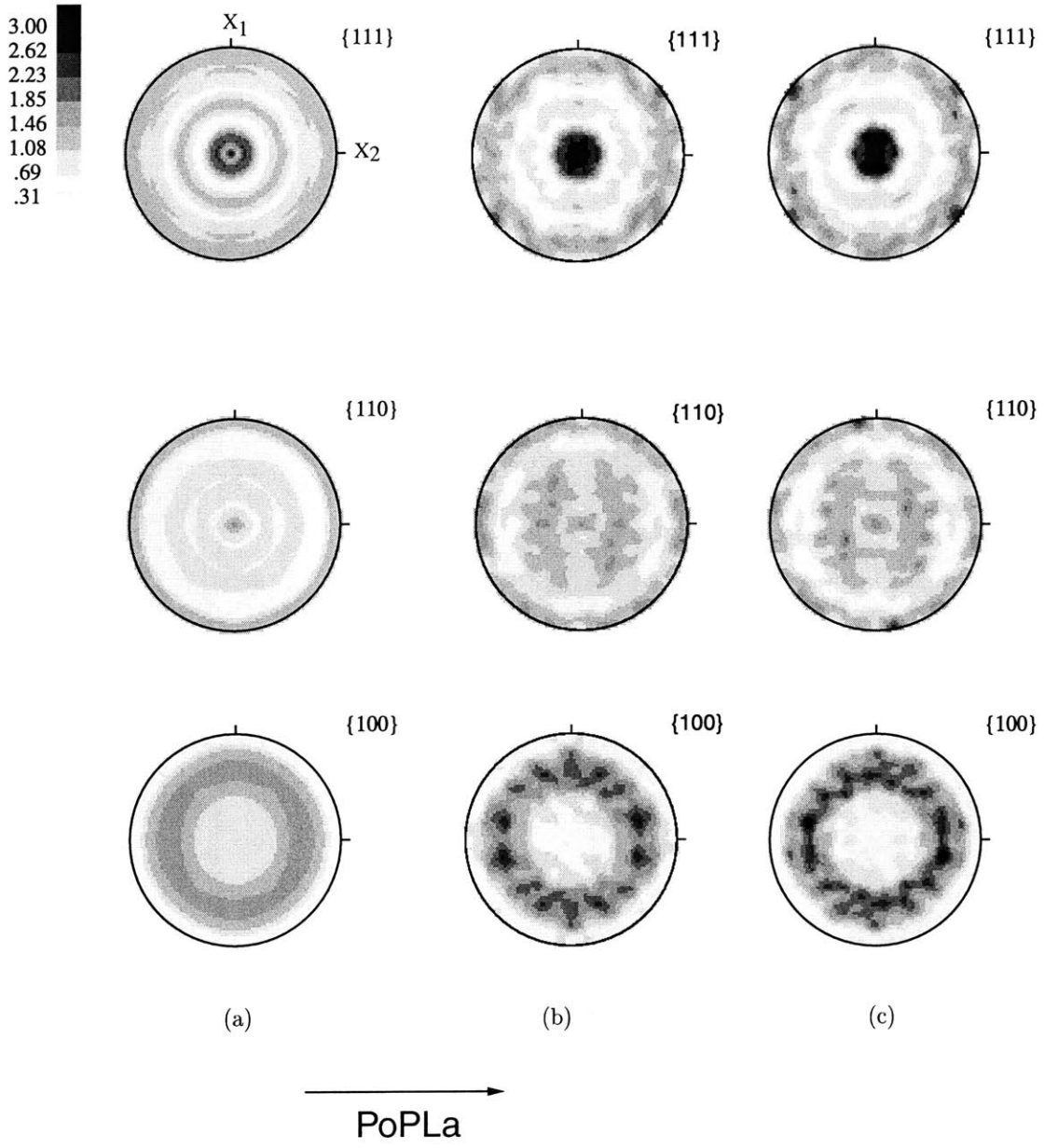

Figure 2-1: (a) Experimentally-measured texture in the as-received Ti-Ni rod, (b) its numerical representation using 729 unweighted discrete crystal orientations, and (c) its numerical representation using 343 unweighted discrete crystal orientations. Pole-figure data were obtained using PoPLa.

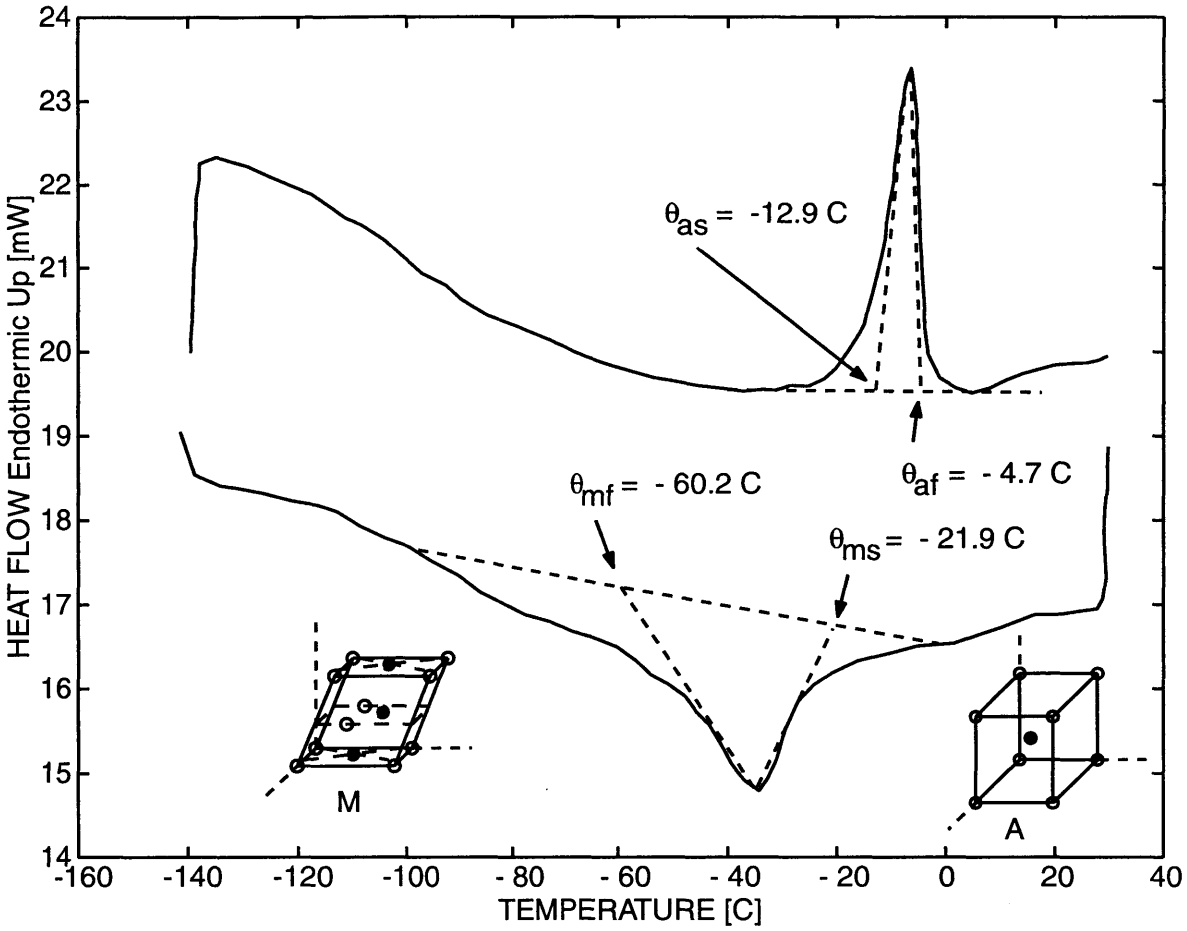

Figure 2-2: Differential scanning calorimetry thermogram for polycrystalline rod Ti-Ni used in experiments.

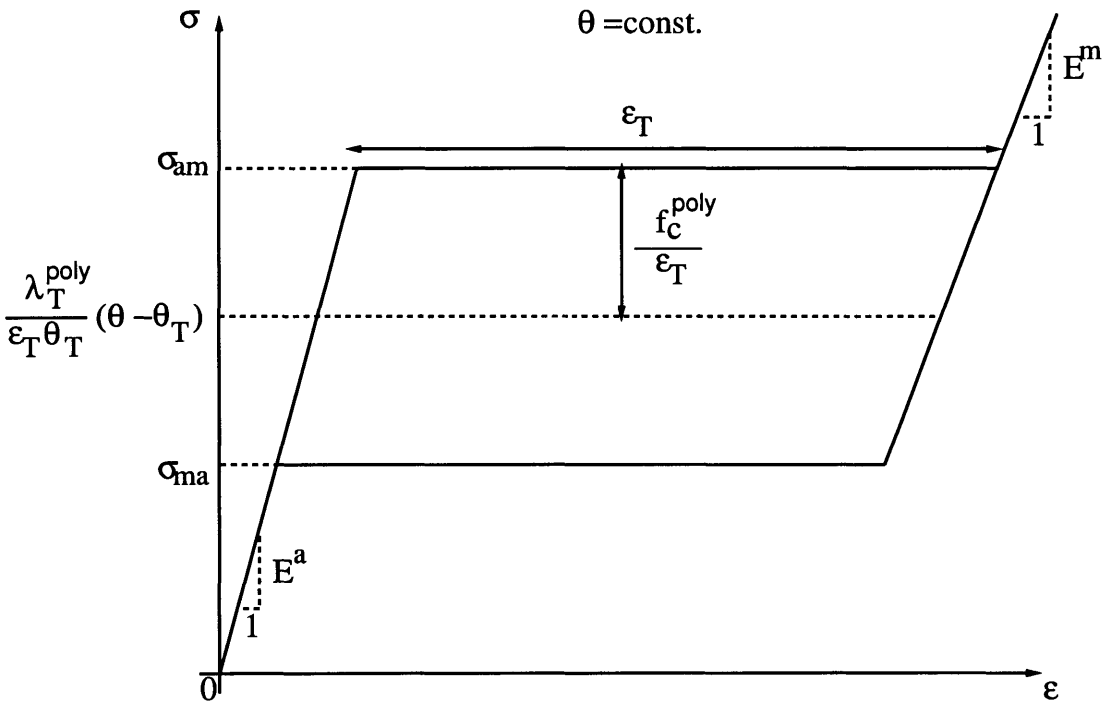

Figure 2-3: Schematic of an isothermal superelastic stress-strain response in simple tension.

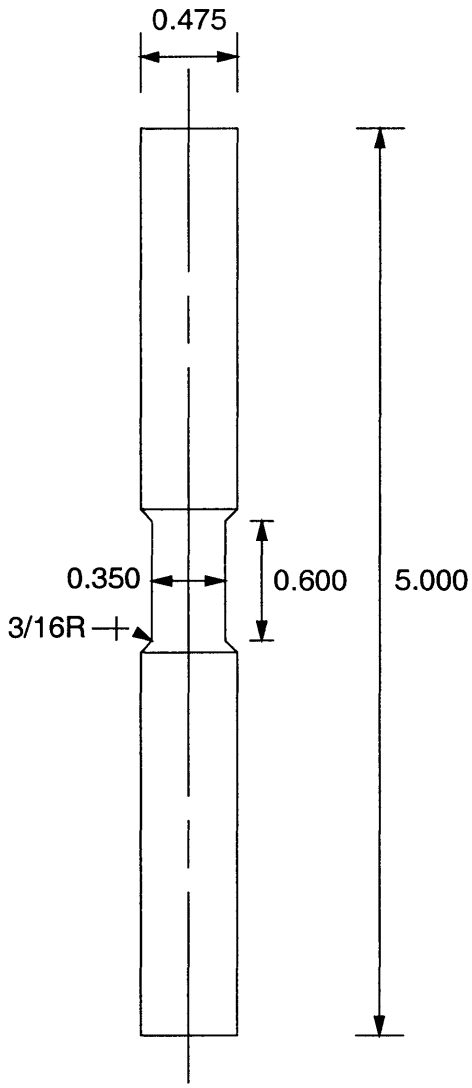

Figure 2-4: Specimen geometry for tension and compression experiments.

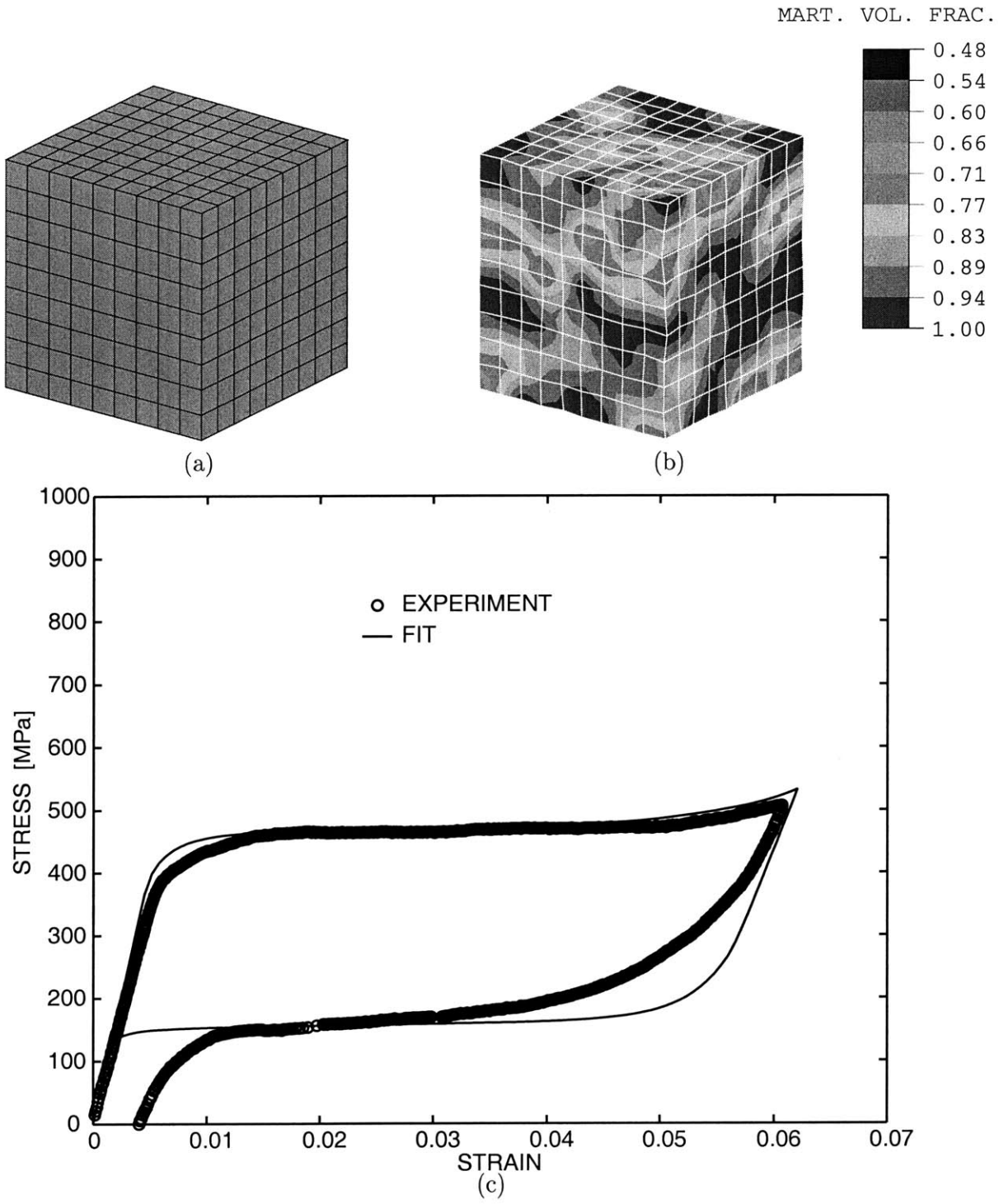

Figure 2-5: (a) Undeformed mesh of 729 ABAQUS C3D8R elements. (b) Deformed mesh at a tensile strain of 6%. Contours of martensite volume fraction are shown. (c) Superelastic stress-strain curve in tension. The experimental data from this test was used to estimate the constitutive parameters. The curve fit using the full finite element model of the polycrystal is also shown.

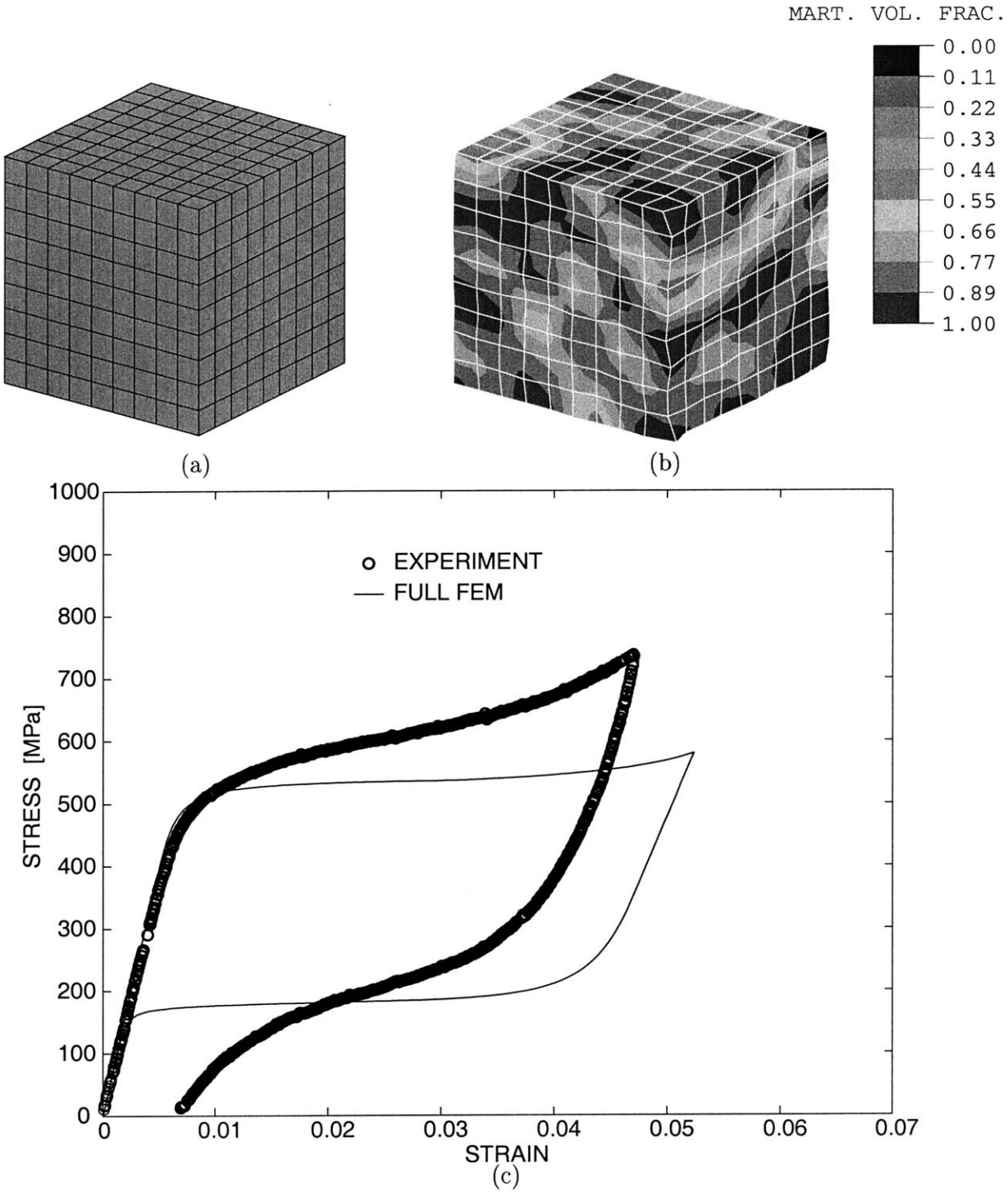

Figure 2-6: (a) Undeformed mesh of 729 ABAQUS C3D8R elements. (b) Deformed mesh at a compressive strain of 5%. Contours of martensite volume fraction are shown. (c) Superelastic stress-strain curve in compression. The absolute values of stress and strain are plotted. The prediction from the full finite-element model for the polycrystal is also shown.

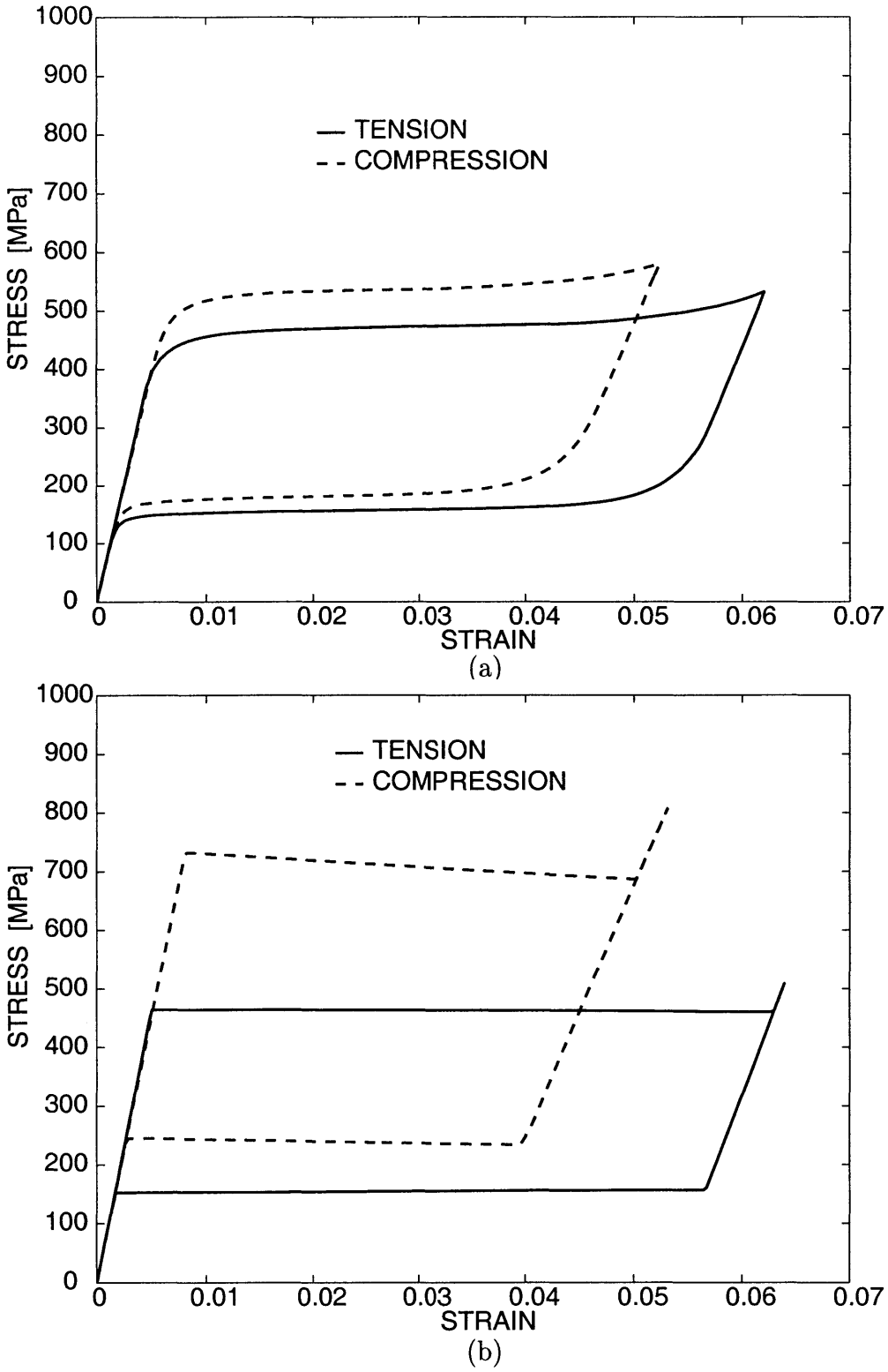

Figure 2-7: Comparison of the predicted response from tension and compression simulations to demonstrate the numerically predicted tension-compression asymmetry for (a) the polycrystal material and (b) single crystal oriented in the $\{111\}$ direction.

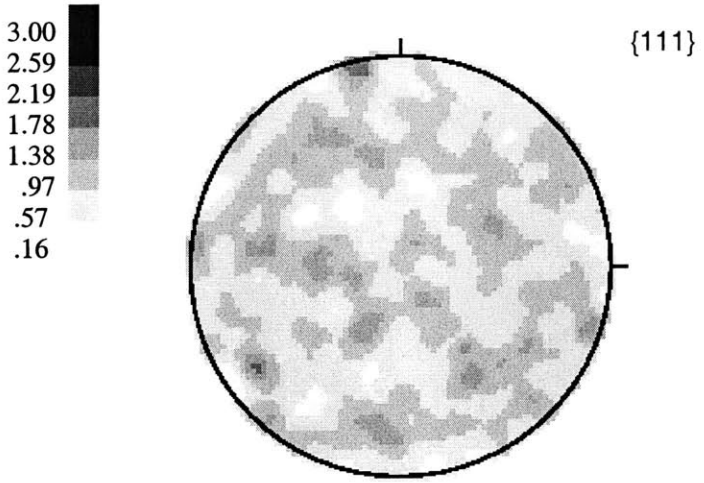

(a)

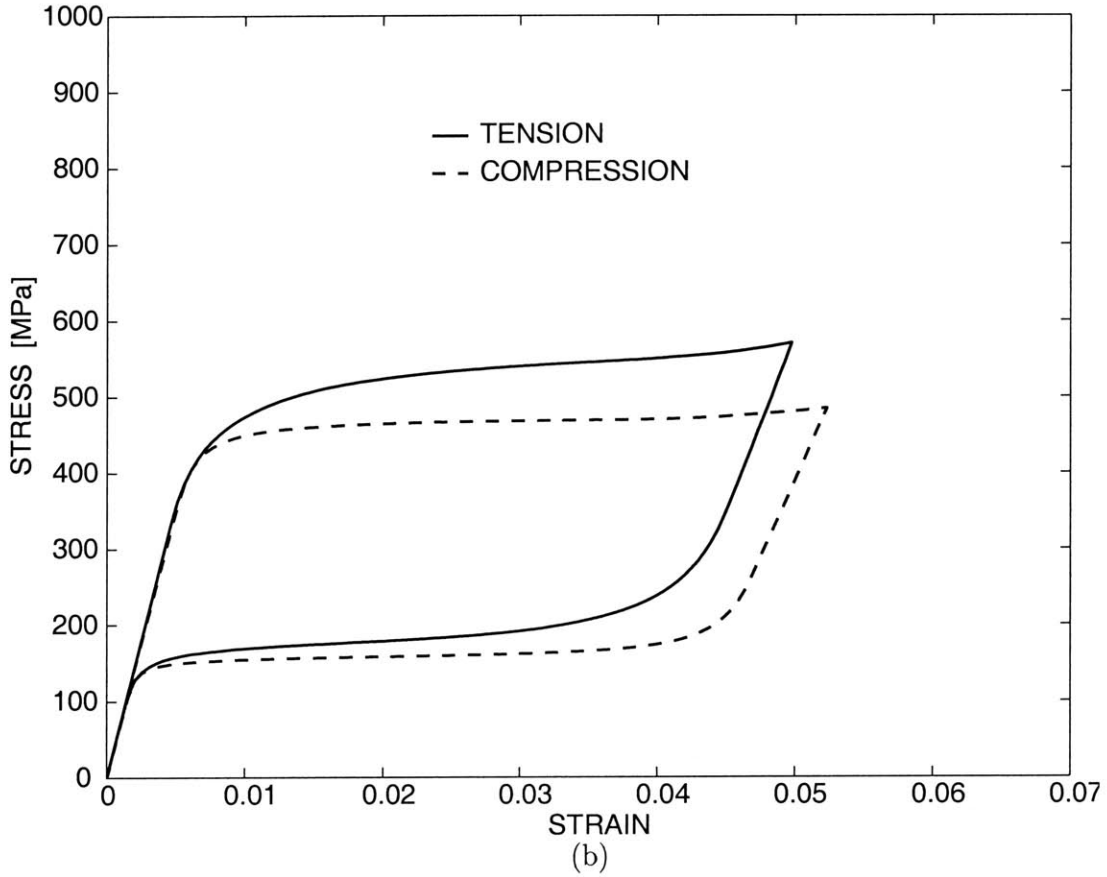

(b)

Figure 2-8: (a) {111} pole figure corresponding to a random initial texture. (b) Comparison of the predicted stress-strain response in tension and compression using a random initial texture.

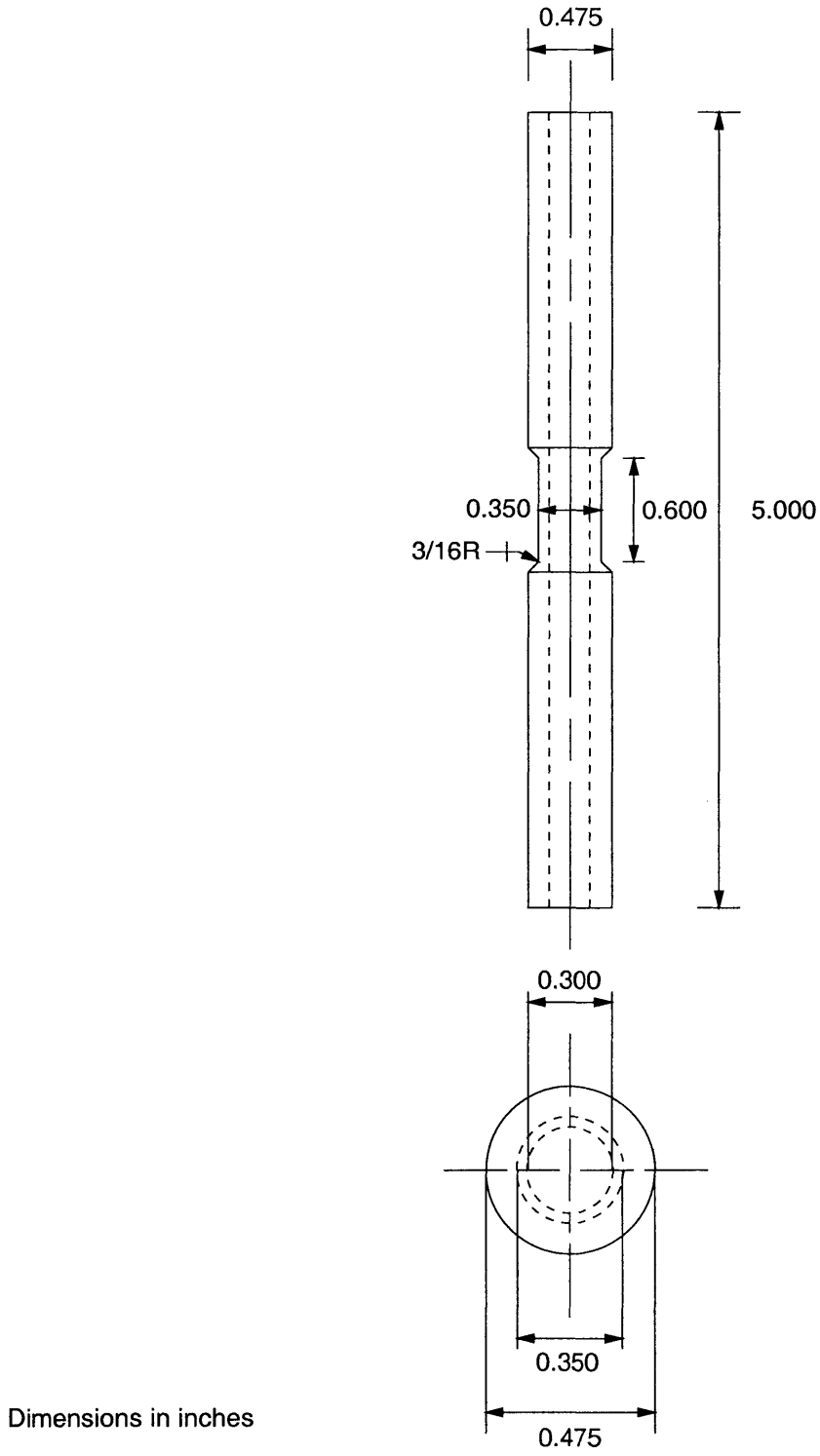

Figure 2-9: Specimen geometry for torsion experiments.

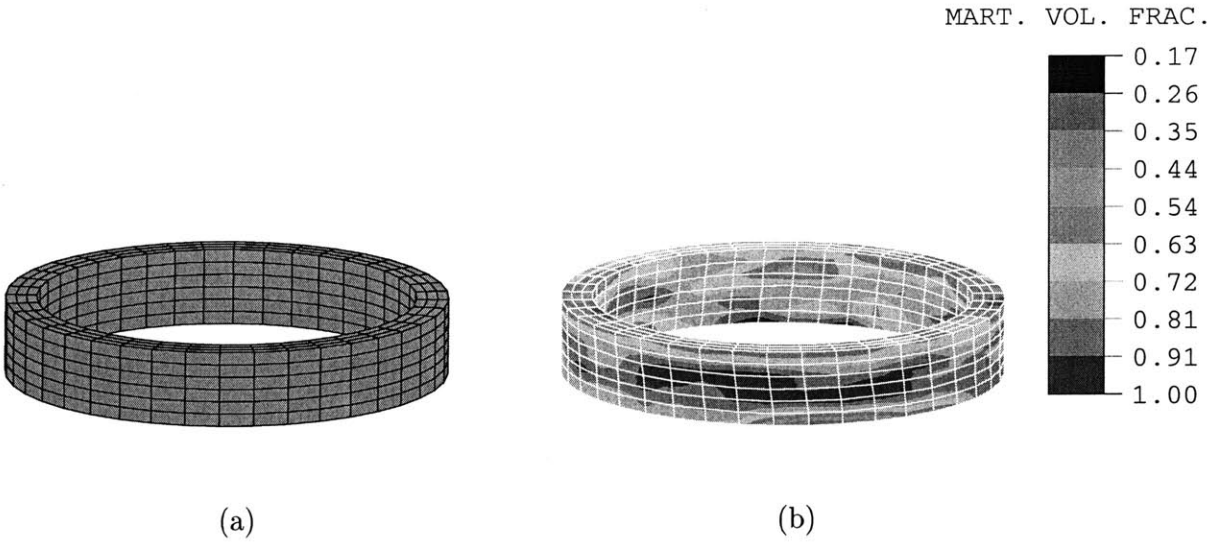

(a) (b)

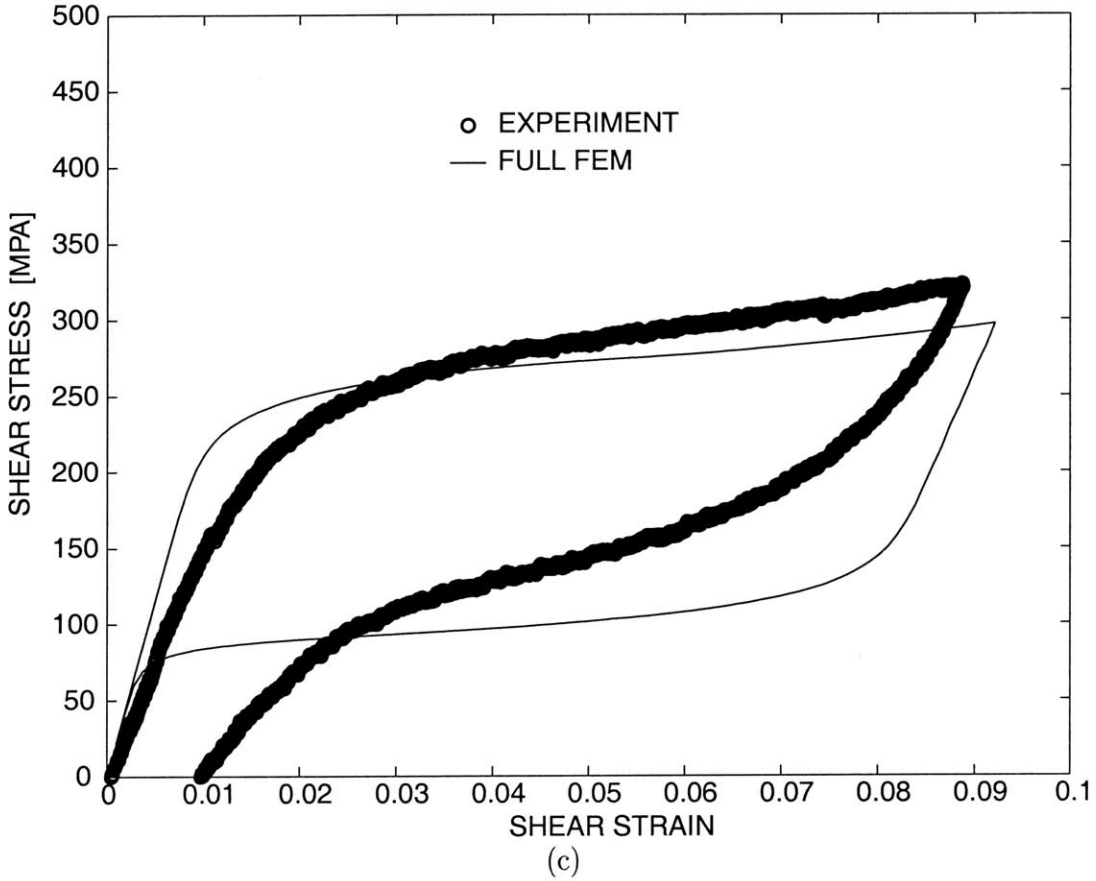

(c)

Figure 2-10: (a) Undeformed mesh of 720 ABAQUS C3D8R elements. (b) Deformed mesh at a shear strain of 9%. Contours of martensite volume fraction are shown. (c) Superelastic stress-strain curve in torsion. The prediction from the full finite-element model for the polycrystal is also shown.

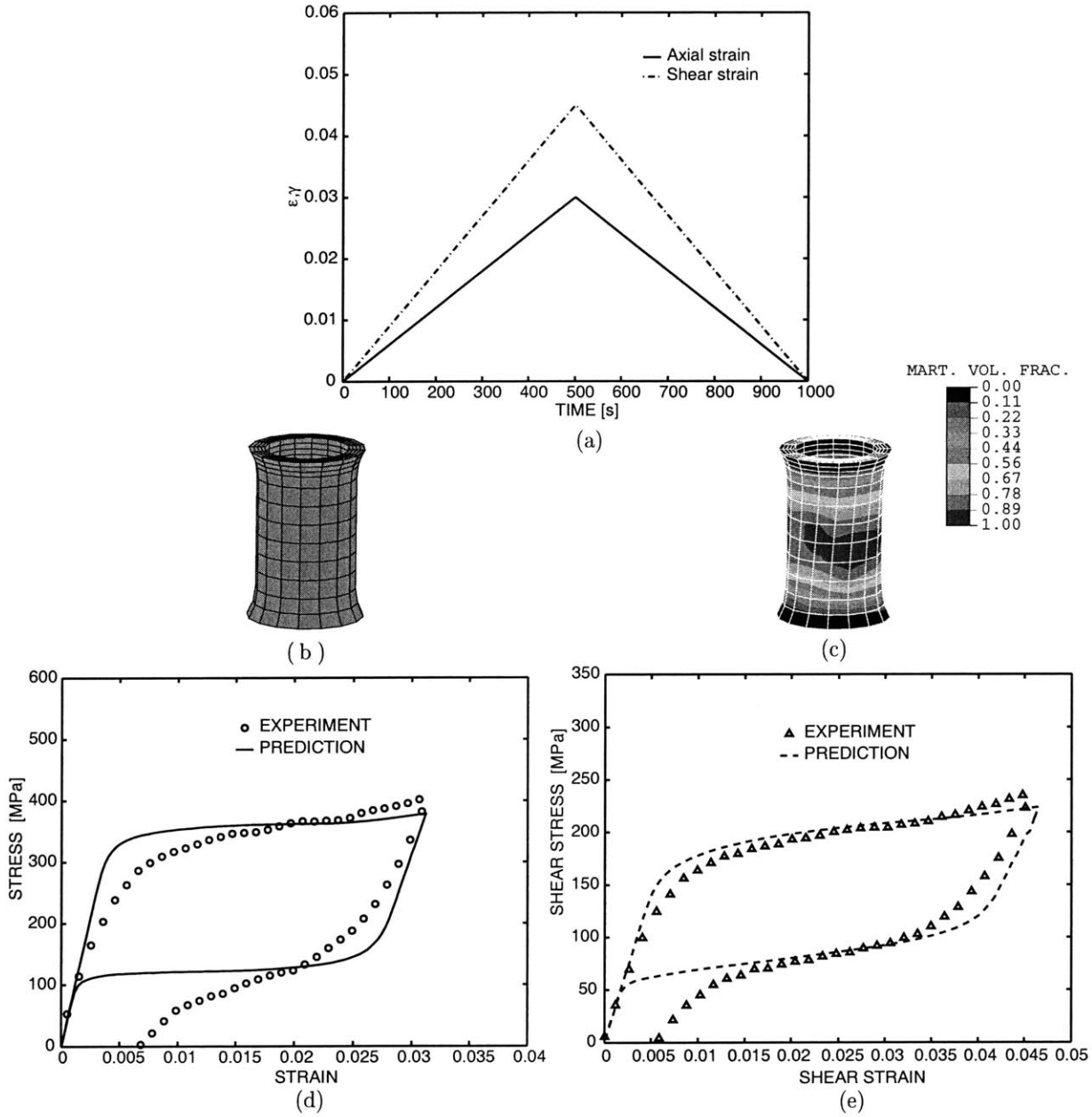

Figure 2-11: (a) Loading program for combined tension-torsion experiment. (b) Undeformed mesh of 768 ABAQUS C3D8R elements. (c) Deformed mesh at a tensile strain of 3% and a shear strain of 4.5%. Contours of martensite volume fraction are shown. (d) Superelastic stress-strain curve in tension. (e) Superelastic stress-strain curve in shear. The prediction from the full finite element model for the polycrystal is also shown.

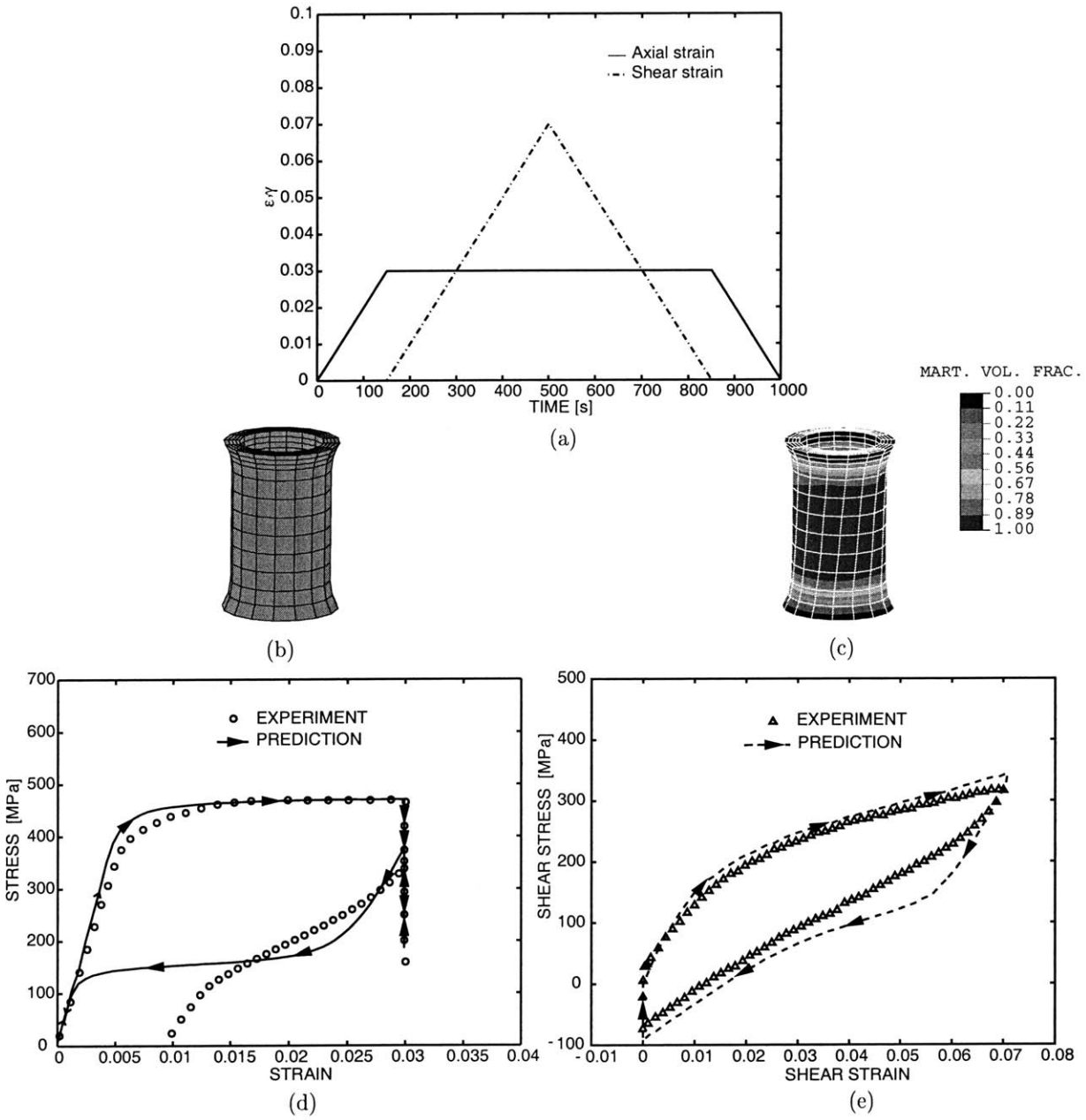

Figure 2-12: (a) Loading program for the path change tension-torsion experiment. (b) Undeformed mesh of 768 ABAQUS C3D8R elements. (c) Deformed mesh at a tensile strain of 3% and a shear strain of 7%. Contours of martensite volume fraction are shown. (d) Superelastic stress-strain curve in tension. (e) Superelastic stress-strain curve in shear. The prediction from the full finite element model for the polycrystal is also shown.

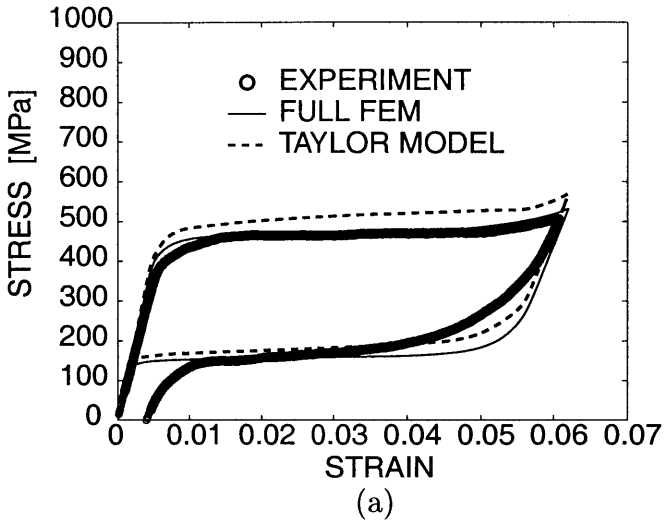

(a)

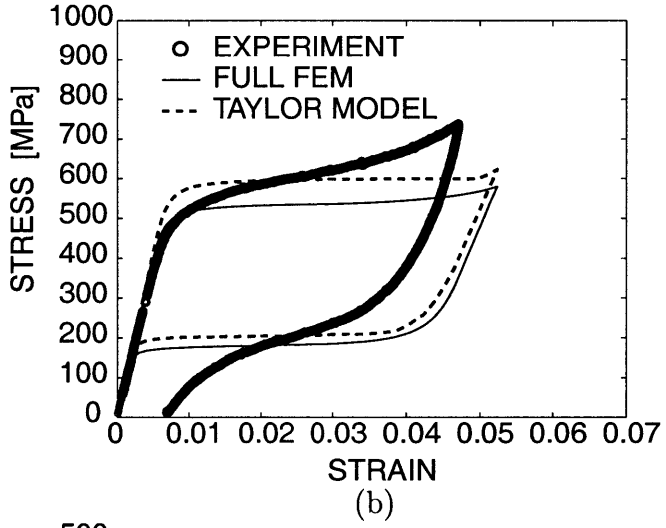

(b)

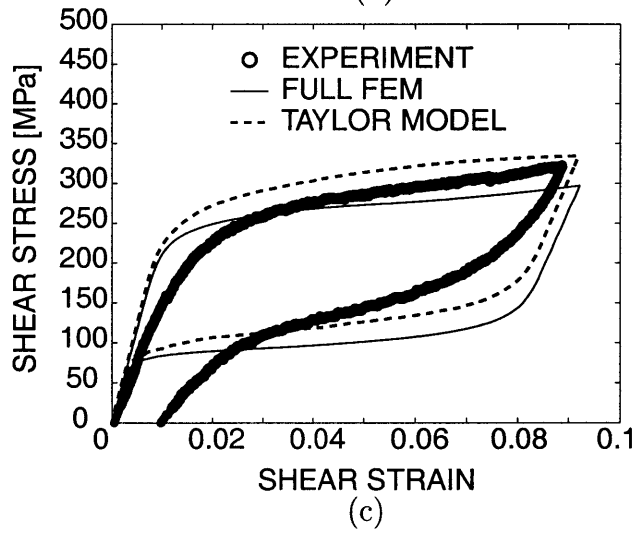

(c)

Figure 2-13: Comparison of the Taylor model against experiment and full finite-element calculation in (a) simple tension, (b) simple compression, and (c) shear.

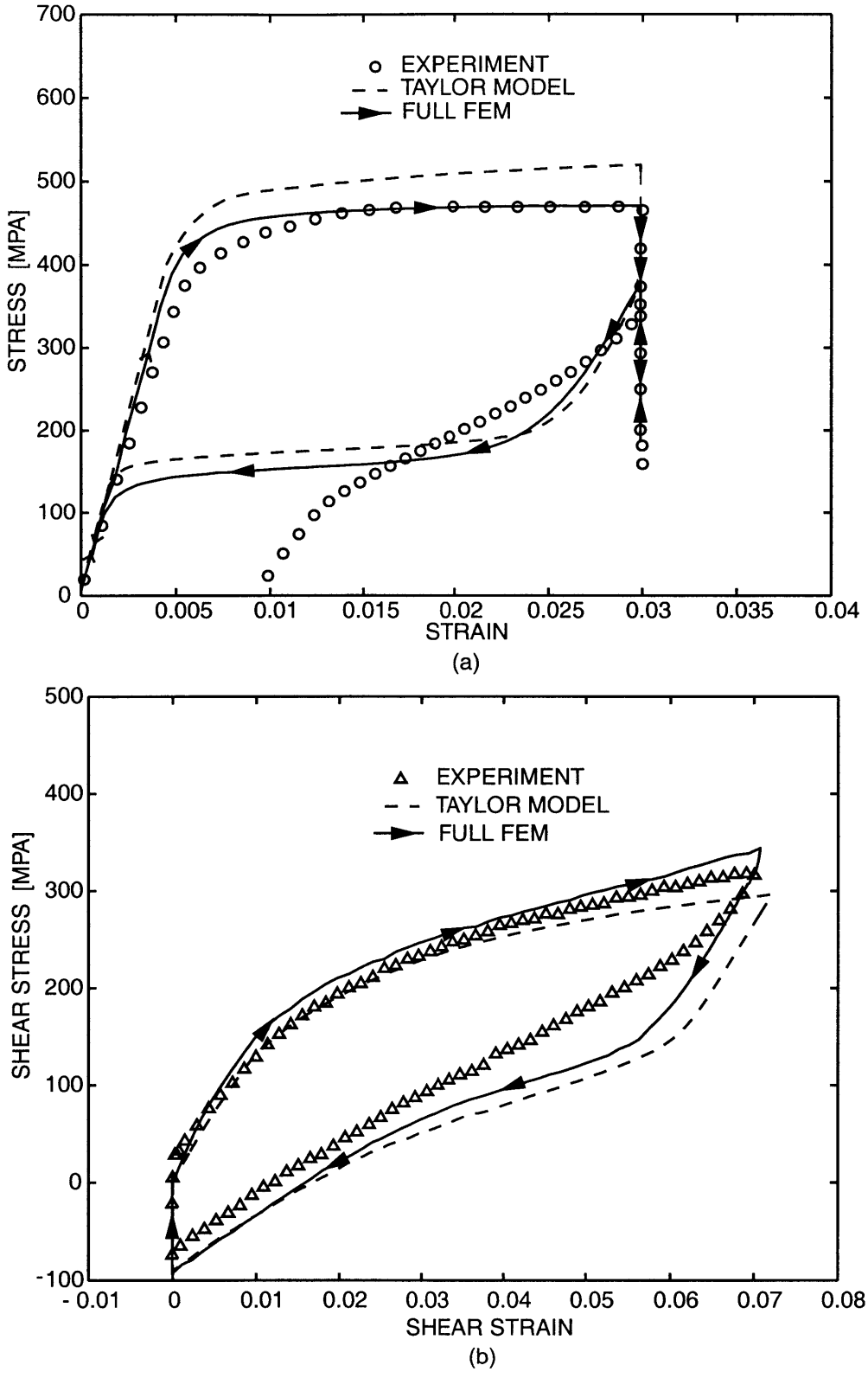

Figure 2-14: Response of the Taylor Model compared against the path change tension-torsion experiment and full finite element calculation in (a) tension and (b) shear.

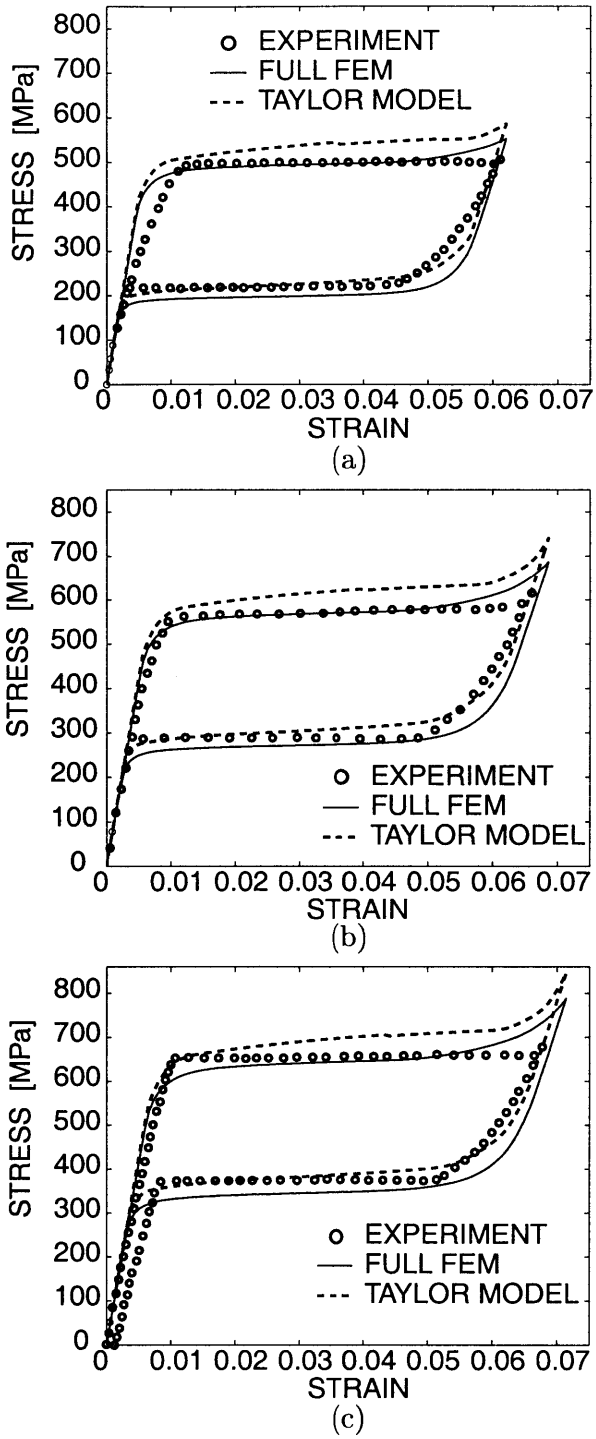

Figure 2-15: Superelastic stress-strain curves in tension (Shaw and Kyriakides, 1995) at three temperatures (a) $\theta = 333.2\,\mathrm{K}$, (b) $\theta = 343.2\,\mathrm{K}$, and (c) $\theta = 353.2\,\mathrm{K}$. Full finite-element and Taylor model prediction from the constitutive model are also shown. The material parameters for the Ti-Ni of Shaw and Kyriakides is obtained from the data at 343.2 K.

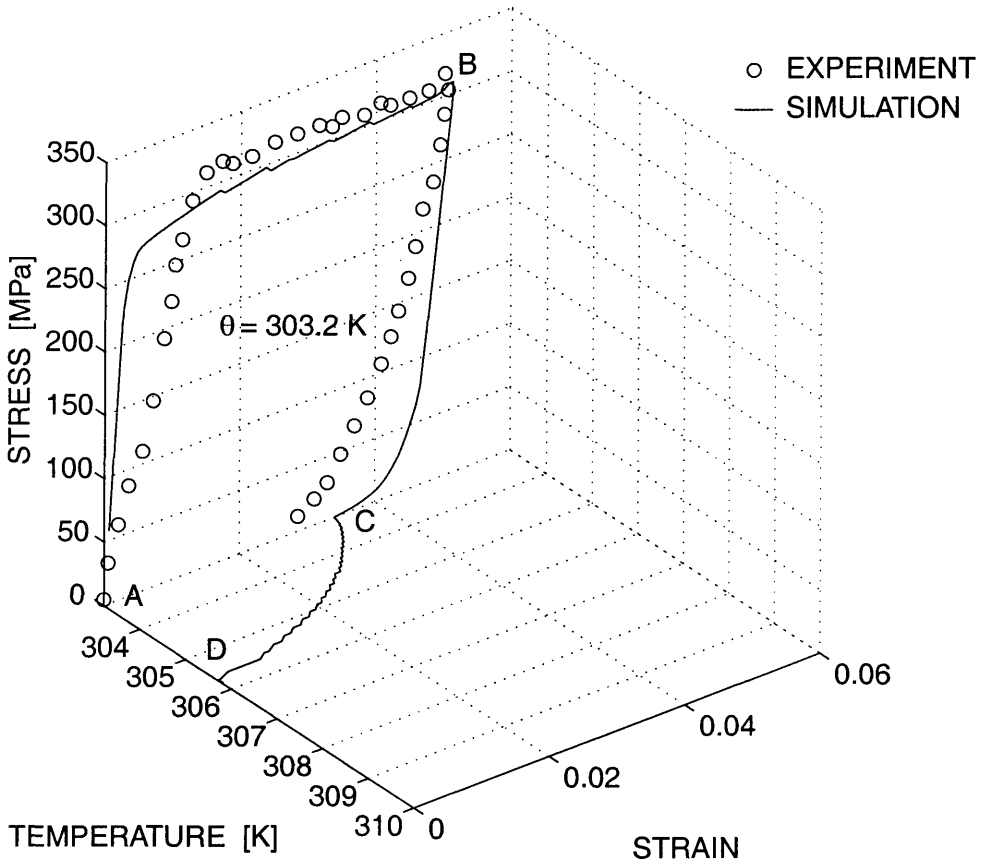

Figure 2-16: Simulation of austenite-martensite-austenite shape memory effect (Shaw and Kyriakides, 1995): Isothermal stress-strain response for straining at constant strain rate (ABC) at $\theta = 303.2\,\mathrm{K}$ followed by a temperature (CD) to $\theta = 305.8\,\mathrm{K}$.

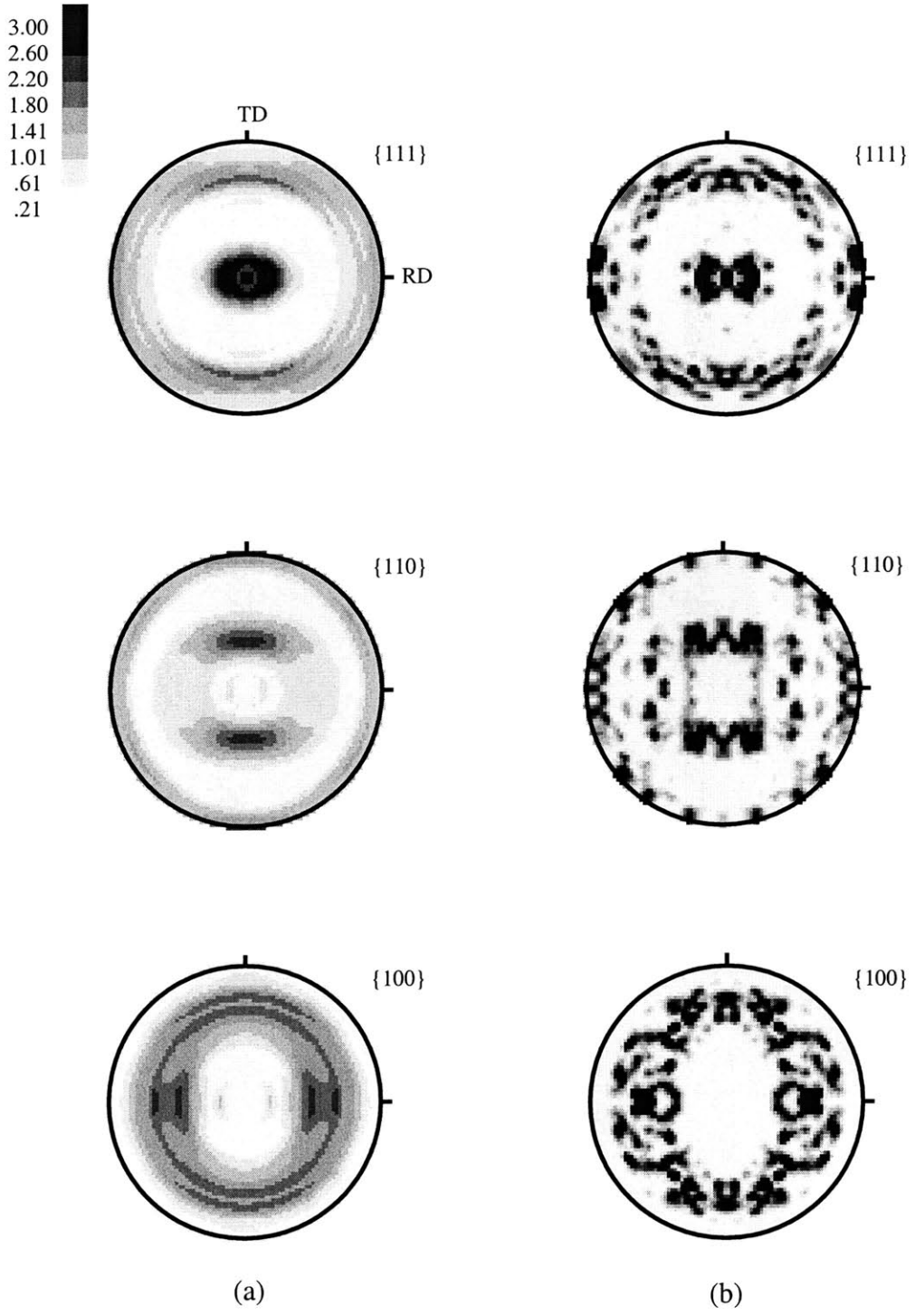

Figure 2-17: (a) Experimentally-measured texture in the as-received Ti-Ni sheet; and (b) its numerical representation using 48 weighted crystal orientations.

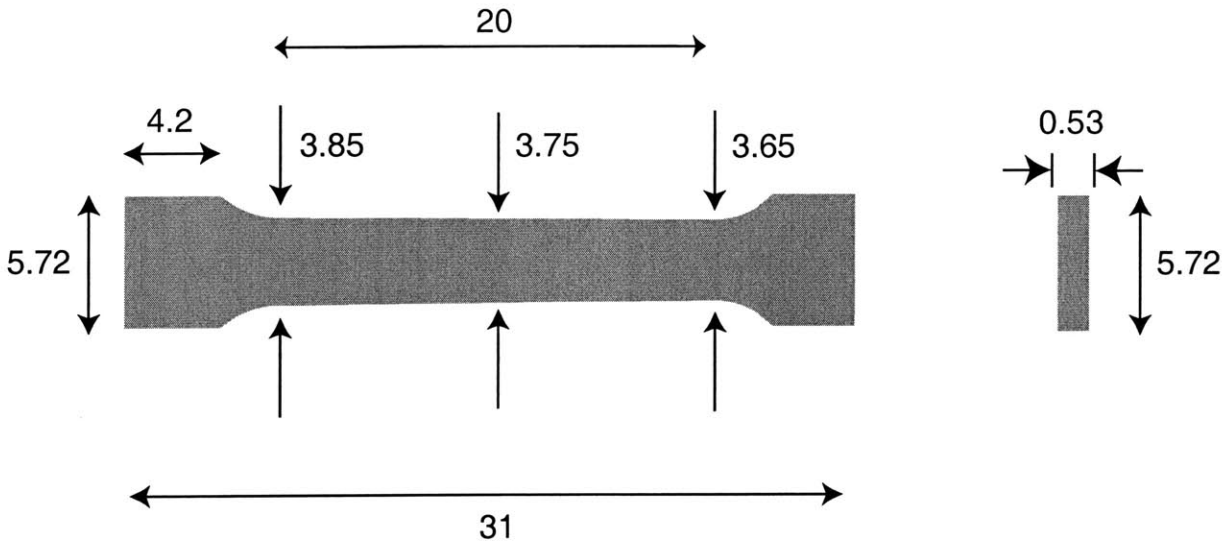

(a)

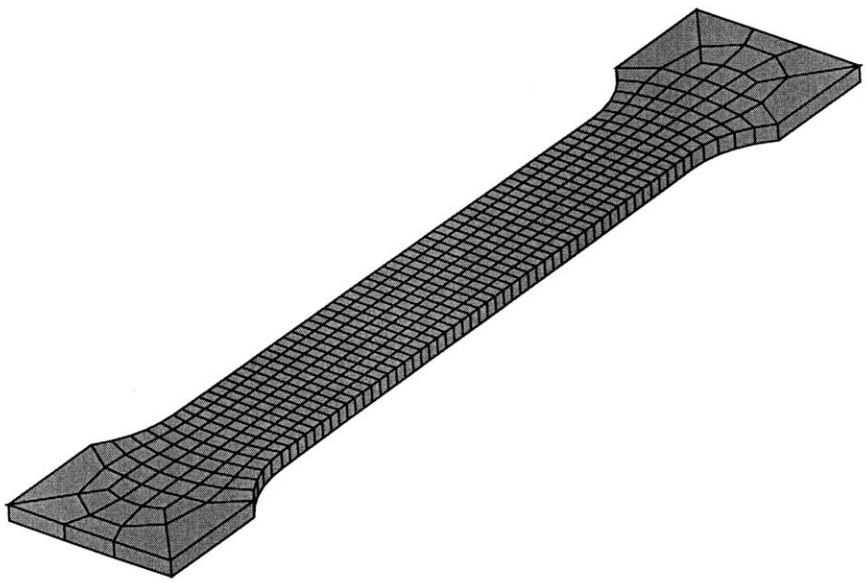

(b)

Figure 2-18: (a) Geometry of the tensile specimen (drawing is not to scale). (b) Undeformed finite-element mesh of the tensile specimen using 446 ABAQUS three-dimensional elements. The gage width of the specimen is linearly tapered from 3.85 mm to 3.65 mm as shown in (a).

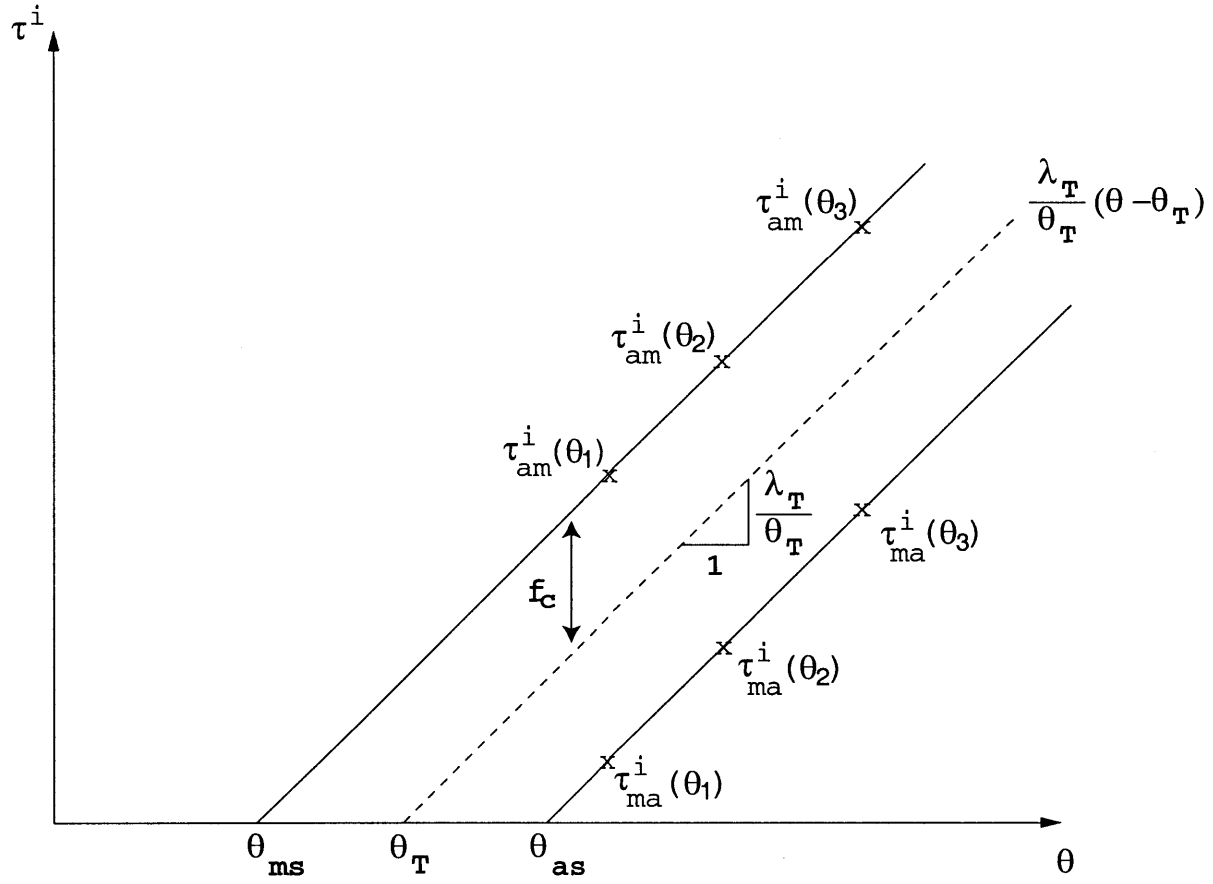

Figure 2-19: Schematic diagram of the variation of resolved forces on an active transformation system i with temperature.

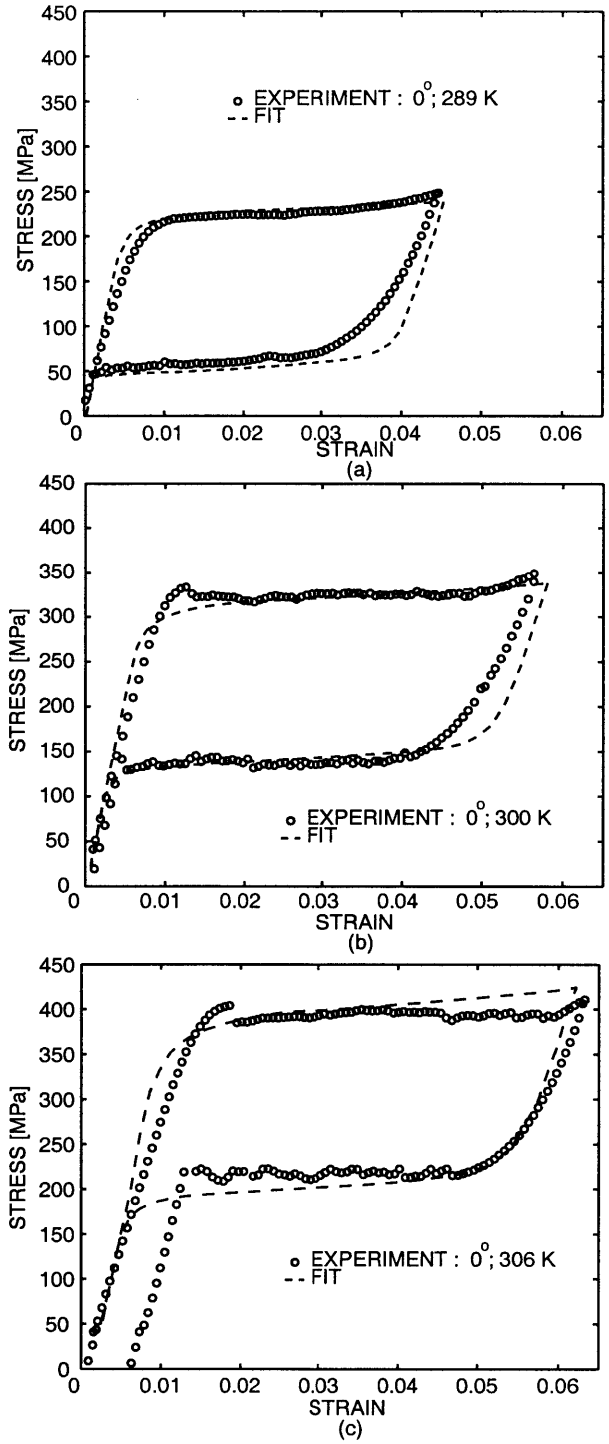

Figure 2-20: Nominal superelastic stress-strain curves from tension tests on 0°-oriented specimens. The tests were conducted under isothermal conditions at (a) 289 K, (b) 300 K, and (c) 306 K. The experimental data from these tests were used to estimate the phase transformation parameters. The curve fit from the finite-element simulations is also shown.

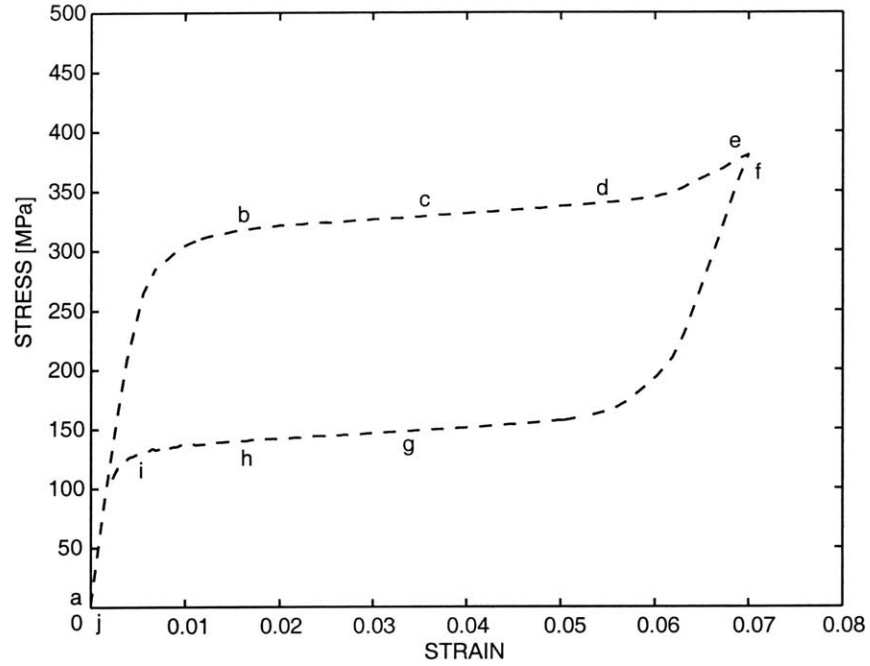

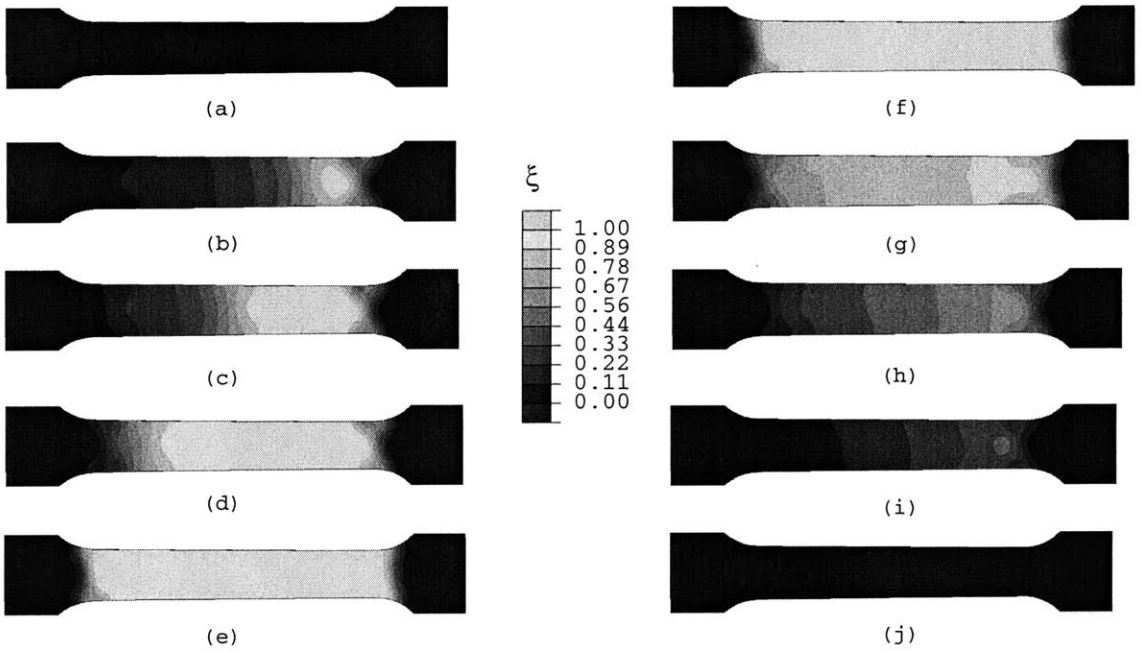

Figure 2-21: A superelastic finite-element simulation of an experiment conducted under isothermal conditions at 300 K. Contour plots of the martensite volume fraction are also shown. The set of contours on the left shows the transformation from austenite-to-martensite during forward transformation, while those on the right show the transformation from martensite-to-austenite during reverse transformation. Note that because of the slight taper in the gage width, the austenite-to-martensite transformation nucleates at the right grip-end and propagates toward the opposing grip-end.

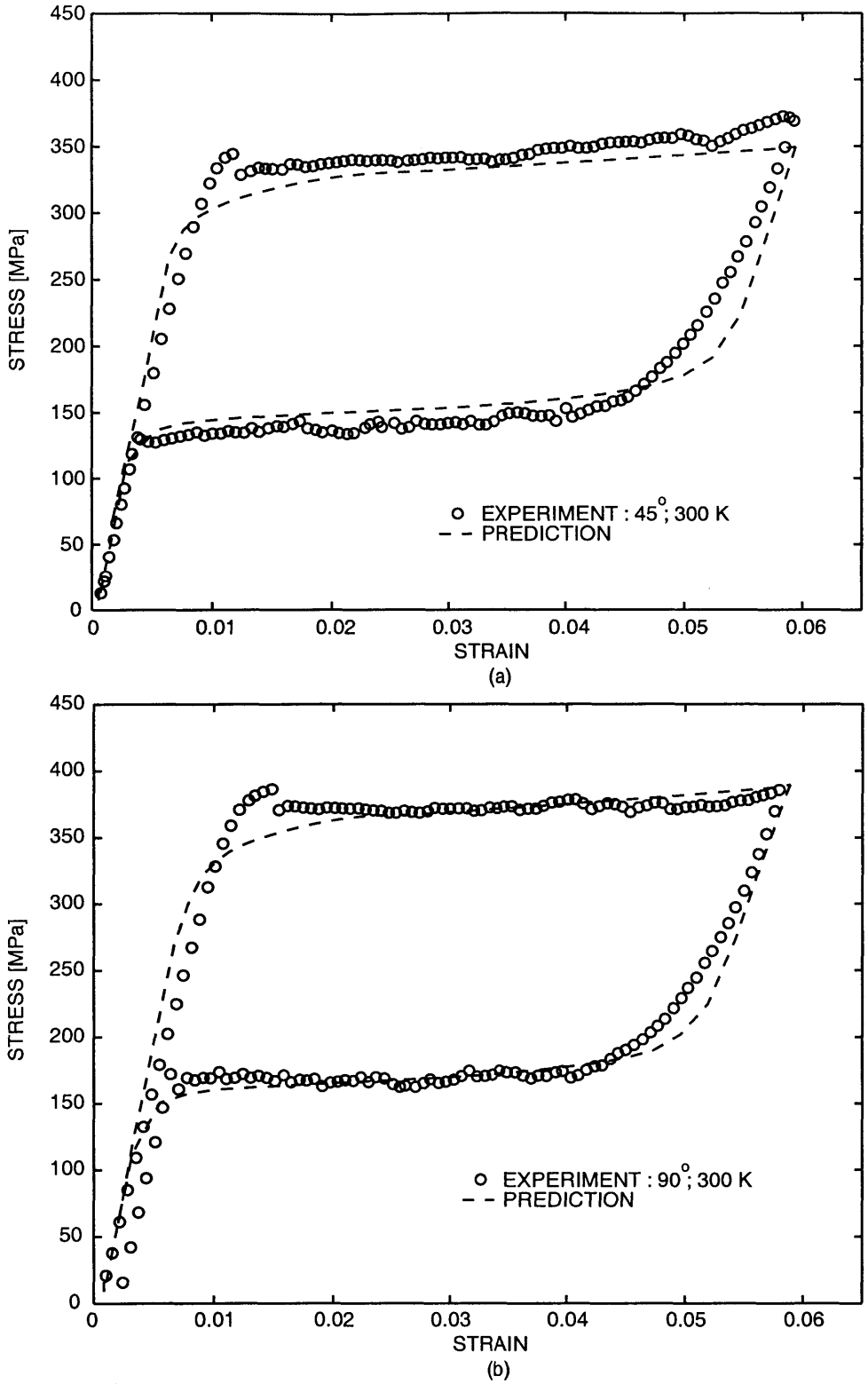

Figure 2-22: Experimental superelastic stress-strain curves in tension at 300 K: (a) 45° orientation; (b) 90° orientation. The corresponding predictions from the finite-element simulations are also shown.

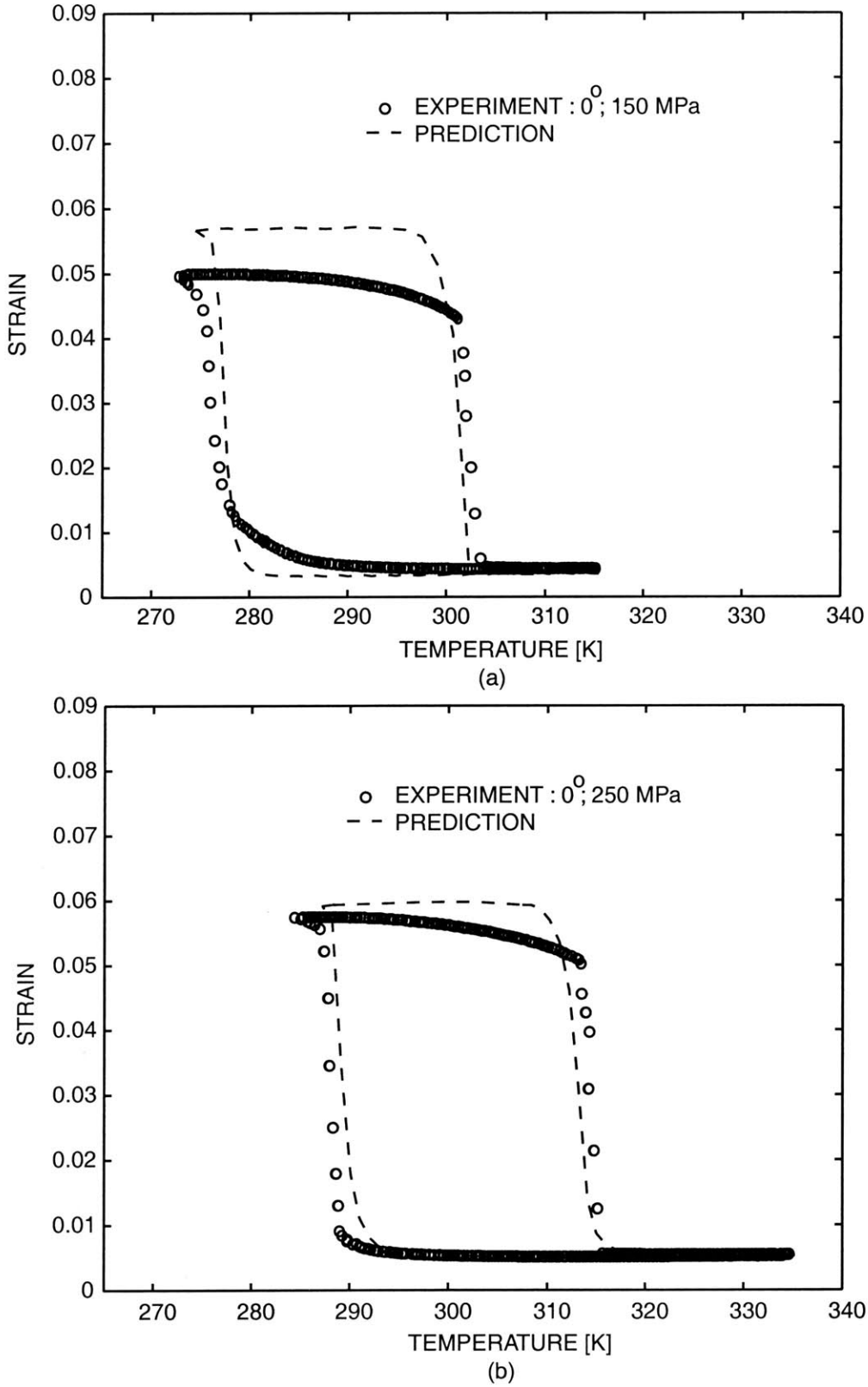

Figure 2-23: Strain-temperature cycling experiments conducted on 0°-oriented specimens at pre-stress levels of (a) 150 MPa; and (b) 250 MPa. The predictions from the finite-element simulations are also shown.

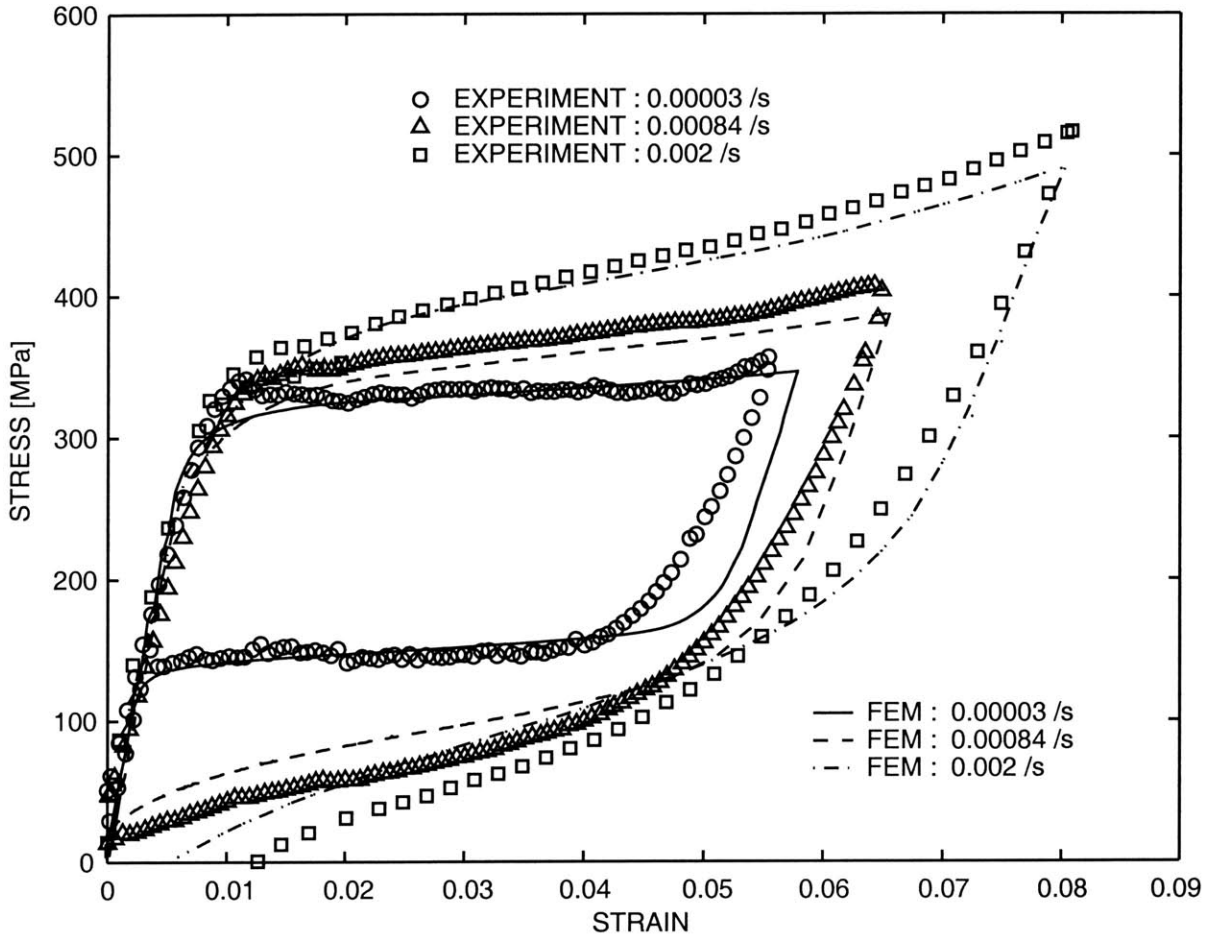

Figure 2-24: Superelastic stress-strain curves in tension along the rolling direction at nominal strain rates of 2×10^{-3} /sec, 8.4×10^{-4} /sec, and 3×10^{-5} /sec ("isothermal condition"). The predictions from the theory are also shown.

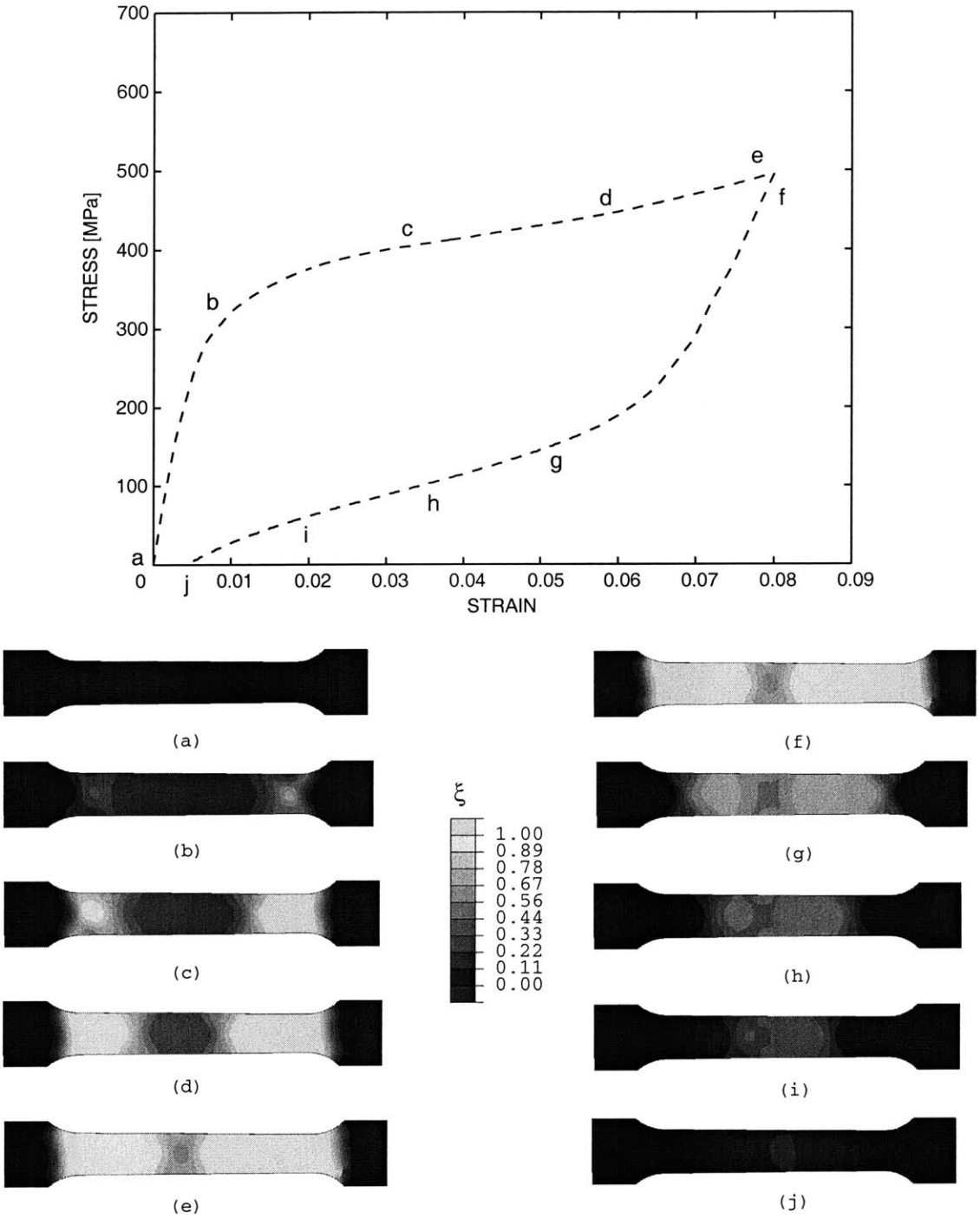

Figure 2-25: A superelastic finite-element simulation of an experiment conducted at a nominal strain rate of 2×10^{-3} /sec. The set of the martensite volume fraction contours on the left show the transformation from austenite-to-martensite during forward transformation, while those on the right show the transformation from martensite-to-austenite during reverse transformation. Note that because of the boundary conditions, both the forward and reverse transformations nucleate from the grip-ends and propagate towards the center of the specimen.

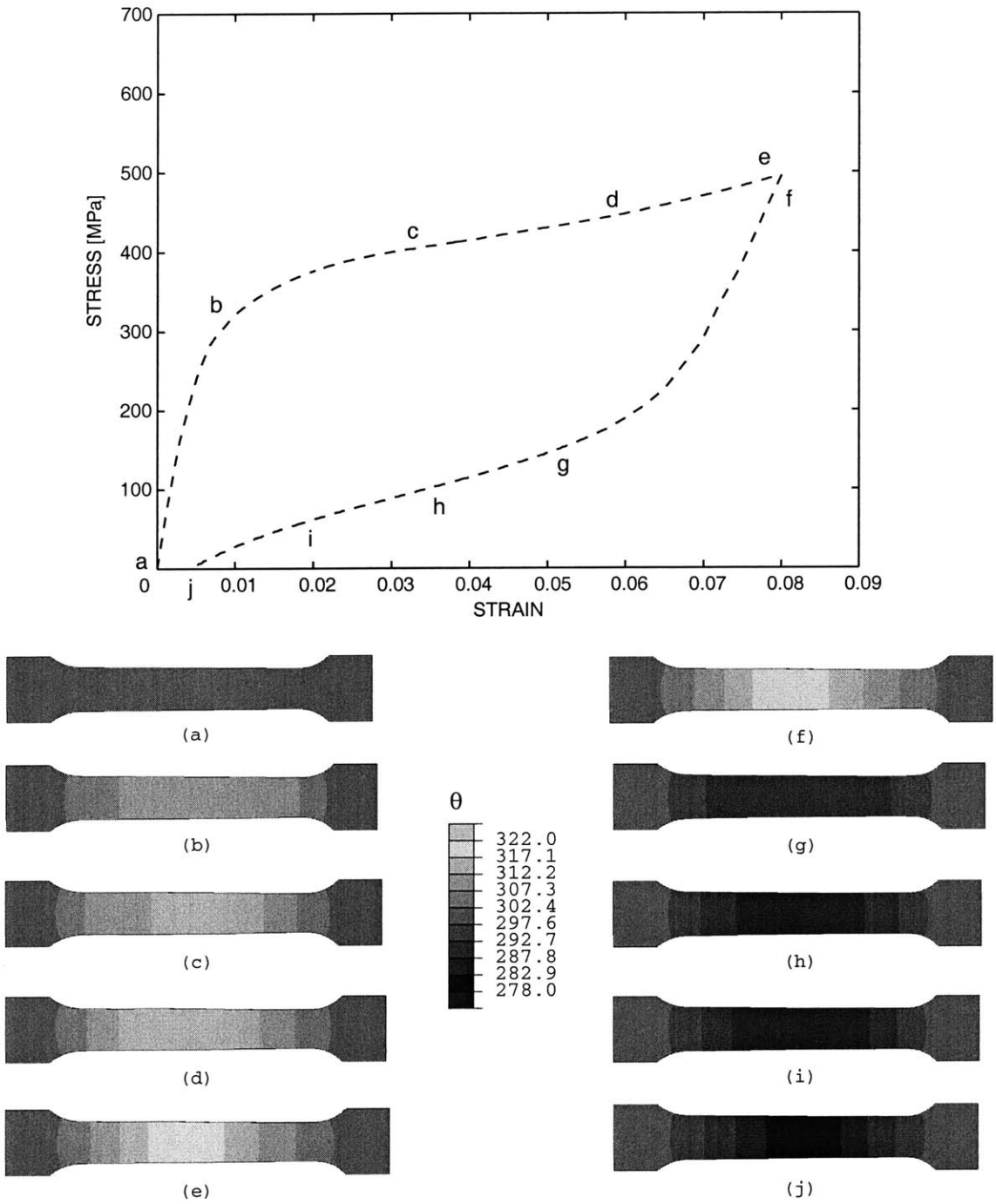

Figure 2-26: A superelastic finite-element simulation of an experiment conducted at a nominal strain rate of 2×10^{-3} /sec. The set of contours on the left shows the temperature *increase* during transformation from austenite-to-martensite, while those on the right show the temperature *decrease* during transformation from martensite-to-austenite. During forward transformation the temperature increases by as much as 22°K above the ambient temperature of 300°K due to the exothermic austenite-to-martensite transformation, whereas it *decreases* by as much as 22°K below the ambient temperature during the reverse endothermic transformation from martensite-to-austenite.

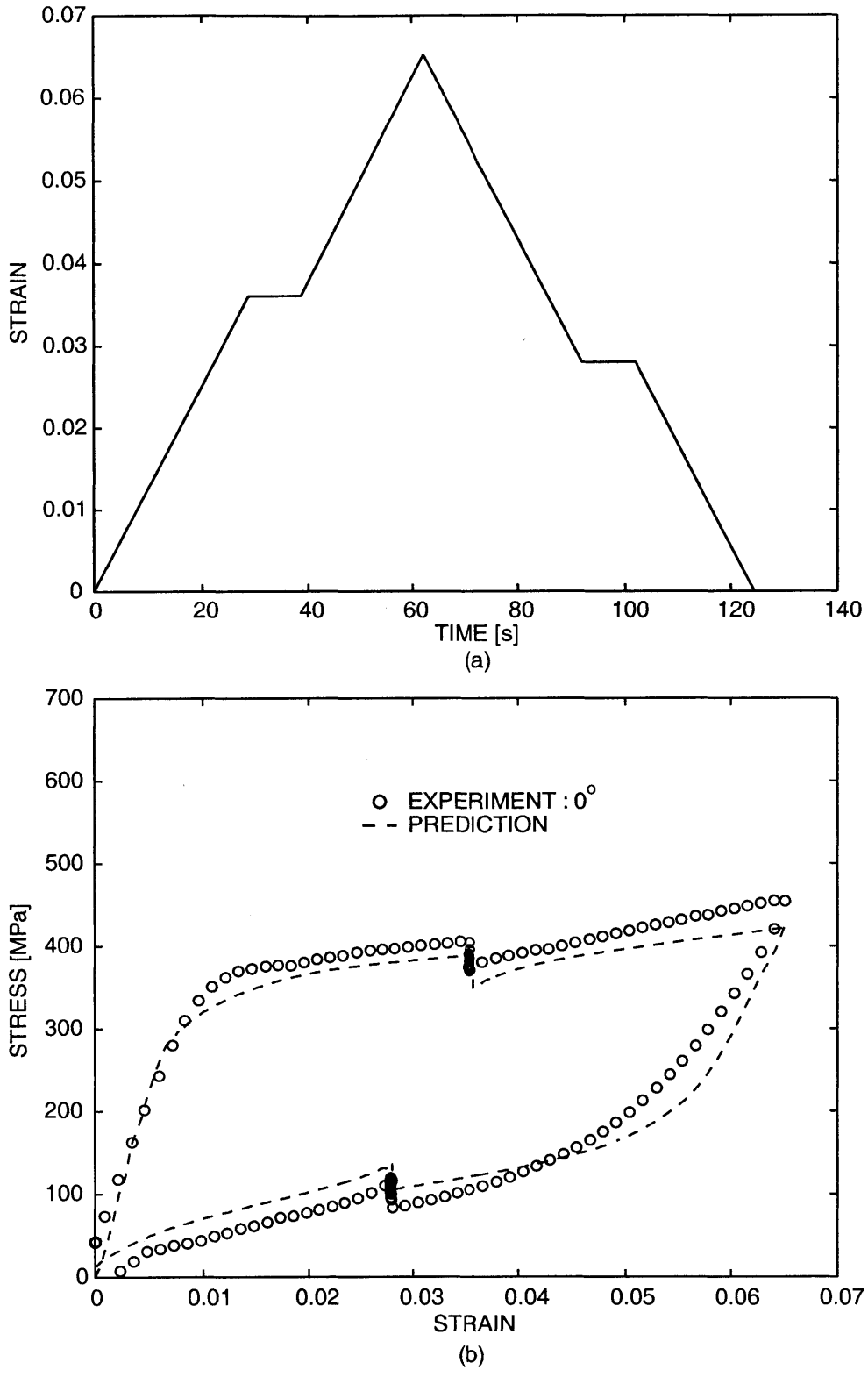

Figure 2-27: (a) Nominal strain versus time profile for the tension-hold experiment at a baseline nominal strain rate of 1.25×10^{-3} /sec and initial temperature of 300 K. (b) Superelastic stress-strain curve measured in the experiment. The prediction from the finite-element simulation is also shown.

Chapter 3

Isotropic-based constitutive model

3.1 Constitutive model

In this section we summarize our three-dimensional constitutive model for the isotropic superelastic response of shape-memory materials. *This model is meant to characterize small elastic strains in the presence of temperature fields close to a fixed reference temperature* θ_0. The constitutive framework is similar in spirit to the crystal-mechanics based theory of Anand and Gurtin (2002).

Using the standard notation of modern continuum mechanics,[1] we recall that the deformation gradient $\mathbf{F}$ maps *referential* segments $\mathbf{dX}$ to segments $\mathbf{dx} = \mathbf{F}\mathbf{dX}$ in the *deformed* configuration. We base the theory on the following multiplicative decomposition of the deformation gradient: $\mathbf{F} = \mathbf{F}^e\mathbf{F}^p$. Here (i) $\mathbf{F}^p(\mathbf{X})$ represents the local deformation of *referential* segments $\mathbf{dX}$ to segments $\mathbf{dl} = \mathbf{F}^p(\mathbf{X})\mathbf{dX}$ in the *relaxed lattice configuration* due to the generation, growth and annihilation of austenitic/martensitic fine structure in a microscopic neighborhood of $\mathbf{X}$. (ii) $\mathbf{F}^e(\mathbf{X})$ represents the mapping of segments $\mathbf{dl}$ in the relaxed lattice configuration into segments $\mathbf{dx} = \mathbf{F}^e(\mathbf{X})\mathbf{dl}$ in

[1] *Notation*: ∇ and Div denote the gradient and divergence with respect to the material point $\mathbf{X}$ in the *reference configuration*; grad and div denote these operators with respect to the point $\mathbf{x} = \mathbf{y}(\mathbf{X}, t)$ in the deformed configuration, where $\mathbf{y}(\mathbf{X}, t)$ is the motion; a superposed dot denotes the material time-derivative. Throughout, we write $\mathbf{F}^{e-1} = (\mathbf{F}^e)^{-1}$, $\mathbf{F}^{p-\top} = (\mathbf{F}^p)^{-\top}$, etc.. For any tensor $\mathbf{A}$, $\mathrm{sym}\mathbf{A} = (1/2)(\mathbf{A} + \mathbf{A}^\top)$, $\mathrm{skw}\mathbf{A} = (1/2)(\mathbf{A} - \mathbf{A}^\top)$, and $\mathbf{A}_0$, the *deviatoric* part of $\mathbf{A}$, is defined by $\mathbf{A}_0 = \mathbf{A} - (1/3)(\mathrm{tr}\,\mathbf{A})\mathbf{1}$; $\mathbf{A}$ is *deviatoric* if $\mathrm{tr}\,\mathbf{A} = 0$. Also, the inner product of tensors $\mathbf{A}$ and $\mathbf{B}$ is denoted by $\mathbf{A} \cdot \mathbf{B}$, and the magnitude of $\mathbf{A}$ by $|\mathbf{A}| = \sqrt{\mathbf{A} \cdot \mathbf{A}}$.

the *deformed* configuration due the "elastic mechanisms" of stretching and rotation of the lattice.

We denote by $\xi(\mathbf{X}, t)$, $0 \leq \xi \leq 1$, the local *volume fraction of martensite* at $\mathbf{X}$. The evolution of $\mathbf{F}^p$ is taken to be governed by the *transformation rate* $\dot{\xi}$ via the relation $\dot{\mathbf{F}}^p = \mathbf{D}^p \mathbf{F}^p$, $\mathbf{D}^p = \dot{\xi}\, \mathbf{N}^p$. where $\mathbf{N}^p$ is a symmetric *transformation tensor* with magnitude $|\mathbf{N}^p| = \sqrt{3/2}\, \epsilon_T$, where ϵ_T is the *transformation strain* in simple tension. *Transformation from austenite to martensite*, abbreviated $a \rightarrow m$, occurs when $\dot{\xi} > 0$; and *transformation from martensite to austenite*, abbreviated $m \rightarrow a$, occurs when $\dot{\xi} < 0$. Shape-memory materials show a slight inelastic volume change during transformation, and this is well-described by the crystal-mechanics theory. However, for the phenomenological isotropic theory under consideration, we shall *neglect any small inelastic volume changes* and assume that $\det \mathbf{F}^p = 1$; accordingly $\operatorname{tr} \mathbf{N}^p = 0$.

The underlying constitutive equations relate the following basic fields:

ψ,		free energy density per unit referential volume,
$\mathbf{F}$,	$\det \mathbf{F} > 0$,	deformation gradient,
θ,	$\theta > 0$,	absolute temperature,
$\mathbf{T}$,	$\mathbf{T} = \mathbf{T}^\top$,	Cauchy stress,
$\mathbf{q}$,		heat flux per unit referential area,
$\mathbf{F}^p$,	$\det \mathbf{F}^p = 1$	transformational part of the deformation gradient,
ξ,	$0 \leq \xi \leq 1$,	martensitic volume fraction,
$\mathbf{F}^e = \mathbf{F}\mathbf{F}^{p-1}$,	$\det \mathbf{F}^e > 0$,	elastic part of the deformation gradient,
$\mathbf{C}^e = \mathbf{F}^{e\top}\mathbf{F}^e$,		elastic right Cauchy-Green strain,
$\mathbf{E}^e = (1/2)\,(\mathbf{C}^e - \mathbf{1})$,		elastic strain,
$\mathbf{T}^e = \mathbf{R}^{e\top}\mathbf{T}\mathbf{R}^e$,		stress conjugate to $\mathbf{E}^e$.

The constitutive equations are:

1. **Free energy**: The *free energy* is taken in the separable form

$$\psi(\mathbf{E}^e, \theta, \xi) = \psi^e(\mathbf{E}^e, \theta, \xi) + \psi^\theta(\theta) + \psi^{tr}(\theta, \xi), \quad \text{with} \tag{3.1}$$

$$\psi^e(\mathbf{E}^e, \theta, \xi) = (1/2)\mathbf{E}^e \cdot \boldsymbol{\mathcal{C}}(\xi)[\mathbf{E}^e] - (\theta - \theta_0)\mathbf{A}(\xi) \cdot \boldsymbol{\mathcal{C}}(\xi)[\mathbf{E}^e], \tag{3.2}$$

$$\psi^\theta(\theta) = c(\theta - \theta_0) - c\theta \ln(\theta/\theta_0), \tag{3.3}$$

$$\psi^{tr}(\theta, \xi) = (\lambda_T/\theta_T)(\theta - \theta_T)\xi. \tag{3.4}$$

Here

$$\boldsymbol{\mathcal{C}}(\xi) = \frac{E(\xi)}{(1+\nu(\xi))}\left[\boldsymbol{\mathcal{I}} + \frac{\nu(\xi)}{(1-2\nu(\xi))}\mathbf{1}\otimes\mathbf{1}\right], \tag{3.5}$$

with E and ν the Young's modulus and Poisson's ratio is the elasticity tensor, and

$$\mathbf{A}(\xi) = \alpha(\xi)\,\mathbf{1}, \tag{3.6}$$

with α the thermal expansion coefficient is the thermal expansion tensor, at the reference temperature θ_0. The constant c is the specific heat per unit volume in the reference configuration. The parameter θ_T is the phase-equilibrium temperature, λ_T is the latent heat of the $a \leftrightarrow m$ transformation at temperature θ_T.

2. **Stress**: The *elastic stress-strain relation* has the form

$$\mathbf{T}^e = \frac{\partial \psi^e}{\partial \mathbf{E}^e} = \boldsymbol{\mathcal{C}}(\xi)[\mathbf{E}^e - \mathbf{A}(\xi)(\theta - \theta_0)]. \tag{3.7}$$

3. **Resolved force. Back force. Dissipative force**: The quantity

$$\bar{\sigma} = \mathbf{T}^e \cdot \mathbf{N}^p \tag{3.8}$$

is a *resolved force*, with $\mathbf{N}^p$ the transformation tensor (defined below). The derivative

$$b = \frac{\partial \psi^{tr}}{\partial \xi} = (\lambda_T/\theta_T)(\theta - \theta_T) \tag{3.9}$$

defines an energetic *backforce*. Let

$$f = (\bar{\sigma} - b), \tag{3.10}$$

then thermodynamic considerations show that

$$f\dot{\xi} \geq 0; \tag{3.11}$$

accordingly f is called the *dissipative force*[2] associated with the phase transformation.

4. **Transformation conditions**: The *transformation conditions* are

$$f = f_c \quad \text{for } \dot{\xi} > 0, \tag{3.12}$$

$$f = -f_c \quad \text{for } \dot{\xi} < 0, \tag{3.13}$$

with $f_c > 0$ a constant *transformation resistance.*

5. **Flow rule**: The *flow rule* is defined by an evolution equation for $\mathbf{F}^p$ of the form

$$\left.\begin{aligned} \dot{\mathbf{F}}^p &= \mathbf{D}^p\mathbf{F}^p, \\ \mathbf{D}^p &= \dot{\xi}\,\mathbf{N}^p, \end{aligned}\right\} \tag{3.14}$$

with martensitic volume fractions ξ consistent with $0 \leq \xi \leq 1$, and where the transformation tensor $\mathbf{N}^p$ is given by

$$\mathbf{N}^p = \begin{cases} \sqrt{(3/2)}\,\epsilon_T \dfrac{\mathbf{T}_0^e}{|\mathbf{T}_0^e|} & \text{if } \xi = 0, \\ \\ \sqrt{(3/2)}\,\epsilon_T \dfrac{\mathbf{T}_0^e(t_c)}{|\mathbf{T}_0^e(t_c)|} & \text{if } 0 < \xi \leq 1. \end{cases} \tag{3.15}$$

Here ϵ_T is a constant *transformation strain* in simple tension. Also, beginning in an austenitic state ($\xi = 0$), the time t_c denotes the instant when the martensite volume fraction ξ becomes positive.[3] Moreover,

---

[2]Also called the driving force for phase transformation.

[3]In Appendix G we show that if following classical isotropic plasticity we take

$$\mathbf{N}^p = \sqrt{(3/2)}\,\epsilon_T \frac{\mathbf{T}_0^e}{|\mathbf{T}_0^e|} \quad \text{for all} \quad 0 \leq \xi \leq 1,$$

then we get *spurious results* in superelastic deformations in simple shear. Whereas, by fixing the transformation direction during a superelastic forward and reverse event to be determined by the stress at the first instance of transformation, yields acceptable results, at least for the *proportional loading* conditions tested in this section.

(i) if $-f_c < f < f_c$, then $\dot{\xi} = 0$;

(ii) if $f = f_c$ and $0 \leq \xi < 1$, then

$$\dot{\xi} \geqslant 0 \quad \text{and} \quad (\dot{\overline{f - f_c}}) \leqslant 0; \tag{3.16}$$

(iii) if $f = -f_c$ and $0 < \xi < 1$, then

$$\dot{\xi} \leqslant 0 \quad \text{and} \quad (\dot{\overline{f + f_c}}) \geqslant 0; \tag{3.17}$$

(iv) if $f = f_c$ and $\xi = 1$, or if $f = -f_c$ and $\xi = 0$, then $\dot{\xi} = 0$.

The *consistency conditions* (3.16) and (3.17) serve to determine the transformation rates $\dot{\xi}$.

6. **Entropy; energy balance; heat flux**:

The *entropy* η is given by

$$\eta = -\frac{\partial \psi}{\partial \theta} = c \ln(\theta/\theta_0) + \mathbf{E}^e \cdot \boldsymbol{\mathcal{C}}(\xi)[\mathbf{A}(\xi)] - (\lambda_T/\theta_T)\xi, \tag{3.18}$$

the balance of energy may be written as

$$\theta \dot{\eta} = -\mathrm{Div}\mathbf{q} + f\dot{\xi} + r, \tag{3.19}$$

where r is the heat supply per unit volume of the reference configuration, and the *referential* heat flux $\mathbf{q}$ is taken to be governed by *Fourier's law*

$$\mathbf{q} = -\mathbf{K}(\xi)\nabla\theta, \tag{3.20}$$

where $\mathbf{K}(\xi)$ is the thermal conductivity tensor at θ_0. Using (3.18) and (3.20), the energy balance (3.19) becomes

$$c\,\dot{\theta} = \mathrm{Div}\left\{\mathbf{K}(\xi)\nabla\theta\right\} + \left((\lambda_T/\theta_T)\,\theta + f\right)\dot{\xi} - \theta\,\dot{\overline{\mathbf{E}^e \cdot \boldsymbol{\mathcal{C}}(\xi)[\mathbf{A}(\xi)]}} + r. \tag{3.21}$$

To complete the theory for a particular material the constitutive parameter/functions that need be specified are

$$\{E(\xi), \nu(\xi), \alpha(\xi), \epsilon_T, \theta_T, \lambda_T, f_c, c, \kappa(\xi)\}\,.$$

Finally, the standard partial differential equation for the stress referred to the deformed configuration is

$$\operatorname{div}\mathbf{T} + J^{-1}\mathbf{f} = \mathbf{0}, \tag{3.22}$$

where div represents the divergence operator in the deformed configuration, $J = \det\mathbf{F}$ and $\mathbf{f}$ is the body force per unit volume in the reference configuration (the body force $\mathbf{f}$ is assumed to include inertial forces). The differential equation for the temperature referred to the deformed configuration is

$$J^{-1}\, c\,\dot{\theta} = \operatorname{div}\left\{J^{-1}\mathbf{F}\mathbf{K}(\xi)\mathbf{F}^{\mathsf{T}}\operatorname{grad}\theta\right\} + J^{-1}\,\left((\lambda_T/\theta_T)\,\theta + f\right)\dot{\xi} - J^{-1}\,\theta\,\dot{\overline{\mathbf{E}^e\cdot\boldsymbol{\mathcal{C}}(\xi)[\mathbf{A}(\xi)]}} + J^{-1}\,r. \tag{3.23}$$

We have implemented our constitutive model in the finite-element computer programs ABAQUS/Explicit and ABAQUS/Standard (2001)[4] by writing user material subroutines. Algorithmic details of the numerical implementation are given in Appendix E. [5]

[4]All the calculations performed in this work were done using ABAQUS/Explicit (2001) unless stated otherwise. The results using both schemes match identically e.g. the finite-element simulations using ABAQUS/Explicit and ABAQUS/Standard for the coupled-temperature displacement analysis for the polycrystalline sheet material in Section 3.2.1 is shown in Figure 3-1.

[5]All calculations reported in this section were performed using ABAQUS/Explicit, while those reported in Section 3.3 were performed using ABAQUS/Standard.

3.2 Evaluation of the constitutive model for polycrystalline Ti-Ni alloy

3.2.1 Sheet material

Suitably processed 0.53 mm thick Ti-Ni sheets, intended for superelastic behavior at room temperature, were obtained from a commercial source. Recall that the material parameters that need to be specified for the theory are

1. The thermo-elastic parameters $\{E(\xi), \nu(\xi), \alpha(\xi)\}$.
2. The phase transformation parameters $\{\epsilon_T, \theta_T, \lambda_T, f_c\}$.
3. The specific heat c and the thermal conductivity $\kappa(\xi)$.

The values of $\{E, \nu, \alpha\}$ for the austenitic and martensitic phases of Ti-Ni are well-documented in the literature. We have used the following values in our calculations:

Young's modulus and Poisson's ratio for austenite: $E^a = 62\,\text{GPa}$, $\nu^a = 0.33$,
Young's modulus and Poisson's ratio for martensite: $E^m = 31\,\text{GPa}$, $\nu^m = 0.33$,
Coefficients of thermal expansion: $\alpha^a = 11 \times 10^{-6}/\text{K}$, $\alpha^m = 6.6 \times 10^{-6}/\text{K}$,

and assumed a simple rule-of-mixtures dependence for the dependence of $E(\xi)$ and $\alpha(\xi)$ on the volume fraction of martensite ξ.

An estimate for the phase transformation parameters $\{\epsilon_T, \theta_T, \lambda_T, f_c\}$ for Ti-Ni is obtained by fitting the constitutive model to a set of superelastic tension experiments at (at least) three different temperatures spanning the range of temperatures of interest. With reference to Figure 3-2, an operational procedure to estimate the material parameters is as follows:

First, estimate the transformation strain ϵ_T from the superelastic tension experiments at each temperature. The measured transformation strains ϵ_T will typically be a a function of temperature. However, for applications, a constant value of ϵ_T

which represents an average over the range of temperatures is usually an adequate approximation.

Next, estimate the stress σ_{am} for forward transformation, and the stress σ_{ma} for reverse transformation at each temperature. A schematic plot of the variation of σ_{am} and σ_{ma} with temperature θ is shown in Figure 3-2b. From this, the intercept of the line σ_{am} versus θ at zero stress defines the martensite start temperature θ_{ms}, while the intercept of the line σ_{ma} versus θ at zero stress defines the austenite start temperature θ_{as}; the mean value

$$\theta_T = \frac{1}{2}(\theta_{as} + \theta_{ms}) \tag{3.24}$$

determines the phase equilibrium temperature. From (3.9), (3.10), (3.12) and (3.13) we note that during forward transformation

$$\sigma_{am}(\theta) - \left(\frac{\lambda_T}{\epsilon_T \theta_T}\right)(\theta - \theta_T) = \frac{f_c}{\epsilon_T} \tag{3.25}$$

holds, while during reverse transformation

$$\sigma_{ma}(\theta) - \left(\frac{\lambda_T}{\epsilon_T \theta_T}\right)(\theta - \theta_T) = -\frac{f_c}{\epsilon_T} \tag{3.26}$$

holds. Thus, the transformation resistance f_c at each temperature is given by

$$f_c = \epsilon_T \times \frac{1}{2}(\sigma_{am}(\theta) - \sigma_{ma}(\theta)). \tag{3.27}$$

Further, the mean values of σ_{am} and σ_{ma} at each temperature vary linearly with temperature, *i.e.*

$$\frac{1}{2}(\sigma_{am}(\theta) + \sigma_{ma}(\theta)) = \left(\frac{\lambda_T}{\epsilon_T \theta_T}\right)(\theta - \theta_T). \tag{3.28}$$

Thus, the slope of the line $\frac{1}{2}(\sigma_{am}(\theta) + \sigma_{ma}(\theta))$ versus θ gives $\left(\frac{\lambda_T}{\epsilon_T \theta_T}\right)$, which in turn gives the latent heat of phase transformation, λ_T.

To evaluate these phase transformation parameters for the Ti-Ni sheet, superelastic tension experiments were conducted on polycrystalline sheet specimens with the tension axis aligned along the sheet rolling direction, 0°-orientation. The geometry of the tension specimens is shown in Figure 2-18a. The experiments were conducted at three different temperatures, 289 K, 300 K and 306 K, under displacement control at a

very low nominal strain rate of 3×10^{-5} /sec, to ensure (near) isothermal conditions. The nominal stress-strain curves from these experiments are shown in Figures 3-3a,b, and c, respectively[6]. Following the procedure outlined above, the value of the estimated phase transformation parameters is

Phase equilibrium temperature: $\theta_T = 271\,\mathrm{K}$;
Latent heat: $\lambda_T = 110\,\mathrm{MJ/m^3}$;
Critical transformation resistance: $f_c = 4.15\,\mathrm{MJ/m^3}$;
Transformation strain: $\epsilon_T = 0.047$.

Corresponding numerical simulations of these superelastic experiments, using the material parameters listed above, were carried out on the finite-element mesh (446 ABAQUS-C3D8R elements) shown in Figure 2-18b. The numerically-calculated nominal stress-strain curves are also shown in Figure 3-3. Although, as anticipated, a constant value of ϵ_T over the three temperatures results in some discrepancy, the overall quality of the fit using a simple isotropic model is very encouraging.[7]

As mentioned previously, phase transformation during superelasticity typically occurs by the nucleation and propagation of phase transformation fronts. Figure 3-4 shows such a phenomenon in our numerical simulations.[8] This figure shows the numerical stress-strain curve from the simulation for 300 K, along with the contours of the martensite volume fraction keyed to instances (a) through (j) at different points along the superelastic stress-strain curve. The contours for (a) through (e) show that martensite nucleates at the right end of the specimen where the gage width is the narrowest, and the transformation front propagates to the left until the gage section is fully transformed to martensite by stage (e). The martensite volume fraction contours for (f) through (j) show that upon reversal of imposed deformation the phase front recedes until the gage section is once again fully austenitic by stage (j).

[6]We use nominal values of stress and strain since the phase transformation occurs in an inhomogeneous fashion along the gage section of the specimen. The permanent set observed in the experiment at 306 K is probably due to some plastic deformation at the higher stresses in this experiment.

[7]The crystal mechanics model used in Chapter 2 gives a much better agreement with experiments, but at a higher computational expense.

[8]A geometric "imperfection" in the form of a slight taper along the gage section is given to provide an initiation site for phase transformation.

An important manifestation of the superelastic response of a shape-memory material is the strain-versus-temperature response at a fixed stress level. By cycling the temperature over a narrow range at a fixed stress, one can obtain a recoverable strain cycle. Figures 3-5a and b show experimental strain-temperature curves from 0°-oriented specimens which were first subjected to fixed axial stress levels of 150 MPa and 250 MPa, and then subjected to a temperature history where the temperature is decreased at a constant rate of 0.016 K/s, and then increased back at the same rate. With respect to Figure 3-5a, the initial elastic strain of ≈ 0.005 is due to the axial stress of 150 MPa. The material is initially in the austenitic state. As the temperature is decreased from 315 K, the strain first decreases slightly due to thermal contraction, and then at $\approx$ 279K the austenite-to martensite-transformation occurs and there is a sudden burst of strain of 4.7%. Upon heating, there is at first a slight increase in the strain due to thermal expansion, and then at $\approx$ 300K the martensite transforms back to austenite with a strain recovery of 4.7%. The temperatures at which the transformations occur can be controlled by the initial stress bias. As shown in Figure 3-5b, an increase in the initial stress increases the austenite-to-martensite as well as the martensite-to-austenite transformation temperatures.

We next consider the *coupled thermo-mechanical* superelastic response of the Ti-Ni sheet. In order to examine the effects of heat generation and conduction, we have performed superelastic tension experiments at three different nominal strain rates on 0°-oriented specimens at an initial temperature of 300 K. In addition to the test at the "low" nominal strain rate of 3×10^{-5}/sec reported previously, Figure 3-3b, where the response was expected to be (close to) isothermal, we have conducted two additional experiments at slightly "higher" rates of 8.4×10^{-4}/sec and 2×10^{-3}/sec, where we expect to see some effects of the changes in temperature. The superelastic stress-strain curves for all three strain rates are shown in Figure 3-6. Note that as the strain rate increases, the stress-strain curves at the two higher strain rates show a "hardening response". This apparent hardening due to thermal effects is qualitatively similar to that reported previously by Entemeyer *et al.* (2000), who have argued that the major contribution to the apparent hardening is due to temperature changes

associated with the exothermic $a \rightarrow m$, and endothermic $m \rightarrow a$ transformations.

Recall that the energy balance (3.23) requires computation of the term

$$\operatorname{div}\left\{J^{-1}\mathbf{F}\mathbf{K}(\xi)\mathbf{F}^{\mathsf{T}}\operatorname{grad}\theta\right\}.$$

The finite-element program ABAQUS/Explicit and ABAQUS/Standard (currently) limits user access to modify the computer code, and allows input of only a single scalar value for the thermal conductivity. We have accordingly made several approximations in our calculations. We shall use a constant value of thermal conductivity $k = (k^a + k^m)/2$ in our numerical calculations, where k^a and k^m is the polycrystalline thermal conductivity coefficient for the austenite and martensite phase, respectively. Further, since the superelastic strains are small, we neglect the contributions from the J and $\mathbf{F}\mathbf{F}^{\mathsf{T}}$ terms, and make the approximation $\operatorname{div}\left\{J^{-1}\mathbf{F}\mathbf{K}(\xi)\mathbf{F}^{\mathsf{T}}\operatorname{grad}\theta\right\} \approx k \operatorname{div}\operatorname{grad}\theta$. We also neglect the terms $J^{-1}\theta\,\overline{\dot{\mathbf{E}}^e \cdot \boldsymbol{\mathcal{C}}(\xi)[\mathbf{A}(\xi)]} + J^{-1}r$ in (3.23). Under these approximative assumptions the equation governing the change in temperature becomes

$$c\,\dot{\theta} \approx k \operatorname{div}\operatorname{grad}\theta + \left(\frac{\lambda_T}{\theta_T}\,\theta + f\right)\dot{\xi}. \tag{3.29}$$

Based on values published in the literature, we use the following values of

$$c = 2.1\,\mathrm{MJ/m^3\,K}, \qquad k = 13\mathrm{W/m\,K}$$

for Ti-Ni in our calculations. The calculations were carried out for a Ti-Ni sheet specimen modelled using the mesh shown in Figure 2-18b, this time using 446 C3D8RT ABAQUS elements. Regarding the thermal boundary conditions, the whole mesh is initially at 300K. The nodes at the grip-ends are kept at 300K throughout the calculation to simulate massive hard grips which act as constant temperature baths. The heat flux from the remaining faces of the tension strip due to convection in air is taken to be governed by boundary conditions on the heat flux $\mathbf{h}$ in the deformed configuration, of the form $\mathbf{h} = h(\theta - \theta_0)\mathbf{n}$, with a film coefficient h and a sink temperature θ_0. In our calculations we take the film coefficient to have a value $h = 12\,\mathrm{W/m^2\,K}$, and a sink temperature of 300K. Figure 3-6 also shows the resulting superelastic stress-strain curves for the two higher strain rates. The stress-strain curves calculated for

the higher strain rates show the experimentally-measured hardening response. Recall that we have set f_c to be constant. Thus, the hardening response is *entirely due to thermal effects associated with the phase transformations.* Figure 3-7 shows evolution of the contours of the martensite volume fraction at representative instances during the forward and reverse transformations for the test at the highest strain rate. Note that because of the boundary conditions, both the forward and reverse transformations start from the grip-ends and propagate as "fronts" towards the center of the specimen. Figure 3-8 shows contours of the temperature at representative instances during the forward and reverse transformations. During forward transformation the temperature increases by as much as 25K from the ambient temperature of 300K due to the exothermic austenite-to-martensite transformation, while it decreases by as much as 25K from the ambient temperature during the reverse endothermic transformation from martensite-to-austenite. The nucleation and propagation of phase transformation fronts and the associated temperature changes in our calculations, are qualitatively similar to the results reported by Shaw and Kyriakides (1997) for their polycrystalline sheet tensile specimens.

The effects of heat conduction into and out of the gage section were further studied by performing a superelastic tension-hold experiment. A representative strain-time profile for such an experiment is as follows: the specimen is extended at a strain rate of 1.25×10^{-3}/sec with an intermediate hold of 10 sec, and then after the desired total strain level the straining direction is reversed at a rate of -1.25×10^{-3} /sec, again with an intermediate hold of 10 sec, Figure 3-9a. The experimental nominal stress-strain curve and the corresponding finite-element prediction of this experiment are shown in Figure 3-9b. The finite-element simulation nicely reproduces the stress-dip observed in the experiment during the forward transformation, and the stress-increase during the reverse transformation. The major cause for the stress-dip and stress-increase is the heat conduction out of and into the specimen, respectively, during the forward and reverse transformations.

3.2.2 Rod material

Suitably thermo-mechanically processed and heat-treated Ti-Ni at 55.96 wt.% Ti drawn rods of 12.70 mm diameter, intended for superelastic applications, were obtained from a commercial source.

The thermo-elastic constants for the rod-material is chosen to be the same as in Section 2.3.1. Using the measured phase transformation temperatures (Figure 2-2), the value for the phase equilibrium temperature, θ_T, is given by

$$\theta_T \equiv (1/2)\{\theta_{ms} + \theta_{as}\} = 256\,\mathrm{K}.$$

To obtain the remaining values of the phase transformation constants $\{\lambda_T, \epsilon_T, f_c\}$, the constitutive model is fitted to a superelastic experiment in simple tension at $\theta = 298\,\mathrm{K}$, Figure 3-10a. The experiment is conducted at a very low strain rate to ensure near-isothermal testing conditions.

The finite-element simulation in simple tension is performed using a single ABAQUS-C3D8R element. Using the procedure for material parameter determination outlined above the fitted phase transformation parameters are
Latent heat: $\lambda_T = 100\,\mathrm{MJ/m^3}$;
Critical transformation resistance: $f_c = 7.6\,\mathrm{MJ/m^3}$;
Transformation strain: $\epsilon_T = 0.05$.

The resulting superelastic stress-strain curve using the material parameters listed above are also shown in Figure 3-10a. The quality of the fit is very encouraging.

With the material parameters calibrated we proceed to perform a tubular-torsion experiment on a thin-walled specimen performed at a very low shearing strain rate. The stress-strain response in torsion at $\theta = 298\,\mathrm{K}$ is shown in Figure 3-10b. The finite-element simulation in simple shear is conducted using a single ABAQUS-C3D8R element. The predicted nominal shear stress-strain curve is shown in Figure 3-10b, where it is compared against the corresponding experimentally-measured curve from a tubular torsion experiment. The prediction is in good accord with the experiment.

Proportional-loading tension-torsion experiment:

The strain-history imposed on a thin-walled tubular specimen during the proportional-loading tension-torsion experiment is shown in Figure 3-11a. The axial strain ϵ is increased at a constant rate from 0% to 3% in 500 seconds, while the shear strain γ is increased at a constant rate from 0% to 4.5% in the same time period. These strains are then linearly reduced to zero, in another 500 seconds.

The initial finite-element mesh using 768 ABAQUS-C3D8R elements for the combined tension-torsion simulation is shown in Figure 3-11b, and the finite-element mesh after 3% strain in tension and 4.5% strain in shear is shown in Figure 3-11c, along with the contours of the martensite volume fraction.

Predictions of the axial-stress versus axial-strain, and shear-stress versus shear-strain from the constitutive model are compared against corresponding experimental measurements conducted at $\theta = 298\,\mathrm{K}$ in Figures 3-11d and 3-11e, respectively. The measured superelastic stress-strain response in this tension-torsion experiment is moderately well-approximated by the predictions from the constitutive model.

3.3 Deformation of a Ti-Ni biomedical stent

The superelastic response of Ti-Ni, along with its bio-compatibility and corrosion resistance, makes it an attractive material for many medical applications including stents which are used to counteract the effects associated with vascular diseases, such as narrowing of blood vessels due to plaque-build-up. A "self-expanding" superelastic stent is a cylindrical metal mesh (typically made by laser-cutting of a tube to the desired pattern, and subsequently electro-polishing to remove any burrs) which is compressed to a smaller diameter than its as-manufactured strain-free diameter, inserted into the problem area in an artery, and allowed to self-expand to its original diameter while exerting a gentle radial force on the wall of the artery to keep it open. An electron-micrograph of a Sci-Med^{tm} stent (Serruys, 1997) with struts which have a square cross-section of 0.15 mm by 0.15 mm is shown in Figure 3-12; this stent has an expanded diameter of 3.8 mm.

A simple way to experimentally study the mechanics of a stent is to analyze the response of its struts. Diamond-shaped strut test specimens, Figure 3-13a, were electro-discharge-machined from our sheet Ti-Ni material. The specimens were deformed in in-plane tension and compression using a special micro-tensile testing device developed by Gudlavaletti et al. (2002). The forces were measured using a built-in load cell, while the relative displacements of the end-sections were measured using a non-contact optical extensometer devised by Su and Anand (2002). To ensure near-isothermal testing conditions, the tests were conducted at a very low loading rate. The experimentally-measured force-displacement curves in tension and compression conducted at room temperature ($\theta = 298K$) are shown in Figure 3-14. Note, that the experiment shows that for the same magnitude of extension in tension and compression, the maximum tensile load is $\approx 15\,\mathrm{N}$, while it is $\approx -13\,\mathrm{N}$ in compression. The initial finite-element mesh used to model the specimen is shown in Figure 3-13b; because of the symmetry of the specimen and the loading conditions, only one quarter of the specimen is modelled. The prediction of the superelastic response based on the material parameters determined in the previous section for the sheet Ti-Ni is also

shown in Figure 3-14. The prediction is in good accord with the experiment. Of particular note is that the experimentally observed tension-compression asymmetry of the load-displacement response is picked up by the numerical simulation. Figure 3-15 compares numerically-predicted deformed geometries of the specimen in tension and compression against photographs of the corresponding experimental configurations. The numerical result also shows the contours of the martensite volume fraction. As expected, the martensite volume fraction is maximum at the corners where bending effects are dominant.

Next, to demonstrate the capability of our model to perform complex three-dimensional superelasticity simulations in a reasonable time, we report on a numerical simulation of the deformation response of a Ti-Ni stent using the implementation of our model in ABAQUS/Standard.[9] A 4 mm long link of the Sci-Med^{tm} stent is meshed using 5,562 ABAQUS-C3D8 elements. The initial finite-element mesh is shown in Figure 3-16a. Representative nodes at the tips of the five V-shaped segments at one end of the link of the stent are fixed so as not to move in the axial direction, while a forward-and-reverse axial displacement is prescribed at corresponding nodes at the other ends of the V-shaped segments. The material parameters in the analysis are taken to be the same as the ones used in the previous section. Figure 3-16b shows the fully extended state of the stent together with the contours of martensite volume fraction. As expected, the largest volume fraction of martensite occurs at the cross-sections where the bending strains are the highest. The final diameter of the stent in the extended state is about four times smaller than the diameter in the initial state. Note that because of the geometric design of the stent there is only a relatively small axial extension $\approx 0.16\,\text{mm}$, even for such a large reduction in diameter. The numerically calculated load-displacement curve is shown in Figure 3-16c; due to its geometric design the stent stiffens considerably as it is being extended. Of course,

[9]Recently, Rebelo and co-workers (e.g., Rebelo and Perry, 2000) have implemented a version of the superelasticity model of Auricchio and Taylor (1996, 1997) in ABAQUS and used it to simulate the deformation response of Ti-Ni stents. Details of the precise constitutive model used and its implementation are not publically known. Simulations of some other medical applications of Ti-Ni using this computer program have also been recently reported by Gong and Pelton (2002).

since the stent material is superelastic, the load returns back to its original position of zero load at zero extension. This reasonably complex three-dimensional calculation took approximately two hours to complete on a present-day workstation-class machine.

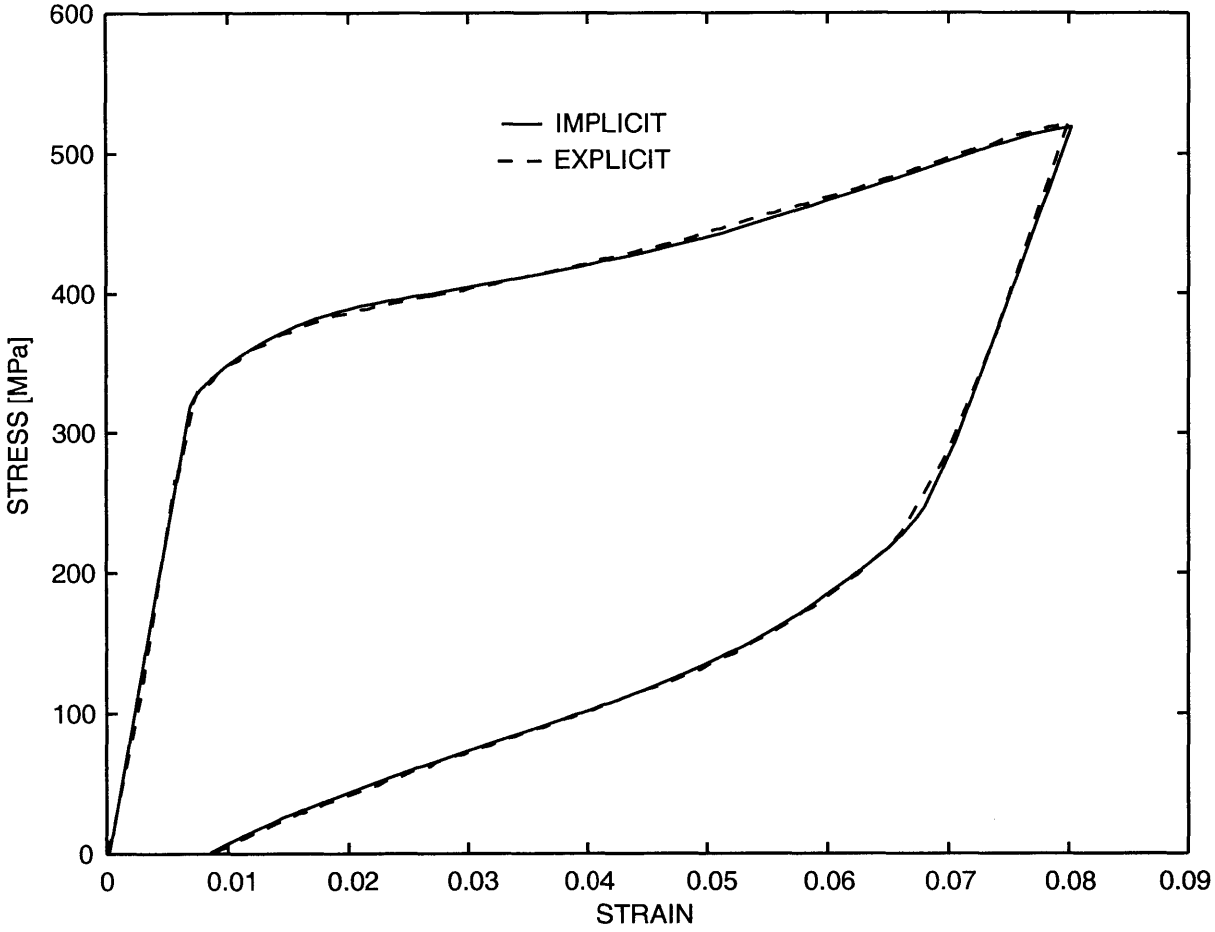

Figure 3-1: Comparison of the implicit and explicit finite-element solution of the tension specimen shown in Figure 2-18b at a tensile strain-rate of 0.002/s at an initial temperature of $\theta = 300\,\mathrm{K}$ using the material parameters in Section 3.2.1.

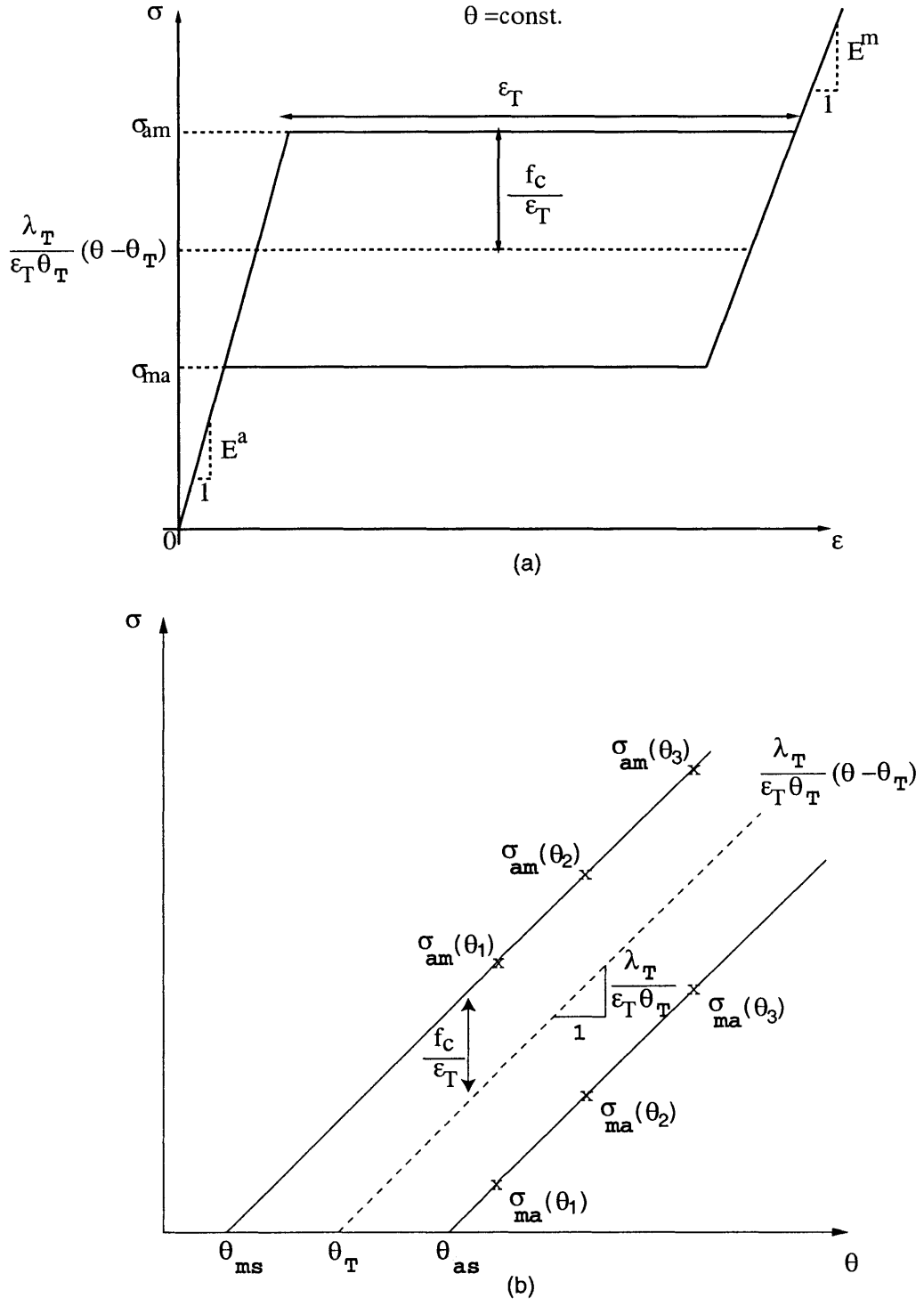

Figure 3-2: (a) Schematic of an isothermal superelastic stress-strain response in simple tension. (b) Schematic diagram of the variation of the nucleation stresses σ_{am} and σ_{ma} with temperature.

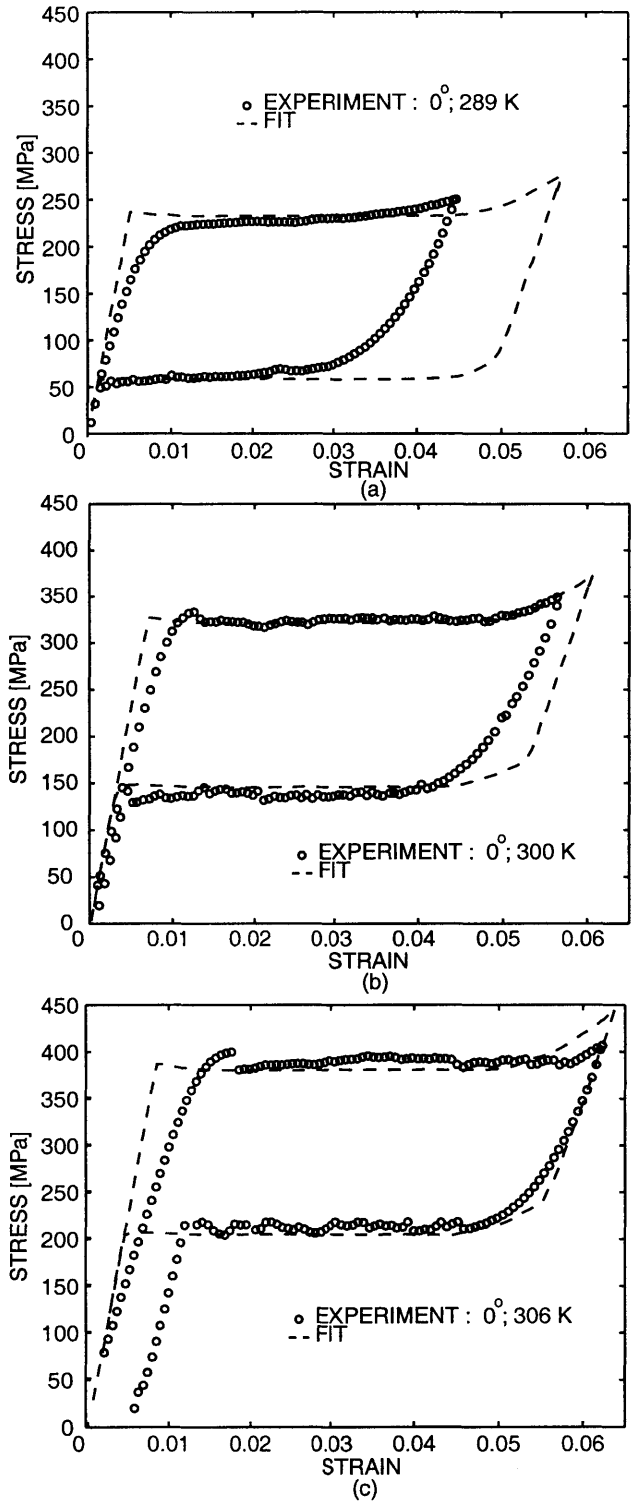

Figure 3-3: Nominal superelastic stress-strain curves from tension tests on 0°-oriented specimens. The tests were conducted under isothermal conditions at (a) 289 K, (b) 300 K, and (c) 306 K. The experimental data from these tests were used to estimate the phase transformation parameters. The curve fit from the finite-element simulations is also shown.

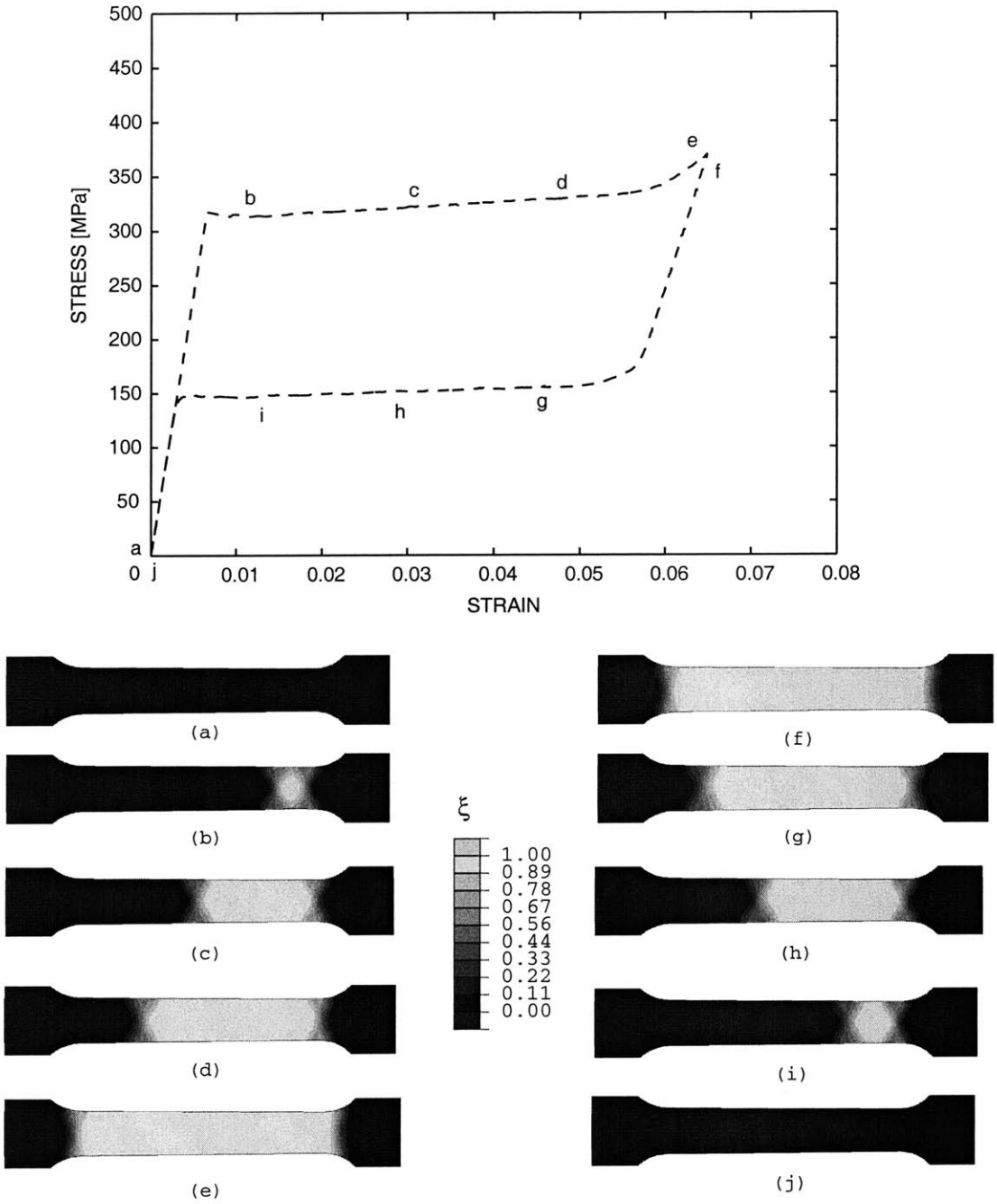

Figure 3-4: A superelastic finite-element simulation of an experiment conducted under isothermal conditions at 300 K. Contour plots of the martensite volume fraction are also shown. The set of contours on the left shows the transformation from austenite-to-martensite during forward transformation, while those on the right show the transformation from martensite-to-austenite during reverse transformation. Note that because of the slight taper in the gage width, the austenite-to-martensite transformation nucleates at the right grip-end and propagates toward the opposing grip-end.

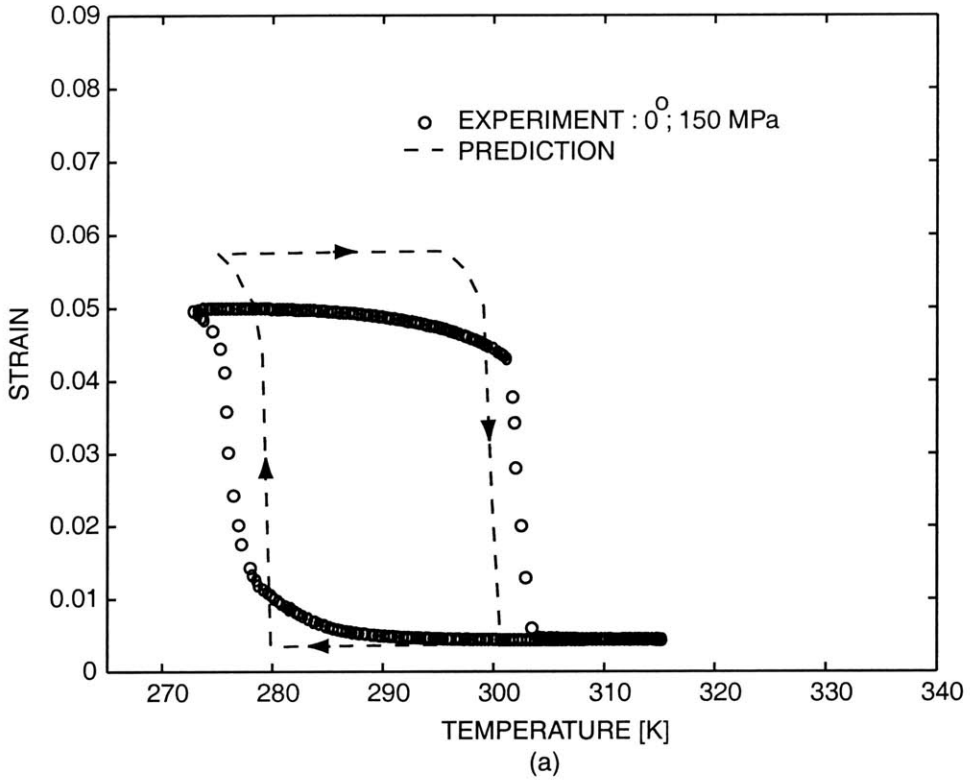

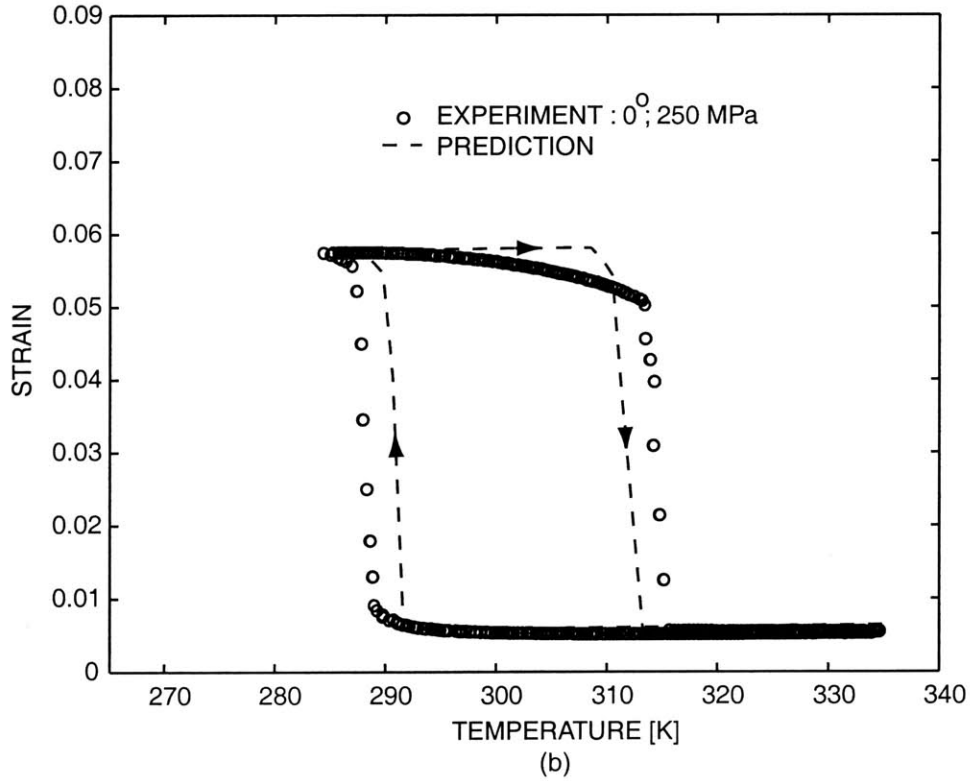

Figure 3-5: Strain-temperature cycling experiments conducted on 0°-oriented specimens at pre-stress levels of (a) 150 MPa; and (b) 250 MPa. The predictions from the finite-element simulations are also shown.

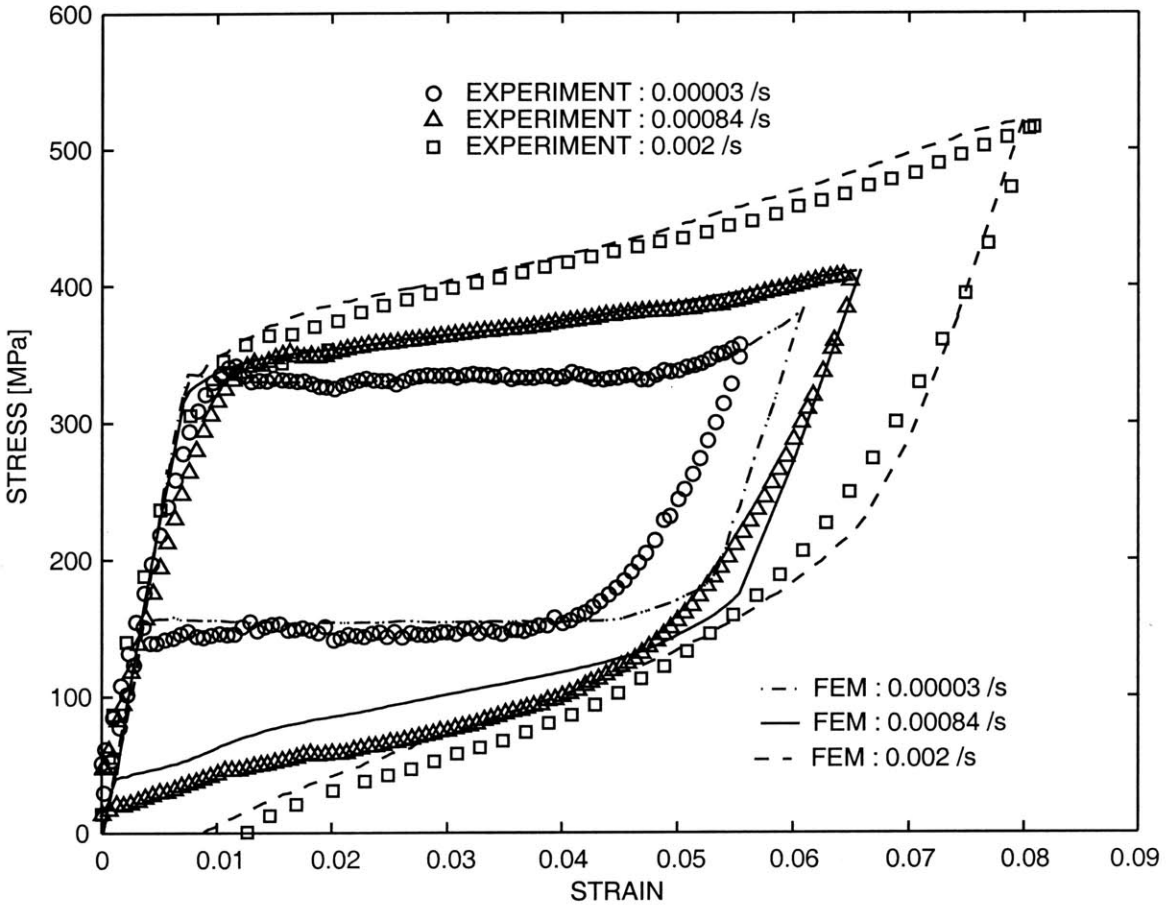

Figure 3-6: Superelastic stress-strain curves in tension along the rolling direction at nominal strain rates of 2×10^{-3} /sec, 8.4×10^{-4} /sec, and 3×10^{-5} /sec ("isothermal condition"). The predictions from the theory are also shown.

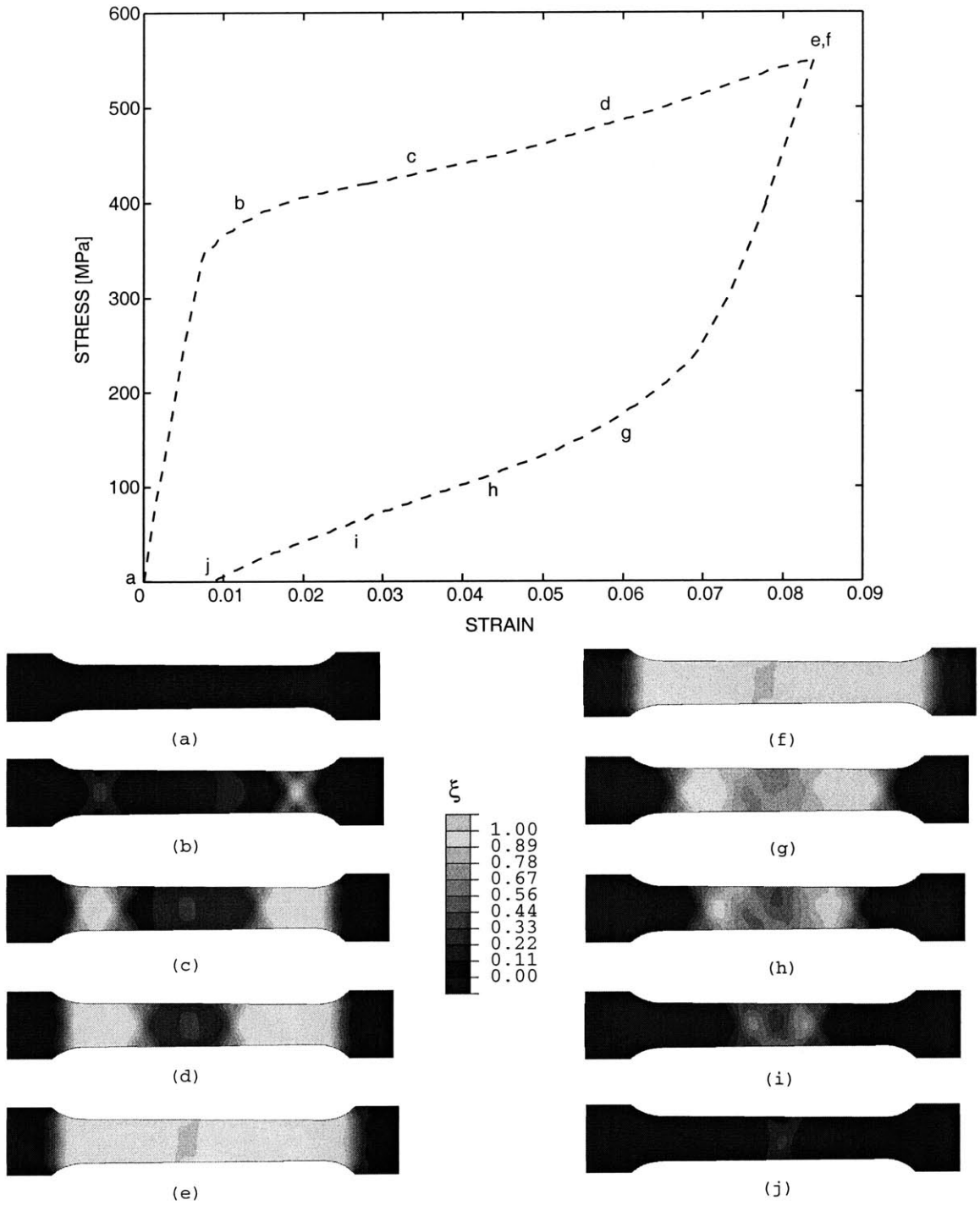

Figure 3-7: A superelastic finite-element simulation of an experiment conducted at a nominal strain rate of 2×10^{-3} /sec. The set of the martensite volume fraction contours on the left show the transformation from austenite-to-martensite during forward transformation, while those on the right show the transformation from martensite-to-austenite during reverse transformation. Note that because of the boundary conditions, both the forward and reverse transformations nucleate from the grip-ends and propagate towards the center of the specimen.

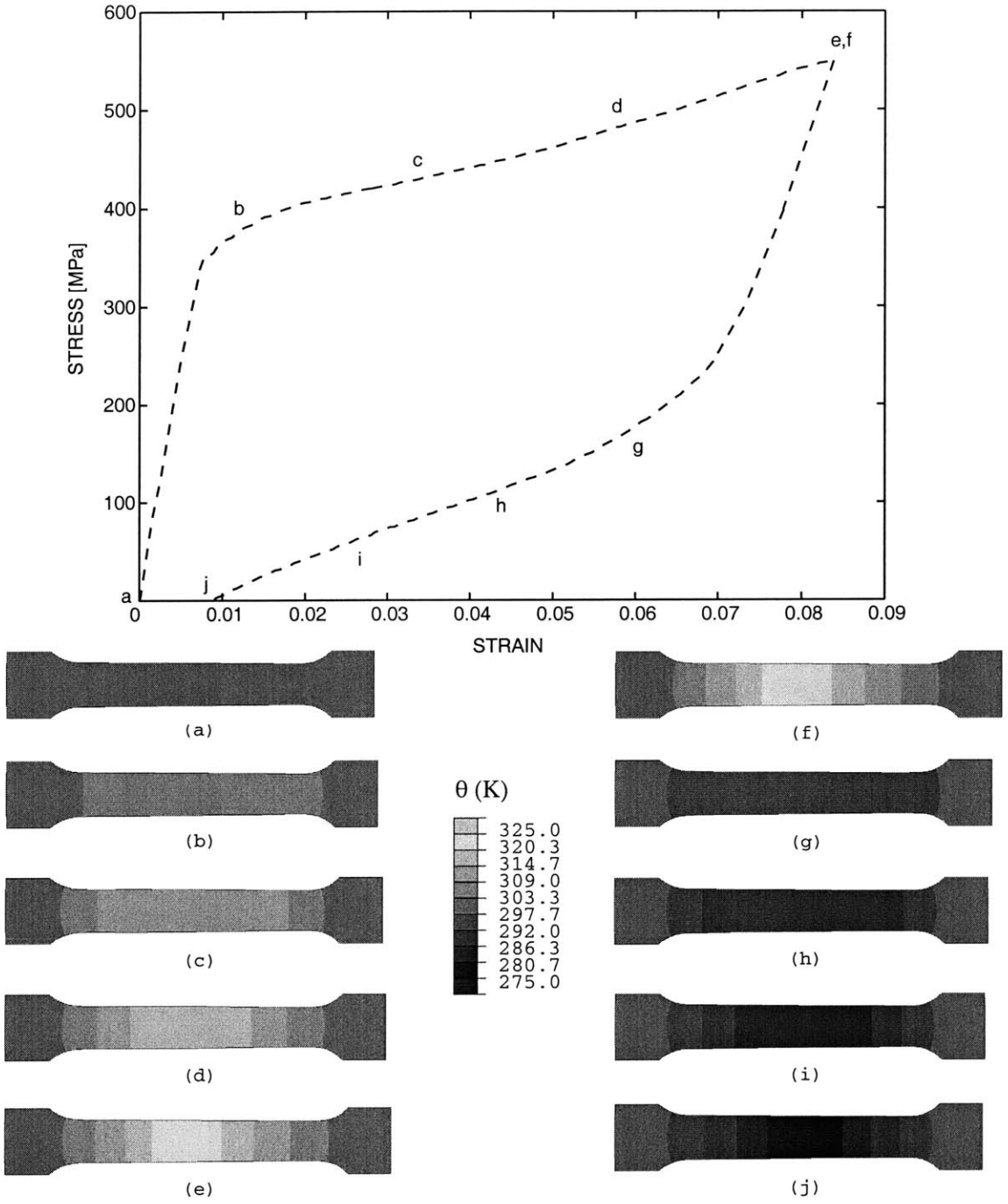

Figure 3-8: A superelastic finite-element simulation of an experiment conducted at a nominal strain rate of 2×10^{-3} /sec. The set of contours on the left shows the temperature *increase* during transformation from austenite-to-martensite, while those on the right show the temperature *decrease* during transformation from martensite-to-austenite. During forward transformation the temperature increases by as much as 25°K above the ambient temperature of 300°K due to the exothermic austenite-to-martensite transformation, whereas it *decreases* by as much as 25°K below the ambient temperature during the reverse endothermic transformation from martensite-to-austenite.

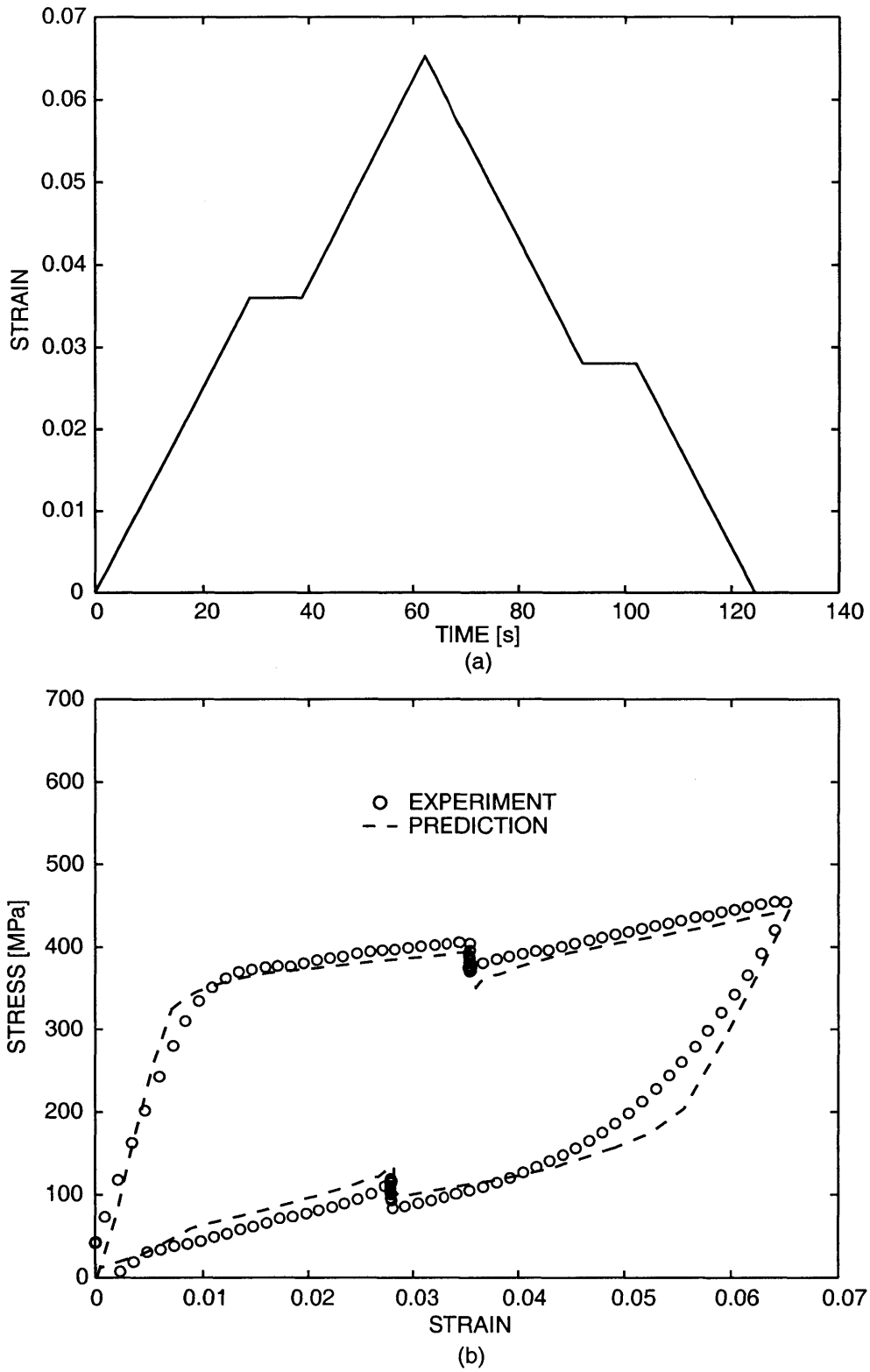

E^e E^p adjusted because of $\nu \neq 0$?

Figure 3-9: (a) Nominal strain versus time profile for the tension-hold experiment at a baseline nominal strain rate of 1.25×10^{-3} /sec and initial temperature of 300 K. (b) Superelastic stress-strain curve measured in the experiment. The prediction from the finite-element simulation is also shown.

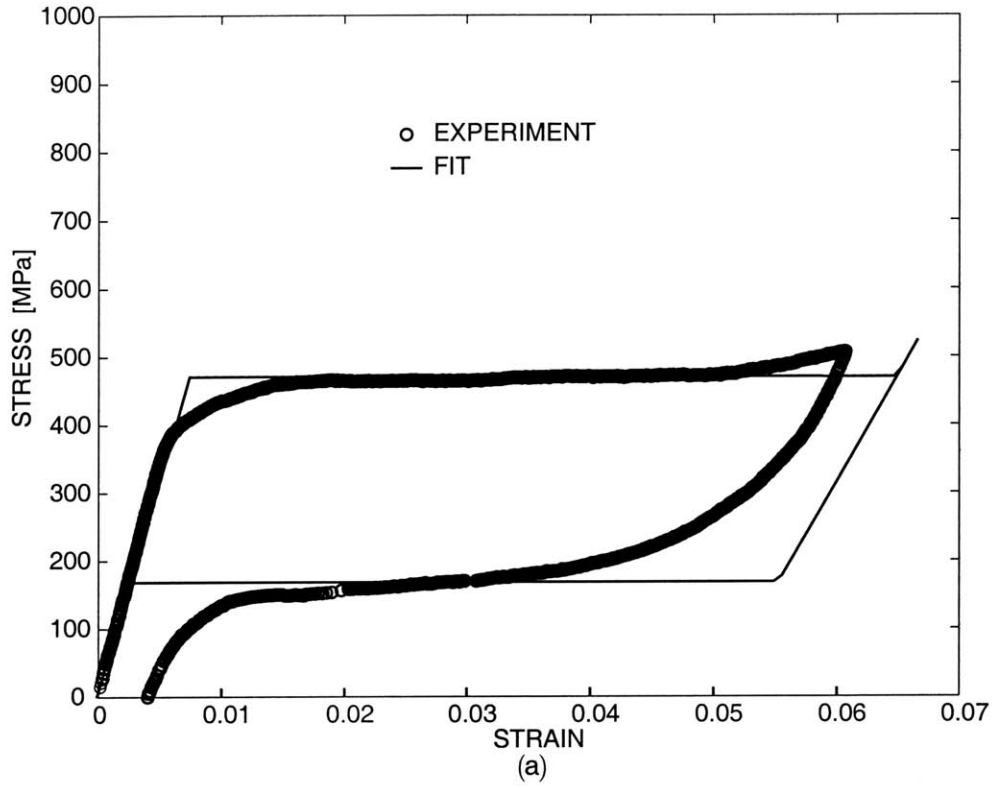

Figure 3-10: (a) Superelastic stress-strain curve in tension. The experimental data from this test were used to estimate the constitutive parameters. The curve fit using the constitutive model is also shown, and (b) Superelastic stress-strain curve in torsion. The prediction from the constitutive model is also shown.

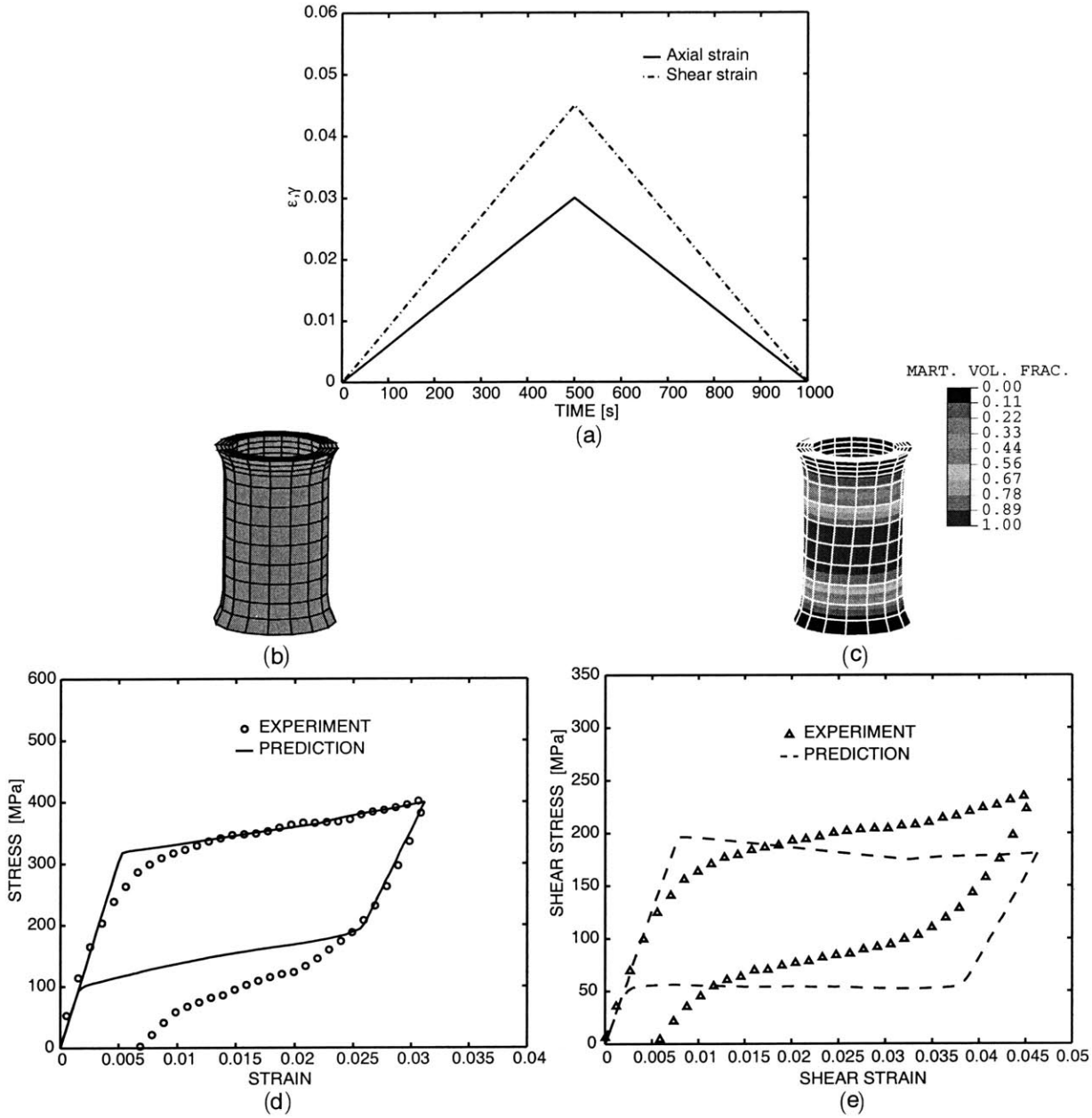

Figure 3-11: (a) Loading program for combined tension-torsion experiment. (b) Undeformed mesh of 768 ABAQUS C3D8R elements. (c) Deformed mesh at a tensile strain of 3% and a shear strain of 4.5%. Contours of martensite volume fraction are shown. (d) Superelastic stress-strain curve in tension. (e) Superelastic stress-strain curve in shear. The prediction from the constitutive model is also shown.

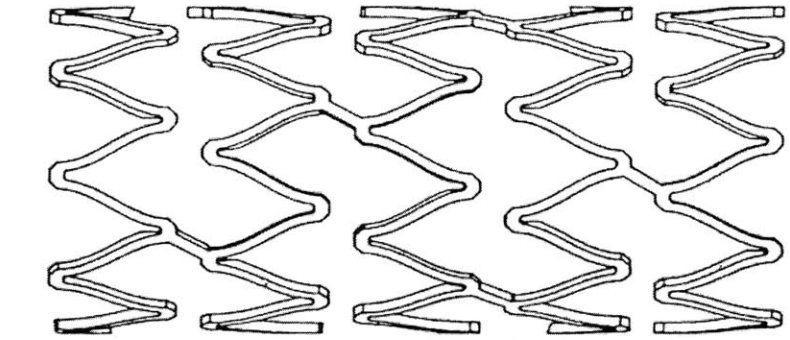

a

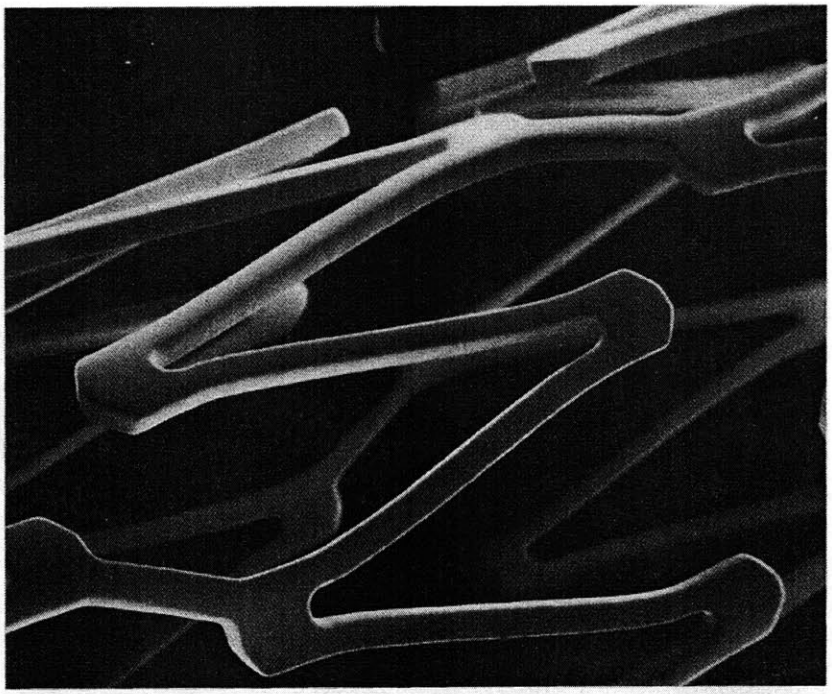

b

Figure 3-12: (a) Illustration of the SciMed stent. The 14-mm stent consists of five segments attached to each other at three sites. This design allows for good support without gaps, and high flexibility, and (b) Scanning electronic microscopic picture of the SciMed stent with full expansion. (Taken from the *Handbook of coronary stents*, (Serruys, 1997)).

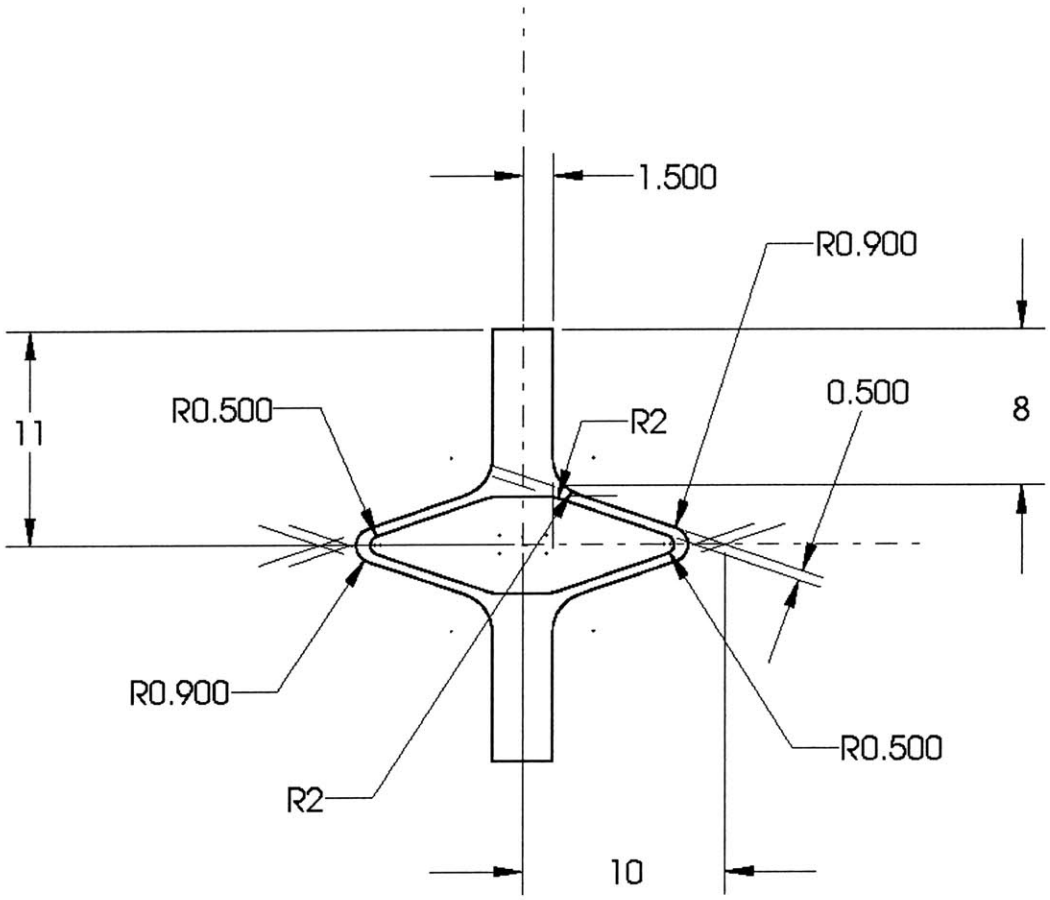

(a)

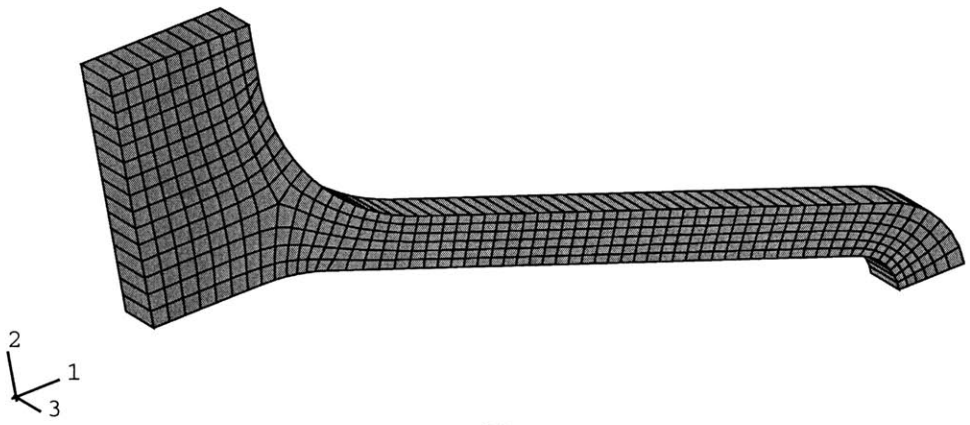

(b)

Figure 3-13: (a) Geometry of diamond-shaped strut test specimens; all dimensions are in millimeters. The sheet form which the specimens were machined is 0.53 mm thick. (b) Initial finite-element mesh of one-quarter of the specimen.

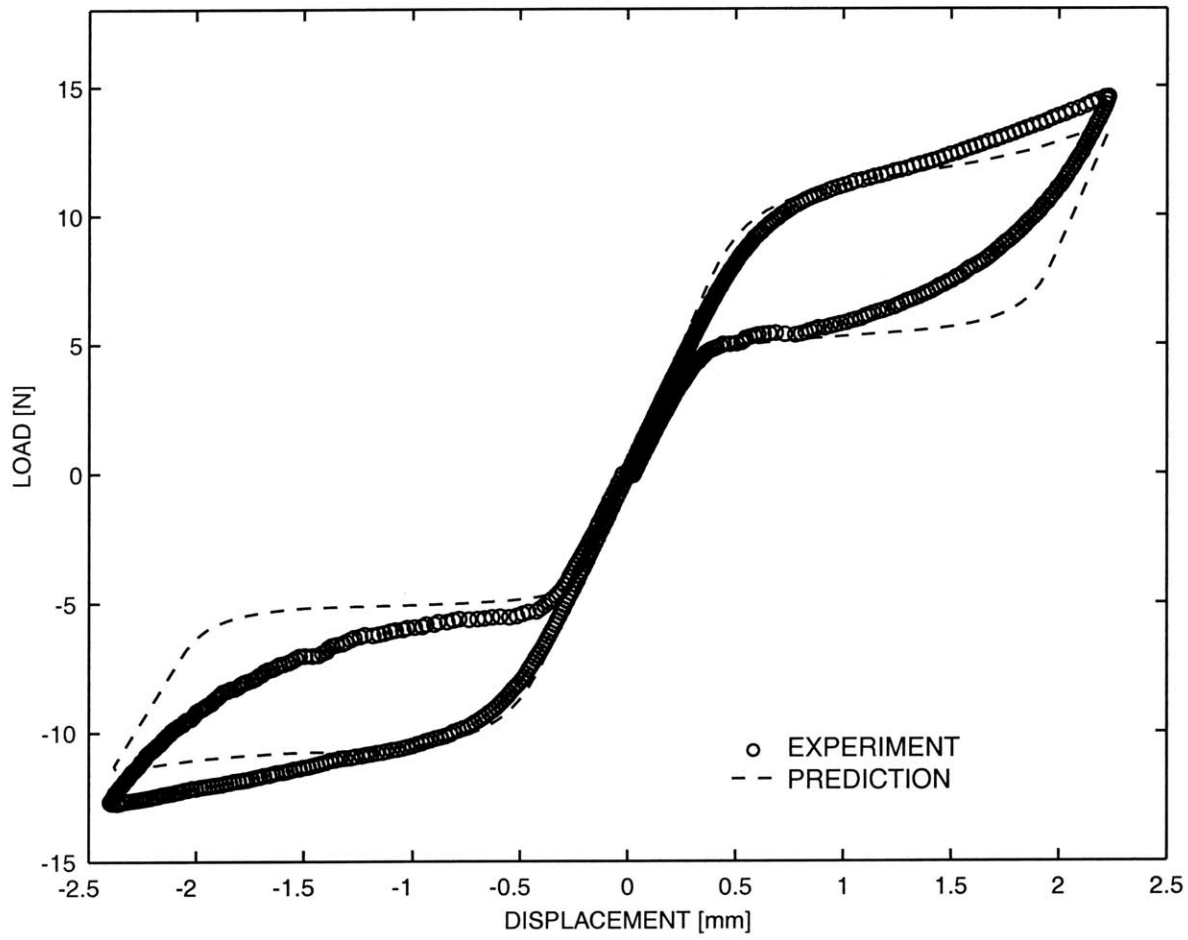

Figure 3-14: Superelastic force-displacement curve of the diamond-shaped strut test specimen in tension and compression. The corresponding prediction from the finite-element simulation is also shown.

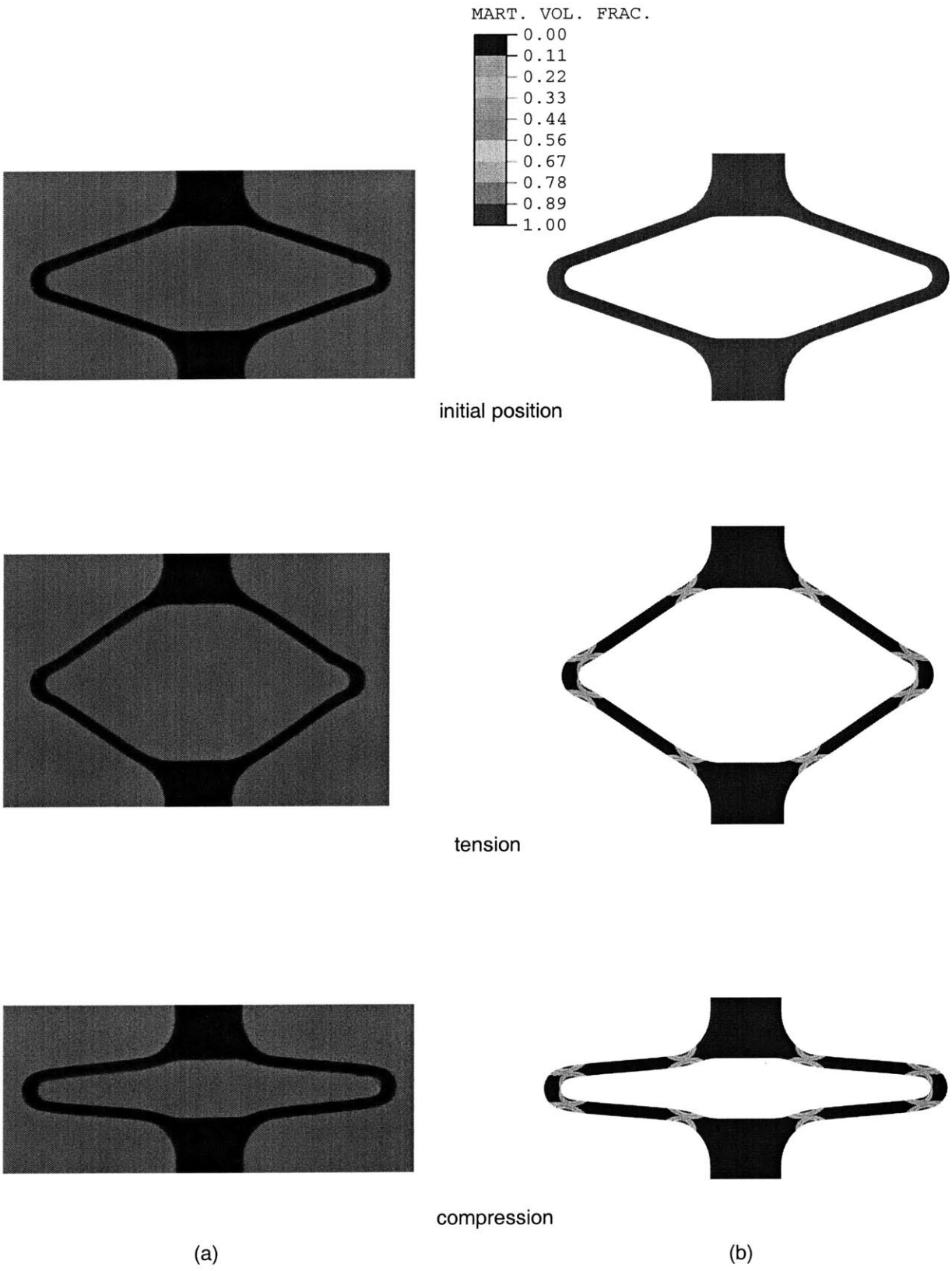

Figure 3-15: (a) The physical position of the diamond-section stent, and (b) the corresponding finite-element mesh with contours of the martensite volume fraction.

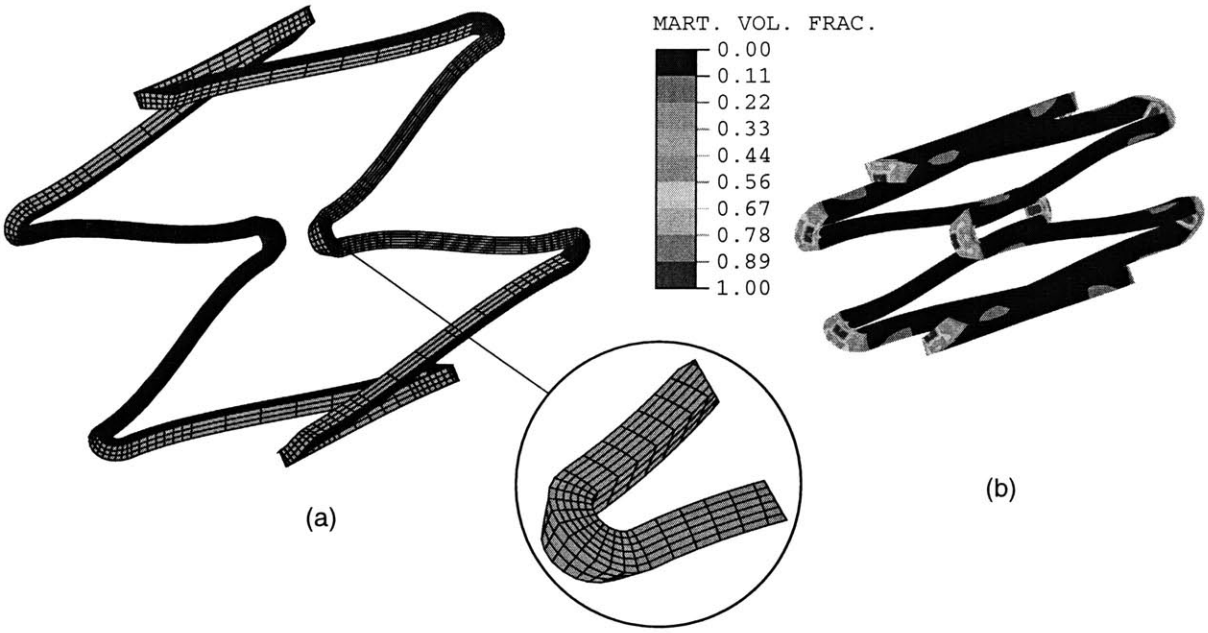

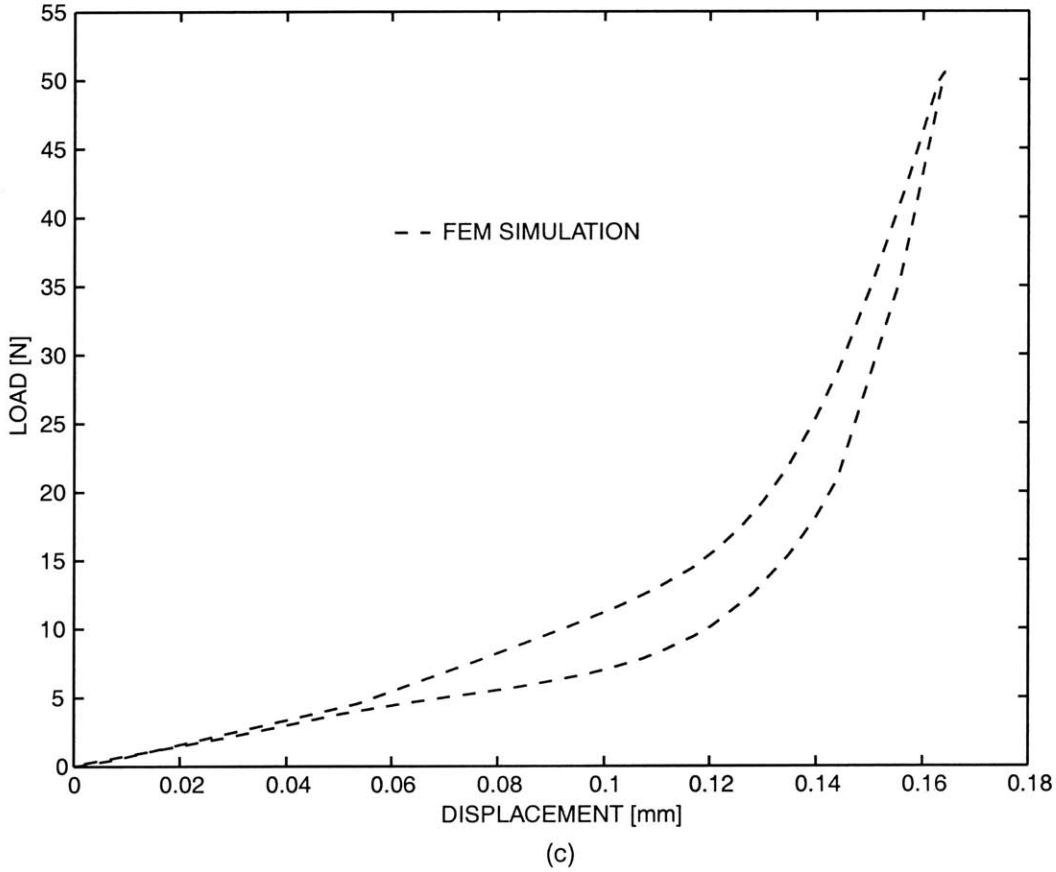

Figure 3-16: (a) Initial finite-element mesh of a segment of the stent.(b) The fully crimped state of the stent with contours of martensite volume fraction. (c) Predicted axial load-displacement curve from the finite-element simulation.

Chapter 4

Conclusion and future work

A crystal-mechanics-based constitutive model to describe the superelastic response of polycrystalline shape-memory alloys has been developed and implemented in a finite-element program. It is shown (to within the idealization of no plastic deformation of austenite and of no de-twinning of martensite) to *quantitatively* predict the superelastic response of initially-textured polycrystalline Ti-Ni rod and sheet in a variety of tension, compression, torsion and combined tension-torsion experiments to good accord. In particular we have shown that crystallographic texture is the main cause for the anisotropic response in shape-memory materials. We have also showed the applicability of the Taylor-type model (1938) as a reasonably accurate and computationally inexpensive method for determining the response of textured Ti-Ni in multi-axial setting.

The non-isothermal and non-homogeneous deformation exhibited by initially-textured Ti-Ni was also investigated. Coupled temperature-displacement analysis to predict the response of non-isothermal superelastic experiments at higher deformation rates were successfully performed. Furthermore the constitutive model is also able to qualitatively capture the phenomena of nucleation and propagation of transformation fronts under isothermal and non-isothermal conditions. The trend of the temperature field in the gage section after a loading and reverse loading step for a specimen conducted under non-isothermal testing conditions were also predicted to

good accord.

Some of the future work includes :

• As the size of a shape-memory material sample becomes very small ($<\approx 1\mu$m), in the case of very thin sputter-deposited SMA films, further analysis by James and Hane (2000) show the possible existence of new types of microstructures such as the "tent" and "tunnel" structures. This has also been experimentally observed in very small specimen sizes but not observed in macroscopic sample sizes which we have investigated here. These additional microstructures have accompanying habit-plane normals and transformation directions which can be calculated according to the theory of James and Hane (2000). This information can be readily incorporated into the constitutive model in its present form.

• As discussed in Chapter 2, shape-memory materials will be in the fully martensitic state below θ_{mf}. In this state, the inelastic strains due to stressing is caused by the motion of the twin boundaries between the martensitic plates and within the martensitic plates itself. This phenomena is called *re-orientation* and *de-twinning*, respectively. De-twinning can even occur during superelasticity if the material is stressed significantly after complete austenite to martensite has occurred. Once re-orientation and de-twinning is completed an increase of temperature to above its austenitic finish temperature θ_{af} will cause complete recovery to back to its parent state without any residual deformation. This phenomenon is called the *shape-memory effect*. A constitutive model that comprehends the re-orientation and de-twinning of the martensitic variants, and the shape-memory effect needs to developed.

Since there is a significant computational expense in implementing crystal-mechanics-based constitutive models for design purposes an isotropic constitutive model for numerical simulation of thermo-mechanically-coupled superelastic response of shape-memory materials has been developed and implemented in a finite-element program. In addition to the standard thermo-elastic material parameters, our simple model contains only four material parameters $\{\epsilon_T, \theta_T, \lambda_T, f_c\}$ to characterize the austenite $\leftrightarrow$ martensite phase transformations, and these parameters are easily determined from isothermal superelastic experiments at a few different temperatures.

Representative isothermal and thermo-mechanically coupled superelastic experiments on polycrystalline Ti-Ni sheet are shown to be predicted with reasonable accuracy by the constitutive model and computational capability. The superelastic behavior of a diamond-section stent has also been experimentally and numerically studied.

The simulation capability demonstrated in Section 3, holds the promise of greatly reducing the time required to design a new device made from a superelastic shape-memory material. The new capability should allow device-designers to relatively rapidly carry out numerous design iterations, and to computer-test their devices before any actual prototypes are built.

Bibliography

• *ABAQUS reference manual.* (1999 & 2001). Providence, R.I.

• Abeyaratne, R., & Knowles, J. (1993). A continuum model for a thermoelastic solid capable of undergoing phase transitions. *Journal of the Mechanics and Physics of Solids*, **41**, 541-571.

• Anand, L., & Gurtin, M.E. (2002). Thermal effects in the superelasticity of crystalline shape-memory materials. Submitted to the Journal of the Mechanics and Physics of Solids.

• Anand, L., & Kothari, M. (1996). A computational procedure for rate-independent crystal plasticity. *Journal of the Mechanics and Physics of Solids*, **44**, 525-558.

• Auricchio, F., & Taylor, R. (1997). Shape-memory alloys : modelling and numerical simulations of the finite-strain superelastic behavior. *Computational Methods in Applied Mechanics and Engineering*, **143**, 175-194.

• Auricchio, F., Taylor, R., & Lubliner, J. (1997). Shape-memory alloys : macromodeling and numerical simulations of the superelastic behavior. *Computational Methods in Applied Mechanics and Engineering*, **146**, 281-312.

• Ball, J., & James, R.D. (1987). Fine phase mixtures and minimizers of energy. *Archive of Rational Mechanics and Analysis*, **100**, 13-52.

• Baron, T., Levine, M. L., Hayward, V., Bolduc, M., Grant, D. 1994. (November, Ottawa). A biologically-motivated robot eye system. Proc. 8th Canadian Astronautics and Space Institute (CASI) Annual Conference. pp. 231-240.

• Bekker, A., & Brinson, L. (1997). Temperature-induced phase transformation in a shape memory alloy : phase diagram based kinetics approach. *Journal of the Mechanics of Solids*, **45**, 949-988.

• Bhattacharya, K., & Kohn, R. (1996). Symmetry, texture and the recoverable strain of shape-memory polycrystals. *Acta Materialia*, **44**, 529-542.

• Bhattacharya, K., & Kohn, R. (1997). Energy minimization and the recoverable strains of polycrystalline shape-memory alloys. *Archive of Rational Mechanics and Analysis*, **139**, 99-180.

• Boyd, J., & Lagoudas, D. (1994). A thermodynamical constitutive model for the shape memory effect due to transformation and reorientation. *Proceedings of SPIE - International Society of Optical Engineering*, **2189**, 276-288.

• Boyd, J., & Lagoudas, D. (1996). A thermodynamical model for shape memory materials. i. The monolithic shape memory alloy. *International Journal of Plasticity*, **12**, 805-842.

• Brill, T., Mittelbach, S., Assmus, W., Mullner, M., & Luthi, B. (1991). Elastic properties of Ni-Ti. *Journal of Physics : Condensed Matter*, **12**, 9621-9627.

• Entemeyer, D., Patoor, E., Eberhardt, A., & Berveiller, M. (2000). *International Journal of Plasticity*, **16**, 1269-1288.

• Gall, K., & Sehitoglu, H. (1999). The role of texture in tension-compression asymmetry in polycrystalline Ni-Ti. *International Journal of Plasticity*, **15**, 69-92.

• Gao, X., Huang, M., & Brinson, L. (2000). A multivariant micromechanical model for SMAs part 1. crystallographic issues for single crystal model. *International Journal of Plasticity*, **16**, 1345-1369.

• Gong, X. Y., & Pelton, A.R. (2002). ABAQUS analysis on Nitinol medical applications. *Proceedings ABAQUS Users' Conference*, 1-10.

• Gudlavaletti, S., Gearing, B.P., & Anand, L. (2002). Design and construction of micro-mechanical testing machines for measuring the bulk and surface properties of materials at the meso-scale. *In preparation.*

• Hane, K., & Shield, T. (1999). Microstructure in the cubic to monoclinic transition in titanium-nickel shape memory alloys. *Acta Materialia*, **47**, 2603-2617.

• Inoue, H., Miwa, N., & Inakazu, W. (1996). Texture and shape memory strain in TiNi alloy sheets. *Acta Materialia*, **46**, 4825-4834.

• Ivshin, Y., & Pence, T. (1994). A thermomechanical model for a one variant shape memory material. *Journal of Intelligent Material, Systems and Structures*, **5**, 455-473.

• James, R., & Hane, K. (2000). Martensitic transformations and shape-memory materials. *Acta Materialia*, **48**, 197-222.

• Kallend, J., Kocks, U., Rollett, S., & Wenk, H. (1989). *The Preferred Orientation*

Package of Los Alamos. Los Alamos National Laboratory (PoPLa), TMS, Warrendale, PA.

• Knowles, J. (1999). Stress-induced phase transitions in elastic solids. *Computational Mechanics*, **22**, 429-436.

• Liang, C., & Rogers, C. (1990). One-dimensional thermomechanical constitutive relations for shape memory materials. *Journal of Intelligent Materials, Systems and Structures*, **1**, 207-234.

• Lim, T., & McDowell, D. (1999). Mechanical behavior of a Ni-Ti shape memory alloy under axial-torsional proportional and on-proportional loading. *Journal of Engineering Materials and Technology - Transactions of the ASME*, **121**, 9-18.

• Lu, Z., & Weng, G. (1998). A self-consistent model for the stress-strain behavior of shape-memory alloy polycrystals. *Acta Materialia*, **46**, 5423-5433.

• Matsumoto, O., Miyazaki, S., Otsuka, K., & Tamura, H. (1987). Crystallography of martensitic transformation in Ti-Ni crystals. *Acta Metallurgica*, **35**, 2137-2144.

• Miyazaki, S., & Otsuka, K. (1989). Development of shape memory alloys. *ISIJ International*, **29**, 353-377.

• Otsuka, K., & Wayman, C. (1999). Shape memory materials. *Cambridge University Press*, Cambridge.

• Patoor, E., Eberhardt, A., & Berveiller, M. (1996). Micromechanical modelling of superelasticity in shape memory alloys. *Journal De Physique IV*, **6**, 277-292.

• Qidwai, M. A., & Lagoudas, D. (2000). Numerical implementation of a shape-memory alloy thermomechanical constitutive model using return mapping algorithms. *International Journal for Numerical Methods in Engineering*, **47**, 1123-1168.

• Rebelo, N., & Perry, M. (2000). Finite element analysis for the design of Nitinol medical devices. *Minimally Invasive Therapy and Allied Technologies*, **9**, 75-80.

• Saburi, T., & Nenno, S. (1981). The shape memory effect and related phenomena. Proceedings of International Conference on Solid-Solid Phase Transformations. *The Metallurgical Society, AIME*, New York, 1455-1479.

• Serruys, P. (1997). Handbook of coronary stents. *Rotterdam Thoraxcentre Interventional Cardiology Group*, Rotterdam.

• Shan, G., & Sung, S. (2001). *Private communication.*

• Shaw, J., & Kyriakides, S. (1995). Thermomechanical aspects of NiTi. *Journal of the Mechanics and Physics of Solids*, **43**, 1243-1281.

• Shaw, J., & Kyriakides, S. (1997). On the nucleation and propagation of phase transformation fronts in a NiTi alloy. *Acta Materialia*, **45**, 683-700.

• Shield, T. (1995). Orientation dependence of the pseudoelastic behavior of single crystals of Cu-Al-Ni in tension. *Journal of the Mechanics and Physics of Solids*, **43**, 869-895.

• Shu, Y., & Bhattacharya, K. (1998). The influence of texture on the shape memory effect in polycrystals. *Acta Materialia*, **46**, 5457-5473.

• Sobin, P. (1977). Mechanical properties of Human Veins. M.S. Thesis, University of California, San Diego, California.

• Su, C., & Anand, L. (2002). Development of a high resolution optical extensometer system. *In preparation.*

• Sun, Q., & Hwang, K. (1993a). Micromechanics modelling for the constitutive behavior of polycrystalline shape memory materials - i. Derivation of general relations. *Journal of the Mechanics and Physics of Solids*, **41**, 1-17.

• Sun, Q., & Hwang, K. (1993b). Micromechanics modelling for the constitutive behavior of polycrystalline shape memory materials - ii. Study of the individual phenomena. *Journal of the Mechanics and Physics of Solids*, **41**, 19-33.

• Taylor, G. (1938). Plastic strain in metals. *Journal of the Institute of Metals*, **62**, 30-324.

• Thamburaja, P., & Anand, L. (2001). Polycrystalline shape-memory materials : effect of crystallographic texture. *Journal of the Mechanics and Physics of Solids*, **49**, 709-737.

• Thamburaja, P., & Anand, L. (2002). Superelastic behavior in tension-torsion of an initially-textured Ti-Ni shape-memory alloy. *To appear in the International Journal of Plasticity.*

• Zhao, L., Willemse, P., Mulder, J., Beyer, J., & Wei, W. (1998). Texture development and transformation strain of a cold-rolled ti50-ni45-cu5 alloy. *Scripta Materialia*, **39**, 1317-1323.

Appendix A

Time-integration procedure : Crystal-mechanics-based constitutive model

In this appendix we summarize the time-integration procedure that we have used for our rate-independent single-crystal constitutive model. With t denoting the current time, Δt is an infinitesimal time increment, and $\tau = t + \Delta t$, the algorithm is as follows:

Given: (1) $\{\mathbf{F}(t), \mathbf{F}(\tau), \theta(t), \theta(\tau)\}$; (2) $\{\mathbf{T}(t), \mathbf{F}^p(t)\}$; (3) $\left\{\mathbf{b}_0^i, \mathbf{m}_0^i, f_c^i\right\}$; (4) the accumulated martensite volume fractions $\xi^i(t)$.

Calculate: (a)$\{\mathbf{T}(\tau), \mathbf{F}^p(\tau)\}$, (b) the accumulated martensite volume fractions $\xi^i(\tau)$, and (c) the inelastic work increment $\Delta\omega^p(\tau)$ and march forward in time.

The steps used in the calculation procedure are:

Step 1. Calculate the trial elastic strain $\mathbf{E}^e(\tau)^{trial}$:

$$\mathbf{F}^e(\tau)^{trial} = \mathbf{F}(\tau)(\mathbf{F}^p(t))^{-1},$$

$$\mathbf{C}^e(\tau)^{trial} = (\mathbf{F}^e(\tau)^{trial})^{\top}\mathbf{F}^e(\tau)^{trial},$$

$$\mathbf{E}^e(\tau)^{trial} = (1/2)\left\{\mathbf{C}^e(\tau)^{trial} - \mathbf{1}\right\}.$$

Step 2. Calculate the trial stress $\mathbf{T}^e(\tau)^{trial}$:

$$\mathbf{T}^e(\tau)^{trial} = \boldsymbol{\mathcal{C}}(t)[\mathbf{E}^e(\tau)^{trial} - \mathbf{A}(t)(\theta(\tau) - \theta_0)].$$

Step 3. Calculate the trial resolved force $\tau^i(\tau)^{trial}$ on each transformation system. The resolved force was defined as $\tau^i(\tau) = \{\mathbf{C}^e(\tau)\mathbf{T}^e(\tau)\} \cdot (\mathbf{b}_0^i \otimes \mathbf{m}_0^i)$. The resolved force $\tau^i(\tau)$ may be approximated at by $\tau^i(\tau) \doteq \mathbf{T}^e(\tau) \cdot (\mathbf{b}_0^i \otimes \mathbf{m}_0^i)$ for infinitesimal elastic stretches. Accordingly, the trial resolved force is calculated as

$$\tau^i(\tau)^{trial} = \mathbf{T}^e(\tau)^{trial} \cdot (\mathbf{b}_0^i \otimes \mathbf{m}_0^i).$$

Step 4. Calculate the trial driving force for phase transformation $f^i(\tau)^{trial}$:

$$f^i(\tau)^{trial} = \tau^i(\tau)^{trial} - (\lambda_T/\theta_T)\,(\theta(\tau) - \theta_T).$$

Step 5. Determine the set $\mathcal{PA}$ of potentially active transformation systems which satisfy

$$f^i(\tau)^{trial} - f_c^i > 0, \quad 0 \leq \xi^i(t) < 1 \quad \text{and} \quad 0 \leq \textstyle\sum_i \xi^i(t) < 1$$

for the $a \rightarrow m$ transformation, and

$$f^i(\tau)^{trial} + f_c^i < 0, \quad 0 < \xi^i(t) \leq 1 \quad \text{and} \quad 0 < \textstyle\sum_i \xi^i(t) \leq 1$$

for the $m \rightarrow a$ transformation.

Step 6. Calculate

$$\mathbf{F}^p(\tau) = \left\{ \mathbf{1} + \sum_{j \in \mathcal{PA}} \Delta\xi^j \, \mathbf{b}_0^j \otimes \mathbf{m}_0^j \right\} \mathbf{F}^p(t), \quad j = 1, ..., N, \tag{A.1}$$

where N is the total number of potentially transforming systems. Of the N potentially active systems in the set $\mathcal{PA}$, only a subset $\mathcal{A}$ with elements $M \leq N$, may actually be active (non-zero volume fraction increments). This set is determined in an iterative fashion described below.

During phase transformation, the active systems must satisfy the consistency conditions

$$f^i(\tau) \mp f_c^i = 0, \tag{A.2}$$

where the $-$ sign holds during $a \rightarrow m$ transformation and the $+$ sign holds during $m \rightarrow a$ transformation, and where

$$f^i(\tau) = \tau^i(\tau) - (\lambda_T/\theta_T)\,(\theta(\tau) - \theta_T). \tag{A.3}$$

Retaining the terms of first order [1] in $\Delta\xi^j$, it is straightforward to show that

$$\tau^i(\tau) = \tau^i(\tau)^{trial} - \sum_{j\in\mathcal{PA}} (\mathbf{b}_0^i \otimes \mathbf{m}_0^i) \cdot \boldsymbol{\mathcal{C}}(t)[\mathrm{sym}(\mathbf{C}^e(\tau)^{trial}(\mathbf{b}_0^j \otimes \mathbf{m}_0^j))]\Delta\xi^j. \tag{A.4}$$

Use of equations (A.3) and (A.4) in the consistency conditions (A.2) give

$$\sum_{j\in\mathcal{PA}} A^{ij}x^j = b^i, \quad i \in \mathcal{PA}, \tag{A.5}$$

with

$$A^{ij} = \left\{(\mathbf{b}_0^i \otimes \mathbf{m}_0^i) \cdot \boldsymbol{\mathcal{C}}(t)[\mathrm{sym}(\mathbf{C}^e(\tau)^{trial}(\mathbf{b}_0^j \otimes \mathbf{m}_0^j))]\right\}, \tag{A.6}$$

$$b^i = f^i(\tau)^{trial} - f_c^i > 0, \quad \text{and} \quad x^i \equiv \Delta\xi^i > 0 \quad \text{for } a \rightarrow m \text{ transformation}, \tag{A.7}$$

$$b^i = f^i(\tau)^{trial} + f_c^i < 0, \quad \text{and} \quad x^i \equiv \Delta\xi^i < 0 \quad \text{for } m \rightarrow a \text{ transformation}. \tag{A.8}$$

Equation (A.5) is a system of linear equations for the martensite volume fraction increments $x^j \equiv \Delta\xi^j$.

The following iterative procedure based on the Singular Value Decomposition (SVD) of the matrix A is used to determine the active transformation systems and the corresponding martensite volume fraction increments (Anand and Kothari, 1996). Calculate

$$x \equiv x^+ = A^+ b,$$

[1] Terms such $(\boldsymbol{\mathcal{C}}^m - \boldsymbol{\mathcal{C}}^a)\sum_{j\in\mathcal{PA}}\Delta\xi^j$ and $(\mathbf{A}^m - \mathbf{A}^a)\sum_{j\in\mathcal{PA}}\Delta\xi^j$ are neglected because $(\boldsymbol{\mathcal{C}}^m - \boldsymbol{\mathcal{C}}^a)\sum_{j\in\mathcal{PA}}\Delta\xi^j << \boldsymbol{\mathcal{C}}(t)$ and $(\mathbf{A}^m - \mathbf{A}^a)\sum_{j\in\mathcal{PA}}\Delta\xi^j << \mathbf{A}(t)$ for $|\Delta\xi^j| << 1$.

where A^+ is the pseudo-inverse matrix of the matrix A; if the matrix A is not singular, then the pseudo-inverse, A^+, is the true inverse, A^{-1}. If for any system the solution $x^j = \Delta\xi^j \leq 0$ when $b^j > 0$ (during $a \rightarrow m$ transformation), then this system is inactive, and it is removed from the set of potentially active systems $\mathcal{PA}$, and a new A matrix is calculated. Similarly, if $x^j = \Delta\xi^j \geq 0$ when $b^j < 0$ (during $m \rightarrow a$ transformation), then this system is also inactive, and it is also not included in the set $\mathcal{PA}$ used to determine the new A matrix. This iterative procedure is continued until all $x^j = \Delta\xi^j > 0$ for $a \rightarrow m$ transformation, and $x^j = \Delta\xi^j < 0$ for $m \rightarrow a$ transformation. The final size of the matrix A is $M \times M$, where M is the number of active systems in the set $\mathcal{A}$.

Step 7. Update the inelastic deformation gradient $\mathbf{F}^p(\tau)$:

$$\mathbf{F}^p(\tau) = \left\{ \mathbf{1} + \sum_{j \in \mathcal{A}} \Delta\xi^j \, \mathbf{b}_0^j \otimes \mathbf{m}_0^j \right\} \mathbf{F}^p(t). \tag{A.9}$$

Step 8. Update the martensite volume fraction for each system $\xi^j(\tau)$ and the total martensite volume fraction for the single crystal $\xi(\tau)$:

$$\xi^j(\tau) = \xi^j(t) + \Delta\xi^j, \tag{A.10}$$

$$\xi(\tau) = \sum_{j=1}^{N} \xi^j(\tau). \tag{A.11}$$

If $\xi^j(\tau) > 1$, then set $\xi^j(\tau) = 1$ and if $\xi^j(\tau) < 0$, then set $\xi^j(\tau) = 0$. Similarly, if $\xi(\tau) > 1$, then set $\xi(\tau) = 1$ and if $\xi(\tau) < 0$, then set $\xi(\tau) = 0$.

Step 9. Update the effective elastic modulus $\boldsymbol{\mathcal{C}}(\tau)$ and thermal expansion $\mathbf{A}(\tau)$:

$$\boldsymbol{\mathcal{C}}(\tau) = \{1 - \xi(\tau)\} \, \boldsymbol{\mathcal{C}}^a + \xi(\tau) \boldsymbol{\mathcal{C}}^m,$$

$$\mathbf{A}(\tau) = \{1 - \xi(\tau)\} \, \mathbf{A}^a + \xi(\tau) \mathbf{A}^m.$$

Step 10. Compute the elastic deformation gradient $\mathbf{F}^e(\tau)$ and the stress $\mathbf{T}^e(\tau)$:

$$\mathbf{F}^e(\tau) = \mathbf{F}(\tau)(\mathbf{F}^p(\tau))^{-1},$$

$$\mathbf{C}^e(\tau) = (\mathbf{F}^e(\tau))^{\top}\mathbf{F}^e(\tau),$$

$$\mathbf{E}^e(\tau) = (1/2)\,\{\mathbf{C}^e(\tau) - \mathbf{1}\},$$

$$\mathbf{T}^e(\tau) = \boldsymbol{\mathcal{C}}(\tau)[\mathbf{E}^e(\tau) - \mathbf{A}(\tau)(\theta(\tau) - \theta_0)].$$

Step 11. Update the Cauchy stress $\mathbf{T}(\tau)$:

$$\mathbf{T}(\tau) = (\det \mathbf{F}(\tau))^{-1}\left\{\mathbf{F}^e(\tau)\mathbf{T}^e(\tau)(\mathbf{F}^e(\tau))^{\top}\right\}.$$

Step 12. Calculate the driving force for phase transformation $f^i(\tau)$ and inelastic work fraction $\Delta\omega^p(\tau)$:

$$\tau^i(\tau) \doteq \mathbf{T}^e(\tau) \cdot (\mathbf{b}_0^i \otimes \mathbf{m}_0^i),$$

$$f^i(\tau) = \tau^i(\tau) - (\lambda_T/\theta_T)(\theta(\tau) - \theta_T),$$

$$\Delta\omega^p(\tau) = \{\textstyle\sum_i f^i(\tau)\Delta\xi^i\} + (\lambda_T/\theta_T)\,\theta(\tau)\Delta\xi.$$

Appendix B

Crystallographic theory of martensite

This theory neglects any elastic strains and assumes that the martensites have stretches $\mathbf{U}_i$ and the austenite is unstrained, even in the presence of stresses. These stretches depend on the constants α, β, γ and ϑ, which are related to the lattice constants of the two phases and will be discussed shortly. Since the stretch in the direction normal to the shearing plane is in general not equal 1.0, the transformation is not a pure shear. Thus it is not possible to kinematically match a single variant with stretch $\mathbf{U}_i$ to undeformed austenite. Therefore the analysis of Ball and James (1987) show that the martensite must then be twinned in order to allow approximate kinematic compatibility at a planar austenite-martensite interface. This analysis is a formulation of the crystallographic theory of martensite (CTM).

The alloy of Ti-Ni considered here exhibits a structural phase transformation from the cubic austenite phase to a low temperature monoclinic martensite phase at the transformation temperature θ_{ms}. There are twelve possible ways to transform the cubic structure to the monoclinic structure. From Hane and Shield (1999) the stretches $\mathbf{U}_i$ are given by

$$\mathbf{U}_1 = \begin{pmatrix} \theta & \rho & \rho \\ \rho & \sigma & \tau \\ \rho & \tau & \sigma \end{pmatrix}, \mathbf{U}_2 = \begin{pmatrix} \theta & -\rho & -\rho \\ -\rho & \sigma & \tau \\ -\rho & \tau & \sigma \end{pmatrix}, \mathbf{U}_3 = \begin{pmatrix} \theta & -\rho & \rho \\ \rho & \sigma & -\tau \\ \rho & -\tau & \sigma \end{pmatrix},$$

$$\mathbf{U}_4 = \begin{pmatrix} \theta & \rho & -\rho \\ \rho & \sigma & -\tau \\ -\rho & -\tau & \sigma \end{pmatrix}, \mathbf{U}_5 = \begin{pmatrix} \sigma & \rho & \tau \\ \rho & \theta & \rho \\ \tau & \rho & \sigma \end{pmatrix}, \mathbf{U}_6 = \begin{pmatrix} \sigma & -\rho & \tau \\ -\rho & \theta & -\rho \\ \tau & -\rho & \sigma \end{pmatrix},$$

$$\mathbf{U}_7 = \begin{pmatrix} \sigma & -\rho & -\tau \\ -\rho & \theta & \rho \\ -\tau & -\rho & \sigma \end{pmatrix}, \mathbf{U}_8 = \begin{pmatrix} \sigma & \rho & -\tau \\ \rho & \theta & -\rho \\ -\tau & -\rho & \sigma \end{pmatrix}, \mathbf{U}_9 = \begin{pmatrix} \sigma & \tau & \rho \\ \tau & \sigma & \rho \\ \rho & \rho & \theta \end{pmatrix},$$

$$\mathbf{U}_{10} = \begin{pmatrix} \sigma & \tau & -\rho \\ \tau & \sigma & -\rho \\ -\rho & -\rho & \theta \end{pmatrix}, \mathbf{U}_{11} = \begin{pmatrix} \sigma & -\tau & \rho \\ -\tau & \sigma & -\rho \\ \rho & -\rho & \theta \end{pmatrix}, \mathbf{U}_{12} = \begin{pmatrix} \sigma & -\tau & -\rho \\ -\tau & \sigma & \rho \\ -\rho & \rho & \theta \end{pmatrix}.$$

These stretches depend on the transformation stretches, α, β and γ, and the monoclinic angle, ϑ. The specific components of the stretches $\mathbf{U}_i$ are

$$\theta = \frac{\alpha(\alpha + \gamma\sin(\vartheta))}{\sqrt{\alpha^2 + \gamma^2 + 2\alpha\gamma\sin(\vartheta)}} \quad ,$$

$$\rho = \frac{\alpha\gamma\cos(\vartheta)}{\sqrt{\alpha^2 + \gamma^2 + 2\alpha\gamma\sin(\vartheta)}} \quad ,$$

$$\sigma = \frac{1}{2}\left(\frac{\gamma(\gamma + \alpha\sin(\vartheta))}{\sqrt{\alpha^2 + \gamma^2 + 2\alpha\gamma\sin(\vartheta)}} + \beta\right) \quad ,$$

$$\tau = \frac{1}{2}\left(\frac{\gamma(\gamma + \alpha\sin(\vartheta))}{\sqrt{\alpha^2 + \gamma^2 + 2\alpha\gamma\sin(\vartheta)}} - \beta\right).$$

The transformation stretches are given as $\alpha = a/a_o$, $\beta = b/(\sqrt{2}\,a_o)$, and $\gamma = c/(\sqrt{2}\,a_o)$, where the lattice parameter of the cubic cell is a_o and the lattice parameters

of the monoclinic cell are a, b and c, and ϑ is the angle between the edges with lengths a and c. The lattice parameter for the austenite phase is measured to be $a_o = 3.015\,\text{A}$. The lattice parameters of the monoclinic phase are measured to be $a = 2.889\,\text{A}$, $b = 4.120\,\text{A}$, $c = 4.622\,\text{A}$ and $\vartheta = 96.80^o$. Therefore the transformation stretches are $\alpha = 0.9582$, $\beta = 0.9663$ and $\gamma = 1.0840$.

The structure of an austenite-twinned martensite interface is shown in Figure B-1. Displacements must be continuous across the two types of interfaces(twin boundaries and the A-M interface) in this structure. Mathematically, this reduces to the statement that the deformation gradients in each region must differ by a rank-one tensor. That is if $\mathbf{F}_A$ and $\mathbf{F}_B$ are the deformation gradients on either side of a planar interface with normal $\mathbf{n}$ (in the reference configuration) then the difference between these two deformation gradients must be of the following form,

$$\mathbf{F}_A - \mathbf{F}_B = \mathbf{a} \otimes \mathbf{n}, \tag{B.1}$$

where $\mathbf{a}$ is the shearing vector. The interface between the two variants of martensite is a twin boundary and kinematic compatibility across this interface requires,

$$\mathbf{R}_{AB}\mathbf{U}_B - \mathbf{U}_A = \mathbf{a} \otimes \mathbf{n}, \tag{B.2}$$

where $\mathbf{R}_{AB}$ is an orthogonal tensor and represents the relative rotation between the two twins. The polar decomposition of a deformation gradient, $\mathbf{F}$, into a rotation times a pure stretch , $\mathbf{RU}$, has also been used. In this equation A and B represent different choices of the integers $\{1..12\}$. The rotation is unknown because the transformation only specifies the stretches. This equation admits three types of solutions which are known as compound, Type I and Type II twins. These types are defined by the number of symmetries the crystal structures exhibits across the twin plane. Compound twins have two planes of symmetry and this gives solutions for $\mathbf{a}$ and $\mathbf{n}$ whose components are integers in the cubic basis. However, compound twins only occur between variants that have shears in the same plane. This results in an average deformation in the martensite region that has a stretch of β in the direction normal to the shear plane. Thus it is impossible for compound twins to be kinematically

compatible with austenite. Therefore, Types I and II solutions can exist and will be allowed.

Because both of these twins are composed of variants that have shears in different planes, it is possible to pick a volume fraction, λ for variant B (so that variant A has volume fraction $(1-\lambda)$) such that the average deformation in the martensite, given by

$$\mathbf{F}_{AB} = \mathbf{R}_H(\lambda \mathbf{R}_{AB}\mathbf{U}_B + (1-\lambda)\mathbf{R}_A) \tag{B.3}$$

is kinematically compatible with the undeformed austenite. The rotation of this average deformation is $\mathbf{R}_H$. Requiring kinematical compatibility between the average martensite deformation and the austenite is termed approximate compatibility. It is useful to use B.2 to write

$$\mathbf{F}_{AB} = \mathbf{R}_H(\mathbf{U}_A + \lambda \mathbf{a} \otimes \mathbf{n}). \tag{B.4}$$

The requirement that the twinned martensite be kinematically compatible with the austenite can then be written,

$$\mathbf{F}_{AB} - \mathbf{I} = \mathbf{b} \otimes \mathbf{m} \tag{B.5}$$

where $\mathbf{I}$ is the identity matrix, which is the deformation gradient in the undeformed austenite. In B.5 $\mathbf{b}$ and $\mathbf{m}$ are the shearing and normal vectors for the A-M interface, respectively.

A solution to the crystallographic theory of martensite (CTM) problem is the quantities $\mathbf{a}$, $\mathbf{n}$, $\mathbf{b}$, $\mathbf{m}$, $\mathbf{R}_{AB}$, $\mathbf{R}_H$ and λ such that B.2 and B.5 are satisfied for a given choice of A and B. If a matrix C, is known to be of the form

$$\mathbf{C} = (\mathbf{I} + \mathbf{n}' \otimes \mathbf{a}')(\mathbf{I} + \mathbf{a}' \otimes \mathbf{n}') \tag{B.6}$$

and it is positive definite with a middle eigenvalue of 1 then Proposition 4 of Ball and James (1987) gives the vectors $\mathbf{a}'$ and $\mathbf{n}'$ to be

$$\mathbf{a}' = \rho \left(\sqrt{\frac{\lambda_3(1-\lambda_1)}{\lambda_3 - \lambda_1}}\, \mathbf{e}_1 + \kappa \sqrt{\frac{\lambda_1(\lambda_3 - 1)}{\lambda_3 - \lambda_1}}\, \mathbf{e}_3 \right) \tag{B.7}$$

and

$$\mathbf{n}' = \rho^{-1}\left(\frac{\sqrt{\lambda_3}-\sqrt{\lambda_1}}{\sqrt{\lambda_3-\lambda_1}}\right)(-\sqrt{1-\lambda_1}\,\mathbf{e}_1 + \kappa\sqrt{\lambda_3-1}\,\mathbf{e}_3), \tag{B.8}$$

where $\lambda_1 \leq (\lambda_2 = 1) \leq \lambda_3$ are the eigenvalues of $\mathbf{C}$ with the corresponding $\mathbf{e}_1$, $\mathbf{e}_2$ and $\mathbf{e}_3$. The constant ρ represents an invariant scaling of the solution and will be used to chose unit normal vectors. The constant κ can take on the values ± 1. The procedure is to solve B.2 first and then solve B.5 by constructing matrices of the form B.6. Equations B.7 and B.8 then give explicit solutions.

To solve for the interface between the martensite twins, we form the matrix

$$\mathbf{C} = \mathbf{U}_A^{-1}\mathbf{U}_B^2\mathbf{U}_A^{-1}. \tag{B.9}$$

If B.2 is satisfied then $\mathbf{C}$ has the form B.6 and following identifications are made,

$$\mathbf{a} = \mathbf{a}', \tag{B.10}$$

and

$$\mathbf{n} = \mathbf{U}_A\mathbf{n}'. \tag{B.11}$$

In this case ρ is chosen such that $\mathbf{n}$ is a unit vector. the two solutions B.7 and B.8 provide to B.2 represent Type I and Type II twins. Once B.7, B.8, B.10 and B.11 are used to find $\mathbf{a}$ and $\mathbf{n}$ then the rotation $\mathbf{R}_{AB}$ is found from B.2 directly for a given choice of κ. The value of κ used in B.7 and B.8 for the solution to B.2 will be called κ_1.

Once the twin interface is known then we can proceed to apply Proposition 4 of Ball and James (1987) to determine the A-M orientation. In this case the matrix $\mathbf{C}_0(\lambda)$, given by

$$\mathbf{C}_0(\lambda) = (\mathbf{U}_A + \lambda\mathbf{n}\otimes\mathbf{a})(\mathbf{U}_A + \lambda\mathbf{a}\otimes\mathbf{n}), \tag{B.12}$$

is of the form

$$\mathbf{C} = (\mathbf{I} + \mathbf{m}\otimes\mathbf{b})(\mathbf{I} + \mathbf{b}\otimes\mathbf{m}) \tag{B.13}$$

if kinematic compatibility as represented by B.6 is satisfied. Here λ needs to be solved. Propositions 5 and 6 of Ball and James (1987) state that a matrix of the form

B.13 has eigenvalues that satisfy the requirement of Proposition 4 of Ball and James (1987) if the value of λ is root of the function

$$g(\lambda) = \det(\mathbf{C}_0(\lambda) - \mathbf{I}). \tag{B.14}$$

Simplifying B.14 yields to equation 5.56 in Ball and James (1987),

$$g(\lambda) = \det(\mathbf{U}_A^2 - \mathbf{I}) + (\lambda^2 - \lambda)(|\mathbf{a}^2| - (\det \mathbf{U}_A^2)|\mathbf{U}_A^{-1}\mathbf{a}|^2|\mathbf{U}_A^{-1}\mathbf{n}|^2). \tag{B.15}$$

Once the roots of $g(\lambda)$ are founds then the application of Proposition 4 proceeds as above and

$$\mathbf{b} = \rho\left(\sqrt{\frac{\lambda_3(1-\lambda_1)}{\lambda_3-\lambda_1}}\,\mathbf{e}_1 + \kappa\sqrt{\frac{\lambda_1(\lambda_3-1)}{\lambda_3-\lambda_1}}\,\mathbf{e}_3\right) \tag{B.16}$$

$$\mathbf{m} = \rho^{-1}\left(\frac{\sqrt{\lambda_3}-\sqrt{\lambda_1}}{\sqrt{\lambda_3-\lambda_1}}\right)(-\sqrt{1-\lambda_1}\,\mathbf{e}_1 + \kappa\sqrt{\lambda_3-1}\,\mathbf{e}_3). \tag{B.17}$$

Note that the solution of λ must be in [0,1]. Equations B.3 and B.5 are then used to determine $\mathbf{R}_H$. Again the value of κ in B.7 and B.8 determines which of the two solutions to B.5 for a given value of λ is found. The value of κ used in B.7 and B.8 when solving B.5 will be called κ_2. Thus there are two roots of $g(\lambda)$ in [0,1] and each root results in two solutions corresponding to the two values of κ_2. Thus, there are four A-M interfaces possible for a given martensite twin. There are 24 choices for A and B (omitting the compound twin case) and each pair can form either a Type I or Type II twinned martensite corresponding to the two values of κ_1. Thus we have $24 \times 2 \times 4 = 192$ A-M interfaces possible in this material.

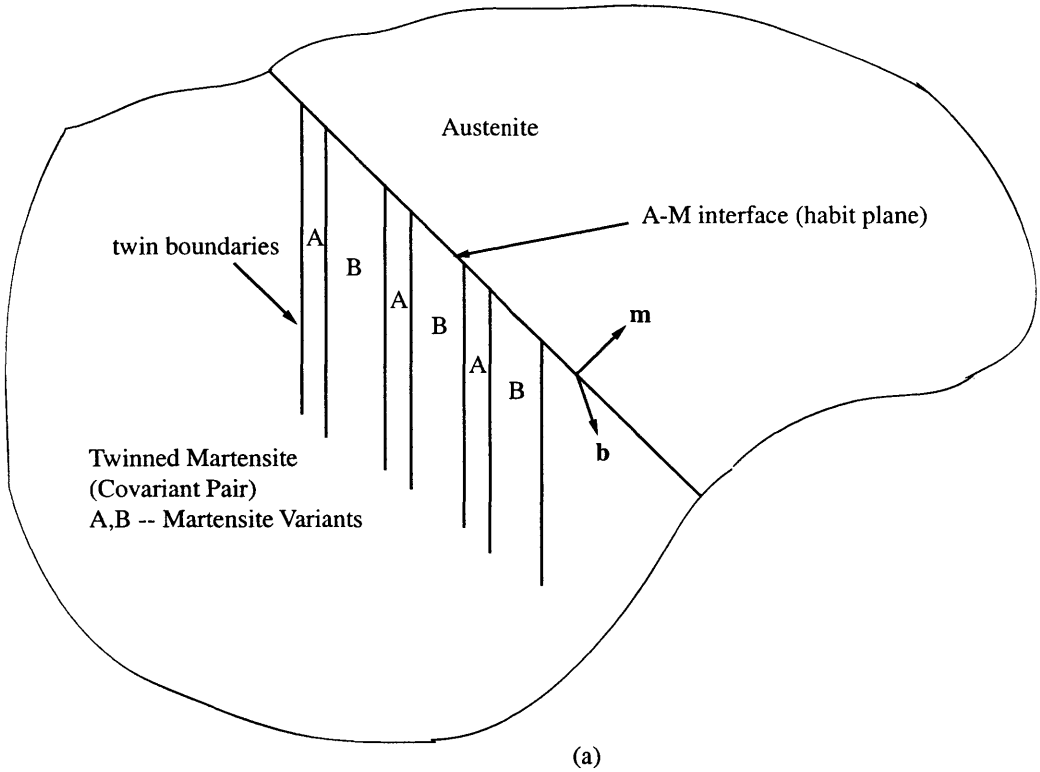

(a)

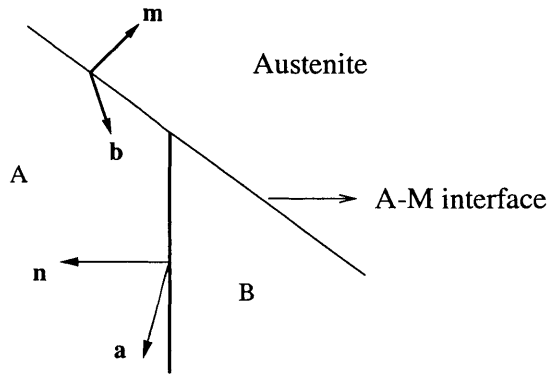

Twinned-Martensite

(b)

Figure B-1: (a) Schematic diagram of an austenite-twinned martensite transformation system, and (b) a magnified schematic diagram of the twinned martensite.

Appendix C

Algorithm to calculate the austenite-martensite transformation systems using the crystallographic theory of martensite

In this appendix we summarize the algorithm to calculate the austenite-martensite transformation systems using the crystallographic theory of martensite. For further details refer to Ball and James (1987) and Hane and Shield (2001).

Given: $\{\mathbf{U}_A, \mathbf{U}_B, \kappa_1 = \pm 1, \kappa_2 = \pm 1\}$.

Calculate: $\{\mathbf{a}, \mathbf{n}, \mathbf{b}, \mathbf{m}, \lambda, \mathbf{R}_{AB}, \mathbf{R}_H\}$.

The steps used in the calculation procedure are:

Step 1. Construct the $\mathbf{C}_{AB}$ matrix:

$$\mathbf{C}_{AB} = \mathbf{U}_A^{-1}\,\mathbf{U}_B^2\,\mathbf{U}_A^{-1}.$$

Step 2. Perform spectral decomposition of $\mathbf{C}_{AB}$ to calculate its eigenvalues λ_I, with $\lambda_1 \leq \lambda_2 = 1 \leq \lambda_3$, and eigenvectors $\mathbf{e}_I$:

$$\mathbf{C}_{AB} = \lambda_1\,\mathbf{e}_1 \otimes \mathbf{e}_1 + \lambda_2\,\mathbf{e}_2 \otimes \mathbf{e}_2 + \lambda_3\,\mathbf{e}_3 \otimes \mathbf{e}_3.$$

Step 3. Calculate $\mathbf{n}'$ and $\mathbf{a}'$:

$$\mathbf{n}' = \left(\frac{\sqrt{\lambda_3}-\sqrt{\lambda_1}}{\sqrt{\lambda_3-\lambda_1}}\right)(-\sqrt{1-\lambda_1}\,\mathbf{e}_1 + \kappa_1\sqrt{\lambda_3-1}\,\mathbf{e}_3),$$

$$\mathbf{a}' = \left(\sqrt{\frac{\lambda_3(1-\lambda_1)}{\lambda_3-\lambda_1}}\,\mathbf{e}_1 + \kappa_1\sqrt{\frac{\lambda_1(\lambda_3-1)}{\lambda_3-\lambda_1}}\,\mathbf{e}_3\right).$$

Step 4. Calculate ρ and scale $\mathbf{n}'$ and $\mathbf{a}'$ to choose unit normal vectors :

$$\rho = |\mathbf{n}'|, \quad \mathbf{n}' = \rho^{-1}\,\mathbf{n}' \quad \text{and} \quad \mathbf{a}' = \rho\,\mathbf{a}'.$$

Step 5. Calculate $\mathbf{n}$ and $\mathbf{a}$:

$$\mathbf{n} = \mathbf{U}_A\,\mathbf{n}',$$

$$\mathbf{a} = \mathbf{a}'.$$

Step 6. Using equation 5.56 from Ball and James (1987) construct the quadratic function $g(\lambda)$ and calculate the roots λ_1 and λ_2 of $g(\lambda)$:

$$g(\lambda) = \det(\mathbf{U}_A^2 - \mathbf{1}) + (\lambda^2-\lambda)\,(|\mathbf{a}|^2 - (\det\mathbf{U}_A^2)\,|\mathbf{U}_A^{-1}\,\mathbf{a}|^2\,|\mathbf{U}_A^{-1}\,\mathbf{n}|^2).$$

Step 7. Construct the $\mathbf{C}(\lambda_1)$ and $\mathbf{C}(\lambda_2)$ matrices :

$$\mathbf{C}(\lambda_1) = (\mathbf{U}_A + \lambda_1\,\mathbf{n}\otimes\mathbf{a})\,(\mathbf{U}_A + \lambda_1\,\mathbf{a}\otimes\mathbf{n}),$$

$$\mathbf{C}(\lambda_2) = (\mathbf{U}_A + \lambda_2\,\mathbf{n}\otimes\mathbf{a})\,(\mathbf{U}_A + \lambda_2\,\mathbf{a}\otimes\mathbf{n}).$$

Step 8. Perform spectral decomposition of $\mathbf{C}(\lambda_1)$ to calculate its eigenvalues λ_I, with $\lambda_1 \le \lambda_2 = 1 \le \lambda_3$, and eigenvectors $\mathbf{e}_I$:

$$\mathbf{C}(\lambda_1) = \lambda_1\,\mathbf{e}_1\otimes\mathbf{e}_1 + \lambda_2\,\mathbf{e}_2\otimes\mathbf{e}_2 + \lambda_3\,\mathbf{e}_3\otimes\mathbf{e}_3.$$

Step 9. Calculate $\mathbf{m}$ and $\mathbf{b}$:

$$\mathbf{m} = \left(\frac{\sqrt{\lambda_3}-\sqrt{\lambda_1}}{\sqrt{\lambda_3-\lambda_1}}\right)(-\sqrt{1-\lambda_1}\,\mathbf{e}_1 + \kappa_2\sqrt{\lambda_3-1}\,\mathbf{e}_3),$$

$$\mathbf{b} = \left(\sqrt{\frac{\lambda_3(1-\lambda_1)}{\lambda_3-\lambda_1}}\,\mathbf{e}_1 + \kappa_2\sqrt{\frac{\lambda_1(\lambda_3-1)}{\lambda_3-\lambda_1}}\,\mathbf{e}_3\right).$$

Step 10. Calculate ρ and scale $\mathbf{m}$ and $\mathbf{b}$ to choose unit normal vectors :

$$\rho = |\mathbf{m}|, \quad \mathbf{m} = \rho^{-1}\,\mathbf{m} \quad \text{and} \quad \mathbf{b} = \rho\,\mathbf{b}.$$

Step 11. Calculate the relative rotation $\mathbf{R}_{AB}$:

$$\mathbf{R}_{AB} = (\mathbf{U}_A + \lambda_2\,\mathbf{a} \otimes \mathbf{n})\,\mathbf{U}_B^{-1}$$

Step 12. Calculate the rotation $\mathbf{R}_H$ of the average austenite-martensite deformation:

$$\mathbf{R}_H = (\mathbf{1} + \mathbf{b} \otimes \mathbf{m})\,(\mathbf{U}_A + \lambda_1\,\mathbf{a} \otimes \mathbf{n})^{-1}.$$

Repeat steps 8-12 for the $C(\lambda_2)$ matrix.

C.1 Results of the CTM theory

The crystallographic theory of martensite (CTM) can be used to calculate the transformation and twinning systems for different alloy systems. For example Titanium-Nickel (Ti-Ni) alloys undergo a cubic to monoclinic transformation. Copper-based alloys such as Cu-Al-Ni undergo a cubic to orthorhombic transformation whereas Indium-Thalium (In-Th) alloys undergo a cubic to tetragonal transformation.

Shield (1995) has calculated the transformation systems for Cu-Al-Ni systems undergoing cubic to orthorhombic transformation. For Cu-Al-Ni undergoing cubic to orthorhombic transformation there are six different variants i.e $\mathbf{U}_1..\mathbf{U}_6$. Corresponding to these six different variants are a possibility of 96 different transformation systems. These transformation systems are documented in Shield (1995).

Transformation systems for Ti-Ni alloys have also been calculated by Hane and Shield (1999). The resulting 192 transformation systems for Ti-Ni alloys are calculated here using the CTM theory and the results are summarized from Tables 2 to 25. Each table has 8 possible transformation systems for a particular variant pairing. The 24 transformation systems which are experimentally observed and used in our calculations are labelled with an asterisk ($*$). The 192 possible transformation systems for Ti-Ni alloys are :

Table 2. $\mathbf{U}_A = \mathbf{U}_1$ and $\mathbf{U}_B = \mathbf{U}_3$

$m_{0,1}$	$m_{0,2}$	$m_{0,3}$	$b_{0,1}$	$b_{0,2}$	$b_{0,3}$
-0.9087	-0.3334	0.2514	0.0527	-0.0535	0.1060
-0.9087	0.3334	0.2514	0.0527	0.0535	0.1060
-0.3464	0.4334	-0.8320	0.1211	0.0397	-0.0257
-0.3464	-0.4334	-0.8320	0.1211	-0.0397	-0.0257
* -0.8888	-0.4045	0.2153	0.0568	-0.0638	0.0991
* -0.8888	0.4045	0.2153	0.0568	0.0638	0.0991
-0.3762	0.5137	-0.7711	0.1195	0.0485	-0.0216
-0.3762	-0.5137	-0.7711	0.1195	-0.0485	-0.0216

Table 3. $\mathbf{U}_A = \mathbf{U}_1$ and $\mathbf{U}_B = \mathbf{U}_4$

$m_{0,1}$	$m_{0,2}$	$m_{0,3}$	$b_{0,1}$	$b_{0,2}$	$b_{0,3}$
* -0.8888	0.2153	-0.4045	0.0568	0.0991	-0.0638
* -0.8888	0.2153	0.4045	0.0568	0.0991	0.0638
-0.3762	-0.7711	0.5137	0.1195	-0.0216	0.0485
-0.3762	-0.7711	-0.5137	0.1195	-0.0216	-0.0485
-0.9087	0.2514	-0.3334	0.0527	0.1060	-0.0535
-0.9087	0.2514	0.3334	0.0527	0.1060	0.0535
-0.3464	-0.8320	0.4334	0.1211	-0.0257	0.0397
-0.3464	-0.8320	-0.4334	0.1211	-0.0257	-0.0397

Table 4. $\mathbf{U}_A = \mathbf{U}_2$ and $\mathbf{U}_B = \mathbf{U}_3$

$m_{0,1}$	$m_{0,2}$	$m_{0,3}$	$b_{0,1}$	$b_{0,2}$	$b_{0,3}$
-0.3762	0.7711	-0.5137	0.1195	0.0216	-0.0485
-0.3762	0.7711	0.5137	0.1195	0.0216	0.0485
* -0.8888	-0.2153	0.4045	0.0568	-0.0991	0.0638
* -0.8888	-0.2153	-0.4045	0.0568	-0.0991	-0.0638
-0.3464	0.8320	-0.4334	0.1211	0.0257	-0.0397
-0.3464	0.8320	0.4334	0.1211	0.0257	0.0397
-0.9087	-0.2514	0.3334	0.0527	-0.1060	0.0535
-0.9087	-0.2514	-0.3334	0.0527	-0.1060	-0.0535

Table 5. $\mathbf{U}_A = \mathbf{U}_2$ and $\mathbf{U}_B = \mathbf{U}_4$

$m_{0,1}$	$m_{0,2}$	$m_{0,3}$	$b_{0,1}$	$b_{0,2}$	$b_{0,3}$
-0.3762	-0.5137	0.7711	0.1195	-0.0485	0.0216
-0.3762	0.5137	0.7711	0.1195	0.0485	0.0216
* -0.8888	0.4045	-0.2153	0.0568	0.0638	-0.0991
* -0.8888	-0.4045	-0.2153	0.0568	-0.0638	-0.0991
-0.3464	-0.4334	0.8320	0.1211	-0.0397	0.0257
-0.3464	0.4334	0.8320	0.1211	0.0397	0.0257
-0.9087	0.3334	-0.2514	0.0527	0.0535	-0.1060
-0.9087	-0.3334	-0.2514	0.0527	-0.0535	-0.1060

Table 6. $\mathbf{U}_A = \mathbf{U}_5$ and $\mathbf{U}_B = \mathbf{U}_7$

$m_{0,1}$	$m_{0,2}$	$m_{0,3}$	$b_{0,1}$	$b_{0,2}$	$b_{0,3}$
-0.3334	-0.9087	0.2514	-0.0535	0.0527	0.1060
0.3334	-0.9087	0.2514	0.0535	0.0527	0.1060
0.4334	-0.3464	-0.8320	0.0397	0.1211	-0.0257
-0.4334	-0.3464	-0.8320	-0.0397	0.1211	-0.0257
0.5137	-0.3762	-0.7711	0.0485	0.1195	-0.0216
* 0.4045	-0.8888	0.2153	0.0638	0.0568	0.0991
* -0.4045	-0.8888	0.2153	-0.0638	0.0568	0.0991
-0.5137	-0.3762	-0.7711	-0.0485	0.1195	-0.0216

Table 7. $\mathbf{U}_A = \mathbf{U}_5$ and $\mathbf{U}_B = \mathbf{U}_8$

$m_{0,1}$	$m_{0,2}$	$m_{0,3}$	$b_{0,1}$	$b_{0,2}$	$b_{0,3}$
* 0.2153	-0.8888	-0.4045	0.0991	0.0568	-0.0638
* 0.2153	-0.8888	0.4045	0.0991	0.0568	0.0638
-0.7711	-0.3762	0.5137	-0.0216	0.1195	0.0485
-0.7711	-0.3762	-0.5137	-0.0216	0.1195	-0.0485
0.2514	-0.9087	-0.3334	0.1060	0.0527	-0.0535
0.2514	-0.9087	0.3334	0.1060	0.0527	0.0535
-0.8320	-0.3464	0.4334	-0.0257	0.1211	0.0397
-0.8320	-0.3464	-0.4334	-0.0257	0.1211	-0.0397

Table 8. $\mathbf{U}_A = \mathbf{U}_6$ and $\mathbf{U}_B = \mathbf{U}_7$

$m_{0,1}$	$m_{0,2}$	$m_{0,3}$	$b_{0,1}$	$b_{0,2}$	$b_{0,3}$
0.7711	-0.3762	-0.5137	0.0216	0.1195	-0.0485
0.7711	-0.3762	0.5137	0.0216	0.1195	0.0485
* -0.2153	-0.8888	0.4045	-0.0991	0.0568	0.0638
* -0.2153	-0.8888	-0.4045	-0.0991	0.0568	-0.0638
0.8320	-0.3464	-0.4334	0.0257	0.1211	-0.0397
0.8320	-0.3464	0.4334	0.0257	0.1211	0.0397
-0.2514	-0.9087	0.3334	-0.1060	0.0527	0.0535
-0.2514	-0.9087	-0.3334	-0.1060	0.0527	-0.0535

Table 9. $\mathbf{U}_A = \mathbf{U}_6$ and $\mathbf{U}_B = \mathbf{U}_8$

$m_{0,1}$	$m_{0,2}$	$m_{0,3}$	$b_{0,1}$	$b_{0,2}$	$b_{0,3}$
* 0.4045	-0.8888	-0.2153	0.0638	0.0568	-0.0991
0.5137	-0.3762	0.7711	0.0485	0.1195	0.0216
-0.5137	-0.3762	0.7711	-0.0485	0.1195	0.0216
* -0.4045	-0.8888	-0.2153	-0.0638	0.0568	-0.0991
-0.4334	-0.3464	0.8320	-0.0397	0.1211	0.0257
0.4334	-0.3464	0.8320	0.0397	0.1211	0.0257
0.3334	-0.9087	-0.2514	0.0535	0.0527	-0.1060
-0.3334	-0.9087	-0.2514	-0.0535	0.0527	-0.1060

Table 10. $\mathbf{U}_A = \mathbf{U}_9$ and $\mathbf{U}_B = \mathbf{U}_{11}$

$m_{0,1}$	$m_{0,2}$	$m_{0,3}$	$b_{0,1}$	$b_{0,2}$	$b_{0,3}$
-0.7711	0.5137	-0.3762	-0.0216	0.0485	0.1195
* 0.2153	0.4045	-0.8888	0.0991	0.0638	0.0568
* 0.2153	-0.4045	-0.8888	0.0991	-0.0638	0.0568
-0.7711	-0.5137	-0.3762	-0.0216	-0.0485	0.1195
0.2514	-0.3334	-0.9087	0.1060	-0.0535	0.0527
0.2514	0.3334	-0.9087	0.1060	0.0535	0.0527
-0.8320	0.4334	-0.3464	-0.0257	0.0397	0.1211
-0.8320	-0.4334	-0.3464	-0.0257	-0.0397	0.1211

Table 11. $\mathbf{U}_A = \mathbf{U}_9$ and $\mathbf{U}_B = \mathbf{U}_{12}$

$m_{0,1}$	$m_{0,2}$	$m_{0,3}$	$b_{0,1}$	$b_{0,2}$	$b_{0,3}$
0.5137	-0.7711	-0.3762	0.0485	-0.0216	0.1195
* 0.4045	0.2153	-0.8888	0.0638	0.0991	0.0568
* -0.4045	0.2153	-0.8888	-0.0638	0.0991	0.0568
-0.5137	-0.7711	-0.3762	-0.0485	-0.0216	0.1195
-0.3334	0.2514	-0.9087	-0.0535	0.1060	0.0527
0.3334	0.2514	-0.9087	0.0535	0.1060	0.0527
0.4334	-0.8320	-0.3464	0.0397	-0.0257	0.1211
-0.4334	-0.8320	-0.3464	-0.0397	-0.0257	0.1211

Table 12. $\mathbf{U}_A = \mathbf{U}_{10}$ and $\mathbf{U}_B = \mathbf{U}_{11}$

$m_{0,1}$	$m_{0,2}$	$m_{0,3}$	$b_{0,1}$	$b_{0,2}$	$b_{0,3}$
* 0.4045	-0.2153	-0.8888	0.0638	-0.0991	0.0568
0.5137	0.7711	-0.3762	0.0485	0.0216	0.1195
-0.5137	0.7711	-0.3762	-0.0485	0.0216	0.1195
* -0.4045	-0.2153	-0.8888	-0.0638	-0.0991	0.0568
-0.4334	0.8320	-0.3464	-0.0397	0.0257	0.1211
0.4334	0.8320	-0.3464	0.0397	0.0257	0.1211
0.3334	-0.2514	-0.9087	0.0535	-0.1060	0.0527
-0.3334	-0.2514	-0.9087	-0.0535	-0.1060	0.0527

Table 13. $\mathbf{U}_A = \mathbf{U}_{10}$ and $\mathbf{U}_B = \mathbf{U}_{12}$

$m_{0,1}$	$m_{0,2}$	$m_{0,3}$	$b_{0,1}$	$b_{0,2}$	$b_{0,3}$
* -0.2153	0.4045	-0.8888	-0.0991	0.0638	0.0568
0.7711	0.5137	-0.3762	0.0216	0.0485	0.1195
0.7711	-0.5137	-0.3762	0.0216	-0.0485	0.1195
* -0.2153	-0.4045	-0.8888	-0.0991	-0.0638	0.0568
0.8320	-0.4334	-0.3464	0.0257	-0.0397	0.1211
0.8320	0.4334	-0.3464	0.0257	0.0397	0.1211
-0.2514	0.3334	-0.9087	-0.1060	0.0535	0.0527
-0.2514	-0.3334	-0.9087	-0.1060	-0.0535	0.0527

Table 14. $\mathbf{U}_A = \mathbf{U}_1$ and $\mathbf{U}_B = \mathbf{U}_5$

$m_{0,1}$	$m_{0,2}$	$m_{0,3}$	$b_{0,1}$	$b_{0,2}$	$b_{0,3}$
-0.0008	-0.8138	0.5811	0.0934	0.0350	0.0433
-0.8138	-0.0008	0.5811	0.0350	0.0934	0.0433
-0.8589	-0.2779	-0.4302	0.0052	0.0901	-0.0607
-0.2779	-0.8589	-0.4302	0.0901	0.0052	-0.0607
0.0419	-0.8887	0.4565	0.1008	0.0278	0.0375
-0.8887	0.0419	0.4565	0.0278	0.1008	0.0375
-0.9098	-0.2012	-0.3629	0.0010	0.0999	-0.0485
-0.2012	-0.9098	-0.3629	0.0999	0.0010	-0.0485

Table 15. $\mathbf{U}_A = \mathbf{U}_1$ and $\mathbf{U}_B = \mathbf{U}_9$

$m_{0,1}$	$m_{0,2}$	$m_{0,3}$	$b_{0,1}$	$b_{0,2}$	$b_{0,3}$
-0.0008	0.5811	-0.8138	0.0934	0.0433	0.0350
-0.8138	0.5811	-0.0008	0.0350	0.0433	0.0934
-0.8589	-0.4302	-0.2779	0.0052	-0.0607	0.0901
-0.2779	-0.4302	-0.8589	0.0901	-0.0607	0.0052
0.0419	0.4565	-0.8887	0.1008	0.0375	0.0278
-0.8887	0.4565	0.0419	0.0278	0.0375	0.1008
-0.9098	-0.3629	-0.2012	0.0010	-0.0485	0.0999
-0.2012	-0.3629	-0.9098	0.0999	-0.0485	0.0010

Table 16. $\mathbf{U}_A = \mathbf{U}_2$ and $\mathbf{U}_B = \mathbf{U}_7$

$m_{0,1}$	$m_{0,2}$	$m_{0,3}$	$b_{0,1}$	$b_{0,2}$	$b_{0,3}$
0.9098	-0.2012	-0.3629	-0.0010	0.0999	-0.0485
-0.2012	0.9098	0.3629	0.0999	-0.0010	0.0485
-0.0419	-0.8887	0.4565	-0.1008	0.0278	0.0375
-0.8887	-0.0419	-0.4565	0.0278	-0.1008	-0.0375
0.8589	-0.2779	-0.4302	-0.0052	0.0901	-0.0607
-0.2779	0.8589	0.4302	0.0901	-0.0052	0.0607
0.0008	-0.8138	0.5811	-0.0934	0.0350	0.0433
-0.8138	0.0008	-0.5811	0.0350	-0.0934	-0.0433

Table 17. $\mathbf{U}_A = \mathbf{U}_2$ and $\mathbf{U}_B = \mathbf{U}_{12}$

$m_{0,1}$	$m_{0,2}$	$m_{0,3}$	$b_{0,1}$	$b_{0,2}$	$b_{0,3}$
-0.0419	0.4565	-0.8887	-0.1008	0.0375	0.0278
-0.2012	0.3629	0.9098	0.0999	0.0485	-0.0010
0.9098	-0.3629	-0.2012	-0.0010	-0.0485	0.0999
-0.8887	-0.4565	-0.0419	0.0278	-0.0375	-0.1008
0.0008	0.5811	-0.8138	-0.0934	0.0433	0.0350
-0.2779	0.4302	0.8589	0.0901	0.0607	-0.0052
0.8589	-0.4302	-0.2779	-0.0052	-0.0607	0.0901
-0.8138	-0.5811	0.0008	0.0350	-0.0433	-0.0934

Table 18. $\mathbf{U}_A = \mathbf{U}_3$ and $\mathbf{U}_B = \mathbf{U}_6$

$m_{0,1}$	$m_{0,2}$	$m_{0,3}$	$b_{0,1}$	$b_{0,2}$	$b_{0,3}$
0.8589	-0.2779	0.4302	-0.0052	0.0901	0.0607
-0.8138	0.0008	0.5811	0.0350	-0.0934	0.0433
0.0008	-0.8138	-0.5811	-0.0934	0.0350	-0.0433
-0.2779	0.8589	-0.4302	0.0901	-0.0052	-0.0607
0.9098	-0.2012	0.3629	-0.0010	0.0999	0.0485
-0.2012	0.9098	-0.3629	0.0999	-0.0010	-0.0485
-0.0419	-0.8887	-0.4565	-0.1008	0.0278	-0.0375
-0.8887	-0.0419	0.4565	0.0278	-0.1008	0.0375

Table 19. $\mathbf{U}_A = \mathbf{U}_3$ and $\mathbf{U}_B = \mathbf{U}_{11}$

$m_{0,1}$	$m_{0,2}$	$m_{0,3}$	$b_{0,1}$	$b_{0,2}$	$b_{0,3}$
-0.8589	0.4302	-0.2779	0.0052	0.0607	0.0901
-0.2779	0.4302	-0.8589	0.0901	0.0607	0.0052
-0.0008	-0.5811	-0.8138	0.0934	-0.0433	0.0350
-0.8138	-0.5811	-0.0008	0.0350	-0.0433	0.0934
-0.9098	0.3629	-0.2012	0.0010	0.0485	0.0999
-0.8887	-0.4565	0.0419	0.0278	-0.0375	0.1008
0.0419	-0.4565	-0.8887	0.1008	-0.0375	0.0278
-0.2012	0.3629	-0.9098	0.0999	0.0485	0.0010

Table 20. $\mathbf{U}_A = \mathbf{U}_4$ and $\mathbf{U}_B = \mathbf{U}_8$

$m_{0,1}$	$m_{0,2}$	$m_{0,3}$	$b_{0,1}$	$b_{0,2}$	$b_{0,3}$
0.0419	-0.8887	-0.4565	0.1008	0.0278	-0.0375
-0.8887	0.0419	-0.4565	0.0278	0.1008	-0.0375
-0.9098	-0.2012	0.3629	0.0010	0.0999	0.0485
-0.2012	-0.9098	0.3629	0.0999	0.0010	0.0485
-0.0008	-0.8138	-0.5811	0.0934	0.0350	-0.0433
-0.2779	-0.8589	0.4302	0.0901	0.0052	0.0607
-0.8589	-0.2779	0.4302	0.0052	0.0901	0.0607
-0.8138	-0.0008	-0.5811	0.0350	0.0934	-0.0433

Table 21. $\mathbf{U}_A = \mathbf{U}_4$ and $\mathbf{U}_B = \mathbf{U}_{10}$

$m_{0,1}$	$m_{0,2}$	$m_{0,3}$	$b_{0,1}$	$b_{0,2}$	$b_{0,3}$
0.9098	0.3629	-0.2012	-0.0010	0.0485	0.0999
-0.2012	-0.3629	0.9098	0.0999	-0.0485	-0.0010
-0.0419	-0.4565	-0.8887	-0.1008	-0.0375	0.0278
-0.8887	0.4565	-0.0419	0.0278	0.0375	-0.1008
0.8589	0.4302	-0.2779	-0.0052	0.0607	0.0901
-0.8138	0.5811	0.0008	0.0350	0.0433	-0.0934
0.0008	-0.5811	-0.8138	-0.0934	-0.0433	0.0350
-0.2779	-0.4302	0.8589	0.0901	-0.0607	-0.0052

Table 22. $\mathbf{U}_A = \mathbf{U}_5$ and $\mathbf{U}_B = \mathbf{U}_9$

$m_{0,1}$	$m_{0,2}$	$m_{0,3}$	$b_{0,1}$	$b_{0,2}$	$b_{0,3}$
0.5811	-0.0008	-0.8138	0.0433	0.0934	0.0350
0.5811	-0.8138	-0.0008	0.0433	0.0350	0.0934
-0.4302	-0.8589	-0.2779	-0.0607	0.0052	0.0901
-0.4302	-0.2779	-0.8589	-0.0607	0.0901	0.0052
0.4565	0.0419	-0.8887	0.0375	0.1008	0.0278
0.4565	-0.8887	0.0419	0.0375	0.0278	0.1008
-0.3629	-0.9098	-0.2012	-0.0485	0.0010	0.0999
-0.3629	-0.2012	-0.9098	-0.0485	0.0999	0.0010

Table 23. $\mathbf{U}_A = \mathbf{U}_6$ and $\mathbf{U}_B = \mathbf{U}_{11}$

$m_{0,1}$	$m_{0,2}$	$m_{0,3}$	$b_{0,1}$	$b_{0,2}$	$b_{0,3}$
0.4565	-0.0419	-0.8887	0.0375	-0.1008	0.0278
0.3629	-0.2012	0.9098	0.0485	0.0999	-0.0010
-0.3629	0.9098	-0.2012	-0.0485	-0.0010	0.0999
-0.4565	-0.8887	-0.0419	-0.0375	0.0278	-0.1008
0.5811	0.0008	-0.8138	0.0433	-0.0934	0.0350
0.4302	-0.2779	0.8589	0.0607	0.0901	-0.0052
-0.4302	0.8589	-0.2779	-0.0607	-0.0052	0.0901
-0.5811	-0.8138	0.0008	-0.0433	0.0350	-0.0934

Table 24. $\mathbf{U}_A = \mathbf{U}_7$ and $\mathbf{U}_B = \mathbf{U}_{12}$

$m_{0,1}$	$m_{0,2}$	$m_{0,3}$	$b_{0,1}$	$b_{0,2}$	$b_{0,3}$
0.3629	-0.9098	-0.2012	0.0485	0.0010	0.0999
0.3629	-0.2012	-0.9098	0.0485	0.0999	0.0010
-0.4565	0.0419	-0.8887	-0.0375	0.1008	0.0278
-0.4565	-0.8887	0.0419	-0.0375	0.0278	0.1008
0.4302	-0.8589	-0.2779	0.0607	0.0052	0.0901
0.4302	-0.2779	-0.8589	0.0607	0.0901	0.0052
-0.5811	-0.0008	-0.8138	-0.0433	0.0934	0.0350
-0.5811	-0.8138	-0.0008	-0.0433	0.0350	0.0934

Table 25. $\mathbf{U}_A = \mathbf{U}_8$ and $\mathbf{U}_B = \mathbf{U}_{10}$

$m_{0,1}$	$m_{0,2}$	$m_{0,3}$	$b_{0,1}$	$b_{0,2}$	$b_{0,3}$
0.4302	0.8589	-0.2779	0.0607	-0.0052	0.0901
0.5811	-0.8138	0.0008	0.0433	0.0350	-0.0934
-0.5811	0.0008	-0.8138	-0.0433	-0.0934	0.0350
-0.4302	-0.2779	0.8589	-0.0607	0.0901	-0.0052
0.3629	0.9098	-0.2012	0.0485	-0.0010	0.0999
0.4565	-0.8887	-0.0419	0.0375	0.0278	-0.1008
-0.4565	-0.0419	-0.8887	-0.0375	-0.1008	0.0278
-0.3629	-0.2012	0.9098	-0.0485	0.0999	-0.0010

Appendix D

Example of a fortran code to calculate the austenite-martensite transformation systems using CTM

```
      PROGRAM MAIN
C*************************************************************
C     THIS PROGRAM CALCULATES THE AUSTENITE/MARTENSITE
C     SYSTEMS FOR TI-NI
C*************************************************************
      IMPLICIT REAL*8(A-H,O-Z)

      PARAMETER(THETA = 0.9563D0, SIGMA = 1.0243D0,TAU = 0.05803D0,
     +          RHO = -0.04266D0 )

      REAL*8 U1(3,3),U2(3,3),U3(3,3),U4(3,3),U5(3,3),U6(3,3),
     +       U7(3,3),U8(3,3),U9(3,3),U10(3,3),U11(3,3),U12(3,3),
     +       UA(3,3),UB(3,3),AVEC(3),NVEC(3),UAINV(3,3),
     +       BVEC1(3),MVEC1(3),BVEC2(3),MVEC2(3),NTILDE(3)
```

CC *Open file for writing output*

```
OPEN (UNIT=21,FILE='systems.dat',STATUS='UNKNOWN')
WRITE(21,*)'RESULTS FROM CRYSTALLOGRAPHIC THEORY OF MARTENSITE'
WRITE(21,*)'------------------------------------------------ '
WRITE(21,*)'192'
WRITE(21,*)' B(1)   B(2)   B(3)   M(1)   M(2)   M(3)'
```

U1(1,1) = THETA

U1(1,2) = RHO

U1(1,3) = RHO

U1(2,2) = SIGMA

U1(2,3) = TAU

U1(3,3) = SIGMA

U1(2,1) = U1(1,2)

U1(3,1) = U1(1,3)

U1(3,2) = U1(2,3)

U2(1,1) = THETA

U2(1,2) = −RHO

U2(1,3) = −RHO

U2(2,2) = SIGMA

U2(2,3) = TAU

U2(3,3) = SIGMA

U2(2,1) = U2(1,2)

U2(3,1) = U2(1,3)

U2(3,2) = U2(2,3)

U3(1,1) = THETA

U3(1,2) = −RHO

U3(1,3) = RHO

U3(2,2) = SIGMA

U3(2,3) = −TAU

U3(3,3) = SIGMA

U3(2,1) = U3(1,2)

U3(3,1) = U3(1,3)

U3(3,2) = U3(2,3)

U4(1,1) = THETA

U4(1,2) = RHO

U4(1,3) = −RHO

U4(2,2) = SIGMA

U4(2,3) = −TAU

U4(3,3) = SIGMA

U4(2,1) = U4(1,2)

U4(3,1) = U4(1,3)

U4(3,2) = U4(2,3)

U5(1,1) = SIGMA

U5(1,2) = RHO

U5(1,3) = TAU

U5(2,2) = THETA

U5(2,3) = RHO

U5(3,3) = SIGMA

U5(2,1) = U5(1,2)

U5(3,1) = U5(1,3)

U5(3,2) = U5(2,3)

U6(1,1) = SIGMA

U6(1,2) = −RHO

U6(1,3) = TAU

U6(2,2) = THETA

U6(2,3) = −RHO

U6(3,3) = SIGMA

U6(2,1) = U6(1,2)

U6(3,1) = U6(1,3)

U6(3,2) = U6(2,3)

U7(1,1) = SIGMA

U7(1,2) = −RHO

U7(1,3) = −TAU

U7(2,2) = THETA

U7(2,3) = RHO

U7(3,3) = SIGMA

U7(2,1) = U7(1,2)

U7(3,1) = U7(1,3)

U7(3,2) = U7(2,3)

U8(1,1) = SIGMA

U8(1,2) = RHO

U8(1,3) = −TAU

U8(2,2) = THETA

U8(2,3) = −RHO

U8(3,3) = SIGMA

U8(2,1) = U8(1,2)

U8(3,1) = U8(1,3)

U8(3,2) = U8(2,3)

U9(1,1) = SIGMA

U9(1,2) = TAU

U9(1,3) = RHO

U9(2,2) = SIGMA

U9(2,3) = RHO

U9(3,3) = THETA

U9(2,1) = U9(1,2)

U9(3,1) = U9(1,3)

U9(3,2) = U9(2,3)

U10(1,1) = SIGMA

U10(1,2) = TAU

U10(1,3) = −RHO

U10(2,2) = SIGMA

U10(2,3) = −RHO

U10(3,3) = THETA

U10(2,1) = U10(1,2)

U10(3,1) = U10(1,3)

U10(3,2) = U10(2,3)

U11(1,1) = SIGMA

U11(1,2) = −TAU

U11(1,3) = RHO

U11(2,2) = SIGMA

U11(2,3) = −RHO

U11(3,3) = THETA

U11(2,1) = U11(1,2)

U11(3,1) = U11(1,3)

U11(3,2) = U11(2,3)

U12(1,1) = SIGMA

U12(1,2) = −TAU

```
      U12(1,3) = -RHO
      U12(2,2) = SIGMA
      U12(2,3) = RHO
      U12(3,3) = THETA
      U12(2,1) = U12(1,2)
      U12(3,1) = U12(1,3)
      U12(3,2) = U12(2,3)

C     PAIR 1     (Example using variant 1 and variant 3)

C     REPEAT FOR ALL OTHER VARIANT COMBINATIONS (Appendix C)

      WRITE(20,*)'---------------------------- PAIR 1'
C
C       SELECT THE MATRICES UA AND UB
C
      DO 10 I=1,3
      DO 10 J=1,3
       UA(I,J) = U1(I,J)
       UB(I,J) = U3(I,J)
10    CONTINUE

C-------------------------------------------------
      AKAPPA1 = 1.D0
      AKAPPA2 = 1.D0
      CALL ZEROV(NVEC,3)
      CALL ZEROV(AVEC,3)
      CALL ZEROV(MVEC1,3)
      CALL ZEROV(BVEC1,3)
      CALL ZEROV(MVEC2,3)
```

```
      CALL ZEROV(BVEC2,3)

      CALL COMPUTE(UA,UB,AKAPPA1,AKAPPA2,NVEC,AVEC,
     +            ROOT1,ROOT2,MVEC1,BVEC1,MVEC2,BVEC2)

C-----------------------------------------------------
      AKAPPA1 = 1.D0
      AKAPPA2 = -1.D0
      CALL ZEROV(NVEC,3)
      CALL ZEROV(AVEC,3)
      CALL ZEROV(MVEC1,3)
      CALL ZEROV(BVEC1,3)
      CALL ZEROV(MVEC2,3)
      CALL ZEROV(BVEC2,3)

      CALL COMPUTE(UA,UB,AKAPPA1,AKAPPA2,NVEC,AVEC,
     +            ROOT1,ROOT2,MVEC1,BVEC1,MVEC2,BVEC2)

C-----------------------------------------------------
      AKAPPA1 = -1.D0
      AKAPPA2 = 1.D0
      CALL ZEROV(NVEC,3)
      CALL ZEROV(AVEC,3)
      CALL ZEROV(MVEC1,3)
      CALL ZEROV(BVEC1,3)
      CALL ZEROV(MVEC2,3)
      CALL ZEROV(BVEC2,3)


      CALL COMPUTE(UA,UB,AKAPPA1,AKAPPA2,NVEC,AVEC,
```

```
     +           ROOT1,ROOT2,MVEC1,BVEC1,MVEC2,BVEC2)

C-------------------------------------------------
      AKAPPA1 = -1.D0
      AKAPPA2 = -1.D0
      CALL ZEROV(NVEC,3)
      CALL ZEROV(AVEC,3)
      CALL ZEROV(MVEC1,3)
      CALL ZEROV(BVEC1,3)
      CALL ZEROV(MVEC2,3)
      CALL ZEROV(BVEC2,3)
      CALL ZEROV(SVEC1,3)
      CALL ZEROV(SVEC2,3)

      CALL COMPUTE(UA,UB,AKAPPA1,AKAPPA2,NVEC,AVEC,
     +           ROOT1,ROOT2,MVEC1,BVEC1,MVEC2,BVEC2)
C-------------------------------------------------
      STOP
      END
C-------------------------------------------------
      SUBROUTINE COMPUTE(UA,UB,AKAPPA1,AKAPPA2,NVEC,AVEC,
     +                ROOT1,ROOT2,MVEC1,BVEC1,MVEC2,BVEC2)
      IMPLICIT REAL*8(A-H,O-Z)

      REAL*8 UA(3,3),UB(3,3),RAB(3,3),RH(3,3),
     +      AVEC(3),NVEC(3),
     +      APRIME(3),NPRIME(3),E1(3),E2(3),E3(3),
     +      UAINV(3,3),C(3,3),C0(3,3),AUX1(3,3),AUX2(3,3),
     +      EIGVAL(3),EIGVEC(3,3),AIDEN(3,3),NTILDE(3),
     +      ATILDE(3),CLAMBDA1(3,3),CLAMBDA2(3,3),
```

```
     +      BVEC1(3),MVEC1(3),BVEC2(3),MVEC2(3)
C
C   CONSTRUCT THE MATRIX C
C

      CALL MPROD(UB,UB,AUX1)
      CALL M3INV(UA,UAINV)
      CALL MPROD(AUX1,UAINV,AUX2)
      CALL MPROD(UAINV,AUX2,C)
C
C   CALCULATE THE EIGENVALUES AND EIGENVECTORS OF C
C
      CALL SPECTRAL(C,EIGVAL,EIGVEC)

C
C         NOTE THAT SPECTRAL CALCULATES THE EIGENVALUES IN
C         DESCENDING ORDER. REORDER THE EIGENVALUES AND EIGENVECTORS
C
      ALAMBDA1 = EIGVAL(3)
      ALAMBDA2 = EIGVAL(2)
      ALAMBDA3 = EIGVAL(1)

      DO 20 I = 1,3
       E1(I) = EIGVEC(I,3)
       E2(I) = EIGVEC(I,2)
       E3(I) = EIGVEC(I,1)
20    CONTINUE

      CALL ZEROV(NPRIME,3)
      CALL ZEROV(APRIME,3)
```

```
      DO 30 I=1,3
        NPRIME(I) =
     +  ((DSQRT(ALAMBDA3)-DSQRT(ALAMBDA1))/DSQRT(ALAMBDA3-ALAMBDA1))
     +  * ( - DSQRT(1.D0 - ALAMBDA1)*E1(I)+
     +  AKAPPA1*DSQRT(ALAMBDA3 - 1.D0)*E3(I) )
30    CONTINUE

      CALL DOTPV(NPRIME,NPRIME,RHO)
      RHO = DSQRT(RHO)
      RHOINV = 1.D0/RHO

      DO 40 I=1,3
        NPRIME(I) = RHOINV*NPRIME(I)
40    CONTINUE

      DO 50 I=1,3
       APRIME(I) = RHO*(
     + DSQRT(ALAMBDA3*(1.D0-ALAMBDA1)/(ALAMBDA3-ALAMBDA1))*E1(I)+
     + AKAPPA1*
     + DSQRT(ALAMBDA1*(ALAMBDA3-1.D0)/(ALAMBDA3-ALAMBDA1))*E3(I))
50    CONTINUE

      DO 60 I=1,3
       AVEC(I)    = APRIME(I)
60    CONTINUE

      DO 70 I=1,3
      DO 70 J=1,3
       NVEC(I) = NVEC(I) + UA(I,J)*NPRIME(J)
```

```
70    CONTINUE

      CALL DOTPV(NVEC,NVEC,AMAG)
      AMAG = DSQRT(AMAG)
C
C   NORMALIZE SO THAT NVEC HAS UNIT NORM
C

      DO 80 I=1,3
        NVEC(I) = NVEC(I)/AMAG
        AVEC(I) = AVEC(I)*AMAG
80    CONTINUE

C
C   CONTRUCT THE FUNCTION G(LAMBDA), EQUATION 5.56 OF BALL AND JAMES
C
      CALL ZEROM(AUX1)
      CALL ONEM(AIDEN)
      CALL MPROD(UA,UA,AUX1)
      CALL MDET(AUX1,DETUA2)
      DO 90 I=1,3
      DO 90 J=1,3
       AUX2(I,J) = AUX1(I,J)-AIDEN(I,J)
90    CONTINUE
      CALL MDET(AUX2,CQUAD)

      CALL ZEROV(NTILDE,3)
      CALL ZEROV(ATILDE,3)
      DO 100 I=1,3
      DO 100 J=1,3
```

```
      NTILDE(I) = NTILDE(I) + UAINV(I,J)*NVEC(J)
      ATILDE(I) = ATILDE(I) + UAINV(I,J)*AVEC(J)
100   CONTINUE

      CALL DOTPV(NTILDE,NTILDE,AMAGNTILDE2)
      CALL DOTPV(ATILDE,ATILDE,AMAGATILDE2)
      CALL DOTPV(ATILDE,ATILDE,SMAG1)
      CALL DOTPV(AVEC,AVEC,AMAGAVEC2)

       DO 236 I=1,3
         ATILDE(I) = ATILDE(I)/DSQRT(SMAG1)
236    CONTINUE

      AQUAD = AMAGAVEC2 - DETUA2*AMAGATILDE2*AMAGNTILDE2
      BQUAD = - AQUAD

      DISCRIM = DSQRT(BQUAD*BQUAD - 4.DO*AQUAD*CQUAD)
      ROOT1   = (- BQUAD + DISCRIM)/(2.DO*AQUAD)
      ROOT2   = (- BQUAD - DISCRIM)/(2.DO*AQUAD)

C
C   CONSTRUCT THE MATRICES CLAMBDA1 AND CLAMBDA2
C
      CALL ZEROM(AUX1)
      CALL ZEROM(AUX2)
      DO 110 I=1,3
      DO 110 J=1,3
       AUX1(I,J) = UA(I,J) + ROOT1*NVEC(I)*AVEC(J)
       AUX2(I,J) = UA(I,J) + ROOT1*AVEC(I)*NVEC(J)
110   CONTINUE
```

```
      CALL MPROD(AUX1,AUX2,CLAMBDA1)

      CALL ZEROM(AUX1)
      CALL ZEROM(AUX2)
      DO 120 I=1,3
      DO 120 J=1,3
       AUX1(I,J) = UA(I,J) + ROOT2*NVEC(I)*AVEC(J)
       AUX2(I,J) = UA(I,J) + ROOT2*AVEC(I)*NVEC(J)
120    CONTINUE
      CALL MPROD(AUX1,AUX2,CLAMBDA2)

C
C   CALCULATE THE EIGENVALUES AND EIGENVECTORS OF CLAMBDA1
C
      CALL SPECTRAL(CLAMBDA1,EIGVAL,EIGVEC)

C         NOTE THAT SPECTRAL CALCULATES THE EIGENVALUES IN
C         DESCENDING ORDER. REORDER THE EIGENVALUES AND EIGENVECTORS
C
      ALAMBDA1 = EIGVAL(3)
      ALAMBDA2 = EIGVAL(2)
      ALAMBDA3 = EIGVAL(1)

      DO 130 I = 1,3
       E1(I) = EIGVEC(I,3)
       E2(I) = EIGVEC(I,2)
       E3(I) = EIGVEC(I,1)
130    CONTINUE

      CALL ZEROV(NPRIME,3)
```

```
      CALL ZEROV(APRIME,3)

      DO 140 I=1,3
        NPRIME(I) =
     +  ((DSQRT(ALAMBDA3)-DSQRT(ALAMBDA1))/DSQRT(ALAMBDA3-ALAMBDA1))
     +  *( - DSQRT(1.D0 - ALAMBDA1)*E1(I)+
     +  AKAPPA2*DSQRT(ALAMBDA3 - 1.D0)*E3(I) )
140    CONTINUE

      CALL DOTPV(NPRIME,NPRIME,RHO)
      RHO = DSQRT(RHO)
      RHOINV = 1.D0/RHO

C     WRITE(20,*)' RHO = ',RHO,' RHOINV = ',RHOINV

      DO 150 I=1,3
        NPRIME(I) = RHOINV*NPRIME(I)
150   CONTINUE


    DO 160 I=1,3
           APRIME(I) = RHO*(
     +     DSQRT(ALAMBDA3*(1.D0-ALAMBDA1)/(ALAMBDA3-ALAMBDA1))*E1(I)+
     +     AKAPPA2*
     +     DSQRT(ALAMBDA1*(ALAMBDA3-1.D0)/(ALAMBDA3-ALAMBDA1))*E3(I)
     +     )
160 CONTINUE


    DO 170 I=1,3
```

```
      BVEC1(I)    = APRIME(I)
      MVEC1(I)    = NPRIME(I)
170    CONTINUE

C
C     CALCULATE MVEC2 AND BVEC2 CORRESPONDING TO CLAMBDA2 AND ROOT2
C
C     CALCULATE THE EIGENVALUES AND EIGENVECTORS OF CLAMBDA1
C
      CALL SPECTRAL(CLAMBDA2,EIGVAL,EIGVEC)

C
C         NOTE THAT SPECTRAL CALCULATES THE EIGENVALUES IN
C         DESCENDING ORDER. REORDER THE EIGENVALUES AND EIGENVECTORS
C
      ALAMBDA1 = EIGVAL(3)
      ALAMBDA2 = EIGVAL(2)
      ALAMBDA3 = EIGVAL(1)

      DO 180 I = 1,3
       E1(I) = EIGVEC(I,3)
       E2(I) = EIGVEC(I,2)
       E3(I) = EIGVEC(I,1)
180    CONTINUE

      CALL ZEROV(NPRIME,3)
      CALL ZEROV(APRIME,3)

      DO 190 I=1,3
        NPRIME(I) =
```

```
     +  ((DSQRT(ALAMBDA3)-DSQRT(ALAMBDA1))/DSQRT(ALAMBDA3-ALAMBDA1))
     +  * ( - DSQRT(1.D0 - ALAMBDA1)*E1(I)+
     +  AKAPPA2*DSQRT(ALAMBDA3 - 1.D0)*E3(I) )
190    CONTINUE

       CALL DOTPV(NPRIME,NPRIME,RHO)
       RHO = DSQRT(RHO)
       RHOINV = 1.D0/RHO

C      WRITE(20,*)' RHO = ',RHO,' RHOINV = ',RHOINV

       DO 200 I=1,3
         NPRIME(I) = RHOINV*NPRIME(I)
200    CONTINUE

       DO 210 I=1,3
          APRIME(I) = RHO*(
     +    DSQRT(ALAMBDA3*(1.D0-ALAMBDA1)/(ALAMBDA3-ALAMBDA1))*E1(I)+
     +    AKAPPA2*
     +    DSQRT(ALAMBDA1*(ALAMBDA3-1.D0)/(ALAMBDA3-ALAMBDA1))*E3(I))
210    CONTINUE

       DO 220 I=1,3
        BVEC2(I)    = APRIME(I)
        MVEC2(I)    = NPRIME(I)
220    CONTINUE

         WRITE(21,7)BVEC1(1),BVEC1(2),BVEC1(3),
     +  MVEC1(1),MVEC1(2),MVEC1(3)
```

```
      WRITE(21,7)BVEC2(1),BVEC2(2),BVEC2(3),
     + MVEC2(1),MVEC2(2),MVEC2(3)

    7  FORMAT(F7.4,4X,F7.4,4X,F7.4,4X,F7.4,4X,F7.4,4X,F7.4)

      RETURN
      END
C ***********************************************************************
C
C  THE FOLLOWING SUBROUTINES CALCULATE THE SPECTRAL
C  DECOMPOSITION OF A SYMMETRIC THREE BY THREE MATRIX
C
C ***********************************************************************
      SUBROUTINE SPECTRAL(A,D,V)

C  THIS SUBROUTINE CALCULATES THE EIGENVALUES AND EIGENVECTORS OF
C  A SYMMETRIC 3 BY 3 MATRIX [A].
C
C  THE OUTPUT CONSISTS OF A VECTOR D CONTAINING THE THREE
C  EIGENVALUES IN ASCENDING ORDER, AND
C  A MATRIX [V] WHOSE COLUMNS CONTAIN THE CORRESPONDING
C  EIGENVECTORS.
C ---------------------------------------------------------------------
      IMPLICIT REAL*8 (A-H,O-Z)
      PARAMETER(NP=3)
      DIMENSION D(NP),V(NP,NP)
      DIMENSION A(3,3),E(NP,NP)

      DO 2 I = 1,3
      DO 1 J= 1,3
```

```
        E(I,J) = A(I,J)
 1    CONTINUE
 2    CONTINUE

      CALL JACOBI(E,3,NP,D,V,NROT)
      CALL EIGSRT(D,V,3,NP)

      RETURN
      END
C *********************************************************************
      SUBROUTINE JACOBI(A,N,NP,D,V,NROT)

C
C   COMPUTES ALL EIGENVALUES AND EIGENVECTORS OF A REAL SYMMETRIC
C   MATRIX [A], WHICH IS OF SIZE N BY N, STORED IN A PHYSICAL
C   NP BY BP ARRAY. ON OUTPUT, ELEMENTS OF [A] ABOVE THE DIAGONAL
C   ARE DESTROYED, BUT THE DIAGONAL AND SUB-DIAGONAL ARE UNCHANGED
C   AND GIVE FULL INFORMATION ABOUT THE ORIGINAL SYMMETRIC MATRIX.
C   VECTOR D RETURNS THE EIGENVALUES OF [A] IN ITS FIRST N ELEMENTS.
C   [V] IS A MATRIX WITH THE SAME LOGICAL AND PHYSICAL DIMENSIONS AS
C   [A] WHOSE COLUMNS CONTAIN, ON OUTPUT, THE NORMALIZED
C   EIGENVECTORSOF [A]. NROT RETURNS THE NUMBER OF JACOBI ROTATIONS
C   WHICH WERE REQUIRED.
C
C   THIS SUBROUTINE IS TAKEN FROM "NUMERICAL RECIPES", PAGE 346.
C ---------------------------------------------------------------------
      IMPLICIT REAL*8 (A-H,O-Z)
      PARAMETER (NMAX =100)
      DIMENSION A(NP,NP),D(NP),V(NP,NP),B(NMAX),Z(NMAX)
```

```
C
C    INITIALIZE [V] TO THE IDENTITY MATRIX
C

     DO 12 IP = 1,N
     DO 11 IQ = 1,N
        V(IP,IQ) = 0.D0
11   CONTINUE
        V(IP,IP) = 1.D0
12   CONTINUE

C    INITIALIZE B AND D TO THE DIAGONAL OF [A], AND Z TO ZERO.
C    THE C   VECTOR Z WILL ACCUMULATE TERMS OF THE FORM T*APQ AS  IN
C    EQUATION (11.1.14)

     DO 13 IP = 1,N
      B(IP) = A(IP,IP)
      D(IP) = B(IP)
      Z(IP) = 0.D0
13   CONTINUE

     NROT = 0

     DO 24 I = 1,99

C
C      SUM OFF-DIAGONAL ELEMENTS
C
     SM = 0.D0
     DO 15 IP = 1, N-1
```

```
      DO 14 IQ = IP + 1, N

          SM = SM + DABS ( A(IP,IQ ))

 14   CONTINUE
 15   CONTINUE
C
C       IF SUM = 0., THEN RETURN. THIS IS THE NORMAL RETURN
C       WHICH RELIES ON QUADRATIC CONVERGENCE TO MACHINE
C       UNDERFLOW.
C
      IF( SM .EQ. 0.D0) RETURN
C       IF( SM .LT. 1.0D-15) RETURN
C       IN THE FIRST THREE
C       SWEEPS CARRY OUT THE PQ ROTATION  ONLY IF
C       |APQ| > TRESH, WHERE TRESH IS SOME THRESHOLD VALUE,
C       SEE EQUATION (11.1.25).  THEREAFTER TRESH = 0.
      IF( I .LT. 4) THEN
         TRESH = 0.2D0*SM/N**2
      ELSE
         TRESH = 0.D0
      END IF

      DO 22 IP = 1, N-1
      DO 21 IQ = IP+1,N
       G = 100.D0*DABS(A(IP,IQ))
C
C             AFTER FOUR SWEEPS, SKIP THE ROTATION IF
C             THE
C             OFF-DIAGONAL ELEMENT IS SMALL.
```

```
C

     IF((I .GT. 4) .AND. ( DABS(D(IP))+G  .EQ.  DABS( D(IP)) )
    +   .AND. ( DABS(D(IQ))+G  .EQ.  DABS( D(IQ)) ) )THEN

           A(IP,IQ) = 0.D0

       ELSE IF( DABS(A(IP,IQ)) .GT. TRESH) THEN

           H = D(IQ) - D(IP)

       IF(DABS(H)+G .EQ. DABS(H)) THEN
C
C            T= 1./(2.*THETA), EQUATION (11.1.10)
C
        T =A(IP,IQ)/H

     ELSE

         THETA = 0.5D0*H/A(IP,IQ)
        T =1.D0/(DABS(THETA)+DSQRT(1.D0+THETA**2))
     IF(THETA .LT. 0.D0) T = -T
     END IF
        C = 1.D0/DSQRT(1.D0 + T**2)
        S = T*C
        TAU = S/(1.D0 + C)
        H = T*A(IP,IQ)
        Z(IP) = Z(IP) - H
        Z(IQ) = Z(IQ) + H
        D(IP) = D(IP) - H
```

```
        D(IQ) = D(IQ) + H
        A(IP,IQ) = 0.D0
C
C             CASE OF ROTATIONS 1<= J < P
C
      DO 16 J = 1, IP-1
       G = A(J,IP)
       H = A(J,IQ)
       A(J,IP) = G - S*(H + G*TAU)
       A(J,IQ) = H + S*(G - H*TAU)
16    CONTINUE
C
C             CASE OF ROTATIONS P < J < Q
C
      DO 17 J = IP+1, IQ-1
      G = A(IP,J)
      H = A(J,IQ)
      A(IP,J) = G - S*(H + G*TAU)
      A(J,IQ) = H + S*(G - H*TAU)
17    CONTINUE
C
C             CASE OF ROTATIONS Q < J <= N
C
      DO 18 J = IQ+1, N
      G = A(IP,J)
      H = A(IQ,J)
      A(IP,J) = G - S*(H + G*TAU)
      A(IQ,J) = H + S*(G - H*TAU)
18    CONTINUE
```

```
      DO 19 J = 1,N
      G = V(J,IP)
      H = V(J,IQ)
      V(J,IP) = G - S*(H + G*TAU)
      V(J,IQ) = H + S*(G - H*TAU)
19    CONTINUE
        NROT = NROT + 1
      END IF
21    CONTINUE
22    CONTINUE

C       UPDATE D WITH THE SUM OF T*APQ, AND REINITIALIZE Z C

      DO 23 IP = 1, N
          B(IP) = B(IP) + Z(IP)
          D(IP) = B(IP)
          Z(IP) = 0.D0
23    CONTINUE

24    CONTINUE
C
C       IF THE ALGORITHM HAS REACHED THIS STAGE, THEN
C       THERE ARE TOO MANY SWEEPS, PRINT A DIAGNOSTIC
C       AND EXIT
C
      WRITE(6,'(/1X,A/)')'FROM JACOBI: 99 ITERS. SHOULD NEVER HAPPEN'
      STOP
      RETURN
      END
C *****************************************************************
```

```
      SUBROUTINE EIGSRT(D,V,N,NP)

C     GIVEN THE EIGENVALUES D AND EIGENVECTORS [V] AS OUTPUT FROM
C     JACOBI, THIS ROUTINE SORTS THE EIGENVALUES INTO ASCENDING ORDER,
C     AND REARRANGES THE COLUMNS OF [V] ACCORDINGLY.
C
C   THIS SUBROUTINE IS TAKEN FROM "NUMERICAL RECIPES", P. 348.
C ----------------------------------------------------------------------
      IMPLICIT REAL*8 (A-H,O-Z)
      DIMENSION D(NP),V(NP,NP)

      DO 13 I = 1,N-1
        K = I
        P = D(I)
      DO 11 J = I+1,N
         IF(D(J) .GE. P) THEN
           K = J
           P = D(J)
         END IF
11    CONTINUE
        IF(K .NE. I) THEN
          D(K) = D(I)
          D(I) = P
          DO 12 J = 1,N
              P = V(J,I)
              V(J,I) = V(J,K)
              V(J,K) = P
12    CONTINUE
      END IF
13    CONTINUE
```

```
      RETURN
      END
C ***********************************************************************
C
C   THE FOLLOWING SUBROUTINES ARE UTILITY ROUTINES
C
C ***********************************************************************
      SUBROUTINE ZEROV(V,SIZE)
C
C   THIS SUBROUTINE STORES THE ZERO VECTOR IN A VECTOR V
C -----------------------------------------------------------------------
      IMPLICIT REAL*8 (A-H,O-Z)
      INTEGER SIZE
      REAL*8 V(SIZE)

      DO 1 I = 1,SIZE
            V(I) = 0.D0
1     CONTINUE

      RETURN
      END
C ***********************************************************************
        SUBROUTINE ZEROM(A)
C
C   THIS SUBROUTINE SETS ALL ENTRIES OF A 3 BY 3 MATRIX TO 0.D0
C -----------------------------------------------------------------------
        REAL*8 A(3,3)

      DO 1 I=1,3
      DO 1 J=1,3
```

```
            A(I,J) = 0.D0
1     CONTINUE

      RETURN
      END
C ***********************************************************************
      SUBROUTINE ONEM(A)
C
C   THIS SUBROUTINE STORES THE IDENTITY MATRIX IN THE
C   3 BY 3 MATRIX [A]
C -----------------------------------------------------------------------
        REAL*8 A(3,3)

      DO 1 I = 1,3
      DO 1 J = 1,3
         IF (I .EQ. J) THEN
            A(I,J)     = 1.0D0
         ELSE
            A(I,J)     = 0.0D0
         END IF
1     CONTINUE

      RETURN
      END
C ***********************************************************************
      SUBROUTINE MTRANS(A,ATRANS)

C   THIS SUBROUTINE CALCULATES THE TRANSPOSE OF AN 3 BY 3
C   MATRIX [A], AND PLACES THE RESULT IN ATRANS.
C -----------------------------------------------------------------------
```

```
C   VARIABLES
C
      REAL*8  A(3,3), ATRANS(3,3)
C ---------------------------------------------------------------------
C   COMPUTATION
C
      DO 1 I = 1, 3
      DO 1 J = 1, 3
        ATRANS(I,J) = A(J,I)
1     CONTINUE
      RETURN
      END
C *********************************************************************
      SUBROUTINE MPROD(A,B,C)

C   THIS SUBROUTINE MULTIPLIES TWO 3 BY 3 MATRICES [A] AND [B],
C   AND PLACE THEIR PRODUCT IN MATRIX [C].
C ---------------------------------------------------------------------
C   VARIABLES
C
      REAL*8 A(3,3), B(3,3), C(3,3)
C ---------------------------------------------------------------------
C   COMPUTATION
C
      DO 2 I = 1, 3
      DO 2 J = 1, 3
        C(I,J) = 0.D0
      DO 1 K = 1, 3
           C(I,J) = C(I,J) + A(I,K) * B(K,J)
1     CONTINUE
```

```
2     CONTINUE
      RETURN
      END
C ***********************************************************************
      SUBROUTINE MPRODVEC(D,E,F)

C   THIS SUBROUTINE MULTIPLIES A 3 BY 3 MATRIX [E] WITH VECTOR [F],
C   AND PLACE THEIR PRODUCT IN VECTOR [D].
C -----------------------------------------------------------------------
C   VARIABLES
C
      REAL*8 D(3), E(3,3), F(3)
C -----------------------------------------------------------------------
C   COMPUTATION
C
      DO 21 I = 1, 3
        D(I) = 0.D0
      DO 11 J = 1, 3
           D(I) = D(I) + E(I,J) * F(J)
11    CONTINUE
21    CONTINUE
      RETURN
      END
C***********************************************************************
      SUBROUTINE  DOTPM(A,B,C)
C
C   THIS SUBROUTINE CALCULATES THE SCALAR PRODUCT OF TWO
C   3 BY 3 MATRICES [A] AND [B] AND STORES THE RESULT IN THE
C   SCALAR C.
C -----------------------------------------------------------------------
```

```
C  VARIABLES
C
      REAL*8 A(3,3),B(3,3),C

      C= 0.DO
      DO 1 I = 1,3
      DO 1 J = 1,3
        C = C + A(I,J)*B(I,J)
1     CONTINUE

      RETURN
      END
C ***************************************************************************
      SUBROUTINE  DOTPV(A,B,C)
C
C  THIS SUBROUTINE CALCULATES THE SCALAR PRODUCT OF TWO
C   3-VECTORS [A] AND [B] AND STORES THE RESULT IN THE
C  SCALAR C.
C ---------------------------------------------------------------------
C  VARIABLES
C
      REAL*8 A(3),B(3),C

      C= 0.DO
      DO 1 I = 1,3
        C = C + A(I)*B(I)
1     CONTINUE

      RETURN
      END
```

```
C ***********************************************************************
      SUBROUTINE MDET(A,DET)

C   THIS SUBROUTINE CALCULATES THE DETERMINANT
C   OF A 3 BY 3 MATRIX [A].
C -----------------------------------------------------------------------
C   VARIABLES
C
      REAL*8  A(3,3), DET
C -----------------------------------------------------------------------
C   COMPUTATION
C
      DET =     A(1,1)*A(2,2)*A(3,3)
     +  + A(1,2)*A(2,3)*A(3,1)
     +  + A(1,3)*A(2,1)*A(3,2)
     +  - A(3,1)*A(2,2)*A(1,3)
     +  - A(3,2)*A(2,3)*A(1,1)
     +  - A(3,3)*A(2,1)*A(1,2)

      RETURN
      END
C ***********************************************************************
      SUBROUTINE M3INV(A,AINV)

C   THIS SUBROUTINE CALCULATES THE THE INVERSE OF A 3 BY 3 MATRIX
C    [A] AND PLACES THE RESULT IN [AINV].
C   IF DET(A) IS ZERO, THE CALCULATION
C   IS TERMINATED AND A DIAGNOSTIC STATEMENT IS PRINTED.
C -----------------------------------------------------------------------
C   VARIABLES
```

```
C

      REAL*8  A(3,3), AINV(3,3), DET, ACOFAC(3,3), AADJ(3,3)

C       A(3,3)  -- THE MATRIX WHOSE INVERSE IS DESIRED.
C       DET -- THE COMPUTED DETERMINANT OF [A].
C       ACOFAC(3,3) -- THE MATRIX OF COFACTORS OF A(I,J).
C       THE SIGNED MINOR (-1)**(I+J)*M\{IJ\}
C       IS CALLED THE COFACTOR OF A(I,J).
C       AADJ(3,3)   -- THE ADJOINT OF [A]. IT IS THE MATRIX
C       OBTAINED BY REPLACING EACH ELEMENT OF
C       [A] BY ITS COFACTOR, AND THEN TAKING
C       TRANSPOSE OF THE RESULTING MATRIX.
C       AINV(3,3)   -- RETURNED AS INVERSE OF [A].
C       [AINV] = [AADJ]/DET. C
-----------------------------------------------------------------------

      CALL MDET(A,DET)

      IF ( DET .EQ. 0.D0 ) THEN
        WRITE(6,10)
        STOP
      END IF

      CALL MCOFAC(A,ACOFAC)
      CALL MTRANS(ACOFAC,AADJ)
      DO 1 I = 1,3
      DO 1 J = 1,3
        AINV(I,J) = AADJ(I,J)/DET
1     CONTINUE
```

```
C ------------------------------------------------------------------
C  FORMAT
C

   10 FORMAT(5X,'--ERROR IN M3INV--- THE MATRIX IS SINGULAR',/,
    +      10X,'PROGRAM TERMINATED')
C-------------------------------------------------------------------
     RETURN
     END
C ******************************************************************
     SUBROUTINE MCOFAC(A,ACOFAC)

C  THIS SUBROUTINE CALCULATES THE COFACTOR OF A 3 BY 3 MATRIX [A],
C  AND PLACES THE RESULT IN ACOFAC.
C ------------------------------------------------------------------
C  VARIABLES
C
     REAL*8  A(3,3), ACOFAC(3,3)
C ------------------------------------------------------------------
C  COMPUTATION
C
     ACOFAC(1,1) = A(2,2)*A(3,3) - A(3,2)*A(2,3)
     ACOFAC(1,2) = -(A(2,1)*A(3,3) - A(3,1)*A(2,3))
     ACOFAC(1,3) = A(2,1)*A(3,2) - A(3,1)*A(2,2)
     ACOFAC(2,1) = -(A(1,2)*A(3,3) - A(3,2)*A(1,3))
     ACOFAC(2,2) = A(1,1)*A(3,3) - A(3,1)*A(1,3)
     ACOFAC(2,3) = -(A(1,1)*A(3,2) - A(3,1)*A(1,2))
     ACOFAC(3,1) = A(1,2)*A(2,3)  - A(2,2)*A(1,3)
     ACOFAC(3,2) = -(A(1,1)*A(2,3) - A(2,1)*A(1,3))
```

```
      ACOFAC(3,3) = A(1,1)*A(2,2) - A(2,1)*A(1,2)

      RETURN
      END

C ***********************************************************************
        SUBROUTINE INVAR(A,IA,IIA,IIIA)
C
C   THIS  SUBROUTINE CALCULATES THE PRINCIPAL INVARIANTS
C   IA, IIA, IIIA OF    A  TENSOR [A].
C -----------------------------------------------------------------------
C       VARIABLES
C
        REAL*8 A(3,3), AD(3,3),AD2(3,3), DETA, IA,IIA,IIIA
C -----------------------------------------------------------------------
C       COMPUTATION
C
      DO 1 I=1,3
      DO 1 J=1,3
           AD(I,J) = A(I,J)
1     CONTINUE

      IA = AD(1,1) + AD(2,2) + AD(3,3)
C
C          CALCULATE THE SQUARE OF [AD]
C
      CALL MPROD(AD,AD,AD2)
C
      IIA =0.5D0 * ( IA*IA - ( AD2(1,1) + AD2(2,2) + AD2(3,3) ) )
C
```

```
      CALL  MDET(AD,DETA)

      IIIA = DETA

      RETURN
      END

C ***********************************************************************
      SUBROUTINE TRACEM(A,TRA)
C
C   THIS SUBROUTINE CALCULATES THE TRACE OF A 3 BY 3 MATRIX [A]
C   AND STORES THE RESULT IN THE SCALAR TRA
C -----------------------------------------------------------------------
C   VARIABLES
C
      REAL*8 A(3,3),TRA

      TRA = A(1,1) + A(2,2) + A(3,3)

      RETURN
      END
C ***********************************************************************
      SUBROUTINE DEVM(A,ADEV)
C
C   THIS SUBROUTINE CALCULATES THE DEVIATORIC PART OF A
C   3 BY 3 MATRIX [A]
C -----------------------------------------------------------------------
C   VARIABLES
C
      REAL*8 A(3,3),TRA,ADEV(3,3),IDEN(3,3)
```

```
      CALL TRACEM(A,TRA)
      CALL ONEM(IDEN)
      CALL ZEROM(ADEV)

      DO 1 I = 1,3
      DO 1 J = 1,3
        ADEV(I,J) = A(I,J) - (1.D0/3.D0)*TRA*IDEN(I,J)
1     CONTINUE

      RETURN
      END
C ***********************************************************************
      SUBROUTINE EQUIVS(S,SB)
C
C   THIS SUBROUTINE CALCULATES THE EQUIVALENT TENSILE STRESS SB
C   CORESSPONDING TO A 3 BY 3 STRESS MATRIX [S]
C -----------------------------------------------------------------------
C   VARIABLES
C
      REAL*8 S(3,3),SDEV(3,3),SDOTS,SB

      SB = 0.D0
      SDOTS = 0.D0

      CALL DEVM(S,SDEV)
      CALL DOTPM(SDEV,SDEV,SDOTS)
      SB = DSQRT(1.5D0* SDOTS)

      RETURN
```

```
      END
C*********************************************************************
      SUBROUTINE PRTMAT(A,M,N)
C*********************************************************************

      INTEGER M,N
      REAL*8 A(M,N)

      DO 10 K=1,M
      WRITE(23,'(2X,6F12.6,2X)') (A(K,L), L=1,N)
10    CONTINUE

      RETURN
      END

C*********************************************************************
      SUBROUTINE PRTVEC(A,M)
C*********************************************************************

      INTEGER M
      REAL*8 A(M)

      WRITE(20,'(2X,6F12.6,2X)') (A(K), K=1,M)

      RETURN
      END
C*********************************************************
        SUBROUTINE SKINEM(F,R,U,ITERERR)
C
C       THIS SUBROUTINE PERFORMS THE RIGHT POLAR DECOMPOSITION
```

```
C      [F]=[R][U] OF THE DEFORMATION GRADIENT [F] INTO
C      A ROTATION [R] AND THE RIGHT  STRETCH TENSOR [U].
C      IS ALSO CALCULATED.
C -------------------------------------------------------------------
C  VARIABLES
C
      IMPLICIT REAL*8 (A-H,O-Z)
      REAL*8 F(3,3),DETF,FTRANS(3,3),
     +   C(3,3), OMEGA(3),EIGVEC(3,3), EIGVECT(3,3),
     +   U(3,3),UINV(3,3),R(3,3),TEMP(3,3)

C -------------------------------------------------------------------
C  COMPUTATION
C


C
C      STORE THE IDENTITY MATRIX IN  [R], [U], AND [UINV]
C
      CALL ONEM(R)
      CALL ONEM(U)
      CALL ONEM(UINV)
C
C      STORE THE ZERO MATRIX IN [E]
C
      CALL ZEROM(E)


C
C      CHECK IF THE DETERMINANT OF [F] IS GREATER THAN ZERO.
C      IF NOT, THEN PRINT DIAGONOSTIC AND EXIT.
C
```

```
      CALL MDET(F,DETF)

      IF (DETF .LE. 0.D0) THEN
         ITERERR = 1
     RETURN
      END IF
C
C      CALCULATE THE RIGHT CAUCHY GREEN STRAIN TENSOR [C]
C
      CALL  MTRANS(F,FTRANS)
      CALL  MPROD(FTRANS,F,C)

C
C      CALCULATE THE EIGENVALUES AND EIGENVECTORS OF  [C]
C

     CALL SPECTRAL(C,OMEGA,EIGVEC)

C
C      CALCULATE THE PRINCIPAL VALUES OF [U] AND [E]
C

     U(1,1) = DSQRT(OMEGA(1))
     U(2,2) = DSQRT(OMEGA(2))
     U(3,3) = DSQRT(OMEGA(3))

C
C      CALCULATE THE COMPLETE TENSORS [U] AND [E]
C
```

```
      CALL MTRANS(EIGVEC,EIGVECT)
      CALL MPROD(EIGVEC,U,TEMP)
      CALL MPROD(TEMP,EIGVECT,U)



C
C       CALCULATE [UINV]
C

      CALL  M3INV(U,UINV)

C       CALCULATE [R]

      CALL MPROD(F,UINV,R)
C ---------------------------------------------------------------------
C   FORMATS
C ---------------------------------------------------------------------
      RETURN
      END
```

Appendix E

Time-integration procedure : Isotropic-based constitutive model

In this appendix we summarize the time-integration procedure that we have used for our rate-independent isotropic-based constitutive model. With t denoting the current time, Δt is an infinitesimal time increment, and $\tau = t + \Delta t$, the algorithm is as follows:
Given: (1) $\{\mathbf{F}(t), \mathbf{F}(\tau), \theta(t), \theta(\tau)\}$; (2) $\{\mathbf{T}(t), \mathbf{F}^p(t)\}$; (3) the accumulated martensite volume fractions $\xi(t)$.
Calculate: (a)$\{\mathbf{T}(\tau), \mathbf{F}^p(\tau)\}$, (b) the accumulated martensite volume fractions $\xi(\tau)$, and (c) the inelastic work increment $\Delta\omega^p(\tau)$ and march forward in time.

The steps used in the calculation procedure are:

Step 1. Calculate the trial elastic strain $\mathbf{E}^e(\tau)^{trial}$:

$$\mathbf{F}^e(\tau)^{trial} = \mathbf{F}(\tau)(\mathbf{F}^p(t))^{-1},$$

$$\mathbf{C}^e(\tau)^{trial} = (\mathbf{F}^e(\tau)^{trial})^{\mathsf{T}}\mathbf{F}^e(\tau)^{trial},$$

$$\mathbf{E}^e(\tau)^{trial} = (1/2)\left\{\mathbf{C}^e(\tau)^{trial} - \mathbf{1}\right\}.$$

Step 2. Calculate the trial stress $\mathbf{T}^e(\tau)^{trial}$:

$$\mathbf{T}^e(\tau)^{trial} = \boldsymbol{\mathcal{C}}(t)[\mathbf{E}^e(\tau)^{trial} - \alpha(t)(\theta(\tau) - \theta_0)\mathbf{1}].$$

Step 3. Calculate the phase transformation flow direction $\mathbf{N}^p$ and the trial resolved force $\bar{\sigma}(\tau)^{trial}$:

$$\mathbf{N}^p = \sqrt{(3/2)}\,\epsilon_T \left(\frac{\mathbf{T}_0^e(t)}{|\mathbf{T}_0^e(t)|} \right) \quad \text{if} \quad \xi(t) = 0,$$

$$\mathbf{N}^p = \sqrt{(3/2)}\,\epsilon_T \left(\frac{\mathbf{T}_0^e(t_c)}{|\mathbf{T}_0^e(t_c)|} \right) \quad \text{if} \quad 0 < \xi(t) \leq 1.$$

The trial resolved force is given by

$$\bar{\sigma}(\tau)^{trial} = \mathbf{T}^e(\tau)^{trial} \cdot \mathbf{N}^p.$$

Step 4. Calculate the trial driving force for phase transformation $f(\tau)^{trial}$:

$$f(\tau)^{trial} = \bar{\sigma}(\tau)^{trial} - (\lambda_T/\theta_T)(\theta(\tau) - \theta_T).$$

Step 5. Calculate

$$\mathbf{F}^p(\tau) = \{\mathbf{1} + \Delta\xi\,\mathbf{N}^p\}\,\mathbf{F}^p(t). \tag{E.1}$$

During phase transformation, the consistency conditions must be satisfied :

$$f(\tau) \mp f_c = 0, \tag{E.2}$$

where the $-$ sign holds during forward transformation and the $+$ sign holds during reverse transformation, and where

$$f(\tau) = \bar{\sigma}(\tau) - (\lambda_T/\theta_T)(\theta(\tau) - \theta_T). \tag{E.3}$$

Retaining the terms of the first order in $\Delta\xi$, it is straightforward to show that

$$\bar{\sigma}(\tau) = \bar{\sigma}(\tau)^{trial} - 2\mu(t)\Delta\xi\,\mathrm{sym}(\mathbf{C}^e(\tau)^{trial}\mathbf{N}^p) \cdot \mathbf{N}^p. \tag{E.4}$$

Using (E.3) and (E.4) in the consistency conditions (E.2) we can calculate $\Delta\xi$.

Step 6. Determine the increment of the martensite volume fraction $\Delta\xi$:

If $f(\tau)^{trial} - f_c > 0$ and $0 \leq \xi(t) < 1$ then for the forward austenite to martensite transformation

$$\Delta\xi = \frac{f(\tau)^{trial} - f_c}{2\mu(t)\,\mathrm{sym}(\mathbf{C}^e(\tau)^{trial}\mathbf{N}^p) \cdot \mathbf{N}^p}.$$

If $f(\tau)^{trial} + f_c < 0$, and $0 < \xi(t) \leq 1$ then for the reverse martensite to austenite transformation

$$\Delta\xi = \frac{f(\tau)^{trial} + f_c}{2\mu(t)\,\mathrm{sym}(\mathbf{C}^e(\tau)^{trial}\mathbf{N}^p)\cdot\mathbf{N}^p}.$$

Or else there is no phase transformation

$$\Delta\xi = 0.$$

Step 7. Update the inelastic deformation gradient $\mathbf{F}^p(\tau)$:

$$\mathbf{F}^p(\tau) = \{\mathbf{1} + \Delta\xi\,\mathbf{N}^p\}\,\mathbf{F}^p(t).$$

Step 8. Update the total martensite volume fraction $\xi(\tau)$:

$$\xi(\tau) = \xi(t) + \Delta\xi.$$

If $\xi(\tau) > 1$, then set $\xi(\tau) = 1$ and if $\xi(\tau) < 0$, then set $\xi(\tau) = 0$.

Step 9. Update the effective elastic modulus $\boldsymbol{\mathcal{C}}(\tau)$ and the coefficient of thermal expansion $\alpha(\tau)$:

$$\boldsymbol{\mathcal{C}}(\tau) = \{1 - \xi(\tau)\}\,\boldsymbol{\mathcal{C}}^a + \xi(\tau)\boldsymbol{\mathcal{C}}^m,$$

$$\alpha(\tau) = \{1 - \xi(\tau)\}\,\alpha^a + \xi(\tau)\alpha^m.$$

Step 10. Compute the elastic deformation gradient $\mathbf{F}^e(\tau)$ and the stress $\mathbf{T}^e(\tau)$:

$$\mathbf{F}^e(\tau) = \mathbf{F}(\tau)(\mathbf{F}^p(\tau))^{-1},$$

$$\mathbf{F}^e(\tau) = \mathbf{R}^e(\tau)\mathbf{U}^e(\tau),$$

$$\mathbf{C}^e(\tau) = (\mathbf{F}^e(\tau))^{\mathsf{T}}\mathbf{F}^e(\tau),$$

$$\mathbf{E}^e(\tau) = (1/2)\,\{\mathbf{C}^e(\tau) - \mathbf{1}\},$$

$$\mathbf{T}^e(\tau) = \boldsymbol{\mathcal{C}}(\tau)[\mathbf{E}^e(\tau) - \mathbf{A}(\tau)(\theta(\tau) - \theta_0)].$$

Step 11. Update the Cauchy stress $\mathbf{T}(\tau)$:

$$\mathbf{T}(\tau) = \mathbf{R}^e(\tau)\mathbf{T}^e(\tau)\mathbf{R}^e(\tau)^\top.$$

Step 12. Calculate the driving force for phase transformation $f(\tau)$ and inelastic work fraction $\Delta\omega^p(\tau)$:

$$\bar{\sigma}(\tau) = \mathbf{T}^e(\tau) \cdot \mathbf{N}^p,$$

$$f(\tau) = \bar{\sigma}(\tau) - (\lambda_T/\theta_T)(\theta(\tau) - \theta_T),$$

$$\Delta\omega^p(\tau) = \{f(\tau) + (\lambda_T/\theta_T)\,\theta(\tau)\}\,\Delta\xi.$$

Appendix F

Hypo-elastic form for the isotropic-based constitutive equations

In this appendix the isotropic-plasticity-based constitutive equations for superelastic shape-memory materials is formulated in the hypo-elastic rate-form. This is done to facilitate the derivation of the Jacobian matrices to be implemented in the ABAQUS/Standard (1999,2001) finite-element package. The solution of the two methods (hyper-elastic vs. hypo-elastic) is identical because the elastic strains experienced in these materials are very small.

The advantage of using an implicit finite-element formulation (ABAQUS/Standard) is that large time steps can be taken while maintaining quasi-static loading conditions. For example the Ti-Ni bio-medical stent calculation performed in Chapter 2 took just 2 hours to complete using ABAQUS/Standard (1999,2001). Performing the same calculation using the ABAQUS/Explicit (1999,2001) finite-element program took 25 hours. This is because large time steps cannot be used while maintaining quasi-static loading conditions.

With that, the governing variables in the hypo-elastic constitutive model are taken to be

$\mathbf{T}$	Cauchy stress
$\mathbf{L} = \mathbf{D} + \mathbf{W}$	Velocity gradient
θ	Absolute temperature
$\mathbf{D}^p$	Inelastic stretching
$\xi,\ 0 \leq \xi \leq 1$	Martensite volume fraction
$\mathbf{D}^e \equiv \mathbf{D} - \mathbf{D}^p$	Elastic stretching
$\mathbf{T}^\nabla \equiv \dot{\mathbf{T}} - \mathbf{W}\mathbf{T} + \mathbf{T}\mathbf{W}$	Jaumann derivative of $\mathbf{T}$

Constitutive equation for stress

$$\mathbf{T}^\nabla = \boldsymbol{\mathcal{C}}\left[\mathbf{D} - \mathbf{A}\dot{\theta} - \mathbf{D}^p\right]$$

$\boldsymbol{\mathcal{C}} = 2\mu\boldsymbol{\mathcal{I}} + (\kappa - (2/3)\mu)\,\mathbf{1}\otimes\mathbf{1}, \quad \mu = \hat{\mu}(\xi,\theta), \quad \kappa = \hat{\kappa}(\xi,\theta)$	Elasticity tensor
$\mathbf{A} = \alpha\mathbf{1}, \quad \alpha = \hat{\alpha}(\xi,\theta)$	Thermal expansion tensor
ξ	Vol. Frac of Martensite

Transformation criteria

Let

$$f$$

denote the driving force for transformation, and

$$f_c > 0$$

a critical value for the driving force. Then the transformation criteria are taken as

$$f = f_c \quad \text{for austenite to martensite}, \dot{\xi} > 0,$$

and

$$f = -f_c \quad \text{for martensite to austenite}, \dot{\xi} < 0.$$

The driving force for transformation is defined by

$$f = \bar{\sigma} - (\lambda_T/\theta_T)(\theta - \theta_T),$$

where

$\bar{\sigma}$ Resolved tensile force

λ_T Latent heat per unit volume

ϵ_T Transformation strain

θ_T Phase equilibrium temperature .

The resolved tensile force is defined by:

$$\bar{\sigma} = \mathbf{T} \cdot \mathbf{N}^p.$$

Here $\mathbf{N}^p$ is the transformation direction after the transformation criterion $f = f_c$ for forward transformation is *first* satisfied and there is a non-zero ξ. That is, the stress used to evaluate the transformation direction $\mathbf{N}^p$ is the stress at the time t_c at which the forward transformation criterion is first satisfied. For a given forward-reverse transformation the direction $\mathbf{N}^p$ is *fixed.*

Flow rule

$$\mathbf{D}^p = \dot{\xi}\,\mathbf{N}^p.$$

The transformation direction $\mathbf{N}^p$ is

$$\mathbf{N}^p = \sqrt{\frac{3}{2}}\,\epsilon_T \left(\frac{\mathbf{T}_0}{|\mathbf{T}_0|}\right) \quad \text{if} \quad \xi = 0,$$

$$\mathbf{N}^p = \sqrt{\frac{3}{2}}\,\epsilon_T \left(\frac{\mathbf{T}_0(t_c)}{\mathbf{T}_0(t_c)}\right) \quad \text{if} \quad 0 < \xi \leq 1.$$

Here, t_c is the critical instant when the martensite volume fraction first becomes non-zero.

For forward transformation:

$$\dot{\xi} \geq 0, \quad (f - f_c) \leq 0, \quad \text{and} \quad \dot{\xi}\,(f - f_c) = 0$$

For reverse transformation:

$$\dot{\xi} \leq 0, \quad (f + f_c) \geq 0, \quad \text{and} \quad \dot{\xi}\,(f + f_c) = 0$$

Consistency conditions

During forward transformations :

$$\dot{\xi}\,\dot{\overline{(f - f_c)}} = 0 \quad \text{if} \quad (f - f_c) = 0$$

During reverse transformations :

$$\dot{\xi}\,\dot{\overline{(f + f_c)}} = 0 \quad \text{if} \quad (f + f_c) = 0$$

The consistency conditions serve to determine the transformation rates $\dot{\xi}$.

For transformation :

$$0 = \dot{\overline{(f \pm f_c)}} \tag{F.1}$$

$$= \dot{f} \tag{F.2}$$

$$= \dot{\overline{\bar{\sigma} - (\lambda_T/\theta_T)(\theta - \theta_T) \pm f_c)}} \tag{F.3}$$

$$= \dot{\bar{\sigma}} - (\lambda_T/\theta_T)\,\dot{\theta} \tag{F.4}$$

$$= \dot{\overline{\mathbf{T} \cdot \mathbf{N}^p}} - (\lambda_T/\theta_T)\,\dot{\theta} \tag{F.5}$$

$$= \dot{\mathbf{T}} \cdot \mathbf{N}^p - (\lambda_T/\theta_T)\,\dot{\theta} \tag{F.6}$$

$$= \mathbf{T}^{\nabla} \cdot \mathbf{N}^p - (\lambda_T/\theta_T)\,\dot{\theta} \tag{F.7}$$

$$= \boldsymbol{\mathcal{C}}\left[\mathbf{D} - \mathbf{A}\dot{\theta} - \mathbf{D}^p\right] \cdot \mathbf{N}^p - (\lambda_T/\theta_T)\,\dot{\theta} \tag{F.8}$$

Let

$$\dot{\mathbf{T}}^* = \boldsymbol{\mathcal{C}}\left[\mathbf{D} - \mathbf{A}\dot{\theta}\right]$$

denote a trial stress rate,

$$\dot{\bar{\sigma}}^* = \boldsymbol{\mathcal{C}}\left[\mathbf{D} - \mathbf{A}\dot{\theta}\right] \cdot \mathbf{N}^p = \boldsymbol{\mathcal{C}}\left[\mathbf{D}\right] \cdot \mathbf{N}^p = \boldsymbol{\mathcal{C}}\left[\mathbf{N}^p\right] \cdot \mathbf{D},$$

or

$$\dot{\bar{\sigma}}^* = 2\,\mu\,\mathbf{N}^p \cdot \mathbf{D},$$

and a trial resolved force, and

$$\dot{f}^* = \dot{\bar{\sigma}}^* - (\lambda_T/\theta_T)\dot{\theta}$$

the rate of change of a trial driving force. Then

$$0 = \dot{f}^* - \boldsymbol{\mathcal{C}}\left[\mathbf{D}^p\right] \cdot \mathbf{N}^p \tag{F.9}$$

$$0 = \dot{f}^* - \boldsymbol{\mathcal{C}}\left[\mathbf{N}^p\right] \cdot \mathbf{D}^p \tag{F.10}$$

$$0 = \dot{f}^* - 2\,\mu\,\mathbf{N}^p \cdot \mathbf{D}^p \tag{F.11}$$

$$0 = \dot{f}^* - 2\,\mu\,\mathbf{N}^p \cdot \left(\dot{\xi}\,\mathbf{N}^p\right) \tag{F.12}$$

$$0 = \dot{f}^* - 3\,\mu\,\dot{\xi}\,\epsilon_T^2, \tag{F.13}$$

or

$$\left(\dot{\xi}\epsilon_T\right) = \frac{\dot{f}^*}{3\,\mu\,\epsilon_T}.$$

Next

$$\mathbf{T}^{\nabla} = \boldsymbol{\mathcal{C}}\left[\mathbf{D} - \mathbf{A}\dot{\theta} - \mathbf{D}^{p}\right] \tag{F.14}$$

$$= \boldsymbol{\mathcal{C}}\left[\mathbf{D} - \mathbf{D}^{p}\right] - \boldsymbol{\mathcal{C}}\left[\mathbf{A}\right]\dot{\theta} \tag{F.15}$$

$$= \boldsymbol{\mathcal{C}}\left[\mathbf{D} - \left(\dot{\xi}\,\mathbf{N}^{p}\right)\right] - \dot{\theta}\boldsymbol{\mathcal{C}}\left[\mathbf{A}\right] \tag{F.16}$$

$$= \boldsymbol{\mathcal{C}}\left[\mathbf{D} - \left(\left(\frac{\dot{f}^{*}}{3\,\mu\,\epsilon_{T}^{2}}\right)\,\mathbf{N}^{p}\right)\right] - \dot{\theta}\,\boldsymbol{\mathcal{C}}\left[\mathbf{A}\right] \tag{F.17}$$

$$= \boldsymbol{\mathcal{C}}\left[\mathbf{D}\right] - \left(\left(\frac{\dot{f}^{*}}{3\,\mu\,\epsilon_{T}^{2}}\right)\,2\mu\mathbf{N}^{p}\right) - \dot{\theta}\,\boldsymbol{\mathcal{C}}\left[\mathbf{A}\right] \tag{F.18}$$

$$= \boldsymbol{\mathcal{C}}\left[\mathbf{D}\right] - \left(\frac{2\dot{f}^{*}}{3\epsilon_{T}^{2}}\,\mathbf{N}^{p}\right) - \dot{\theta}\boldsymbol{\mathcal{C}}\left[\mathbf{A}\right] \tag{F.19}$$

$$= \boldsymbol{\mathcal{C}}\left[\mathbf{D}\right] - \left((2/3)\left\{\frac{\dot{\bar{\sigma}}^{*} - (\lambda_{T}/\theta_{T})\,\dot{\theta}}{\epsilon_{T}^{2}}\right\}\,\mathbf{N}^{p}\right) - \dot{\theta}\,\boldsymbol{\mathcal{C}}\left[\mathbf{A}\right] \tag{F.20}$$

$$= \boldsymbol{\mathcal{C}}\left[\mathbf{D}\right] - \left((4\mu/3\epsilon_{T}^{2})\;(\mathbf{N}^{p}\cdot\mathbf{D})\;\mathbf{N}^{p}\right) + \left\{(2/3)\,(\lambda_{T}/\epsilon_{T}^{2}\,\theta_{T})\,\mathbf{N}^{p} - \boldsymbol{\mathcal{C}}\left[\mathbf{A}\right]\right\}\dot{\theta} \tag{F.21}$$

or

$$\mathbf{T}^{\nabla} = \boldsymbol{\mathcal{L}}\left[\mathbf{D}\right] + \left\{(2/3)\,(\lambda_{T}/\epsilon_{T}^{2}\,\theta_{T})\,\mathbf{N}^{p} - \boldsymbol{\mathcal{C}}\left[\mathbf{A}\right]\right\}\dot{\theta}$$

where

$$\boldsymbol{\mathcal{L}} = \boldsymbol{\mathcal{C}} - (4\mu/3\epsilon_{T}^{2})\,\mathbf{N}^{p}\otimes\mathbf{N}^{p}.$$

F.1 Incremental form

Let

$$\mathbf{F}_{t}(\tau) = \mathbf{F}(\tau)(\mathbf{F}(t))^{-1} \tag{F.22}$$

$$\mathbf{F}_{t}(\tau) = \mathbf{R}_{t}(\tau)\mathbf{U}_{t}(\tau) \tag{F.23}$$

$$\mathbf{E}_{t}(\tau) = \ln\mathbf{U}_{t}(\tau) \tag{F.24}$$

$$\bar{\mathbf{T}}(\tau) = (\mathbf{R}_{t}(\tau))^{\top}(\mathbf{T}(\tau))(\mathbf{R}_{t}(\tau)) \tag{F.25}$$

Constitutive equation for stress

$$\bar{\mathbf{T}}(\tau) = \bar{\mathbf{T}}(t) + \boldsymbol{\mathcal{C}}(t)\left[\mathbf{E}_t(\tau) - \mathbf{A}(t)\left(\theta(\tau) - \theta(t)\right) - \mathbf{E}_t^p(\tau)\right]$$

$\boldsymbol{\mathcal{C}}(t) = 2\mu(t)\boldsymbol{\mathcal{I}} + (\kappa(t) - (2/3)\mu(t))\,\mathbf{1}\otimes\mathbf{1}$ Elasticity tensor

$\mu(t) = \hat{\mu}(\xi(t), \theta(t)), \quad \kappa(t) = \hat{\kappa}(\xi(t), \theta(t))$ Elastic moduli

$\mathbf{A}(t) = \alpha(t)\mathbf{1}, \quad \alpha(t) = \hat{\alpha}(\xi(t), \theta(t))$ Thermal expansion tensor

$\mathbf{E}_t^p(\tau) = \Delta\xi\,\mathbf{N}^p, \qquad \mathbf{N}^p = \sqrt{(3/2)}\,\epsilon_T\left(\dfrac{\bar{\mathbf{T}}_0(t_c)}{|\bar{\mathbf{T}}_0(t_c)|}\right)$ Inelastic strain increment,

where the stress used to evaluate the transformation direction $\mathbf{N}^p$ is the stress at the time t_c at which the forward transformation criterion $f^*(\tau) > f_c$ is first satisfied; see below.

Trial driving force for phase transformation

Trial value of stress:

$$\bar{\mathbf{T}}^*(\tau) = \bar{\mathbf{T}}(t) + \boldsymbol{\mathcal{C}}(t)\left[\mathbf{E}_t(\tau) - \mathbf{A}(t)\left(\theta(\tau) - \theta(t)\right)\right]$$

Trial value of driving force:

$$f^*(\tau) = \bar{\sigma}^*(\tau) - (\lambda_T/\theta_T)(\theta - \theta_T),$$

where

$\bar{\sigma}^*(\tau)$ Trial resolved force

ϵ_T Transformation strain

λ_T Latent heat per unit volume

θ_T Phase equilibrium temperature

The trial resolved force is defined by:

$$\bar{\sigma}^*(\tau) = \bar{\mathbf{T}}^*(\tau) \cdot \mathbf{N}^p$$

Here $\mathbf{N}^p$ is the transformation direction after the transformation criterion $f^*(\tau) > f_c$ for forward transformation is *first* satisfied at time $t = t_c$. That is, the stress used to evaluate the transformation direction $\mathbf{N}^p$ is the stress at the time t_c at which the forward transformation criterion is first satisfied, and ξ becomes positive valued. For a given forward-reverse transformation the direction $\mathbf{N}^p$ is *fixed.* The transformation direction $\mathbf{N}^p$ is

$$\mathbf{N}^p = \sqrt{\frac{3}{2}}\,\epsilon_T \left(\frac{\bar{\mathbf{T}}_0(t)}{|\bar{\mathbf{T}}_0(t)|} \right) \quad \text{if} \quad \xi(t) = 0,$$

$$\mathbf{N}^p = \sqrt{\frac{3}{2}}\,\epsilon_T \left(\frac{\bar{\mathbf{T}}_0(t_c)}{|\bar{\mathbf{T}}_0(t_c)|} \right) \quad \text{if} \quad 0 < \xi(t) \leq 1.$$

Transformation criteria

If $0 \leq \xi(t) < 1$ then, for austenite to martensite, $\dot{\xi} > 0$:

$$f^*(\tau) > f_c.$$

If $0 < \xi(t) \leq 1$ then, for martensite to austenite, $\dot{\xi} < 0$:

$$f^*(\tau) < -f_c.$$

Consistency conditions

$$f(\tau) = \bar{\sigma}(\tau) - (\lambda_T/\theta_T)(\theta - \theta_T)$$

$\bar{\sigma}(\tau) = \bar{\mathbf{T}}(\tau) \cdot \mathbf{N}^p$	Resolved force,
λ_T	Latent heat per unit volume,
ϵ_T	Transformation strain,
θ_T	Phase equilibrium temperature.

During forward transformations :

$$f(\tau) = f_c$$

During reverse transformations :

$$f(\tau) = -f_c$$

The consistency conditions serve to determine the transformation increments $\Delta\xi$.

F.2 Time integration procedure

Here we suppress the argument t in $\mu(t)$ until the end.

$$\mathbf{E}_t^p(\tau) = \Delta\xi\,\mathbf{N}^p, \qquad \mathbf{N}^p = \sqrt{(3/2)}\,\epsilon_T \left(\frac{\bar{\mathbf{T}}_0(t_c)}{|\bar{\mathbf{T}}_0(t_c)|}\right) \tag{F.26}$$

$$\bar{\mathbf{T}}(\tau) = \bar{\mathbf{T}}(t) + \boldsymbol{\mathcal{C}}(t)\,[\mathbf{E}_t(\tau) - \mathbf{A}(t)(\theta(\tau) - \theta(t))] - \Delta\xi\,\boldsymbol{\mathcal{C}}(t)\,[\mathbf{N}^p] \tag{F.27}$$

$$\bar{\mathbf{T}}(\tau) = \bar{\mathbf{T}}(t) + \boldsymbol{\mathcal{C}}(t)\,[\mathbf{E}_t(\tau) - \mathbf{A}(t)(\theta(\tau) - \theta(t))] - 2\mu\,\Delta\xi\,\mathbf{N}^p \tag{F.28}$$

$$\bar{\mathbf{T}}^*(\tau) = \bar{\mathbf{T}}(t) + \boldsymbol{\mathcal{C}}(t)\,[\mathbf{E}_t(\tau) - \mathbf{A}(t)(\theta(\tau) - \theta(t))] \tag{F.29}$$

$$\bar{\mathbf{T}}(\tau) = \bar{\mathbf{T}}^*(\tau) - 2\mu\,\Delta\xi\,\mathbf{N}^p \tag{F.30}$$

$$\bar{\mathbf{T}}(\tau) \cdot \mathbf{N}^p = \bar{\mathbf{T}}^*(\tau) \cdot \mathbf{N}^p - 2\mu\,\Delta\xi\,\mathbf{N}^p \cdot \mathbf{N}^p \tag{F.31}$$

$$\bar{\sigma}(\tau) = \bar{\sigma}^*(\tau) - 3\mu\Delta\xi\epsilon_T^2 \tag{F.32}$$

Consistency condition for forward transformation:

$$f(\tau) = f_c \tag{F.33}$$

$$\bar{\sigma}^*(\tau) - 3\mu\Delta\xi\,\epsilon_T^2 - (\lambda_T/\theta_T)\,(\theta(\tau) - \theta_T) = f_c \tag{F.34}$$

$$\bar{\sigma}^*(\tau) - (\lambda_T/\epsilon_T)\,(\theta(\tau) - \theta_T) - f_c = 3\mu\Delta\xi\,\epsilon_T^2 \tag{F.35}$$

$$\frac{\{\bar{\sigma}^*(\tau) - (\lambda_T/\theta_T)\,(\theta(\tau) - \theta_T)\} - f_c}{3\mu\,\epsilon_T^2} = \Delta\xi \tag{F.36}$$

$$\Big(\Delta\xi\epsilon_T\Big) = \frac{f^*(\tau) - f_c}{3\mu(t)\,\epsilon_T} \tag{F.37}$$

where

$$f^*(\tau) = \bar{\sigma}^*(\tau) - (\lambda_T/\theta_T)(\theta(\tau) - \theta_T)$$

is trial driving force for phase transformation.

Consistency condition for reverse transformation:

$$f(\tau) = -f_c \tag{F.38}$$

$$\bar{\sigma}^*(\tau) - 3\mu\Delta\xi\,\epsilon_T^2 - (\lambda_T/\theta_T)\,(\theta(\tau) - \theta_T) = -f_c \tag{F.39}$$

$$\bar{\sigma}^*(\tau) - (\lambda_T/\epsilon_T)\,(\theta(\tau) - \theta_T) + f_c = (3\mu)\Delta\xi\,\epsilon_T^2\epsilon_T \tag{F.40}$$

$$\frac{\{\bar{\sigma}^*(\tau) - (\lambda_T/\theta_T)\,(\theta(\tau) - \theta_T)\} + f_c}{3\mu\,\epsilon_T^2} = \Delta\xi \tag{F.41}$$

$$\Big(\Delta\xi\epsilon_T\Big) = \frac{f^*(\tau) + f_c}{3\mu(t)\,\epsilon_T} \tag{F.42}$$

F.3 Jacobian Matrices

For a coupled temperature-displacement analysis four Jacobian matrices need to be supplied into the numerical algorithm. They are

$$\mathcal{L}(t) = \frac{\partial \bar{\mathbf{T}}(\tau)}{\partial \Delta \mathbf{E}},$$

$$\mathcal{M}(t) = \frac{\partial \bar{\mathbf{T}}(\tau)}{\partial \Delta \theta} = \frac{\partial \bar{\mathbf{T}}(\tau)}{\partial \theta(\tau)},$$

$$\mathcal{N}(t) = \frac{\partial (RPL(\tau))}{\partial \Delta \mathbf{E}},$$

$$\mathcal{O}(t) = \frac{\partial (RPL(\tau))}{\partial \Delta \theta} = \frac{\partial (RPL(\tau))}{\partial \theta(\tau)},$$

where $RPL(\tau)$ is the rate of volumetric heat generation at end of the step. It is given by

$$RPL(\tau) = \{f(\tau) + (\lambda_T/\theta_T)\,\theta(\tau)\}\,(\Delta\xi/\Delta t). \tag{F.43}$$

Here we suppress the argument t in $\mu(t)$ until the end.

Derivation of $\mathcal{L}(t)$

$$\bar{\mathbf{T}}^*(\tau) = \bar{\mathbf{T}}(t) + \mathcal{C}(t)\,[\mathbf{E}_t(\tau) - \mathbf{A}(t)(\theta(\tau) - \theta(t))] \tag{F.44}$$

$$\mathbf{N}^p = \sqrt{(3/2)}\,\epsilon_T \left(\frac{\bar{\mathbf{T}}_0(t_c)}{|\bar{\mathbf{T}}_0(t_c)|}\right) \tag{F.45}$$

$$\bar{\sigma}^*(\tau) = \bar{\mathbf{T}}^*(\tau) \cdot \mathbf{N}^p \tag{F.46}$$

$$\bar{\mathbf{T}}(\tau) = \bar{\mathbf{T}}^*(\tau) - 2\mu\Delta\,\xi\,\mathbf{N}^p \tag{F.47}$$

Let

$$\Delta \mathbf{E} = \mathbf{E}_t(\tau),$$

then the Jacobian is

$$\boldsymbol{\mathcal{L}}(t) = \frac{\partial \bar{\mathbf{T}}(\tau)}{\partial \Delta \mathbf{E}} \tag{F.48}$$

$$= \frac{\partial \bar{\mathbf{T}}^*(\tau)}{\partial \Delta \mathbf{E}} - 2\mu \frac{\partial (\Delta \xi \, \mathbf{N}^p)}{\partial \Delta \mathbf{E}} \tag{F.49}$$

$$= \boldsymbol{\mathcal{C}}(t) - 2\mu \left[(1/\epsilon_T)\mathbf{N}^p \otimes \frac{\partial (\Delta \xi \, \epsilon_T)}{\partial \Delta \mathbf{E}} \right]. \tag{F.50}$$

Recall that

$$\Delta \xi \, \epsilon_T = \frac{f^*(\tau) - f_c}{3\mu \epsilon_T}, \quad \text{for forward transformation} \tag{F.51}$$

$$\Delta \xi \, \epsilon_T = \frac{f^*(\tau) + f_c}{3\mu \epsilon_T}, \quad \text{for reverse transformation.} \tag{F.52}$$

Thus

$$\frac{\partial (\Delta \xi \, \epsilon_T)}{\partial \Delta \mathbf{E}} = \frac{1}{3\mu \epsilon_T} \frac{\partial f^*(\tau)}{\partial \Delta \mathbf{E}} \tag{F.53}$$

$$\frac{\partial (\Delta \xi \, \epsilon_T)}{\partial \Delta \mathbf{E}} = \frac{1}{3\mu \epsilon_T} \frac{\partial \Big(\bar{\sigma}^*(\tau) - (\lambda_T/\theta_T)\,(\theta(\tau) - \theta_T) \Big)}{\partial \Delta \mathbf{E}} \tag{F.54}$$

$$\frac{\partial (\Delta \xi \, \epsilon_T)}{\partial \Delta \mathbf{E}} = \frac{1}{3\mu \epsilon_T} \frac{\partial \bar{\sigma}^*(\tau)}{\partial \Delta \mathbf{E}} \tag{F.55}$$

$$\frac{\partial (\Delta \xi \, \epsilon_T)}{\partial \Delta \mathbf{E}} = \frac{1}{3\mu \epsilon_T} \frac{\partial \Big(\bar{\mathbf{T}}^*(\tau) \cdot \mathbf{N}^p \Big)}{\partial \Delta \mathbf{E}}. \tag{F.56}$$

Note that for a function $f(\mathbf{T}(\mathbf{E}))$

$$\frac{\partial f}{\partial \mathbf{E}} \cdot \mathbf{A} = \frac{d}{d\alpha} \{ f(\mathbf{T}(\mathbf{E} + \alpha \mathbf{A})) \} \, |_{\alpha=0} \tag{F.57}$$

$$= \frac{\partial f}{\partial \mathbf{T}} \cdot \frac{d}{d\alpha} \{ \mathbf{T}(\mathbf{E} + \alpha \mathbf{A}) \} \, |_{\alpha=0} \tag{F.58}$$

$$= \frac{\partial f}{\partial \mathbf{T}} \cdot \frac{\partial \mathbf{T}}{\partial \mathbf{E}} \, [\mathbf{A}] \tag{F.59}$$

$$= \left(\frac{\partial \mathbf{T}}{\partial \mathbf{E}} \right)^{\mathsf{T}} \left[\frac{\partial f}{\partial \mathbf{T}} \right] \cdot \mathbf{A} \tag{F.60}$$

$$\frac{\partial f}{\partial \mathbf{E}} = \left(\frac{\partial \mathbf{T}}{\partial \mathbf{E}} \right)^{\mathsf{T}} \left[\frac{\partial f}{\partial \mathbf{T}} \right]. \tag{F.61}$$

Thus

$$\frac{\partial\left(\bar{\mathbf{T}}^*(\tau)\cdot\mathbf{N}^p\right)}{\partial\Delta\mathbf{E}} = \left(\frac{\partial\bar{\mathbf{T}}^*(\tau)}{\partial\Delta\mathbf{E}}\right)^{\mathsf{T}}\left[\frac{\partial\left(\bar{\mathbf{T}}^*(\tau)\cdot\mathbf{N}^p\right)}{\partial\bar{\mathbf{T}}^*(\tau)}\right] \tag{F.62}$$

$$= \boldsymbol{\mathcal{C}}(t)\,[\mathbf{N}^p] \tag{F.63}$$

$$= 2\mu\,\mathbf{N}^p. \tag{F.64}$$

Hence

$$\frac{\partial(\Delta\xi\,\epsilon_T)}{\partial\Delta\mathbf{E}} = \frac{1}{3\mu\,\epsilon_T}\,\frac{\partial\left(\bar{\mathbf{T}}^*(\tau)\cdot\mathbf{N}^p\right)}{\partial\Delta\mathbf{E}} \tag{F.65}$$

$$\frac{\partial(\Delta\xi\,\epsilon_T)}{\partial\Delta\mathbf{E}} = (2/3\epsilon_T)\,\mathbf{N}^p, \tag{F.66}$$

and the Jacobian is

$$\boldsymbol{\mathcal{L}}(t) = \boldsymbol{\mathcal{C}}(t) - (2\mu/\epsilon_T)\left[\mathbf{N}^p\otimes\frac{\partial(\Delta\xi\,\epsilon_T)}{\partial\Delta\mathbf{E}}\right] \tag{F.67}$$

$$= \boldsymbol{\mathcal{C}}(t) - (2\mu/\epsilon_T^2)\,[\mathbf{N}^p\otimes(2/3)\,\mathbf{N}^p] \tag{F.68}$$

or finally

$$\boldsymbol{\mathcal{L}}(t) = \boldsymbol{\mathcal{C}}(t) - (4\mu(t)/3\,\epsilon_T^2)\,\mathbf{N}^p\otimes\mathbf{N}^p. \tag{F.69}$$

Derivation of $\boldsymbol{\mathcal{M}}(t)$

From equation F.47 the Jacobian matrix $\boldsymbol{\mathcal{M}}(t)$:

$$\boldsymbol{\mathcal{M}}(t) = \frac{\partial\bar{\mathbf{T}}(\tau)}{\partial\theta(\tau)} \tag{F.70}$$

$$= \frac{\partial\bar{\mathbf{T}}^*(\tau)}{\partial\theta(\tau)} - 2\mu\,\frac{\partial(\Delta\xi\,\mathbf{N}^p)}{\partial\theta(\tau)} \tag{F.71}$$

$$= -\boldsymbol{\mathcal{C}}(t)[\mathbf{A}(t)] - 2\mu\left[(1/\epsilon_T)\,\frac{\partial(\Delta\xi\,\epsilon_T)}{\partial\theta(\tau)}\,\mathbf{N}^p\right]. \tag{F.72}$$

From equations F.51 and F.52

$$\boldsymbol{\mathcal{M}}(t) = -\boldsymbol{\mathcal{C}}(t)[\mathbf{A}(t)] - (2\mu)\left[(1/3\mu\,\epsilon_T^2)\,\frac{\partial f^*(\tau)}{\partial\theta(\tau)}\,\mathbf{N}^p\right]. \tag{F.73}$$

Since

$$\frac{\partial f^*(\tau)}{\partial\theta(\tau)} = -\lambda_T/\theta_T, \tag{F.74}$$

We obtain

$$\boldsymbol{\mathcal{M}}(t) = -3\kappa(t)\alpha(t)1 + (2/3)\,(\lambda_T/\theta_T\epsilon_T^2)\,\mathbf{N}^p. \tag{F.75}$$

Derivation of $\boldsymbol{\mathcal{N}}(t)$

From equation F.43 the Jacobian matrix $\boldsymbol{\mathcal{N}}(t)$:

$$\boldsymbol{\mathcal{N}}(t) = \frac{\partial(RPL(\tau))}{\partial\Delta\mathbf{E}} \tag{F.76}$$

$$= \frac{\partial f(\tau)}{\partial\Delta\mathbf{E}}\,(\Delta\xi/\Delta t) + \{f(\tau) + (\lambda_T/\theta_T)\,\theta(\tau)\}\,(1/\epsilon_T\Delta t)\,\frac{\partial(\Delta\,\xi\,\epsilon_T)}{\partial\Delta\mathbf{E}}\,. \tag{F.77}$$

From the consistency conditions, $f(\tau) = \mp f^c \equiv constant$. Therefore

$$\frac{\partial f(\tau)}{\partial\Delta\mathbf{E}} = 0. \tag{F.78}$$

Using equations F.66 and F.78 yield :

$$\boldsymbol{\mathcal{N}}(t) = (2/3)\,(1/\epsilon_T^2\Delta t)\,\{f(\tau) + (\lambda_T/\theta_T)\,\theta(\tau)\}\,\mathbf{N}^p. \tag{F.79}$$

Derivation of $\boldsymbol{\mathcal{O}}(t)$

Again from equation F.43 the Jacobian matrix $\boldsymbol{\mathcal{O}}(t)$:

$$\boldsymbol{\mathcal{O}}(t) = \frac{\partial(RPL(\tau))}{\partial\theta(\tau)} \tag{F.80}$$

$$= \left\{\frac{\partial f(\tau)}{\partial\theta(\tau)} + (\lambda_T/\theta_T)\right\}(\Delta\xi/\Delta t) + \{f(\tau) + (\lambda_T/\theta_T)\,\theta(\tau)\}\,(1/\epsilon_T\Delta t)\,\frac{\partial(\Delta\,\xi\,\epsilon_T)}{\partial\theta(\tau)}\,. \tag{F.81}$$

From the consistency conditions, $f(\tau) = \mp f^c \equiv constant$. Therefore

$$\frac{\partial f(\tau)}{\partial\theta(\tau)} = 0. \tag{F.82}$$

From equations F.51, F.52 and F.74 we obtain

$$\frac{\partial\Delta\xi\,\epsilon_T}{\partial\theta(\tau)} = -(1/3\mu\epsilon_T)\,(\lambda_T/\theta_T). \tag{F.83}$$

Therefore using equations F.82 and F.83 the Jacobian matrix $\boldsymbol{\mathcal{O}}(t)$ is

$$\boldsymbol{\mathcal{O}}(t) = (\lambda_T/\theta_T\Delta t)\left[\Delta\,\xi - (1/3\mu(t)\epsilon_T^2)\,\{f(\tau) + (\lambda_T/\theta_T)\,\theta(\tau)\}\right]. \tag{F.84}$$

Appendix G

Simple shear problem in the isotropic-based constitutive model

Consider the simple shear of a single element in the $(1,3)$-plane, Figure G-1a. Velocity boundary conditions are applied to the top nodes to result in a shear strain rate of +0.001/sec for 110 sec, and reverse deformation is prescribed to take place at a shear strain rate of -0.001/sec in another 110 sec. The material parameters for the constitutive model are taken to be the same as in Section 3, but this time a standard Mises-type flow rule is used in which the direction of plastic flow is taken to be given by

$$\mathbf{N}^p = \sqrt{(3/2)}\,\epsilon_T\,\frac{\mathbf{T}_0^e}{|\mathbf{T}_0^e|} \quad \text{for all} \quad 0 \leq \xi \leq 1, \tag{G.1}$$

instead of (3.15). The solution for the non-zero components of the Cauchy stress $\mathbf{T}$ as a function of time is shown in Figure G-1b. Note that in addition to the shear stress T_{13}, non-zero and substantially large values of normal stresses T_{33} and T_{11} develop during the reverse deformation.

This stress history results in a shear stress versus shear strain response shown in Figure G-1b, which does not have the character of a closed flag-type superelastic response. Figure G-1c also shows the result of a calculation for the same problem, but upon using the non-standard flow rule (3.15) used in the body of the paper; this time one obtains the expected closed hysteresis loop.

The spurious result using the standard flow rule (G.1) occurs due to subtle normal-stress effects that arise upon using a large deformation theory in simple shear. The non-standard flow rule (3.15) predicts full recovery of stress upon complete reversal of deformation, at least for the *proportional loading* conditions tested in this section. [1]

[1] A non-standard flow rule with a stress-based flow direction for forward transformation, and a strain-based flow direction for reverse transformation has been previously used by Qidwai and Lagoudas (2000), but they do not provide a discussion or a motivation for why they made their particular choice.

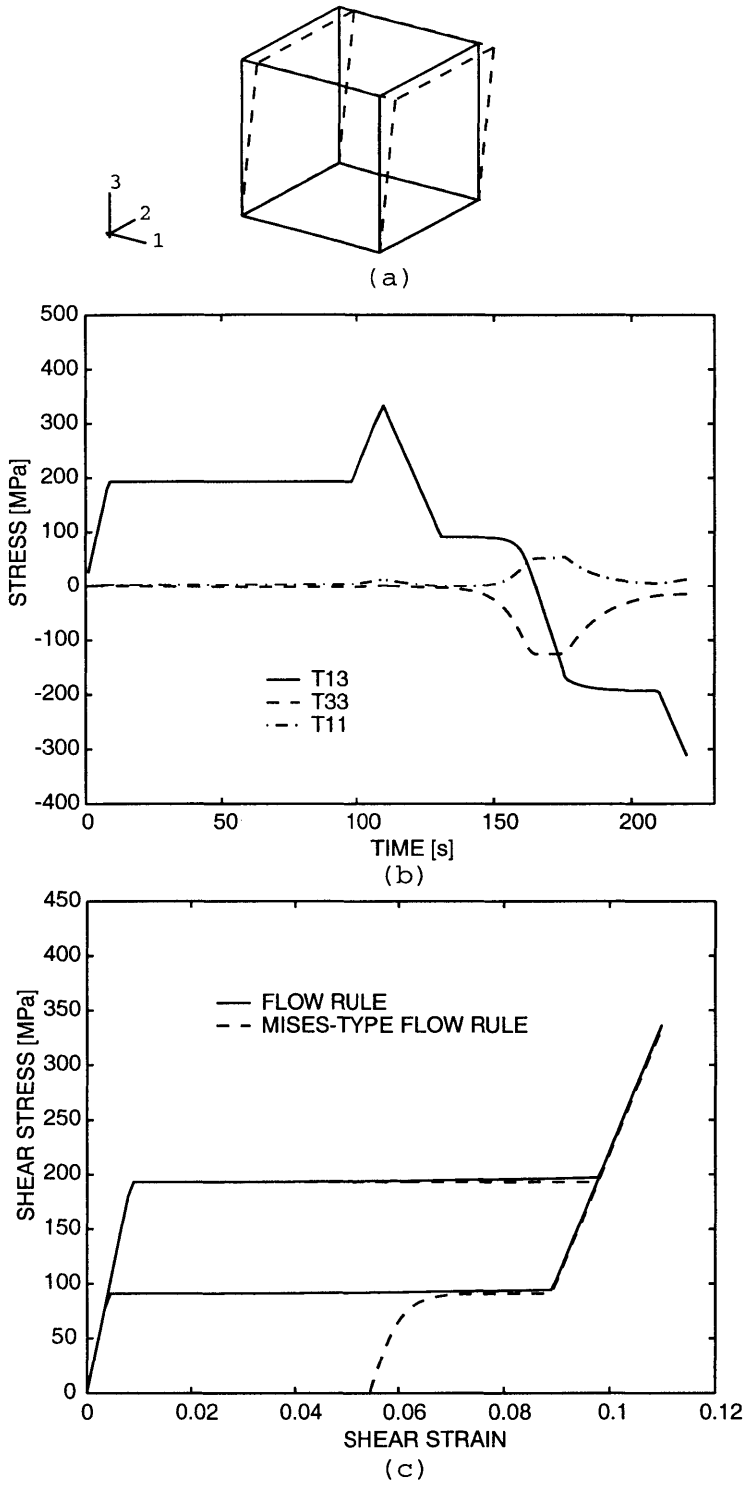

Figure G-1: Comparison of the shear-stress versus shear-strain response in simple shear predicted by the non-standard flow rule versus that predicted by the standard-Mises type flow rule. The nonstandard flow rule predicts the expected closed flag-type hysteresis loop.

Appendix H

Anisotropic superelasticity of textured sheet Ti-Ni

Here we shall evaluate our recently developed crystal-mechanics-based constitutive model to examine the in-plane anisotropic response shown by another polycrystalline Ti-Ni sheet. Shan and Sung (2000) have conducted extensive superelastic tension experiments on Ti-Ni sheets along different directions, and the experimental results show the in-plane anisotropic superelastic response. The purpose of this section is to show that our developed crystal-mechanics-based constitutive model adequately captures the in-plane anisotropy for a different Ti-Ni sheet.

Superelastic Ti-Ni sheets were obtained from a commercial source. Tensile specimens were cut along different directions and tested, ranging from 0^o (rolling direction) to 90^o (transverse direction) at 10^o intervals. Superelastic tension experiments were conducted at room temperature ($\theta = 298\,\mathrm{K}$) under displacement control at very low strain rates to ensure near isothermal testing conditions.

Experimental pole figure measurements of the initially-textured sheet were obtained using a Rigaku 200 X-ray diffraction machine. The {111}, {110} and {100} experimental pole figure is shown in Figure H-1a. A numerical representation of the experimental pole figures using 420 discrete unweighted crystal orientations was obtained by using the computer program PoPLa (Kallend et al., 1989). The numerical

representation of the experimental pole figures is shown in Figure H-1b.

The initial finite-element mesh used to model a representative volume element (RVE) of the polycrystalline material is shown in Figure H-2a. In our finite-element model of a polycrystal, each element represents a single crystal, and it is assigned a crystal orientation from the set of crystal orientations which approximate the initial crystallographic texture of the material shown in Figure H-1a.

The material parameters in the constitutive model were calibrated to the tension experiment conducted along the rolling direction. The procedure to determine the material parameters is outlined in Section 2.2.

The thermo-elastic constants used in our calculations are

Elastic moduli for austenite: $C_{11}^a = 130\,\text{GPa}, C_{12}^a = 98\,\text{GPa}, C_{44}^a = 22\,\text{GPa}$;

Elastic moduli for martensite: $C_{11}^m = 65\,\text{GPa}, C_{12}^m = 49\,\text{GPa}, \ C_{44}^m = 11\,\text{GPa}$;

Coefficients of thermal expansion: $\alpha^a = 11 \times 10^{-6}/\text{K}$, $\alpha^m = 6.6 \times 10^{-6}/\text{K}$.

An estimate for the phase transformation parameters $\{\theta_T, \lambda_T, f_c\}$ for Ti-Ni single crystals is obtained by fitting the constitutive model to tension experiment conducted along the rolling direction. Since the experiments were only done at one particular temperature we can obtain the temperature dependence of the driving force $(\lambda_T/\theta_T)(\theta - \theta_T)$ for the aforementioned temperature.

The single-crystal material parameters used to obtain this fit are:

Temperature dependence of driving force : $(\lambda_T/\theta_T)\,(\theta - \theta_T) = 13.3\,\text{MJ/m}^3$ at $\theta = 298\,\text{K}$.

Critical driving force: $f_c = 6.9\,\text{MJ/m}^3$.

The fit of the constitutive model to the tension experiment conducted along the rolling direction is shown in Figure H-2b. With the constitutive model calibrated to the rolling direction, the superelastic tensile response along other directions (Figures H-3 to H-7) can be predicted. The superelastic response in all these orientations is well-approximated by the predictions from the constitutive model. Of particular note, the anisotropic response between the rolling and transverse direction, as shown in Figure H-7b, is captured by the model. In Figure H-8 we plot the nucleation stresses during forward and reverse transformation for the differently-oriented specimens at a

representative strain of 2%. Note that the nucleation stresses in the middle-oriented specimens *i.e.* the 40^o and 50^o specimen lies in between of the rolling and transverse-direction specimens. This effect is also predicted reasonably well by the constitutive model.

To the best of our knowledge, this is the first time such calculations have been reported in the literature.

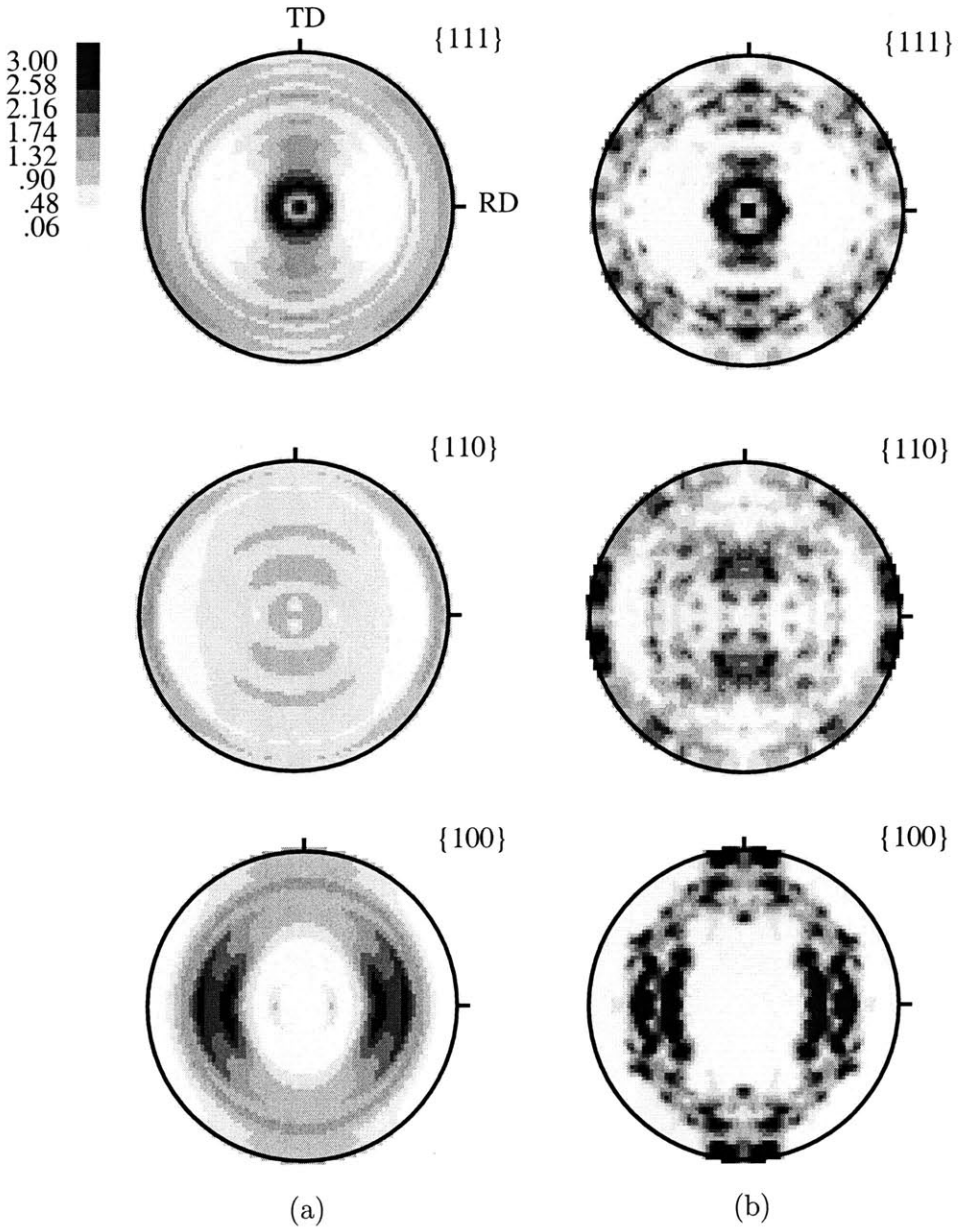

Figure H-1: (a) Experimentally-measured texture in the as-received Ti-Ni sheet, and (b) its numerical representation using 420 discrete unweighted crystal orientations.

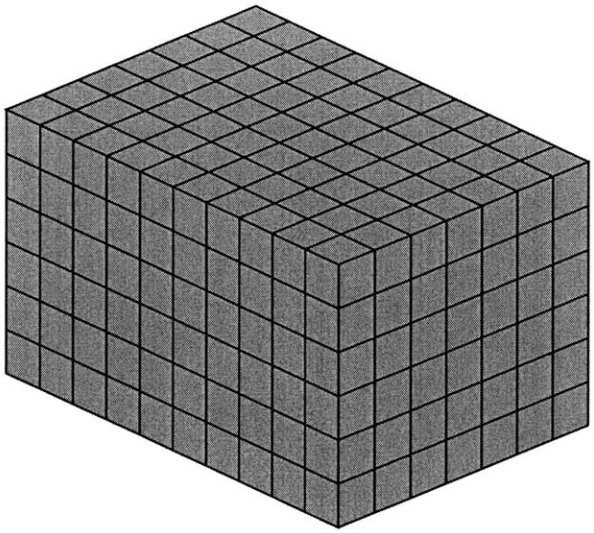

(a)

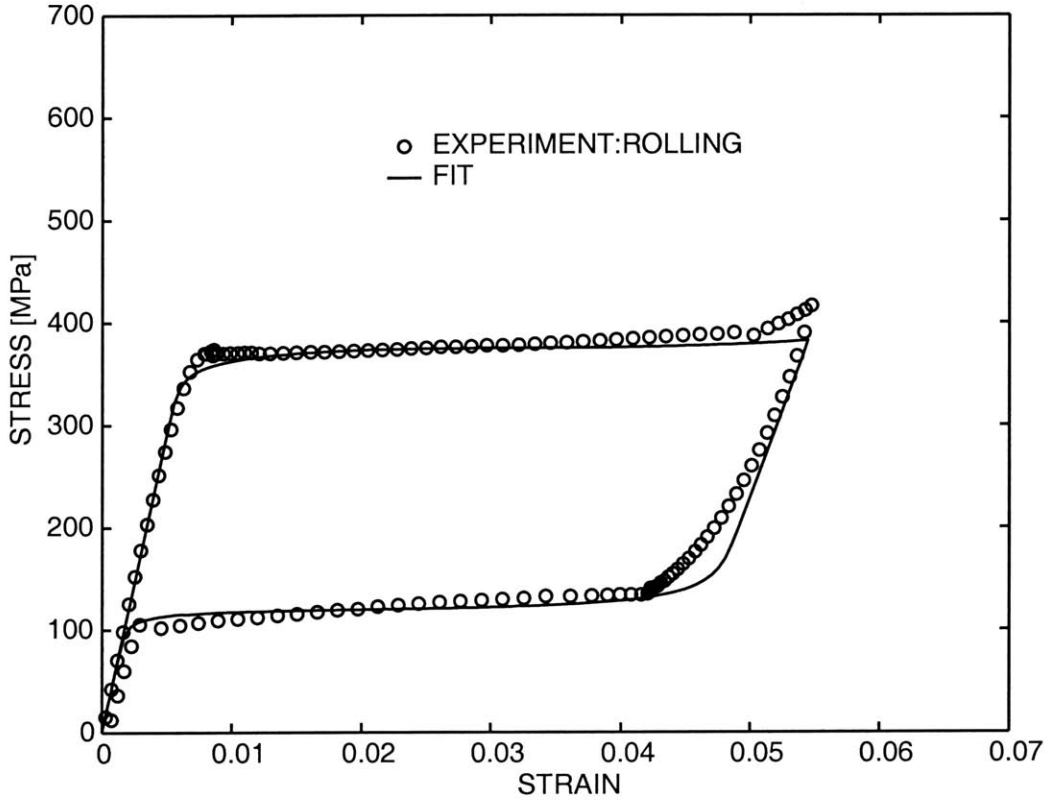

(b)

Figure H-2: (a) Undeformed mesh of 420 ABAQUS C3D8R elements used to represent a textured polycrystal aggregate. (b) Superelastic stress-strain curve in tension along the rolling direction. The experimental data from this test were used to estimate the constitutive parameters. The curve fit using the full finite-element model of the polycrystal is also shown.

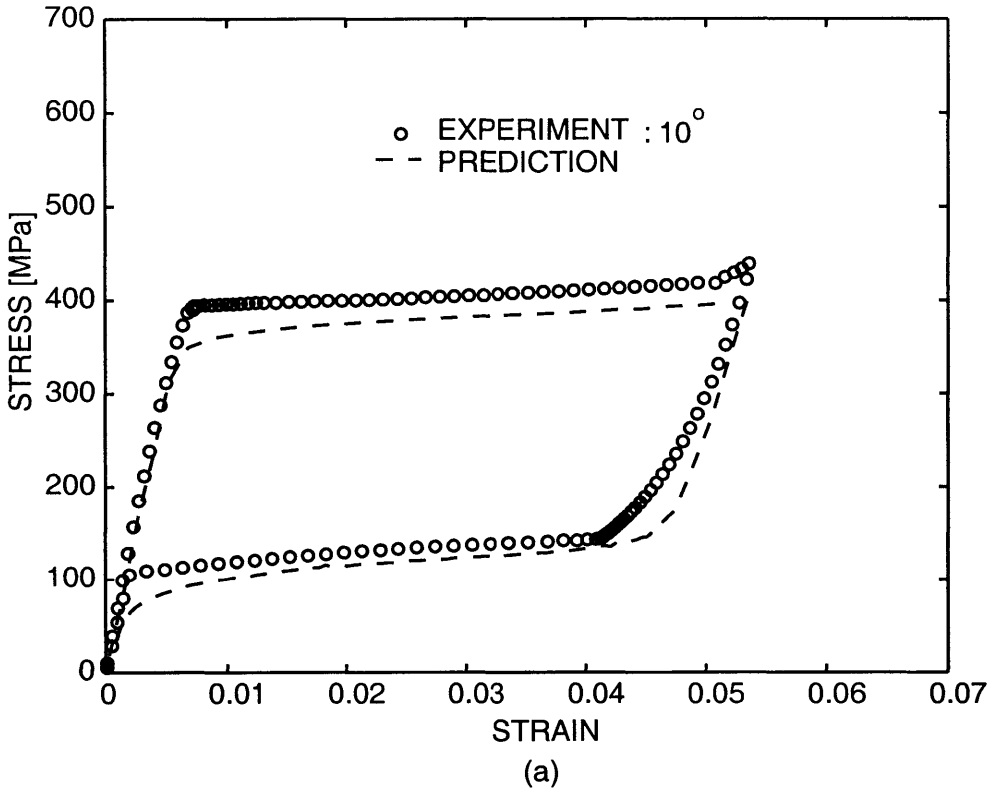

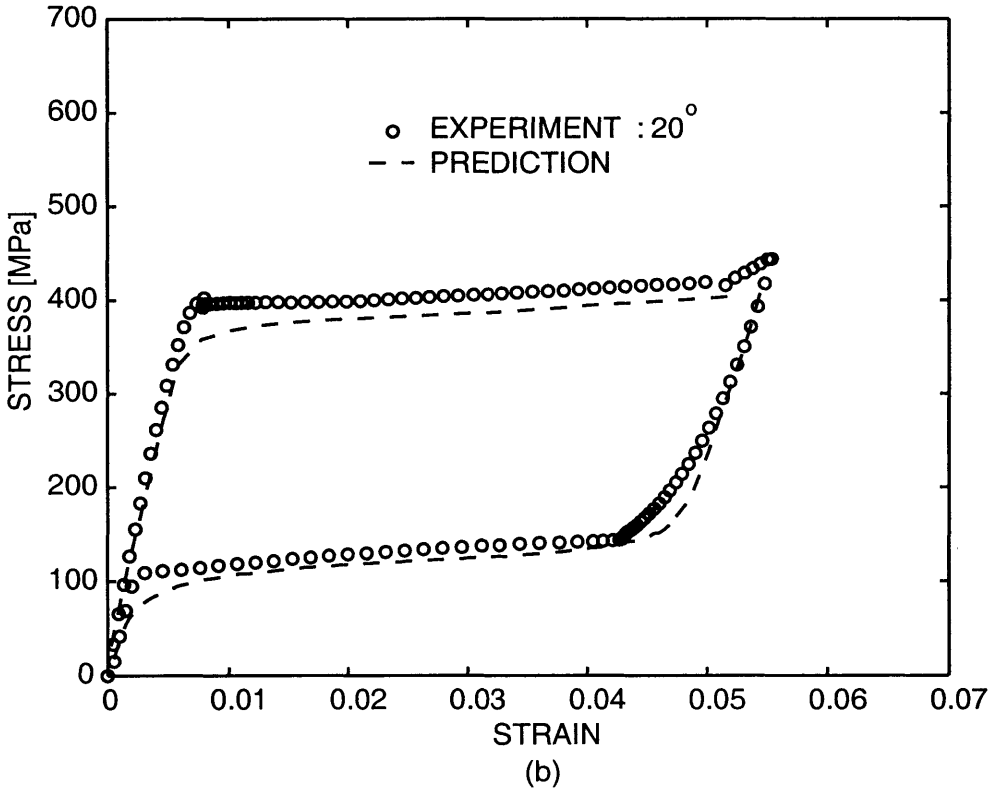

Figure H-3: (a) Superelastic experiment conducted along the (a) 10^o and (b) 20^o direction. The prediction from the finite-element simulations are also shown.

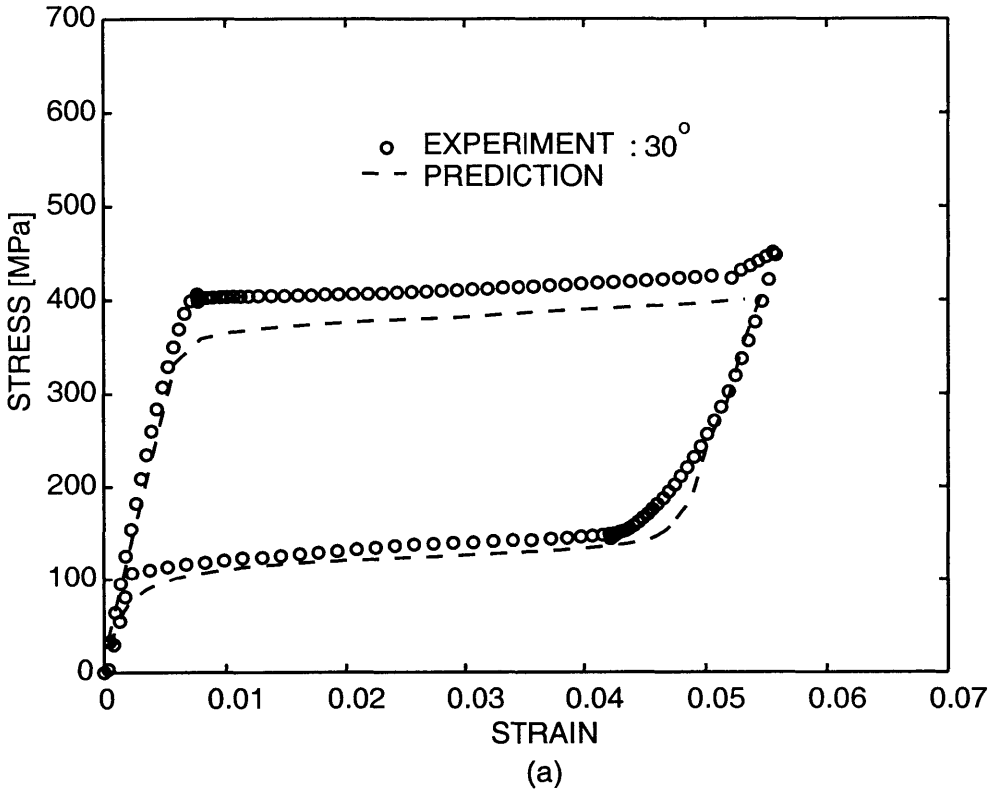

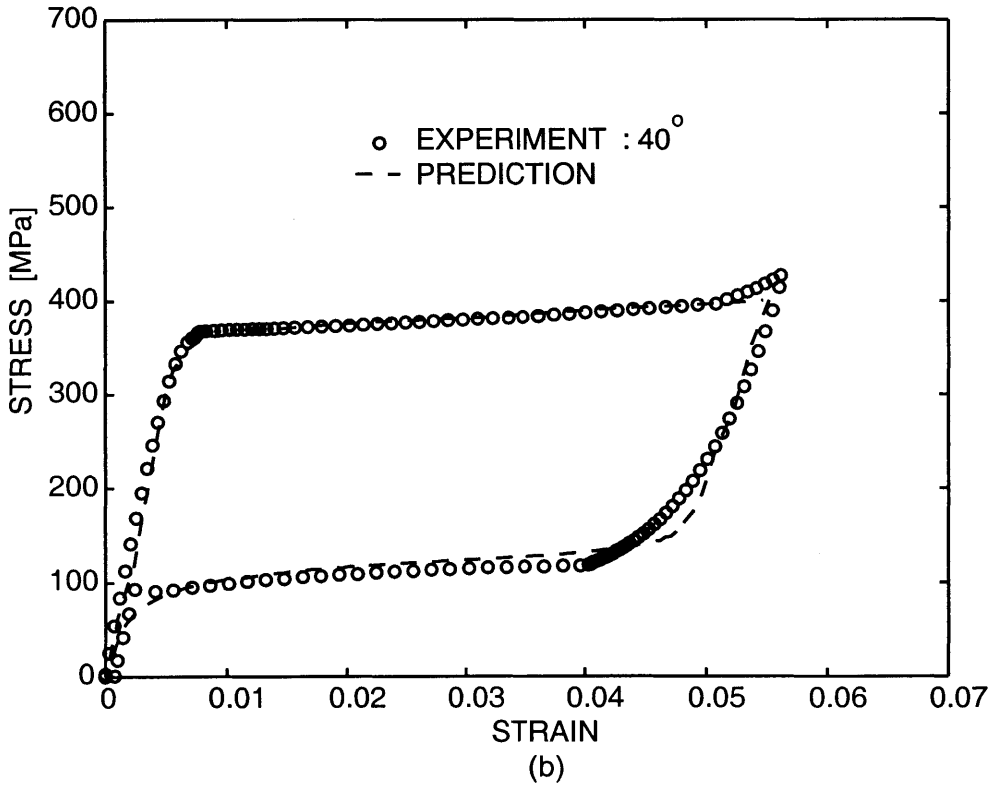

Figure H-4: (a) Superelastic experiment conducted along the (a) 30^o and (b) 40^o direction. The prediction from the finite-element simulations are also shown.

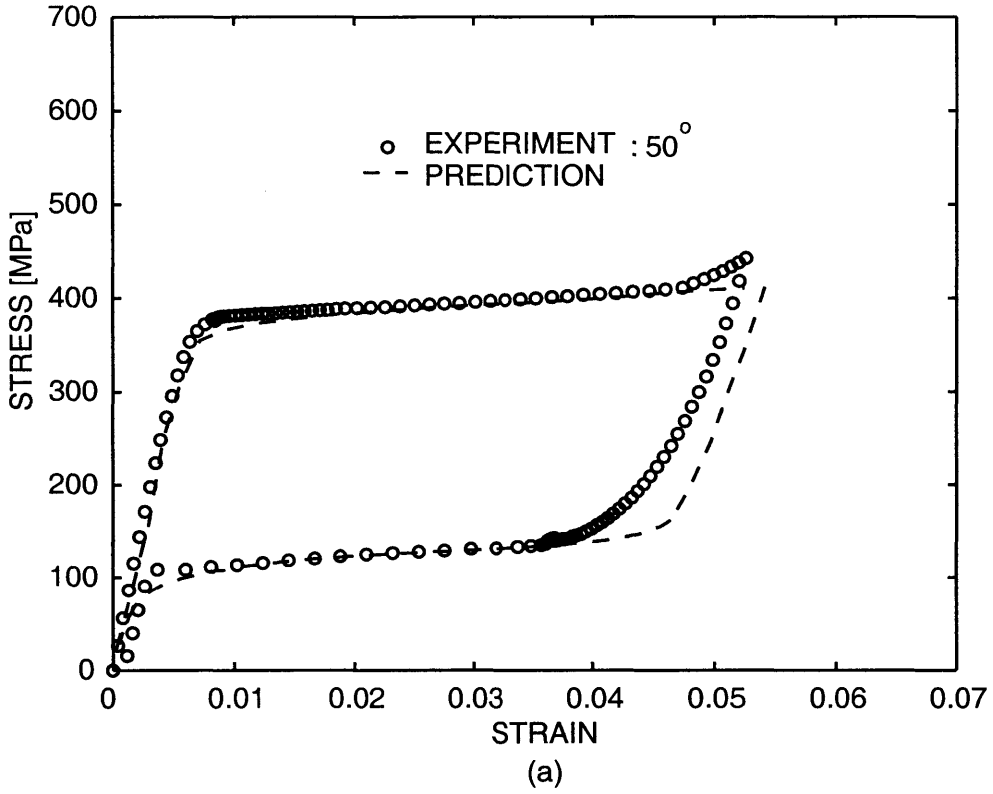

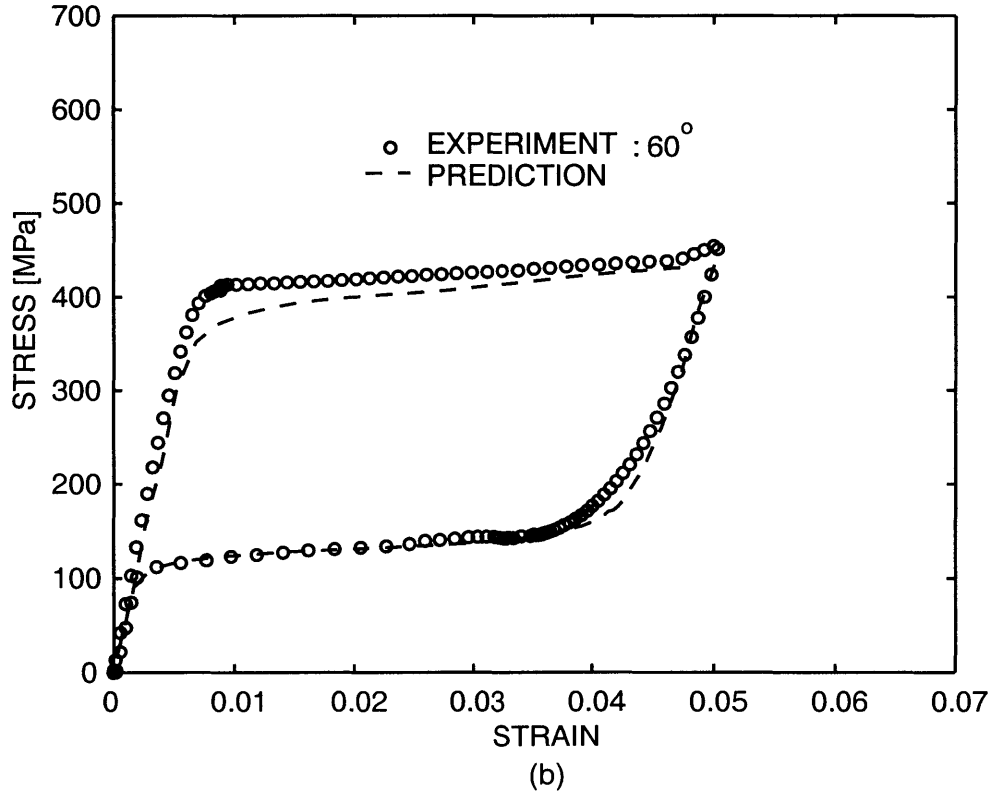

Figure H-5: (a) Superelastic experiment conducted along the (a) 50^o and (b) 60^o direction. The prediction from the finite-element simulations are also shown.

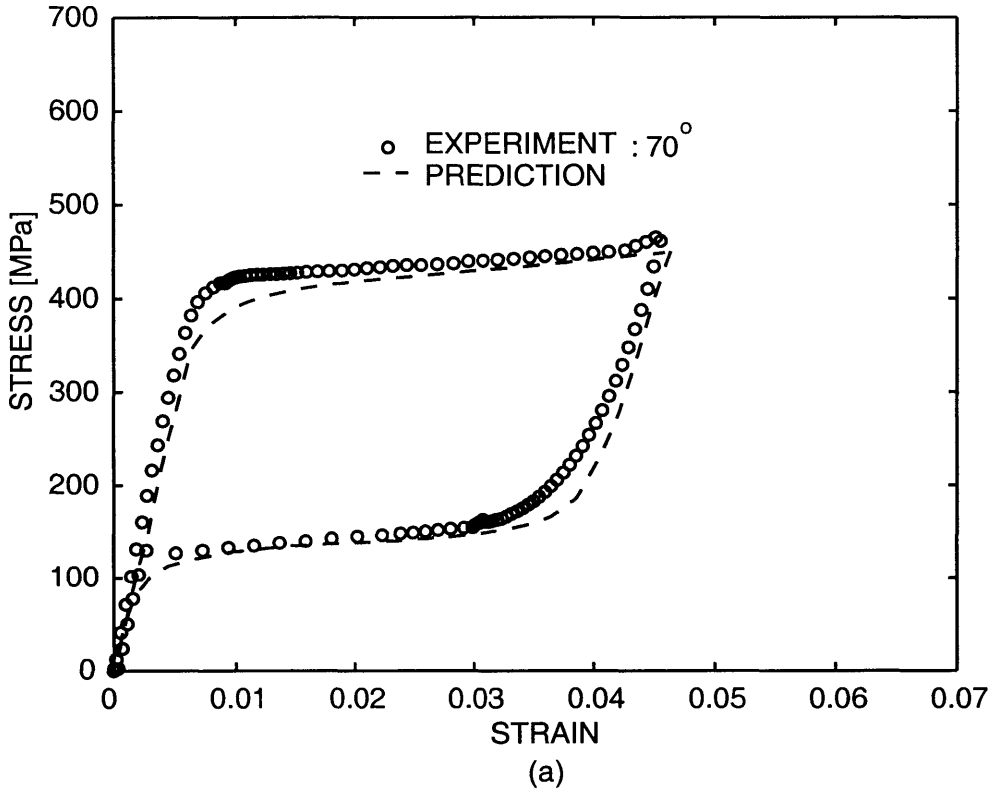

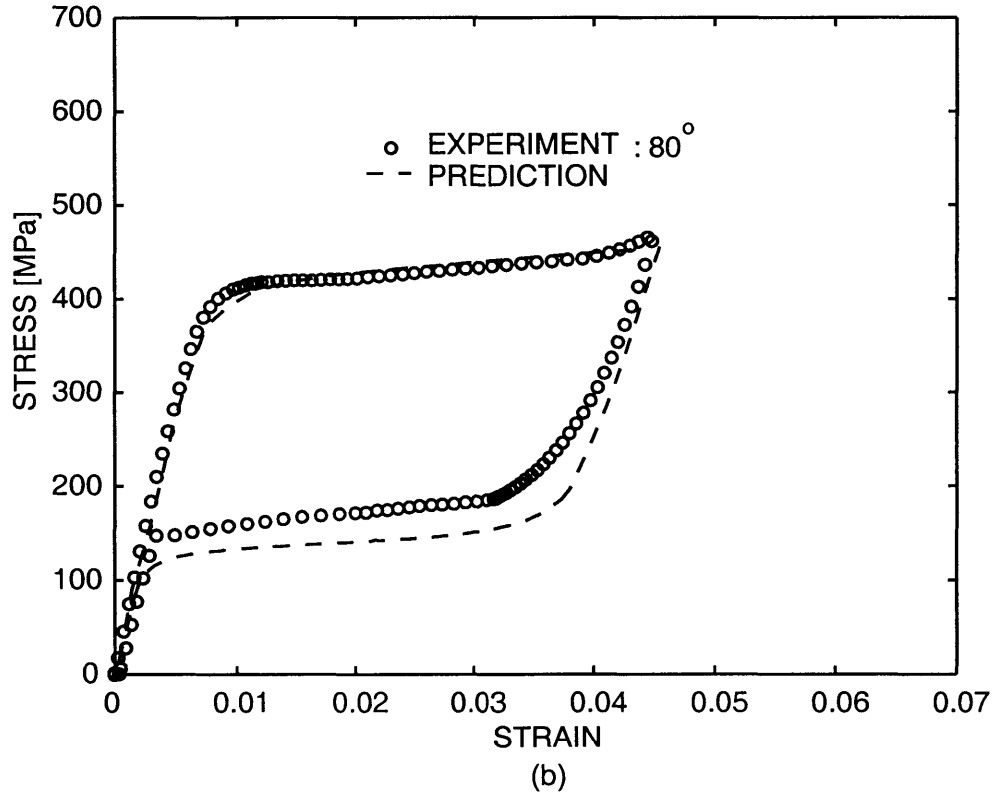

Figure H-6: (a) Superelastic experiment conducted along the (a) 70^o and (b) 80^o direction. The prediction from the finite-element simulations are also shown.

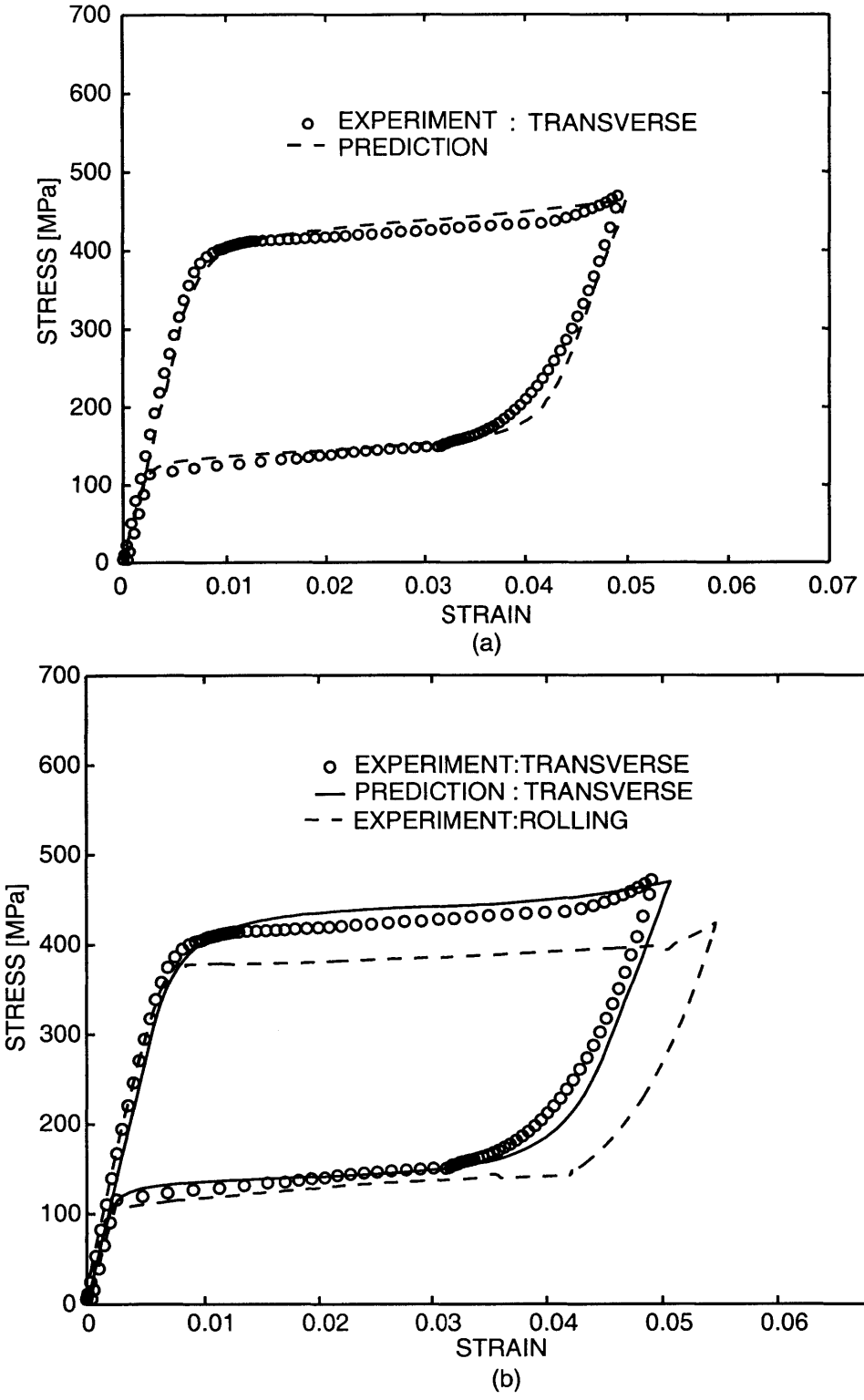

Figure H-7: (a) Superelastic experiment conducted along the transverse direction. The prediction from the finite-element simulations is also shown, and (b) Superelastic experiment along the rolling direction compared with the transverse direction. The finite-element simulation along the transverse direction is also shown.

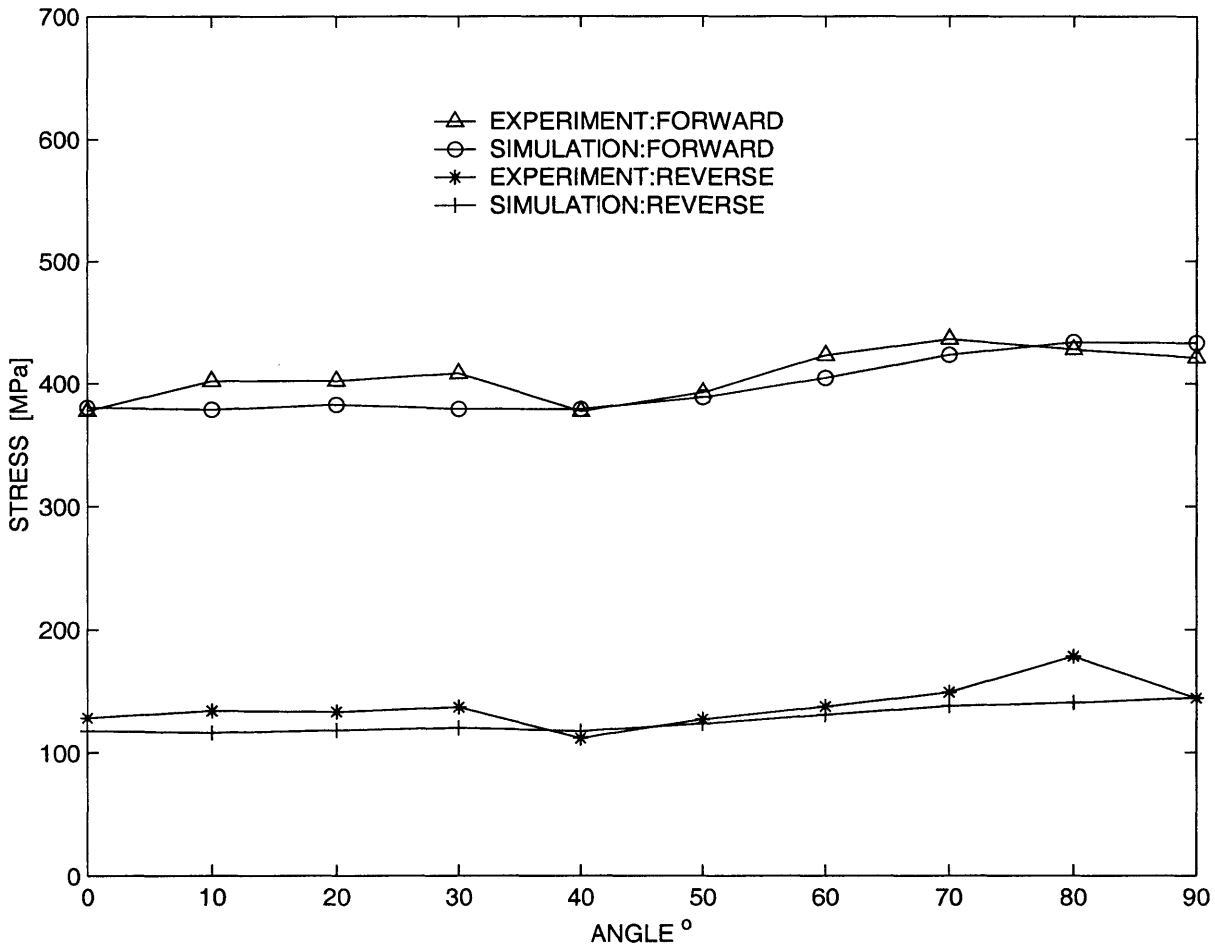

Figure H-8: Comparison of the nucleation stresses of the differently-oriented specimens during the forward and reverse transformation at 2% strain with respect to the prediction from the finite-element simulations.

Appendix I

Operating procedure for the RigaKu200 & 300 X-ray Diffraction machine

Operating procedures for the RU200 & 300:

1. Check the status of the x-ray generator: Determine whether the x-rays are ON or OFF by observing the tube tower and the RED light on the front of the HIGH VOLTAGE CONTROLLER. Make sure that the SHUTTER is closed! Do not open the door in any circumstances if the SHUTTER is not turned off.

2. If the X-RAYS are NOT ON, CHECK the status of the TUBE TOWER VACUUM. The THREE GREEN LIGHTS on the VACUUM CONTROLLER indicate the quality of the vacuum. If all three green lights are on, then the vacuum is o.k. If not, report this immediately to the person in charge of the machines.

3. If the X-RAYS are ON determine if either of the X-RAY SHUTTERS are OPEN by observing the RED lights ON EITHER SIDES OF THE TUBE TOWER. If a SHUTTER is OPEN, determine whether or not that DIFFRACTOMETER is RUNNING. If neither diffractometer is in the process of COLLECTING DATA, something is WRONG. X-RAYS SHOULD BE ON and the SHUTTERS OPEN ONLY WHEN

THE DIFFRACTOMETERS ARE COLLECTING DATA.

4. You may open the diffractometer doors when the X-RAYS are ONLY under these following conditions: (a) There is a shield in between the two sides, (b) Your shutter is closed, (c) You must survey your diffractometer area with the hand held Geiger counter, (d) The intensity of the background around your diffractometer should be close to that outside the enclosure.

5. If you are the only one using the X-RAY generator, you must turn off the X-RAYS every time you enter the enclosure to change samples etc.

Start-up procedure:

1. Make sure of the experiment you intend to conduct. Different experiments require different slits to be used. The slits that exist are the DIVERGENCE slits, SCATTER slits, RECEIVING slits and the SCHULTZ slits.

2. The DIVERGENCE slit is the one closest to the TUBE TOWER. The SCATTER slit has the same size as the DIVERGENCE slit. The SCATTER slit is the next slit in the diffracted slit path. It is in the front of the receiving SOLLER slits and is the next one after the sample.

3. Check the RECEIVING slit. It is located on the back side of the SOLLER slits after the SCATTER slit. Different experiments require different combinations of these slits the type of slits used will be discussed later.

4. INSERT the SAMPLE. This ia done by mounting the sample on a aluminum mounter. After mounting it, make sure it is tight against the post. You can use scotch to anchor the specimen mounter to the post BUT do not anchor the scotch tape to the STEEL part of the machine because it is stationary.

5. Before starting up the X-RAY, make sure that the SHUTTER is CLOSED! To start-up the X-RAY generator, press the T-REV button. The AMBER LIGHT on the HIGH VOLTAGE CONTROLLER should come ON. If the light does not come on, check that the doors are closed and the KV and Ma selector switches are fully at their minimum positions. Then press the ON button to activate the X-RAYS.

6. Turn up the KV slowly and wait for the meter stabilize before turning it up again.
7. Then turn up the MA slowly. The selection of KV and MA depends on you and the operator of the other machine. DO NOT USE COMBINATIONS WHICH BRING EITHER METERS TO THE RED ZONE!
8. INITIALIZE the DIFFRACTOMETER. Although this is not necessary, it is done to assure that the THETA and 2THETA are properly coupled.
9. Now it is ready to take data. Proceed to either the POSITION GONIOMETER program, the FIXED TIME COUNT or the MEASUREMENT program.

Shutting off procedure:

1. The shutting off procedure is the exact opposite of the starting up procedure. First turn the MA down.
2. The turn the KV down slowly and turn it down one step a time. Do this after the meter stabilizes.
3. TURN THE SHUTTER OFF.
4. Press the OFF button.
5. To get the specimen, turn the FAILSAFE key first. You will hear a beeping sound. Then open the door.
6. Then check the radiation level in the equipment by using the Geiger counter working your way into the chamber. If it is safe enough to do so, take off the specimen.

For 2THETA measurements:

1. Use the 1 degree DIVERGENCE slit, 1 degree SCATTER silt and the 0.3 mm RECEIVING slit.
2. Repeat the start-up procedure.
3. Once the start-up procedures have been performed, turn the SHUTTER to EXT.
4. Start-up JADE program by C>MENU from the computer.
5. Once the opening window appears go to QUALITATIVE PROGRAMS.

6. Go to the SET DATUM program. Normally, let the datum remain the same as before. Exit the window by pressing ENTER until you get out of this window.

7. Then go to the SET HV/PHA program. Normally, the values given on the window should not be tampered with. Exit the window by pressing ENTER until you get out.

8. Then proceed to the SCAN CONDITIONS menu. When the cursor appears on the SET NUMBERS just enter to get to the next menu.

9. Then go to the AXIS menu and make sure that is says 2 THETA/THETA-REFL. This can be changed using the arrow keys on the keyboard.

10. Then choose the START and STOP angles. The angle ranges from 15 degrees to 120 degrees.

11. Change the SAMPLING INTERVAL to the interval which you want.

12. Leave the DATA TYPE and FULL SCALE range to the default value. To exit this menu press Ctrl Z. After all of these steps, go to the MEASUREMENT menu to start data acquisition.

For POLEFIGURE measurements:

1. The divergence slit will remain at 1 degree but the scatter slit must one size larger than the size of the receiving slit (in mm). The Schultz slit must be fixed as well. DO NOT FORGET THIS.

2. From the main menu, go to the POLE FIGURE DATA COLLECTION PROGRAM. Do not set the datum but go straight to the SET SCAN CONDITIONS menu.

3. To obtain the pole figure values, use the beta step to be 5 degrees, beta speed to be 360 degrees per minute and the alpha step at 5 degrees.

4. Then exit this menu to go to the MEASUREMENT menu to start collecting data of the pole figure measurements.

5. To obtain the values for the background measurements, the procedure is the same except that data is taken approximately 2 degrees away from the peaks. This is done

at a place where the values obtained from the 2THETA measurements are relatively flat. This is due to the background radiation.

6. Go back to the SET SCAN CONDITIONS in the POLE FIGURE DATA COLLECTION PROGRAM.

7. Change the beta step to 360 degrees with beta speed of 640 degrees per minute.

8. Then go the MEASUREMENT menu to start collecting the data for the background emission.

9. Always remember the name of files you are working on because there are always many files which are saved into the hard disk.